Mechanics of Flapping Flight: Analytical Formulations of Unsteady Aerodynamics, Kinematic Optimization, Flight Dynamics, and Control

Haithem E. Taha

Dissertation submitted to the Faculty of the
Virginia Polytechnic Institute and State University
in partial fulfillment of the requirements for the degree of

Doctor of Philosophy
in
Engineering Mechanics

Muhammad R. Hajj, Chair
Ali H. Nayfeh, Co-chair
Craig A. Woolsey
Robert A. Canfield
Saad A. Ragab
Jeff Borggaard

Oct 25, 2013
Blacksburg, Virginia

Keywords: Flapping Flight, Finite-State Unsteady Aerodynamics, Calculus of Variations and Optimal Control, Flight Dynamics, Nonlinear Time-Periodic Systems, Averaging Theorem, Geometric Control, Nonlinear Dynamics and Saturation

Mechanics of Flapping Flight: Analytical Formulations of Unsteady Aerodynamics, Kinematic Optimization, Flight Dynamics, and Control

Haithem E. Taha

ABSTRACT

A flapping-wing micro-air-vehicle (FWMAV) represents a complex multi-disciplinary system whose analysis invokes the frontiers of the aerospace engineering disciplines. From the aerodynamic point of view, a nonlinear, unsteady flow is created by the flapping motion. In addition, non-conventional contributors, such as the leading edge vortex, to the aerodynamic loads become dominant in flight. On the other hand, the flight dynamics of a FWMAV constitutes a nonlinear, non-autonomous dynamical system. Furthermore, the stringent weight and size constraints that are always imposed on FWMAVs invoke design with minimal actuation. In addition to the numerous motivating applications, all these features of FWMAVs make it an interesting research point for engineers.

In this Dissertation, some challenging points related to FWMAVs are considered. First, an analytical unsteady aerodynamic model that accounts for the leading edge vortex contribution by a feasible computational burden is developed to enable sensitivity and optimization analyses, flight dynamics analysis, and control synthesis. Second, wing kinematics optimization is considered for both aerodynamic performance and maneuverability. For each case, an infinite-dimensional optimization problem is formulated using the calculus of variations to relax any unnecessary constraints induced by approximating the problem as a finite-dimensional one. As such, theoretical upper bounds for the aerodynamic performance and maneuverability are obtained. Third, a design methodology for the actuation mechanism is developed. The proposed actuation mechanism is able to provide the required kinematics for both of hovering and forward flight using only one actuator. This is achieved by exploiting the nonlinearities of the wing dynamics to induce the saturation phenomenon to transfer energy from one mode to another. Fourth, the nonlinear, time-periodic flight dynamics of FWMAVs is analyzed using direct and higher-order averaging. The region of applicability of direct averaging is determined and the effects of the aerodynamic-induced parametric excitation are assessed. Finally, tools combining geometric control theory and averaging are used to derive analytic expressions for the *Symmetric Products*, which are vector fields that directly affect the acceleration of the averaged dynamics. A design optimization problem is then formulated to bring the maneuverability index/criterion early in the design process to maximize the FWMAV maneuverability near hover.

Dedication

The almighty Allah says in his holy book, the Quran, chapter Al-Haj (the pilgrimage), verses 73-74

which may be translated as

O people, an example is presented, so listen to it. Indeed, those you invoke besides Allah will never create [as much as] a fly, even if they gathered together for that purpose. And if the fly should steal away from them a [tiny] thing, they could not recover it from him. Weak are the pursuer and pursued. They have not appraised Allah with true appraisal. Indeed, Allah is Powerful and Exalted in Might.

Acknowledgments

I would like to thank my supervisor Prof. Muhammad Hajj for his unprecedented technical, spiritual, and financial supports. I was lucky to have a lot of very fruitful discussions with him during the course of this work. In addition, he was always providing me with sincere beneficial advices regarding my career. Also, I would like to thank my co-advisor Prof. Ali Nayfeh for his very rich technical support and guidance; a great scientist who is really keen to teach his students. He is the kind of professor who endows confidence and enthusiasm to his students.

I would like to thank Prof. Craig Woolsey for his tremendous help and support. He is my nonlinear and geometric control mentor. I have really learnt a lot from him. Indeed, he has shaped my future career. I am so grateful to Prof. Robert Canfield for his valuable discussions and suggestions that have really led to better final works. In addition to being my mentor for the optimization world, I would say that my contact with Prof. Canfield has considerably affected my academic personality. Also, I am so grateful for Professors Saad Ragab and Jeff Borggaard for their continuous help and cooperation. I am so grateful to Prof. Mayuresh Patil for his continuous valuable suggestions and recommendations during our MAV weekly meetings. I would like to express my deepest gratefulness to Prof. John Burns for his engraved teachings and Prof. Mokhtar Elnomrossy for his inspiration and guidance.

I would like to thank my wife Shaimaa and my daughter Nour for their surpassing help and indescribable endurance. Indeed, without them, I would never be able to make it. Also, I would like to express my deepest gratitude to my parents for their extra-ordinary spiritual support and encouragement. They were always unflinching pillars to my self, family and work.

I would like to thank my colleagues Dr. Ghommem, Dr. Aboelkassem, Dr. Abdelkefi, Dr. Mehmood, Sevak Tahmasian, Ahmed Roman, Mostafa Ramadan, Zhimiao Yan, and Yasmin Selim for their help and support. I would also like to thank my colleagues Youssef Bichiou, Hassan Fayed, Mohammed Zakaria, Mohammed Zein, Nejib Masghouni, Mohamed Jrad, Farid Jafary, and Hogjat Pendar for their continuous encouragement. Finally, I would like to thank my friends Mostafa Ali, Michael Tomaszewicz, Ahmed Adam,

Mohamed Mohamedin, Mohammed Magdy, Ahmed El-Sayed, Amr Nabil, Amr Hilal, Dr El-Boraei, Tariq Abuhamdia, Moatassim Fouda, Mohammed Shorbagy, and Mahmoud Zonfol for their continuous encouragement, sincere wishes of success, and lovely moments that made me pursue and overcome any hardships. Special thanks go to Prof. Sedki Riad for his continuous help, support and sincere advices.

Contents

List of Figures

List of Tables

Chapter 1

Introduction

In this chapter, a thorough literature review of the significant work done so far in the broad area of flight dynamics and control of flapping-wing micro-air-vehicles (FWMAVs) is presented. The review includes discussions of the design of wing kinematics, aerodynamic modeling, dynamic stability analysis, and control synthesis. The aim is to point to un-answered questions in these areas that would help in advancing knowledge about flapping flight. Section 1.1 provides the background and general analysis framework of flight dynamics of FWMAVs. In Sections 1.2, 1.3, and 1.4, flapping kinematics, aerodynamic modeling, and dynamic stability analysis are reviewed, respectively, and the associated issues and recommendations for future work are presented in each corresponding section. In Section 1.2, design and parametrization of flapping kinematics to achieve a high-control authority are discussed as well as designing flapping kinematics that is suitable for multiple flight modes. In Section 1.3, the physical aspects of the aerodynamics associated with flapping flight are listed. A review of most of the aerodynamic models in the literature of flapping flight is presented, stating what each model captures from those physical aspects. However, emphasis is given only to models used within the framework of flight dynamics and control of FWMAVs. In Section 1.4, the body dynamics and stability analysis are considered. The assumptions usually made in the literature of dynamics and control of FWMAVs (e.g., neglecting the wing inertia and averaging) are discussed along with their limitations. A review of the two main approaches for analyzing the dynamic stability of FWMAVs is provided. In Section 1.5, a review of the linear control design techniques as well as trials for nonlinear control design and motion planning for FWMAVs are provided. Section 1.6 concludes the review and provides recommendations for future work.

1.1 Preface

A general framework for the flight dynamics and control of FWMAVs is presented in Fig. 1.1. The flight dynamics encompass the flapping kinematics, the aerodynamic modeling, and the dynamic equations of motion. The kinematics design is performed to enhance the control authority, maneuverability, and aerodynamic performance. This design is also driven by the enabling actuation mechanism and the available power. The aerodynamic modeling is then performed using the wing motions selected in the kinematics design; this modeling can be performed with different fidelity levels. The loads obtained from the aerodynamic model are applied on the FWMAV body through the dynamic equations of motion, which in turn are used to analyze the dynamics of the flapping flight. This analysis includes simulation of the body motion, dynamic stability analysis, and design of the controller and actuation mechanism. The control block is used to assign kinematics modifications to the actuation mechanism in order to control the dynamics of the FWMAV body.

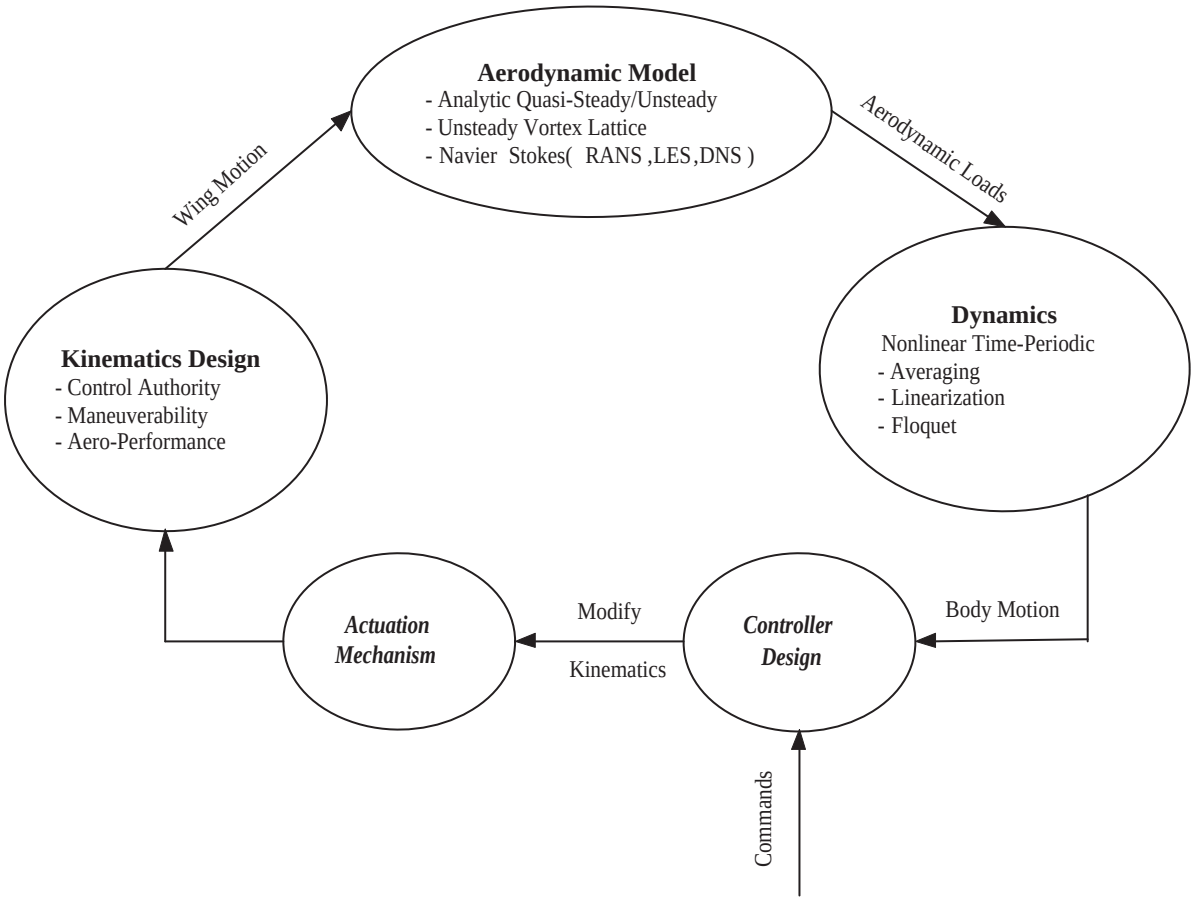

Figure 1.1: Framework of the flight dynamics of a FWMAV.

The flapping kinematics are usually described by the Euler angles of the wing with respect to the body: the back and forth flapping angle φ, the plunging angle ϑ, and the pitching angle η. These angles manipulate the velocity vector seen by the airfoil section. This velocity vector, along with the pitching angle and their time derivatives determine the aerodynamic loads. Figure 1.2 shows the three axis systems needed to formulate the problem of flight dynamics of a FWMAV: an inertially-fixed frame x_I, y_I, and z_I; a body-fixed frame x_b, y_b, and z_b; and a wing-fixed frame x_w, y_w, and z_w. If the wing flexibility is considered, a wing-deformed frame would be also needed. The x_b-axis points forward, the y_b-axis points to the right wing, and the z_b-axis completes the triad. Any sequence of the Euler angles could be used to describe the body-fixed frame with respect to the inertial frame. However, the Euler angles sequence yaw-pitch-roll $\psi - \theta - \phi$, commonly used with conventional aircraft (13), has also been used for flapping flight (14; 15; 11; 16). The wing-fixed frame is taken to coincide with the body-fixed frame for zero wing kinematic angles. Thus, the sequence of Euler angles $\varphi - \vartheta - \eta$, flapping-plunging-pitching, is then used to describe the wing frame with respect to the body frame.

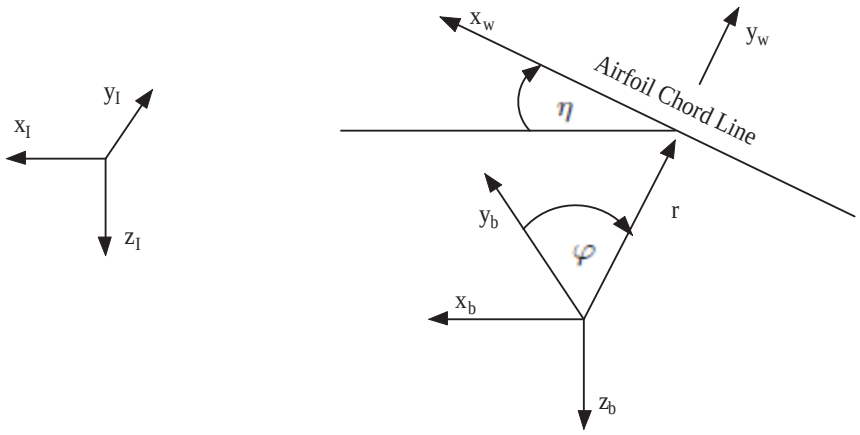

Figure 1.2: Axis systems used to describe the dynamics of a FWMAV.

Because the target of the kinematics is to manipulate the velocity vector seen by the airfoil section, it is essential to provide a mathematical relation between these quantities. The velocity vector seen by the airfoil section $\boldsymbol{V_a}$ consists of two parts: the first is due to the flapping kinematics relative to the body and the second is due to the body motion itself $\boldsymbol{V_b}$. Hence,

$$\boldsymbol{V_a} = \boldsymbol{V_b} + \boldsymbol{\omega}_{I-b} \times \boldsymbol{r} + \boldsymbol{\omega}_{b-w} \times \boldsymbol{r} \tag{1.1}$$

where $\boldsymbol{r}$ is the position vector of the origin of the wing-frame with respect to the origin of the body-fixed

frame and $\boldsymbol{\omega}_{I-b}$ and $\boldsymbol{\omega}_{b-w}$ are the angular velocity vectors of the body with respect to the inertial frame and the wing with respect to the body-fixed frame, respectively. Hedrick et al. (17) and Faruque and Humbert (18) emphasized the effect of the airfoil velocity due to the body motion; that is, the first two terms in Eq. (1.1). Yet, in hovering configurations, where high-frequency flapping and slow or even no body maneuvers exist, it is justifiable to neglect these terms and consider only the velocity due to flapping (1; 15; 11; 16; 19; 8; 9; 7). Doing so yields the airfoil velocity in the wing frame as

$$\begin{aligned} V_{x_w} &= -r\dot{\varphi}\cos\vartheta\cos\eta - r\dot{\vartheta}\sin\eta \\ V_{z_w} &= -r\dot{\varphi}\cos\vartheta\sin\eta + r\dot{\vartheta}\cos\eta \end{aligned} \tag{1.2}$$

The velocity seen by the airfoil section, as presented in Eq. (1.2), is the input to the aerodynamic model, which yields the aerodynamic forces and moments. The resulting aerodynamic loads are usually represented either in the relative-wind frame (lift and drag) or in the wing frame (normal and tangential forces). The relative-wind frame is the same as the wing frame but before the last pitching rotation. Thus, the relation between the loads in the two frames is given by

$$\begin{aligned} C_L &= C_N\cos\eta - C_T\sin\eta \\ C_D &= C_N\sin\eta + C_T\cos\eta \end{aligned} \tag{1.3}$$

where C_L and C_D are the lift and drag coefficients, respectively, and C_N and C_T are the normal and tangential force coefficients, respectively.

The dynamic equations of the body motion are usually written in the body frame. As such, it is necessary to transfer the aerodynamic loads from the relative-wind frame to the body frame; that is,

$$\begin{pmatrix} X \\ Y \\ Z \end{pmatrix} = \left[R_\vartheta R_\varphi\right]^T \begin{pmatrix} -d \\ 0 \\ -\ell \end{pmatrix} \tag{1.4}$$

$$\begin{pmatrix} L \\ M \\ N \end{pmatrix} = \left[R_\vartheta R_\varphi\right]^T \left(\boldsymbol{r}_{cp}^{(w)} \times \begin{pmatrix} -d \\ 0 \\ -\ell \end{pmatrix} \right) \tag{1.5}$$

where $\boldsymbol{r}_{cp}^{(w)}$ is the position vector of the wing center of pressure in the wing frame whose components are

$(x_{cp}^{(w)}, y_{cp}^{(w)}, 0)$ and X, Y, Z, L, M, and N, are the contributions of the lift and drag (ℓ and d) of the airfoil section to the generalized forces in the body-fixed frame. Most insects have an approximately horizontal stroke plane in hover (20; 21); that is, no out-of-plane motion (the plunging angle $\vartheta = 0$). As such, the total flapping velocity, seen by an airfoil section that is a distance r from the wing root, is just $r\dot{\varphi}$ with an angle of attack $\alpha \equiv \eta$. This latter configuration is used in Refs. (1; 15; 11; 16; 22; 19; 9; 7). Using this formulation with the blade-element approach, one obtains the lift and drag forces as

$$\begin{aligned} \ell &= 2\int_0^R \tfrac{1}{2}\rho_{air}(r\dot{\varphi})^2 c(r) C_L(\alpha)\, dr = K_L\dot{\varphi}^2 \\ d &= 2\int_0^R \tfrac{1}{2}\rho_{air}(r\dot{\varphi})^2 c(r) C_D(\alpha)\, dr = K_D\dot{\varphi}^2 \end{aligned} \tag{1.6}$$

where ρ_{air} is the air density and $c(r)$ is the spanwise chord-distribution. The aerodynamic loads in the body frame are then given by

$$\begin{pmatrix} X \\ Y \\ Z \end{pmatrix} = \begin{pmatrix} -d\cos\varphi \\ -d\sin\varphi \\ -\ell \end{pmatrix} \tag{1.7}$$

$$\begin{pmatrix} L \\ M \\ N \end{pmatrix} = \begin{pmatrix} -\ell(y_{cp}^{(w)}\cos\varphi + x_{cp}^{(w)}\sin\varphi) \\ -\ell(y_{cp}^{(w)}\sin\varphi - x_{cp}^{(w)}\cos\varphi) \\ dy_{cp}^{(w)} \end{pmatrix} \tag{1.8}$$

For a high flapping frequency relative to the natural frequencies of the body motion, the cycle-average aerodynamic loads can be used instead of the instantaneous aerodynamic loads (23; 2; 15; 11; 16; 7; 24; 8; 9; 10; 25). From a dynamics perspective, this converts the system from a non-autonomous (time-variant) system to an autonomous system. Details about the validity of the averaging assumption are discussed in Section 1.4. Furthermore, the inertia effects of the wings on the body are usually neglected in the averaged sense (2; 15; 16; 26; 27; 7; 24; 8; 9; 10; 25). With these two assumptions, the dynamic equations of motion

are exactly the same as those used in conventional aircraft (13); that is,

$$\begin{aligned} m(\dot{u} + qw - rv + g\sin\theta) &= X \\ m(\dot{v} + ru - pw - g\sin\phi\cos\theta) &= Y \\ m(\dot{w} + pv - qu - g\cos\phi\cos\theta) &= Z \\ I_x\dot{p} - I_{xz}\dot{r} + (I_z - I_y)qr_\omega - I_{xz}pq &= L \\ I_y\dot{q} + (I_x - I_z)r_\omega p + I_{xz}(p^2 - r_\omega^2) &= M \\ I_z\dot{r_\omega} - I_{xz}\dot{p} + (I_y - I_x)pq + I_{xz}r_\omega q &= N \end{aligned} \tag{1.9}$$

and the kinematic equations are

$$\begin{aligned} \dot{\psi} &= (q\sin\phi + r\cos\phi)/\cos\theta \\ \dot{\theta} &= q\cos\phi - r\sin\phi \\ \dot{\phi} &= p + (q\sin\phi + r\cos\phi)\tan\theta \end{aligned} \tag{1.10}$$

Equations (1.9,1.10) comprise nine dynamic equations for the body velocities (u, v, and w), the angular velocities (p, q, and r_ω), and the body Euler angles (ψ, θ, and ϕ). These equations are augmented with the kinematic equations that relate the body velocities to the rate of change of the position of the body center of mass in the inertial frame.

1.2 Flapping Kinematics

Configurations of the flapping kinematics that have been used in the literature for FWMAVs can be divided into three types. In the first type, harmonic functions are assumed to ease the analysis (1; 2; 26; 28; 29; 22). In the second type, observed kinematics from insects in nature are used (24; 15; 11; 16). In the third type, the kinematics are designed for specific control purposes (7; 27; 8; 9; 10; 25). The latter type is discussed in details here.

1.2.1 Design and Parametrization of Flapping Kinematics for High-Control Authority

Schenato, Campolo, and Sastry (7) were the first to propose hovering kinematics, with specific parametrization to obtain high-control authority over the FWMAV. They considered only one actuator per wing to

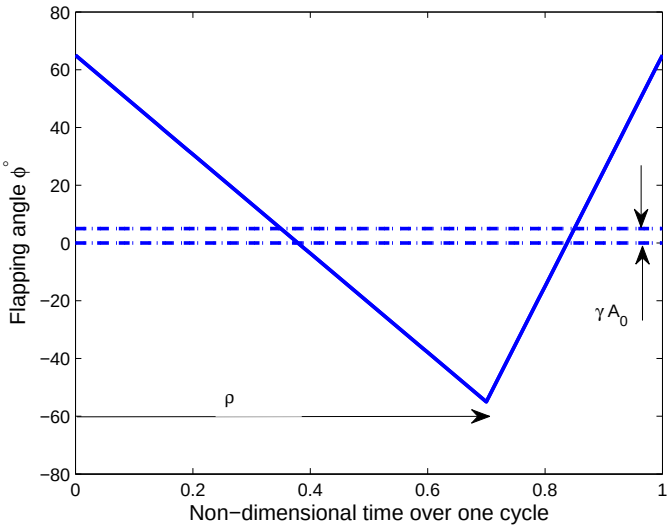

Figure 1.3: The flapping position angle proposed by Schenato et al. (7)

control the back and forth flapping position angle φ. They proposed flapping with a constant angular velocity during each half stroke, like the saw tooth function (shown in Fig. 1.3). They also used passive pitching to maintain a constant angle of attack of 45° throughout the cycle because it is thought that this configuration gives maximum lift. They did not consider plunging (out-of-plane motion). Their kinematics are then described by

$$\varphi(t) = \begin{cases} A_0(1+\kappa)(1-\frac{2t}{\rho T}) + \gamma A_0, & 0 \le t \le \rho T \\ A_0(1+\kappa)(2\frac{t-\rho T}{(1-\rho)T} - 1) + \gamma A_0, & \rho T \le t \le T \end{cases} \tag{1.11}$$

where γA_0 is used to represent an offset/bias for the motion, κ is used to manipulate the amplitude of the motion, and ρ represents the duration of the downstroke relative to the whole cycle; that is, $\rho = 1/2$ indicates symmetric flapping. An asymmetric flapping is needed to generate forward/backward thrust on both wings and, consequently, yawing moments. Thus, three kinematic parameters are tunable for each wing (κ, ρ, and γ). Figure 1.3 shows the flapping position angle throughout the cycle.

As for aerodynamic modeling, they used a quasi-steady (QS) aerodynamic model based on the measurements of Dickinson, Lehmann, and Sane (3). They took only the normal force into account, with the normal force coefficient being $C_N = 3.4 \sin\alpha$ where α is the angle of attack, which they kept fixed at 45°. They concentrated the normal forces at the $c/4$ point of the $0.7R$ section. They used these parameters to estimate the aerodynamic loads from Eqs. (1.3), (1.6), (1.7), and (1.8). Averaging these aerodynamic loads over the

cycle and linearizing the averaged forces about hovering (i.e, $\gamma = \kappa = 0$ and $\rho = 1/2$), they obtained

$$\begin{pmatrix} \overline{X} \\ \overline{Y} \\ \overline{Z} \end{pmatrix} = F_0 \begin{pmatrix} 0 \\ 0 \\ -1 \end{pmatrix} + F_0 \begin{pmatrix} -w_1 \\ 0 \\ -w_2 \end{pmatrix} \tag{1.12}$$

$$\begin{pmatrix} \overline{L} \\ \overline{M} \\ \overline{N} \end{pmatrix} = M_0 \begin{pmatrix} -w_3 \\ w_4 \\ -w_5 \end{pmatrix} \tag{1.13}$$

where

$$F_0 = \frac{32FA_0^2}{T^2},\ M_0 = \frac{32FRA_0^3}{T^2},\ F = \frac{1}{4}\rho_{air}R^2SC_N$$

and A_0 and T can be chosen to make F_0 balance the FWMAV weight. The linearized forces and moments are then related to the kinematic parameters through

$$\begin{aligned} w_1 &= -\mathrm{sinc}(\tfrac{\mathrm{A}_0}{4})[(\rho_{\mathrm{LW}} - \tfrac{1}{2}) + (\rho_{\mathrm{RW}} - \tfrac{1}{2})] \\ w_2 &= \kappa_{LW} + \kappa_{RW} \\ w_3 &= -\mathrm{sinc}(\tfrac{\mathrm{A}_0}{4})[\kappa_{\mathrm{LW}} - \kappa_{\mathrm{RW}}] \\ w_4 &= -\mathrm{sinc}(\tfrac{\mathrm{A}_0}{4})[\gamma_{\mathrm{LW}} + \gamma_{\mathrm{RW}}] \\ w_5 &= (\rho_{LW} - \tfrac{1}{2}) - (\rho_{RW} - \tfrac{1}{2}) \end{aligned} \tag{1.14}$$

Equation (1.14) represents a linear map between the six kinematic parameters for both wings and the aerodynamic loads. Each equation can be intuitively interpreted from the physics of flight. Firstly, we note that the amplitude manipulates the vertical lift. Thus, any change in the amplitudes from the hovering values (i.e., $\kappa's \neq 0$) would change the vertical lift force w_2. A rolling moment w_3 can be generated if the amplitude change is performed asymmetrically on the two wings (i.e., $\kappa_{LW} \neq \kappa_{RW}$). Secondly, the relative timing between the upstroke and the downstroke (parameterized by ρ) manipulates the forward thrust. As such, any difference in the speed between the upstroke and downstroke on both wings (i.e., $\rho_{LW} = \rho_{RW} \neq \frac{1}{2}$) would result in forward/backward thrust w_1. A yawing moment w_5 can be generated if the speeds are changed asymmetrically on the two wings (i.e., $\rho_{LW} \neq \rho_{RW}$). Thirdly, the offset shifts the center of pressure of the resultant aerodynamic forces longitudinally. Thus, a non-zero pitching moment w_4 can be produced by making some offset. This linear map can be thought of as a control effectiveness matrix, whose rank

indicates how many degrees of freedom can be controlled independently. Using the proposed kinematic parametrization, they obtained a rank five control effectiveness matrix. All of the degrees of freedom, except the translation in the y_b-direction, can be independently controlled. They proved that the full nonlinear system is locally accessible and its linearization about hover is controllable.

Doman, Oppenheimer, and Sigthorsson in (19; 8; 9) emphasized the importance of minimal actuation in FWMAVs, as this aspect was the main reason for the successful flapping flight of the Harvard Robofly (30). It had only one actuator for both wings to control the back and forth flapping position angle φ symmetrically. That configuration was, however, only intended for climbing upward, no asymmetric maneuvers were required. Doman et al. adopted the same idea used by Schenato et al. (7); they had only one actuator per wing and used passive pitching to maintain a constant angle of attack throughout the cycle. However, Doman et al. (9) proposed different kinematic functions based on the flapping angle used in the Harvard Robofly (30) and observed by Willmott and Ellington (31) in the hawkmoth flight; it is a simple harmonic $\varphi(t) = \cos \omega t$. In order to produce forward/backward thrust, they introduced asymmetry between the upstroke and the downstroke. Their kinematics are then described by

$$\varphi_u(t) = \cos[(\omega - \delta)t] \text{ and } \varphi_d(t) = \cos[(\omega + \sigma)t] \tag{1.15}$$

where δ is "what they called" the split-cycle parameter and is used to produce the asymmetry. The combination of the two modified-frequency half strokes must have the same period as the original one; that is, $\frac{1}{2}T_u + \frac{1}{2}T_d = T$, where $T_u = \frac{2\pi}{\omega-\delta}$ is the upstroke period, $T_d = \frac{2\pi}{\omega+\sigma}$ is the downstroke period, and $T = \frac{2\pi}{\omega}$ is the full period. This condition dictates that $\sigma = \frac{\omega\delta}{\omega-2\delta}$, which in turn results in a discontinuity at the end of each cycle. Because the upstroke ends at $t = \frac{\pi}{\omega-\delta}$, $\varphi_u(t = \frac{\pi}{\omega-\delta}) = \cos \pi = -1$, while

$$\varphi_d\left(t = \frac{\pi}{\omega - \delta}\right) = \cos\left(\frac{\pi(\omega + \sigma)}{\omega - \delta}\right) = \cos\left(\frac{\pi\omega}{\omega - 2\delta}\right)$$

To eliminate this discontinuity in the wing position at the end of each cycle, they applied a phase shift to the downstroke; that is, $\varphi_d = \cos[(\omega + \sigma)t + \zeta]$ where $\zeta = \frac{-2\pi\delta}{\omega-2\delta}$. As such, their proposed kinematics are given by

$$\begin{aligned} \varphi_u(t) &= \cos[(\omega - \delta)t], \qquad 0 \le t \le \tfrac{\pi}{\omega-\delta} \\ \varphi_d(t) &= \cos[(\omega + \sigma)t + \zeta], \; \tfrac{\pi}{\omega-\delta} \le t \le \tfrac{2\pi}{\omega} \end{aligned} \tag{1.16}$$

where $\sigma = \frac{\omega\delta}{\omega-2\delta}$ and $\zeta = \frac{-2\pi\delta}{\omega-2\delta}$. Figure 1.4 shows the symmetric flapping case ($\delta = 0$), along with cases for advanced-downstroke, impeded-upstroke ($\delta > 0$) and advanced-upstroke, impeded-downstroke ($\delta < 0$). Clearly two parameters are used to parameterize the kinematics of each wing: the fundamental frequency ω

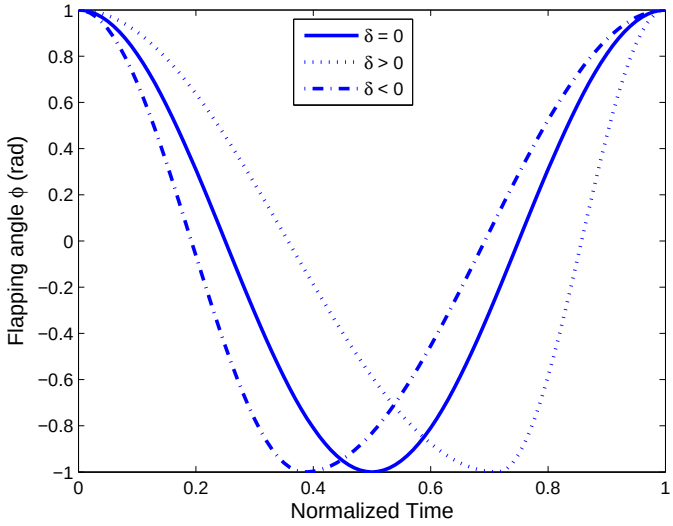

Figure 1.4: The flapping position angle proposed by Oppenheimer et al. (8) and Doman et al. (9)

and the split-cycle parameter δ.

As for the aerodynamic modeling, Doman et al. (19; 9) used the aerodynamic model of Dickinson, Lehmann, and Sane (3). Because of its simplicity, it is the most common aerodynamic model used in the literature of flight dynamics of FWMAVs. The lift and drag coefficients are given by

$$\begin{aligned} C_L &= 0.225 + 1.58\sin(2.13\alpha - 7.20) \\ C_D &= 1.92 - 1.55\cos(2.04\alpha - 9.82) \end{aligned} \tag{1.17}$$

They substituted these coefficients into Eqs. (1.6)-(1.8) to obtain the aerodynamic loads in the body frame and then averaged the outcomes over the flapping cycle. For any generalized force G, they obtained the cycle average by

$$\overline{G} = \frac{\omega}{2\pi}\int_0^{\frac{2\pi}{\omega}} G(\varphi(t))\,dt = \frac{\omega}{2\pi}\left[\int_0^{\frac{\pi}{\omega-\delta}} G(\varphi_u(t))\,dt + \int_{\frac{\pi}{\omega-\delta}}^{\frac{2\pi}{\omega}} G(\varphi_d(t))\,dt\right] \tag{1.18}$$

Substituting the proposed kinematics for $\varphi(t)$ into the aerodynamic loads, Eqs. (1.6)-(1.8), and averaging the outcomes using Eq. (1.18) results in quite difficult integrals. They found integrands like $\cos(\cos\omega t)$ and $\sin(\cos\omega t)$, which do not have indefinite integral solutions. Fortunately, Oppenheimer et al. (8) evaluated these integrals over the required intervals from the results presented in Ref. (32). The evaluations required the Bessel function of first kind $J_1(.)$ and the Struve function. The Struve function vanishes at the boundaries

of the integrals. Finally, they obtained

$$
\begin{aligned}
\overline{X}_{R,LW} &= -\tfrac{1}{2}K_D J_1(1)\omega_{R,LW}(\delta_{R,LW}+\sigma_{R,LW}) \\
\overline{Y}_{R,LW} &= 0 \\
\overline{Z}_{R,LW} &= -\tfrac{1}{4}K_L\omega_{R,LW}(2\omega_{R,LW}-\delta_{R,LW}+\sigma_{R,LW}) \\
\overline{L}_{R,LW} &= \mp\tfrac{1}{2}K_L\omega_{R,LW}[(y_{cp}^{(w)}J_1(1)+\tfrac{1}{4}\varpi)(2\omega_{R,LW}-\delta_{R,LW}+\sigma_{R,LW})] \\
\overline{M}_{R,LW} &= \tfrac{1}{2}K_L\omega_{R,LW}\left[x_{cp}^{(w)}J_1(1)\cos\alpha(\delta_{R,LW}+\sigma_{R,LW})+\tfrac{1}{2}\Delta X_{R,LW}(2\omega_{R,LW}-\delta_{R,LW}+\sigma_{R,LW})\right] \\
&\quad +\tfrac{1}{2}K_D J_1(1)\omega_{R,LW}(\delta_{R,LW}+\sigma_{R,LW})(x_{cp}^{(w)}\sin\alpha-\Delta Z_{R,LW}) \\
\overline{N}_{R,LW} &= \pm\tfrac{1}{4}K_D\omega_{R,LW}(\delta_{R,LW}+\sigma_{R,LW})[y_{cp}^{(w)}+\varpi J_1(1)]
\end{aligned}
\tag{1.19}
$$

where K_L and K_D are defined in Eq. (1.6), $\Delta X_{R,LW}$ and $\Delta Z_{R,LW}$ are the shifts from the origin (vehicle center of gravity cg) to the root hinge in the body frame, and ϖ is the width of the vehicle fuselage (insect abdomen).

One can extract some physical aspects from Eq. (1.19). The produced average lift force $-\overline{Z}$ is always positive and the average side force is strictly zero with these kinematics. For a zero split-cycle parameter δ, one cannot produce average forward thrust $\overline{X}$ or yawing moment $\overline{N}$. However, one can produce rolling moment $\overline{L}$ by running one wing faster than the other $\omega_{RW}\neq\omega_{LW}$. It is interesting to note that, even with a zero δ, there still exists an average pitching moment $\overline{M}$ for non zero ΔX. So, from a design point of view, it is better to align the hinges of the wings with the vehicle cg to obtain zero pitching moment during hover naturally without any active pitch trim.

Oppenheimer et al. (8) derived analytic formulas for the following control derivatives (sensitivities) near hover where $\omega_{R,LW}=\omega_0=\sqrt{\frac{mg}{K_L(\alpha)}}$ and $\delta_{R,LW}=0$:

$$
\frac{\partial\overline{G}}{\partial\omega_{RW}},\ \frac{\partial\overline{G}}{\partial\delta_{RW}},\ \frac{\partial\overline{G}}{\partial\omega_{LW}},\ \frac{\partial\overline{G}}{\partial\delta_{LW}}
$$

We recall that a zero ΔX is favorable for a self-pitch trim. However, the resulting control derivative $\frac{\partial\overline{M}}{\partial\omega_{R,LW}}=0$; that is, the wings angular frequencies have no control authority over the pitching motion around hover. This means that pitch control is achieved via the split-cycle parameters $\delta_{R,LW}$, which, in turn, give rise to undesirable forward forces, indicating the need for an independent pitch control. To overcome this ptoblem, Oppenheimer et al. (8) and Doman et al. (9) proposed the use of a bob-weight that shifts the vehicle cg longitudinally along the x_b-direction which yields independent pitch control. The bob-weight results in a new moment term that must be added to the aerodynamic moments; that is, the moment due to the cg shift,

which yields

$$\begin{pmatrix} L \\ M \\ N \end{pmatrix} = \begin{pmatrix} L \\ M \\ N \end{pmatrix}_{aero} + \begin{pmatrix} x_{cg} \\ 0 \\ 0 \end{pmatrix} \times (m_0 + m_B)g \begin{pmatrix} -\sin\theta \\ \sin\phi\cos\theta \\ \cos\phi\cos\theta \end{pmatrix} \tag{1.20}$$

where x_{cg} is the cg deflection of the whole vehicle from the original point, which is related to the bob-weight displacement x_B through the simple relation $x_{cg} = \frac{x_B m_B}{m_0 + m_B}$, with m_0 and m_B being the masses of the vehicle and the bob-weight, respectively. The deflection in the z_b-direction is neglected, and a linear relation between the bob-weight control voltage and its displacement is assumed; that is, $\frac{\partial x_B}{\partial V_B} = K_B$.

Oppenheimer et al. (8) and Doman et al. (9) constructed the following linear map, similar to Eq. (1.14), between the change in the generalized forces in the body frame and the control parameters (four kinematic parameters and the bob-weight voltage):

$$\begin{pmatrix} \Delta\overline{X} \\ \Delta\overline{Y} \\ \Delta\overline{Z} \\ \Delta\overline{L} \\ \Delta\overline{M} \\ \Delta\overline{N} \end{pmatrix} = \begin{bmatrix} -K_D J_1(1)\omega_0 & 0 & -K_D J_1(1)\omega_0 & 0 & 0 \\ 0 & 0 & 0 & 0 & 0 \\ 0 & B_{32} & 0 & B_{34} & 0 \\ 0 & B_{42} & 0 & B_{44} & 0 \\ B_{51} & 0 & B_{53} & 0 & B_{55} \\ \frac{1}{2}K_D J_1(1)\omega_0(y_{cp}^{(w)} + \varpi J_1(1)) & 0 & -\frac{1}{2}K_D J_1(1)\omega_0(y_{cp}^{(w)} + \varpi J_1(1)) & 0 & 0 \end{bmatrix} \begin{pmatrix} \delta_{RW} \\ \Delta\omega_{RW} \\ \delta_{LW} \\ \Delta\omega_{LW} \\ V_B \end{pmatrix}$$

$$= [B_{6x5}](\hat{\boldsymbol{u}}_{\boldsymbol{5x1}}) \tag{1.21}$$

where

$$B_{32} = B_{34} = -K_L\omega_0, \;\; B_{42} = -B_{44} = -2K_L\omega_0 \left[y_{cp}^{(w)} J_1(1) + \frac{1}{4}\varpi \right],$$

$$B_{51,3} = J_1(1)\omega_0 \left[K_L x_{cp}^{(w)} \cos\alpha + K_D(x_{cp}^{(w)} \sin\alpha - \Delta Z_{R,LW}) \right],$$

$$B_{55} = K_B m_B g \cos\theta_{hover}$$

The matrix $[B]$ can be thought of as a control effectiveness matrix for the vector of the control parameters $\hat{\boldsymbol{u}}$. The rank of $[B]$ is five, indicating the authority to independently control five degrees of freedom; that is, all but the translational motion in the y_B-direction. This result is similar to that of Schenato et al. (7), with the exception that the latter did not need a bob-weight. On the other hand, the proposed kinematics by Oppenheimer et al. (8) are more feasible because the kinematic functions are smoother and the kinematic

parametrization is more realizable. Both works have a split-cycle parameter. Oppenheimer et al. used the frequency of the wings for vertical force manipulation, which is realizable through some speed control of the actuator. Schenato et al. used the amplitude of the motion instead, which might be more difficult to realize.

Doman et al. (9) linearized the dynamic equations about hover, thereby reducing them to second-order decoupled equations of the form $\ddot{\chi} = \hat{u}$. Hence, a single-channel control could be applied on each equation separately. The following control law guarantees the desired under-damped response for the state variable χ with a natural frequency ω_n and damping ratio ζ:

$$\hat{u} = -\omega_n^2(\chi - \chi_d) - 2\zeta\omega_n(\dot{\chi} - \dot{\chi_d}) \tag{1.22}$$

where χ_d and $\dot{\chi}_d$ are the desired/command values for this degree of freedom and its velocity, respectively. This control law is applied on all channels (degrees of freedom) except the y_B-channel; that is,

$$\begin{aligned} \Delta\overline{X}_{com} &= -\omega_{n,X}^2 x_e^{(b)} - 2\zeta_X\omega_{n,X}\dot{x}_e^{(b)} \\ &\vdots \\ \Delta\overline{N}_{com} &= -\omega_{n,N}^2\psi_e - 2\zeta_N\omega_{n,N}\dot{\psi}_e \end{aligned} \tag{1.23}$$

where the subscript e refers to the error in the signal from the desired trajectory. Having obtained the commands for these attainable five forces and moments, they augmented them with zero $\Delta\overline{Y}_{com}$. Performing a pseudo inverse for $[B]$ in Eq. (1.21), they obtained the five control inputs. These inputs were then passed through a zero-order hold to keep them unchanged during the cycle. This is the inner-loop control. Additionally, there is an outer loop control that was used to determine the error in the vehicle position and attitude. In the outer-loop, they followed the technique of yaw-transfer. In this technique, the vehicle first adjusts its heading while hovering to head toward the desired target, and then it transfers in that direction while adjusting its attitude. They simulated their designed controller to fly over five way points. The controller performed well except for the excessive required displacements from the bob-weight, which exceeded $2.2mm$. In fact, this limitation stimulated their follow-on research (33; 10; 25).

Doman et al. (9) found that an excessive bob-weight displacement is required during the simulation of their designed controller, which makes its use questionable. Furthermore, Doman and co-workers (19; 8; 9; 33; 10; 25; 34) noted the importance of minimum actuation in flapping flight. In their more recent work, Oppenheimer, Doman, and Sigthorsson (33; 10; 25) proposed kinematics to get rid of the bob-weight and obtain higher control authority over the FWMAV. Comparing the works of Schentao et al (7) and Doman et al. (9), we find that both have some manipulation for the vertical force: motion amplitude in the work

of Schenato et al. and wing frequency in the work of Doman et al. Also, both of them have a split-cycle parameter for manipulating the forward thrust. However, Doman et al. did not include any offset for the wing motion as Schenato et al. This was the main reason for the lack in pitch control authority with the previous proposed kinematics of Doman et al., and they overcame it by using the bob-weight. So, Doman et al. (10) and Oppenheimer et al. (25), in their recent work, included an offset for the motion. This offset seems to solve all of the problems; they were able to get rid of the bob-weight and provide a full rank (rank 6) control effectiveness matrix. They introduced a bias γ to the kinematic functions, which leads to

$$\begin{aligned} \varphi_u(t) &= \cos[(\omega-\delta)t] + \gamma, \qquad 0 \le t \le \tfrac{\pi}{\omega-\delta} \\ \varphi_d(t) &= \cos[(\omega+\sigma)t + \zeta] + \gamma, \; \tfrac{\pi}{\omega-\delta} \le t \le \tfrac{2\pi}{\omega} \end{aligned} \tag{1.24}$$

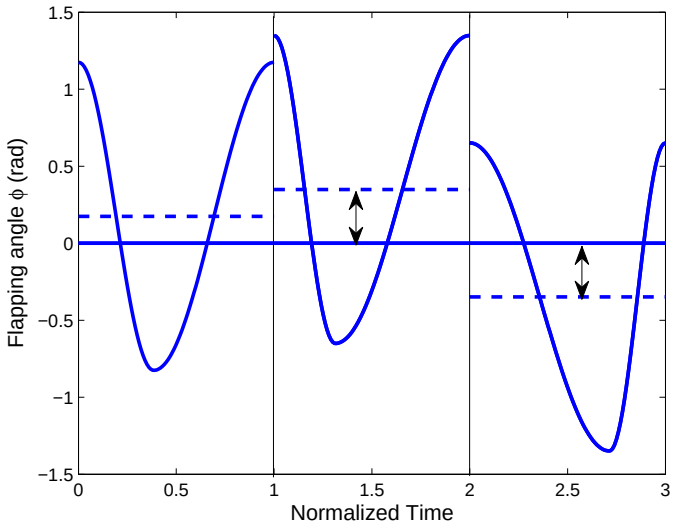

Figure 1.5: Discontinuity of Doman et al. (10) kinematics with a biasing term.

If the required bias for a certain cycle is different from that of the previous cycle, discontinuity will occur between the adjacent cycles (see Fig. 1.5). Doman et al. (10) solved this problem by modifying the amplitude of the second half of the downstroke as follows:

$$\varphi_{d2}(t) = (1+\Delta A)\cos[(\omega+\sigma)t+\zeta] + \gamma$$

The continuity between cycles ($\varphi_u(t=\frac{2\pi}{\omega}) = \varphi_{d2}(t=\frac{2\pi}{\omega})$) gives $\Delta A = \gamma_1 - \gamma_0$, which dictates a one-period

delay for applying the bias. Thus, the final form of the proposed kinematics is expressed as

$$\begin{aligned}
\varphi_u(t) &= \cos[(\omega-\delta)t]+\gamma, && 0 \le t \le \tfrac{\pi}{\omega-\delta} \\
\varphi_{d1}(t) &= \cos[(\omega+\sigma)t+\zeta]+\gamma, && \tfrac{\pi}{\omega-\delta} \le t \le \tfrac{\pi(3\omega-2\delta)}{2\omega(\omega-\delta)} \\
\varphi_{d2}(t) &= (1+\Delta A)\cos[(\omega+\sigma)t+\zeta]+\gamma, && \tfrac{\pi(3\omega-2\delta)}{2\omega(\omega-\delta)} \le t \le \tfrac{2\pi}{\omega}
\end{aligned} \tag{1.25}$$

where ω, δ, γ, and ΔA are all calculated at the beginning of the upstroke; ω and δ are applied immediately for the whole cycle; ΔA is applied for the second half of the down stroke of the current cycle; and γ is applied for the whole next cycle.

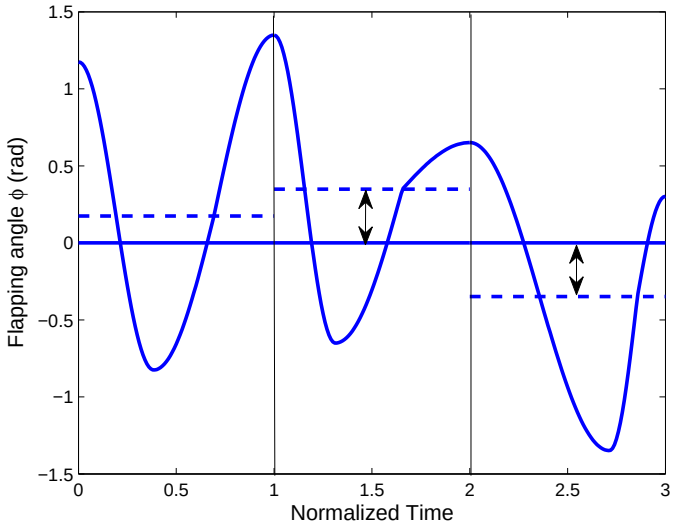

Figure 1.6: Doman et al. (10) final kinematics with a biasing term

.

Figure 1.6 shows the final proposed kinematics with the biasing term. They have three kinematic parameters (ω, δ, and γ) per wing. This results in a full rank control effectiveness matrix (rank 6), which means having full control authority over the six degrees of freedom of the FWMAV. The addition of the biasing term removes the need for a bob-weight and also adds the ability to produce a Y-force independently. On the other hand, the proposed kinematic functions are not smooth, they exhibit slope discontinuity between cycles, which might produce complex dynamics.

1.2.2 Design of Flapping Kinematics Suitable for Multiple Flight Modes

In contrast to the design and parametrization of flapping kinematics to obtain a high-control authority with minimum actuation, Chung and Dorothy (27) introduced the concept of Central Pattern Generators (CPGs). According to Hooper (35), CPGs "are neural networks that can endogenously (without rhythmic sensory or central brain input) produce coordinated patterns of rhythmic outputs". So, in application to flapping flight, the degrees of freedom for the wing relative to the body (flapping, plunging, and pitching) are all driven by a particular pattern, say some oscillatory function. The main controller is not directly responsible for generating these patterns, but it is rather used to command the frequencies, amplitudes, and relative phase shifts for these patterns. As such, the CPG-based control reduces the dimensionality and bandwidth of the signals required from the main controller. An ideal, robust, simplified dynamic model for CPGs is a stable limit cycle. Chung and Dorothy chose the Hopf oscillator as their CPG model, whose dynamics are given by

$$\frac{d}{dt}\begin{pmatrix}\chi_1 - a\\ \chi_2\end{pmatrix} = \begin{bmatrix}-\lambda(\frac{(\chi_1-a)^2+\chi_2^2}{\rho^2}-\sigma) & -\omega(t)\\ \omega(t) & -\lambda(\frac{(\chi_1-a)^2+\chi_2^2}{\rho^2}-\sigma)\end{bmatrix}\begin{pmatrix}\chi_1 - a\\ \chi_2\end{pmatrix} + \boldsymbol{U}(t) \tag{1.26}$$

Equivalently, $\dot{\boldsymbol{\chi}} = \boldsymbol{f}(\boldsymbol{\chi};\rho;\sigma)+\boldsymbol{U}(t), \boldsymbol{\chi} = (\chi_1 - a, \chi_2)^T$, where $\rho > 0$ is the radius of the circular limit cycle of the Hopf oscillator. The rate of convergence to the stable limit cycle is determined by $\lambda > 0$ and $\boldsymbol{U}(t)$ is an external or input signal. The time-varying parameters $\omega(t)$ and $a(t)$ represent the frequency of oscillations and the bias of the limit cycle, respectively. The limit cycle is defined by the solution to Eq. (1.26):

$$\chi_1(t) = \rho\cos(\omega t + \delta) + a \;\text{ and }\; \chi_2(t) = \rho\sin(\omega t + \delta)$$

Only the first state $\chi_1(t)$ of the Hopf oscillator was used to generate the desired oscillatory motion (CPG Pattern) of the joints of the wings. For control purposes, the degrees of freedom are coupled by synchronizing the oscillators (exact matching of the scaled amplitude with a desired phase difference). Coupling between the oscillators and their phase-rotated neighbors is applied by replacing the external input signal $\boldsymbol{U}(t)$ with

$$-k(t)\sum_{j\in N_i}^{m_i}(\boldsymbol{\chi}_i - \frac{\rho_i}{\rho_j}R(\delta_{ij})\boldsymbol{\chi}_j)$$

in Eq.(1.26), which yields

$$\dot{\boldsymbol{\chi}}_i = \boldsymbol{f}(\boldsymbol{\chi}_i;\rho_i) - k(t)\sum_{j\in N_i}^{m_i}(\boldsymbol{\chi}_i - \frac{\rho_i}{\rho_j}R(\delta_{ij})\boldsymbol{\chi}_j) \tag{1.27}$$

where $\boldsymbol{f}(\boldsymbol{\chi}_i;\rho_i)$ represents the Hopf oscillator dynamics defined in Eq. (1.26) with $\sigma = 1$. Here, N_i represents the set of local neighbors to the i^{th} oscillator, m_i is the number of these neighbors, $R(\delta_{ij})$ is a two-dimensional

rotation matrix of the phase difference δ_{ij} between the i^{th} and j^{th} oscillators, and $k(t) > 0$ represents the coupling gain, which is allowed to be time-varying for different flight modes.

A single Hopf oscillator with $\boldsymbol{U}(t) = 0$ has a globally uniformly asymptotically stable limit cycle when the bifurcation parameter $\sigma = 1$, with a Lyaponuv function $V = \left[\frac{(\chi_1 - a)^2 + \chi_2^2}{\rho^2} - 1\right]^2$, see Strogatz (36). For $\sigma = -1$, the system has a globally uniformly asymptotically stable equilibrium point at the origin ($\chi_1 = a, \chi_2 = 0$), with a Lyaponuv function $V = \left[\frac{(\chi_1 - a)^2 + \chi_2^2}{\rho^2} + 1\right]$ (36). As such, a single Hopf oscillator without external input signals is stable, but there is still a need to prove stability for the coupled Hopf oscillators. Chung and Dorothy used the contraction theory (37; 38) to prove stability for the synchronized Hopf oscillators. The stability analysis of coupled Hopf oscillators can also be found in Refs. (39; 40; 37). The choice of Chung and Dorothy for the Hopf oscillator as a CPG model is justified by two reasons, namely, its symmetry property and smooth bifurcation. The symmetry property of the Hopf oscillator, as opposed to the van der Pol and Rayleigh oscillators (36), is essential for proving stability for the synchronized oscillators. This property can be interpreted mathematically as

$$\boldsymbol{f}(R(\delta)\boldsymbol{\chi}; \rho; \sigma) = \boldsymbol{R}(\delta)\boldsymbol{f}(\boldsymbol{\chi}; \rho; \sigma) \tag{1.28}$$

That is to say the vector field $\boldsymbol{f}$, representing the dynamics, of a rotated state vector $\boldsymbol{R}(\delta)\boldsymbol{\chi}$ is the rotation of $\boldsymbol{f}$ of the un-rotated state. Furthermore, the symmetry property prevents the instability arising from switching between two stable systems because one of the systems has to be asymmetric for the instability to arise (41). In their proof of stability for the synchronized oscillators, Chung and Dorothy (27) exploited the scaling property $\boldsymbol{f}(\lambda\boldsymbol{\chi}; \rho; \sigma) = \lambda\boldsymbol{f}(\boldsymbol{\chi}; \rho/\lambda; \sigma)$ of a symmetric oscillator. The smooth bifurcation, represented by the bifurcation parameter σ, is used to smoothly switch from flapping to gliding flight. When the FWMAV's airspeed and altitude exceed some prescribed values, its potential and kinetic energy are enough to drive the flight, without a need for continuous flapping. To stop flapping, the bifurcation parameter σ is switched from 1 to -1, which in turn bifurcates the oscillators from their oscillatory motions to fixed positions corresponding to the centers of rotations ($\chi_1(t) = a$). It is noteworthy to mention that setting $\omega = 0$ would also drive the FWMAV to steady-state gliding. However, the converged steady-state values would depend on the initial conditions. In contrast, switching σ to -1 guarantees convergence to the desired values ($\chi_1 = a$), irrespective of the initial conditions and without having to set $\omega = 0$.

For the aerodynamic loads, they used the QS aerodynamic model of Dickinson et al. (3) along with the potential flow formula for the rotational lift (to be discussed below). For the equations of motion, they used the 6 DOF rigid-body dynamic equations, shown in Eq. (1.9). For control purposes, they had eight joints (four per wing): three Euler angles and one intermediate joint for wing flexing to reduce drag in the upstroke. Clearly their approach was too far from the minimal actuation concept emphasized by Wood (30)

and Doman et al. (19; 8; 9; 33; 10; 25).

The previous three subsections introduced kinematics or dynamic models for the wing joints that are designed from a pure control point of view. A question that arises is "What about the aerodynamic performance of such control-based optimum kinematics?" Using the calculus of variation, Taha et al. (42) proved that the triangular waveform of Schenato et al. (7) yields the minimum hovering aerodynamic power requirements. In contrast, the harmonic waveform used by Doman et al. (9; 10) and Oppenheimer et al. (8; 25) requires 20 % more aerodynamic power for hovering than when using the triangular waveform. Later on, Doman et al. (34) switched to the triangular waveform because of analytic and practical reasons. On the other hand Berman and Wang (43) proposed kinematic parametrization (11 parameters) that sweeps a very wide family of functions. They used both gradient-based and global optimization techniques to minimize the required power (aerodynamic + inertial) under lift constraint. Also, Ghommem et al. (44) considered the same problem with different kinematics and aerodynamic model. They used the unsteady vortex lattice method as their aerodynamic model and did not incorporate the inertial power. Considering these investigations, the above question can be reversed to "What is the the resulting control authority of those aero-optimum kinematics?" The answer to these two questions is in a multi-disciplinary framework that encompasses control authority/controllability/maneuverability and aerodynamic performance. Stanford et al. (45) performed a multi-disciplinary optimization the flapping wing planform, structure, and kinematics. Their objective was to minimize the aerodynamic power under lift constraint and also minimize the largest Floquet multiplier to ensure flight stability.

1.3 Aerodynamic Modeling

Aerodynamics of flapping flight has been a subject of investigation for almost a century, mainly by biologists (46; 47). Most of the results relevant to aerodynamics of flapping flight before the 1950's were summarized in the review by Weis-Fogh and Jensen (48). They reviewed many models, with detailed explanations for what they referred to as the most complete models (49; 50; 51; 52). Holst and Kuchemann (49) assumed a sinusoidal plunging motion of the whole wing without flapping about the fulcrum, but with a phase-shifted, biased pitching oscillation. Because these kinematics describe the oscillatory motions of the tails of whales, Parry (53) used their results to calculate the thrust due to plunging oscillations of these tails. It is noteworthy that Holst and Kuchemann were the first to show that maximal thrust is attained at 90° phase difference between pitch and plunge. Stolpe and Zimmer (54) and Chadwick (55) were the first to note the horizontal stroke plane in hovering insects. In both works, they noted that the wing twist is used to ensure lift during both half strokes. All of these early investigations were based on quasi-steady (QS) aerodynamics, which

may be valid for slow flapping (low reduced frequency) in forward flight of large birds.

Models for General Aerodynamic Analysis: Ellington (56; 57; 21; 58; 59; 60) used QS aerodynamics to analyze flapping flight of insects. Weis-Fogh (61) discussed the role of the unsteady aerodynamics in hovering insects. He stated that there are two counteracting unsteady mechanisms: the delayed stall and the Wagner effect. In the delayed stall, the wing can attain higher lift coefficients at angles of attack that exceed the stall value. The reason is that it takes time to exchange energy for boundary-layer separation and that time is not available when the wings flap at high frequencies. On the other hand, time is required for the circulation to build up and for the wing to attain the steady lift corresponding to the geometric angle of attack (Wagner effect (62)). He noted that it takes 2-3 chord lengths of wing travel for both of the dynamic stall and Wagner effect to diminish. Considering that, in hover of the humming bird and drosophila, the 70% semi-span section travels about 5-6 chord lengths, these two effects would only be important at the onset of each stroke. Because these effects have opposite impacts in terms of aerodynamic loads, the use of QS models has been justified.

Ellington et al. (63) discussed the phenomenon of the Leading Edge Vortex (LEV) and its importance in insect flight and noted that the LEV is a translatory effect, meaning that it could be modeled as a QS effect. This notion led Dickinson et al. (3) to develop a QS empirical model for the lift and drag at high angles of attack due to a stabilized LEV. The quasi-steady aerodynamic models are ideal for optimization, sensitivity analysis, dynamic stability analysis, and control design. These models have also been refined via augmentation with some inflow models, such as the actuator disk theory (64) and Peters' inflow model (65; 66).

Ellington (67) indicated the importance of the unsteady effects on the aerodynamics of insect flight. Phlips et al. (68) developed and applied an unsteady lifting line theory to the forward flight of birds. They assessed some relationships between the geometric and kinematic parameters and the forces and power required. They generated the power-speed curve for some birds and compared their results with those of Rayner (69; 70; 71). Fritz and Long (72) were the first to apply the Unsteady Vortex Lattice Method (UVLM) to flapping in forward flight and exploit the object-oriented C++ in dealing with the UVLM algorithm. The fact that UVLM can be performed with a feasible computation burden makes its use convenient for optimization and sensitivity analyses. Stanford and Beran (73) performed gradient-based optimization of flapping wing morphing kinematics using the UVLM as an aerodynamic model. Their objective was to maximize the aerodynamic efficiency under lift and thrust constraints. Ghommem et al. (74) tackled the same problem using global and hybrid optimization techniques.

Because of issues with vorticity accumulation in hovering flight, the use of three-dimensional UVLM may

result in noisy flow quantities. Ghommem et al. (44) used the two-dimensional UVLM instead to obtain the hovering kinematics that minimize the required aerodynamic power under a lift constraint. In fact, the use of 2-D unsteady aerodynamics is somehow justifiable for such a problem because, for high-frequency flapping associated with hover, the 3-D effects are negligible. Reissner (75) stated that the 3-D induction effects on the unsteady aerodynamics are diminished as the reduced frequency k increases. Reissner and Stevens (76) found that the finite-span effects are negligible for wings of aspect ratio 6 when k exceeds 1.0 and for wings of aspect ratio 3 when k exceeds 2.0. This is due, in case of high-reduced frequencies, to the dominance of the contribution of the added mass to the loads, in comparison to that of the circulatory component. It should be noted here that, according to Reissner's unsteady theory of finite wings, the added mass effects do not change whether the flow is 2-D or 3-D. This notion has also been supported by Jones (77; 78) who found a negligible 3-D induction near the start of an impulsive motion. The reason is that a high acceleration is associated with the initial motion and dominates the added mass effects, which are well predicted by the 2-D aerodynamics.

Five terms can be identified as contributors to flow quantities during hover. They include the translatory effects due to wing translation and the leading edge vortex (LEV), the rotational lift, the effects of wake capture, the viscous effects, and the added mass effects. The UVLM captures all but the viscous and the LEV effects. As shown by the experiments of Dickinson et al. (3; 79), the viscous effects for the range of Reynolds numbers (75-4000) of hovering FWMAVs/insects can be neglected. However, the LEV contribution can be very considerable in this range of Reynolds numbers with the high angles of attack encountered in hovering, and as such it cannot be neglected. Ansari et al. (80; 81) extended the work of Von Karman and Sears (82) to include the LEV effects by shedding vortices from both of the leading and trailing edges. They derived two nonlinear integral equations for the shed wake and leading edge vortices. Because of the computational cost associated with this formulation, its use in optimization, sensitivity analysis, and dynamics and control is still limited. Gogulapati et al. (83) implemented the previous formulation to study aeroelasticity of a flapping wing and to analyze the flexible hawkmoth wings in hover (84).

Ramamurti and Sandberg (85) solved the incompressible Navier-Stokes equations on the Drosophila wing. Sun and Tang (86) solved the Navier-Stokes equations on the wing of a hovering of Drosophila to calculate the lift generated and power required. Sun and Du (87) performed the same study on a wide range of eight insects. Sun and Wu (88) solved the Navier-Stokes equations on the wing and body of the fruit fly in forward flight. Sun and Tang (89) calculated the aerodynamic forces and consequently the stability derivatives needed to analyze the dynamic stability of flapping flight (15; 11; 16). Finally, it is worthy to note the model of DeLaurier (90) for the forward flight. This model aimed at checking the aerodynamic calculations of the pterosaur developed by Aerovironment. The model included low-fidelity representations

of the 3-D unsteady effects, friction effects, a partial leading edge suction, and a post-stall behavior. For more details on the aerodynamics of flapping flight, the reader is referred to Mueller (91), Shyy et al. (92), Sane (93), and Wang (94).

Models for Dynamics and Control: Almost all of the aerodynamic models, used within the framework of dynamics and control of flapping flight, are experimentally-based; that is, data fitting is used to construct approximate formulas for the measured aerodynamic loads. One may classify these models based on their representation as unsteady and quasi-steady. Trials to develop an unsteady aerodynamic model, via representing the aerodynamic loads in a Fourier series, tend to be ad-hoc (23; 95; 96). Unfortunately, these models may not be applicable or satisfactorily corrected if the wing kinematics or geometry are varied and, as such, cannot be used with arbitrary kinematics and wing shapes. On the other hand, representation of the aerodynamic loads in a quasi-steady model (1; 2) tends to be somehow more general. The QS model of Dickinson et al. (3) is ubiquitously used in the literature of flight dynamics of FWMAVs (28; 29; 22; 7; 97; 24; 27; 19; 8; 9; 33; 10; 25). This model gives algebraic expressions for the lift and drag coefficients as functions of the angle of attack. It captures the translatory leading edge vortex (LEV) effect. Pesavento and Wang (4) and Andersen et al. (5; 6) added some modifications to the model of Dickinson et al. by including the rotational lift and the viscous and added mass effects.

Berman and Wang (43) used the model of Andersen et al. (5; 6) to obtain optimum hovering kinematics that minimize the total required power (aerodynamic + inertial) under a lift constraint. Dietl and Garcia (26), and Orlowski et al. (98; 99; 100) used this model within the framework of flight dynamics. Weihua and Cesnik (29) used two unsteady aerodynamic models within the framework of coupled aeroelasticity and flight dynamic simulation: the model of Ansari et al. (80; 81) which allows for shedding vortices from both of the leading and trailing edges and the finite-state airfoil theory of Peters (65; 66). Using the model of Ansari et al. shedding vortices from both of the leading and trailing edges, they encountered high-frequency components for the aerodynamic loads, which caused numerical problems. Consequently, the solution diverged before completing one cycle of the coupled aeroelastic-flight dynamic simulation. The results of the model of Ansari et al. without shedding vortices from the leading edge match very well those of Peters' theory.

Off line direct numerical simulations have also been used by Sun and Xiong (15; 16) and Sun et al. (11) to obtain the stability derivatives and consequently analyze the local stability of insects in both hovering and forward flight. Gao et al. (101) also used the same aerodynamic model and approach for analyzing the stability of the hawkmoth in hover. This model is useful for the local stability assessment about specific equilibrium points. However, it may not be suitable for simulation purposes, where it is required to call the aerodynamic sub-routine at every time step while marching the dynamics forward in time. Details of the

aerodynamic models are provided next.

1.3.1 Unsteady Aerodynamic Representation

Thomas and Taylor (102) were the first to tackle the flight dynamics problem of animals. They (23) measured the forces on a tethered locust in the wind-tunnel at different speeds and angles of attack. Then, they averaged these aerodynamic loads over one cycle to obtain cycle-averaged longitudinal stability derivatives. These derivatives were incorporated into the linearized equations of motion to yield the longitudinal natural modes. One mode is similar to the short-period mode seen in conventional aircraft. However, their results for the short-period natural frequency is 10 Hz, which is about only one-half the beat frequency (22 Hz) for the locust. This indicates coupling between the periodic forcing and this mode, which refutes the assumption that the body just feels the averaged forces. Actually, this motivated their later work (95), in which they represented the measured forces in a Fourier series.

The aerodynamic loads $X(t), Z(t)$ and $M(t)$ were measured over a range of angles of attack α and forward speeds U on a tethered locust. They represented the forces in a Fourier series with eight harmonics that were found to be sufficient. At the equilibrium (reference) point, each force/moment, P, was written as

$$P_{ref}(t) = \sum_{n=0}^{8} (a_{1,n} \cos n\omega t + b_{1,n} \sin n\omega t) \tag{1.29}$$

For the α-series, and the U-series, they wrote

$$P(\alpha, t) = P_{ref}(t) + P_{\alpha}(t)(\alpha - \alpha_{ref}) \tag{1.30}$$

$$P(U, t) = P_{ref}(t) + P_{U}(t)(U - U_{ref}) \tag{1.31}$$

where

$$P_{\alpha}(t) = \sum_{n=0}^{8} (a_{2,n} \cos n\omega t + b_{2,n} \sin n\omega t)$$

$$P_{U}(t) = \sum_{n=0}^{8} (a_{3,n} \cos n\omega t + b_{3,n} \sin n\omega t)$$

Their generalized forces at any α and U were written as

$$P(\alpha, U, t) = P_{ref}(t) + P_{\alpha}(t)(\alpha - \alpha_{ref}) + P_{U}(t)(U - U_{ref}) \tag{1.32}$$

Thus the X force, for example, in Eq. (1.9) would be substituted as

$$X_{ref}(t) + X_{\alpha}(t)\left(\arctan\frac{w}{u} - \alpha_{ref}\right) + X_{U}(t)\left(\sqrt{u^2+w^2} - U_{ref}\right)$$

It is clear that their model is quite strong for their specific problem because it captures all of the (experimentally-based) physics. Furthermore, it allows the dynamic model to be nonlinear time periodic, which is the most rigorous representative form. On the other hand, the model is only applicable for a specific case, as the determined Fourier coefficients could not be used with arbitrary kinematics and wing shapes.

1.3.2 The Quasi-Steady Model of Khan and Agrawal (1; 2)

Khan and Agrawal (1) developed an aerodynamic model for a wing undergoing back and forth flapping φ and pitching η, without an out-of-plane motion ϑ. The total velocity seen by the airfoil section is simply $r\dot{\varphi}$. The velocity components in the wing frame were then determined from Eq. (1.2) by setting $\vartheta = 0$; that is,

$$V_{x_w} = -r\dot{\varphi}\cos\eta \;\text{ and }\; V_{z_w} = -r\dot{\varphi}\sin\eta$$

They considered the translatory effects, the rotational lift, and the added mass effects, and neglected the viscous effects.

For a wing section of width dr at a distance r from the root, the translatory force is written as

$$dF_{QS+LEV} = \frac{1}{2}\rho_{air}(r\dot{\varphi})^2 C_1(\alpha)c(r)dr \tag{1.33}$$

where $C_1(\alpha)$ represents the translatory force coefficient. A similar equation can be written for the rotational force using a different coefficient. However, they represented it in another way. They considered the translatory and rotational effects simultaneously to appear exactly as Eq. (1.33) with the velocity being taken at a point, different from that of the pitch-axis whose velocity is just $r\dot{\varphi}$. For a point that is a normalized distance d ahead of the pitch axis, the velocity components in the wing frame are written as

$$V_{x_w} = -r\dot{\varphi}\cos\eta \;\text{ and }\; V_{z_w} = -r\dot{\varphi}\sin\eta - dc\dot{\eta} \tag{1.34}$$

The total velocity is then given by $V_{tot} = \sqrt{V_{x_w}^2 + V_{z_w}^2}$. As such, the total force, including the translatory and rotational effects, is written exactly as Eq. (1.33) with $r\dot{\varphi}$ being replaced by V_{tot}.

As for the added mass effects, they considered only the effect of the acceleration normal to the chord

(plunging like). They took the added mass to be the mass of a cylinder whose radius is the semi-chord, see (103); that is,

$$dF_{\text{added mass}} = \frac{1}{4} C_3 \rho_{air} \pi c^2(r)(-\dot{V}_{z_w})dr \tag{1.35}$$

where

$$\dot{V}_{z_w} = -r\ddot{\varphi}\cos\eta + r\dot{\varphi}\dot{\eta}\sin\eta - dc\ddot{\eta}$$

Three coefficients need to be determined: C_1, C_3, and the effective point in rotation represented by d. To obtain these parameters, they chose the following kinematics:

$$\varphi(t) = A_\varphi \sin\omega t \;\text{ and }\; \eta(t) = -A_\eta \cos\omega t$$

They picked instants where two effects vanish or diminish while the other attains its maximum. At the mid-stroke where $\varphi = 0, \dot{\eta} = 0$, and $\dot{\varphi}$ and $\ddot{\eta}$ attain their maxima, the rotational effects vanish while the translatory and added mass effects attain their maximum values. However, the translatory effects outweigh the added mass effects. As such,

$$C_1 = \frac{\text{Total measured force}}{\frac{1}{2}\rho_{air}\dot{\varphi}^2 \int_0^R r^2 c(r)\, dr},\ \varphi = 0 \tag{1.36}$$

They considered 24 configurations of different A_φ, A_η, Reynolds numbers, and frequencies. For all configurations, the translatory coefficient could be fitted by $C_1(\alpha) = \frac{7}{\pi}\alpha$, although one cannot expect to find a pure linear relation between the normal force coefficient and the angle of attack up to 90°. Then, they set $\eta = 0$ (no rotational effects) during the whole cycle to estimate the coefficient C_3 associated with the added mass effects. As such, at the end of each half stroke, the translatory effect vanishes, while the added mass effect attains its maximum. Thus,

$$C_3 = \frac{\text{Total measured force}}{\frac{\pi}{4}\rho_{air} \int_0^R c^2(r)(-V(r,t)_{z_w})\, dr},\ \varphi = \pm A_\varphi \tag{1.37}$$

The value of C_3 was found to vary from 0.5-1.0 in the 24 configurations. On the other hand, they tuned d in the model to match the experimental results and found $d = 0.75 - \widehat{x}_0$, where $\widehat{x}_0$ is the normalized position of the pitch axis, to be the most appropriate. This exactly matches the result of the rotational lift as derived from potential flow, see Ellington (58; 59). The rotational circulation is given by $\Gamma_{rot} = \pi\dot{\eta}c^2(0.75 - \widehat{x}_0)$. This indicates that the effective point in rotation is the three-quarter chord point, which is also found to be the effective point in all potential flow analysis according to the Pistolesi theorem (104), see (105). In their work, Khan and Agrawal managed to make their coefficients independent of the kinematics. However, these coefficients are strong functions of the wing geometry (aspect ratio and sweep), especially the coefficient representing the translatory effect.

1.3.3 The Quasi-Steady Model of Dickinson et al. (3)

Almost all of the early trials of explaining insect flight invoked non-conventional high-lift mechanisms. Ellington et al. (63) explained how insects exploit the Leading Edge Vortex (LEV) as a high-lift mechanism, which is also known to be critical for lift generation of highly swept and delta wings aircraft. These wings are always associated with low-aspect ratios, which result in low lift-curve slopes. To attain the high lift needed for takeoff, large angles of attack would be required. This may cause tail scrape on the ground. So, the exploitation of the LEV is inevitable for highly swept and delta wings. The LEV augments the bound vortex on the wing and, as such, the lift increases. This phenomenon is similar to the one observed in dynamic stall when the wing exhibits a rapid variation in the angle of attack. There is no immediate pressure change on the airfoil surface corresponding to the new geometric angle of attack because of the lag associated with unsteady aerodynamics. It is as if the airfoil sees a lower angle of attack than the geometric one and, consequently, a LEV is formed. This vortex grows and moves downstream on the upper surface. At this stage, 50-100% additional lift could be generated (106). The LEV movement shifts the center of pressure downstream as well, causing highly nose down moment, which is the start of stall. As the LEV leaves the trailing edge, a complete flow separation occurs.

In contrast to the dynamic stall situation, the LEV formed in insect flight has stable characteristics. What stabilizes the LEV is the outward spanwise flow, which convects the LEV towards the tip (63; 107; 108; 109). This spanwise flow is generated by the flow component parallel to the highly swept leading edge in delta wings. In insect flight, similar to helicopters and propellers, the rotational motion creates a spanwise velocity gradient, which in turn creates a pressure gradient that generates the spanwise flow. The LEV is due to the translational motion of the wing. Thus, Dickinson et al. (3) let their model wing move with a constant velocity at different angles of attack in an arc of 180° and measured the resulting aerodynamic loads. We note that the curved motion along the arc is necessary to simulate flapping and to stabilize the LEV by the spanwise flow as discussed above. They measured the lift and drag, normal and parallel to the instantaneous velocity, respectively, and fitted the data to represent the lift and drag coefficients due to translational motions by

$$\begin{aligned} C_L &= 0.225 + 1.58\sin(2.13\alpha - 7.20) \\ C_D &= 1.92 - 1.55\cos(2.04\alpha - 9.82) \end{aligned} \tag{1.38}$$

Wang, Birch, and Dickinson (110) fit their data with simpler forms, namely

$$C_L = A\sin 2\alpha,\ C_D = B - C\cos 2\alpha \text{ or } C_D = C_D(0)\cos^2\alpha + C_D(\frac{\pi}{2})\sin^2\alpha$$

where the coefficients $A, B, C, C_D(0)$, and $C_D(\frac{\pi}{2})$ depend mainly on the Reynolds number and the wing shape. Equation (1.38) could model one of the high-lift mechanisms exploited by flying insects (LEV). It is applicable for the whole range of the angles of attack $(-\frac{\pi}{2}, \frac{\pi}{2})$. Sane and Dickinson (111) provided a revised model that accounts for the added mass effects. Dickson and Dickinson (112) considered forward flight and determined the coefficients in Eq. (1.38) as functions of the reduced frequency. Polhamus (113), who was the first to model the LEV contribution on highly swept and delta wings by a leading edge suction analogy, identified two components for the lift. They are the potential flow lift with zero leading edge suction $C_{Lp} = K_1 \sin\alpha \cos^2\alpha$ and the vortex lift $C_{Lv} = K_2 \cos\alpha \sin^2\alpha$. Both of K_1, and K_2 are functions of the aspect ratio (AR). Particularly, K_1, which becomes the lift-curve slope in the limit of small angles of attack, is a strong function of the AR. Consequently, the coefficients in the model of Dickinson et al., Eq. (1.38), are not be valid for any arbitrary wing because they can drastically change with variations in AR.

In the same work, Dickinson et al. (3) emphasized the importance of two other high-lift mechanisms, namely the rotational lift and wake-capture effects. They obtained the contributions of these effects by measuring the total forces due to flapping over one cycle and subtracting the forces due to the translatory effect, as predicted by Eq. (1.38). They found peaks at the beginning and end of each half stroke. The rotational lift is mainly due to the wing rotation at the end of each half stroke to adjust the angle of attack for the next half stroke. This rotational velocity of the wing creates a rotational circulation $\Gamma_{rot} = \pi\dot{\eta}c^2(0.75-\widehat{x}_0)$, which can be accurately predicted by the potential flow (3; 111). It is interesting to note that the resulting circulation may be favorable (creates upward lift) or unfavorable (creates downward force), it depends on the phase between the wing rotation and the reversal of the translational motion. If the rotation starts before the wing reversal, a favorable circulation forms and vice versa. Actually, this notion can be clearly seen if one recalls the circulation necessary to generate lift on a circular cylinder, hence, Dickinson et al. (3) related this effect to the magnus effect (a circular cylinder rotating in an oncoming free stream). On the other hand, although the rotation may add to the resulting lift, it essentially leads to an increase in the angle of attack, which may in turn decrease the lift due to the nonlinearity of the C_L-α curve at these high values of α. Therefore, there is an optimum rotation schedule that is usually sought by researchers.

The rotational mechanism is related to the high-lift peaks found near the end of each half stroke. On the other hand, the peaks observed at the beginning of half strokes, where there is almost zero forward speed for the wing sections, cannot not be explained by the same mechanism. These peaks are actually due to the lingering wake created during the previous half stroke (3). Unfortunately, this effect is very difficult to be independently modeled; that is, separated from the translational and rotational effects. Dickinson et al. noted that the wing rotation strengthens the lingering wake and set the wing at the appropriate angle to make use of the shed vorticity. As such, the rotational and wake-capture mechanisms can simultaneously

interact to control the aerodynamic forces during maneuvers. Dickinson et al. found that, although the rotational and wake-capture mechanisms exist for quite small periods during the cycle, they can contribute by 35% of the total lift produced during the whole cycle. A rotation phase advance of 8% of the cycle period results in a 40% increase in the average lift coefficient.

1.3.4 The Quasi-Steady Model of Pesavento and Wang(4) and Andersen et al. (5; 6)

This model is a quasi-staedy, quasi-2D model based on the blade element theory. It captures the leading edge vortex (LEV) and rotational effects into a circulation term, along with the viscous and added mass effects. It is presented in terms of the velocity seen by the airfoil section and the pitching angle. The forces and moment in the plane of the wing section are given by

$$\begin{aligned} dF_{x_w} &= \left[-\left(\tfrac{m_w c(r)}{\bar{c}} + m_{22} \right) V_{z_w} \dot{\eta} + \rho_{air} V_{z_w} \Gamma - m_{11} \dot{V}_{x_w} \right] dr - dF_{vx} \\ dF_{z_w} &= \left[\left(\tfrac{m_w c(r)}{\bar{c}} + m_{11} \right) V_{x_w} \dot{\eta} - \rho_{air} V_{x_w} \Gamma - m_{22} \dot{V}_{z_w} \right] dr - dF_{vz} \\ d\tau &= \left[(m_{22} - m_{11}) V_{x_w} V_{z_w} - I_a \ddot{\eta} \right] dr - d\tau_v \end{aligned} \tag{1.39}$$

where m_w represents the wing mass, $m_w c(r)/\bar{c}$ represents the mass of the wing-section, F_v and τ_v are the viscous force and torque, respectively, and

$$m_{11} = \frac{1}{4}\pi\rho_{air} t^2(r),\ m_{22} = \frac{1}{4}\pi\rho_{air} c^2(r),\ I_a = \frac{1}{128}\pi\rho_{air}\big(c^2(r) + t^2(r)\big)^2$$

The first term in each force equation compensates for the centripetal forces due to the rotation of the force-measurement frame. The second term is due to the circulation, which includes both of the translatory and rotational effects. The last term is the viscous term, which accounts for the viscous boundary layer and the pressure drag due to separation. The same terms exist in the moment equation except for the circulation term with the moment being taken at the center of pressure. The circulation is given by

$$\Gamma = -\frac{1}{2} C_L(\alpha) c(r) V_{tot} + \frac{\pi}{2} c^2(r) \dot{\eta}$$

with the signs being adjusted for $\alpha = \arctan \frac{-V_{z_w}}{V_{x_w}}$ and the lift coefficient is being given by $C_L = A \sin 2\alpha$. The first term represents the translatory effect and the second term represents the rotational circulation. Although the rotational circulation is supposed to depend on the location of the pitch-axis, it seems that the pitching axis was taken at the quarter-chord point.

The viscous forces and moment are then written as

$$\begin{aligned} \begin{pmatrix} dF_{vx} \\ dF_{vz} \end{pmatrix} &= \tfrac{1}{2}\rho_{air} c(r) C_D V_{tot} \begin{pmatrix} V_{x_w} \\ V_{z_w} \end{pmatrix} dr \\ d\tau_v \qquad &= \tfrac{1}{16}\pi\rho_{air} c^4(r) \left[\mu_1 f + \mu_2 |\dot{\eta}|\right] \dot{\eta} dr \end{aligned} \tag{1.40}$$

where the viscous drag coefficient is given by $C_D = C_{D0}\cos^2\alpha + C_{D\frac{\pi}{2}}\sin^2\alpha$. As discussed previously, the coefficients A, C_{D0}, $C_{D\frac{\pi}{2}}$, μ_1, and μ_2 depend mainly on the Reynolds number. However, Berman and Wang (43) varied μ_1 and μ_2 in the range (0,20) and found less than 1% change in both of the lift and power and recommended a value of 0.2 for both of them.

1.4 Dynamic Stability Analysis

Three assumptions are ubiquitously made when deriving the equations of motion in the literature of flight dynamics of FWMAVs. These assumptions include (a) neglecting the wing inertia effects, (b) averaging the body dynamics over the flapping cycle to obtain an autonomous system, and (c) linearizing this system to obtain a linear time invariant system whose stability and controllability analyses are well posed. Next, the issues associated with each of those assumptions are discussed in detail.

1.4.1 Wing Inertia Effects

The inertial effects of the wing on the body are usually neglected (102; 114; 23; 95; 96; 1; 2; 15; 16; 26; 27; 19; 8; 9; 33; 10; 25). In contrast, Gebert and Gallmeier (14) derived the equations of motion of FWMAVs, taking into account the effect of the wing inertia forces and the variation of the vehicle mass distribution and moments of inertia in the body frame and consequently variation of the center of gravity cg during the flapping cycle. Sun et al. (11) noted some errors in the equations of Gebert and Gallmeier, re-derived them, and obtained

$$\begin{aligned} \boldsymbol{F}_A^{(b)} &= m_b\left(\boldsymbol{g}^{(b)} + \dot{\boldsymbol{V}}_{cg}^{(b)} + \boldsymbol{\omega}^{(b)} \times \boldsymbol{V}_{cg}^{(b)}\right) + \boldsymbol{a}_1 + \boldsymbol{b}_1 \\ \boldsymbol{M}_A^{(b)} &= [\boldsymbol{I}_b]^{(b)}\dot{\boldsymbol{\omega}}^{(b)} + \boldsymbol{\omega}^{(b)} \times \left([\boldsymbol{I}_b]^{(b)}\boldsymbol{\omega}^{(b)}\right) + \boldsymbol{a}_2 + \boldsymbol{b}_2 \end{aligned} \tag{1.41}$$

where $\boldsymbol{F}_A$ and $\boldsymbol{M}_A$ are the aerodynamic forces and moments, respectively, m_b is the body mass, $[\boldsymbol{I}_b]$ is the body inertia matrix, $\boldsymbol{V}_{cg}$ is the linear velocity of the body cg, $\boldsymbol{\omega}$ is the body angular velocity, and the superscript b denotes a vector represented in the body frame. The vectors $\boldsymbol{a}_1$ and $\boldsymbol{a}_2$ represent, respectively, the forces and moments due to the wings' weight and the inertia contributions by the body motion. The vectors

$\boldsymbol{b}_1$ and $\boldsymbol{b}_2$ represent, respectively, the the wings' inertia forces and moments due to flapping. Neglecting these four vectors $\boldsymbol{a}_1, \boldsymbol{a}_2, \boldsymbol{b}_1$, and $\boldsymbol{b}_2$ yields the equations of motion governing the dynamics of conventional aircraft, as presented above, see Eq. (1.9). It is reasonable to neglect $\boldsymbol{a}_1$ and $\boldsymbol{a}_2$ in cases where the wing mass is much less than the body mass. Neglecting $\boldsymbol{a}_1$ and $\boldsymbol{a}_2$, replacing each variable in Eq. (1.41) by its cycle-average plus the flapping-frequency component or the fast perturbation, $\upsilon = \overline{\upsilon} + \widehat{\upsilon}$, and averaging over one flapping cycle yields the following averaged equations:

$$\begin{aligned}
\overline{\boldsymbol{F}}_A^{(b)} &= m_b \left(\boldsymbol{g}^{(b)} + \dot{\overline{\boldsymbol{V}}}_{cg}^{(b)} + \overline{\boldsymbol{\omega}}^{(b)} \times \overline{\boldsymbol{V}}_{cg}^{(b)} + \overline{\widehat{\boldsymbol{\omega}}^{(b)} \times \widehat{\boldsymbol{V}}_{cg}^{(b)}} \right) + \overline{\boldsymbol{b}}_1 \\
\overline{\boldsymbol{M}}_A^{(b)} &= [\boldsymbol{I}_b]^{(b)} \dot{\overline{\boldsymbol{\omega}}}^{(b)} + \overline{\boldsymbol{\omega}}^{(b)} \times \left([\boldsymbol{I}_b]^{(b)} \overline{\boldsymbol{\omega}}^{(b)} \right) + \overline{\widehat{\boldsymbol{\omega}}^{(b)} \times \left([\boldsymbol{I}_b]^{(b)} \widehat{\boldsymbol{\omega}}^{(b)} \right)} + \overline{\boldsymbol{b}}_2
\end{aligned} \tag{1.42}$$

To recover the equations of motion for the 6 DOF rigid body, Eq. (1.9), $\overline{\boldsymbol{b}}_1, \overline{\boldsymbol{b}}_2$ and the product terms $\overline{\widehat{\boldsymbol{\omega}} \times \widehat{\boldsymbol{V}}}, \overline{\widehat{\boldsymbol{\omega}} \times ([\boldsymbol{I}_b]\widehat{\boldsymbol{\omega}})}$ must be eliminated. Sun et al. (11) justified this elimination by performing a simulation for the reduced system and quantifying the eliminated terms. It turns out that each of the product terms is $O(10^{-2})$, meaning the product is $O(10^{-4})$, while the retained terms for the aerodynamic acceleration are $O(10^{-1})$. As for $\overline{\boldsymbol{b}}_1$ and $\overline{\boldsymbol{b}}_2$, they represent the mean inertia forces and moments due to flapping, which are almost zero for symmetric upstroke-downstroke flapping. The same simulation quantified these terms to be $O(10^{-6})$. It is important to note that neglecting these terms is justifiable only when considering the averaged quantities. Orlowski and Girard (115) represented the equations of motion in a form that is the standard form of conventional aircraft plus terms $O(\varepsilon)$ and $O(\varepsilon^2)$ perturbations containing the wing inertia effects; that is,

$$\dot{\boldsymbol{\chi}} \simeq \boldsymbol{f}^{(0)}(\boldsymbol{\chi}, t) + \varepsilon \boldsymbol{f}^{(1)}(\boldsymbol{\chi}, t) + \varepsilon^2 \boldsymbol{f}^{(2)}(\boldsymbol{\chi}, t)$$

Orlowski and Girard (100) showed that neglecting the wing mass may be problematic in dynamics and control studies as it may lead to different behaviors. Bolender (116) stated that, for proper development of control laws for FWMAVs, the wing mass should be included. Weihua and Cesnik (22) studied the dynamic stability of flexible FWMAVs using the QS aerodynamic model of Dickinson et al.(3) and a nonlinear beam element. They used the Floquet theory to analyze the stability of the linearized time periodic system and to plot a root locus for the system's eigenvalues as the wing inertia increases. It was found that increasing the wing inertia leads to destabilizing effects in both of the longitudinal and lateral dynamics. This notion supports the above claim that the wing inertia effects may be neglected on an average basis as long as the averaging is valid. Because the work of Weihua and Cesnik is for relatively low flapping frequency (10 Hz), at which the averaging assumption may be questionable, neglecting the wing inertia may not be justifiable.

1.4.2 Averaging Effects

The flight dynamics of a FWMAV constitute a nonlinear time-periodic system (NLTP). In general, such systems can be converted to autonomous ones using the averaging theorem (102; 114; 23; 7; 97; 24; 1; 2; 15; 11; 16; 19; 8; 9; 33; 10; 25). The averaging theorem is an application of the singular perturbation theorem, see Khalil (117). A non-autonomous dynamical system is written as

$$\dot{\boldsymbol{\chi}} = \epsilon \boldsymbol{f}(t, \boldsymbol{\chi}, \epsilon) \tag{1.43}$$

Assuming that $\boldsymbol{f}$ is T-periodic in t, the averaged dynamical system corresponding to Eq. (1.43) is written as

$$\dot{\overline{\boldsymbol{\chi}}} = \epsilon \overline{\boldsymbol{f}}(\overline{\boldsymbol{\chi}}) \tag{1.44}$$

where $\overline{\boldsymbol{f}}(\boldsymbol{\chi}) = \frac{1}{T}\int_0^T \boldsymbol{f}(\tau, \boldsymbol{\chi}, 0)\, d\tau$. According to the averaging theorem:

- If $\boldsymbol{\chi}(0) - \overline{\boldsymbol{\chi}}(0) = O(\epsilon)$, then there exist b and ϵ^* such that $\boldsymbol{\chi}(t) - \overline{\boldsymbol{\chi}}(t) = O(\epsilon)\ \forall t \in [0, b/\epsilon]$ and $\forall \epsilon \in [0,\epsilon^*]$.
- If the origin $\overline{\boldsymbol{\chi}} = 0$ is an exponentially stable equilibrium point of Eq. (1.44) and if $\boldsymbol{\chi}(0) - \overline{\boldsymbol{\chi}}(0) = O(\epsilon)$, then there exists an ϵ^* such that $\boldsymbol{\chi}(t) - \overline{\boldsymbol{\chi}}(t) = O(\epsilon)\ \forall t > 0$ and $\forall \epsilon \in [0,\epsilon^*]$. Moreover, the system (1.43) has a unique, exponentially stable, T-periodic solution $\boldsymbol{\chi}_T(t)$ with the property $\|\boldsymbol{\chi}_T(t)\| \leq k\epsilon$ for some k.

For FWMAVs, ϵ is represented by the ratio of flapping period T to one of the periods of the body motion. Clearly, the faster the flapping is, the smaller the error associated with averaging is, and vice versa. In fact, the key issue is in the difference between the flapping (forcing) frequency and the natural frequencies of the body motion. In cases where the flapping frequency is much larger than the body natural frequencies, the body will mostly be affected by the average forces only.

Taylor and Thomas (114) were the first to discuss this issue. They recalled the approximate expressions for the natural frequencies of symmetric motions (longitudinal) for conventional aircraft: the phugoid mode and the short-period mode. Lanchester's approximation for the phugoid period (118) is $T_{ph} \approx \sqrt{2}\pi\frac{U_0}{g}$; that is, it depends only on the forward speed U_0. The phugoid frequency for fast birds is about one seventieth of the flapping frequency and, for even slow birds, it is about one ninth of the flapping frequency. As such, the phugoid mode is too slow to be affected by the oscillation of the aerodynamic forces about their mean values. On the other hand, the period of the short-period mode can be approximated by $T_{sp} \approx \frac{2\pi}{\sqrt{-M_\alpha}}$, see (13). This period depends on the common stability derivative $M_\alpha = \frac{\partial M}{\partial \alpha}/I_y$, where I_y is the moment

of inertia about the pitch axis, M_α has to be negative for static stability, and the higher its magnitude is, the heavier the stability is. Thus, the short-period frequency can be seen as a direct measure for static pitch stability. In conventional aircraft, the short-period frequency ranges between 0.15-1.5 Hz (119). So, the claim of Taylor and Thomas is that, since the flapping flight is expected to be less stable than the conventional aircraft, they would have less short-period frequencies or even fall in the same range. Thus, for a high-flapping frequency, too far above this range, the short-period mode as well as the phugoid would not be affected by the oscillations of the aerodynamic forces. As an evidence, the smooth trajectories, which small insects (flapping at frequencies higher than 100 Hz) exhibit, give no hint about the periodic nature of the driving forces. On the other hand, for slow flapping animals (like large birds), their wobbling motion is an evidence for the coupling between the oscillating aerodynamic forces and the body modes.

For simulation purposes, Orlowski and Girard (115) introduced the concept of local averaging over each quarter-cycle. They showed that, when the cycle-averaged pitching moment is zero, there is no variation in the pitch angle. However, the full simulation exhibits pitch divergence, and the local averaging over the cycle-quarter was sufficient to match the response of the full simulation. The local averaging introduced by Orlowski and Girard may lower the computation burden for simulation purposes. Yet, from a dynamics point of view, the system is still non-autonomous.

Several experimental studies (120; 121) suggest that averaging of the high-frequency excitation might lead to erroneous results because of the interaction between high- and low-frequency modes. In these experiments, a high-frequency mode was directly excited either perimetrically (122) or externally (123), yet the response contained a large contribution from the first mode. In another experiment, Nayfeh and Nayfeh (124) excited a circular rod near its fifth-mode frequency (83.105 Hz), yet observed a large response near its first-mode frequency (1.303 Hz). In a fourth experiment, Oh and Nayfeh (125) excited a composite plate near its seventh-mode frequency (1001.4 Hz) and observed a large response near its first-mode frequency (42.79 Hz). In a fifth experiment, Popovic et al. (126) excited a three-beam-frame structure near its eighth-mode frequency (195.6Hz.) and yet observed a large response near its first-mode frequency (3.7Hz). The presence of the first mode was accompanied by a slow modulation of the amplitude and phase of the high-frequency mode with the frequency of the modulation being nearly equal to the natural frequency associated with the first mode. The results indicate that the mechanism for the excitation of the first mode is neither a classical internal resonance nor an external or a parametric combination resonance involving the first mode. Rather, the appearance of the first mode is accompanied by a slow modulation of the high-frequency modes. Thus, the mechanism for this energy transfer is the interaction between slow dynamics of the high-frequency mode, represented by its amplitude and phase, with the dynamics, which is slow, of the low-frequency mode, as shown analytically by Nayfeh and Nayfeh (127) for externally excited systems and by Nayfeh and Chin (128)

for parametrically excited systems. These studies indicate that averaging the dynamic forcing in FWMAVs may not reveal important aspects, such as the possible energy transfer from the high-frequency modes to the low-frequency modes of the body motions.

1.4.3 Stability Analysis

Two different approaches have been proposed in the literature to check the dynamic stability of flapping flight. The first approach, adopted in the early studies (102; 114; 23; 15; 11; 16), is to average the system dynamics over a flapping cycle to convert the nonlinear time periodic (NLTP) system to a nonlinear time invariant (NLTI) system. Linearization of the NLTI system leads to a linear time invariant (LTI) system whose stability analysis could be easily checked via the eigenvalues of its matrix. Then, asymptotic stability of the averaged system implies asymptotic stability for the original NLTP system, by the averaging theorem. The second approach, first adopted by Dietl and Garcia (26) and then by Weihua and Cesnik (22), is to use Floquet theory to study the stability of the linearized time periodic system. Dietl and Garcia stated that the first approach, which encompasses averaging of the dynamics, is not suitable for a large ornithopter whose beat frequency is close to the natural frequencies of its body motion. In contrast, Floquet theory is suitable for analyzing the stability of linear time periodic (LTP) systems, independent of the value of their period.

Floquet theory, as illustrated in Nayfeh and Balachandaran (129), Nayfeh and Mook (130), or Strogatz (36), is used as a tool for linear stability analysis of periodic orbits. Floquet theory can be applied to both autonomous and non-autonomous systems. To determine the stability of a periodic solution $\vec{\chi}_T(t)$ of minimal period T of a non-autonomous nonlinear system

$$\dot{\boldsymbol{\chi}} = \boldsymbol{f}(\boldsymbol{\chi}, t) \tag{1.45}$$

where $\boldsymbol{f}$ is periodic in its argument with a period related to T, a perturbation $\boldsymbol{y} = \boldsymbol{\chi} - \boldsymbol{\chi}_T$ is introduced to obtain

$$\dot{\boldsymbol{y}} + \dot{\boldsymbol{\chi}}_T = \boldsymbol{f}(\boldsymbol{y} + \boldsymbol{\chi}_T, t)$$

Expanding the right-hand side of this equation around $\boldsymbol{\chi}_T$, using the fact that $\dot{\boldsymbol{\chi}}_T = \boldsymbol{f}(\boldsymbol{\chi}_T)$, and linearizing the outcome, one obtains the following linear system with periodic coefficients:

$$\dot{\boldsymbol{y}} = [\boldsymbol{A}]\boldsymbol{y} \tag{1.46}$$

where $[\boldsymbol{A}] = D_\chi \boldsymbol{f}(\boldsymbol{\chi}_T, t)$ is a periodic matrix with period T. We note that if the system (1.45) is autonomous, it would have the same representation as (1.46) when linearized about the periodic solution of interest. Then,

the problem of determining the stability of the periodic solution $\boldsymbol{\chi}_T(t)$ of Eq. (1.45) has been transformed into the problem of finding the stability of solutions of Eq. (1.46). It is also assumed that this periodic solution is isolated and hence it is a limit cycle.

To determine the stability of the solutions of Eq. (1.46), one constructs n linearly independent solutions of it and collect them into what is called a fundamental matrix solution $\boldsymbol{Y}(t)$ with its columns being the n linearly independent solutions. Then, the matrix $\boldsymbol{M} = \boldsymbol{Y}(0)^{-1}\boldsymbol{Y}(T)$ is called the monodromy matrix. According to Floquet theory, the stability of the solutions of Eq. (1.46) are ascertained from the eigenvalues ρ_i of the monodromy matrix. These eigenvalues are referred to as the Floquet multipliers. Note that the monodromy matrix depends on the initial conditions used to construct it. However, the Floquet multipliers are unique. For autonomous systems, at least one Floquet multiplier equals unity ($\rho_j = 1$ for some j), called the trivial multiplier. Because the eigenvector associated with this trivial multiplier points toward the limit cycle trajectory, any disturbance provided along this direction (tangent to the periodic orbit) would neither grow nor decay. If none of the Floquet multipliers except the trivial one lies on the unit circle, the limit cycle is called hyperbolic. On the other hand, if one or more Floquet multipliers besides the trivial one lie on the unit circle, the limit cycle is called nonhyperbolic. A limit cycle is asymptotically stable if it is hyperbolic and none of its Floquet multipliers lies outside the unit circle. On the other hand, a limit cycle is unstable if one or more Floquet multipliers lie outside the limit cycle. If none of the Floquet multipliers of a nonhyperbolic limit cycle lies outside the unit circle, linearization is not sufficient to ascertain its stability. In contrast, for non-autonomous systems such as Eq. (1.45), there is no trivial multiplier and all the eigenvalues must lie inside the unit circle in order to conclude stability. It is noteworthy that Dietl and Garcia (26) provided an improved numerical algorithm, based on Lust's work (131), for determining the Floquet multipliers.

It is noteworthy that the monodromy matrix is the state matrix for the discretized form of Eq. (1.46); that is, $\boldsymbol{y}(k+1) = [\boldsymbol{M}]\boldsymbol{y}(k)$. So, it is as if the time periodic continuous system is converted into an autonomous discrete-time system with the sampling period being the minimal period T of the original continuous system.

1.4.4 Stability Results

Research reports on the dynamics of flapping flight have had significant discrepancies about the instability types or the associated modes. Taylor and Thomas (23) setup an experiment to measure the longitudinal stability derivatives for a tethered locust in a wind tunnel. Their set up did not enable them to measure the pitch rate derivatives. They neglected the wing inertia effects and used the 6 DOF rigid-body equations of motion, Eq. (1.9). They averaged the aerodynamic forces over the flapping cycle to obtain a NLTI system. Then, they linearized their system to obtain a LTI system, which allowed them to study the stability of the

system through eigenvalue analysis. Their analysis showed a stable oscillatory mode, a subsidence mode, and an unstable divergence mode.

Taylor and Zbikowsky (95) utilized the measured data of Taylor and Thomas (23) and analyzed them in a more rigorous form based on a time periodic representation of the aerodynamic forces in an 8-harmonics Fourier series, Eq. (1.32), which yielded a NLTP system. They studied the stability of both of the NLTI and the NLTP systems via simulation. All of the models, including the NLTP, NLTI, and the LTI predicted instability and failed to explain stability of the locust. The NLTP even predicted instability without any perturbation of the equilibrium state; that is, just by starting simulation. Taylor and Zbikowsky (95) listed six reasons as to why these models fail to explain stability. The most two important reasons are tethering and the absence of pitch damping in their measurements. One important conclusion of their work is that the asymptotic stability of flapping flight should be an asymptotic orbital stability, which is analogous to stability of limit cycle oscillations (LCO). Consequently, LCO control strategies are best suited for control of flapping flight. Such control strategies are difficult to be implemented on non-autonomous systems. As such, implementation of these strategies on FWMAVs demands the dynamical system to be asymptotically autonomous; that is, its trajectories converge asymptotically to the same orbit irrespective of the initial conditions. Taylor et al. (96) modified their setup (23) to allow for measurement of the pitch rate derivatives. They found out that the unstable root can be stabilized using just pitch feedback with a gain of about -0.0014 $N.m/rad$. This value of the control gain is equivalent to moving the center of pressure by less than $1mm$ along the locust body for every 1° of pitch disturbance, indicating the possibility of the control. On the other hand, they concluded that the oscillatory mode is close to the wing beat frequency, which undermines the quasi-static assumption (averaging of the dynamics) on which the NLTI and LTI models are based.

Sun and Xiong (15) studied the stability of the bumblebee in hover and Sun et al. (11) generalized their analysis to cover four other insects in the range of 11 - 1,648 mg in mass and 26-157 Hz in the flapping frequency. They solved the Navier-Stokes equations on the wing in hover. Xiong and Sun (16) added the body in the case of forward flight. However, they did not consider the interactions between the two wings or between the wings and the body. Sun et al. (11) included the wing inertia effects in the equations of motion and reduced them to the 6 DOF rigid-body system. They justified this reduction by quantifying the neglected terms using quantities from simulations of the reduced system. Like others, they averaged the aerodynamics and the dynamics over the cycle to obtain an autonomous system. They justified this step for insects having relatively large beat frequencies, above 150 Hz (hoverfly, dragonfly, and bumblebee) because the largest body natural frequency is about 1/30 of the beat frequency. For insects having relatively a small beat frequency (24-45 Hz) like the cranefly and hawkmoth, the largest body natural frequency is only about 1/8 of the beat frequency, which makes the 6 DOF rigid-body assumption questionable. Under

these assumptions, for all of the four insects studied by Sun et al. (11) and the bumblebee studied by Sun and Xiong (15), they found an unstable mode, a fast subsidence mode, and a slow subsidence mode.

Gao et al. (101) used the same aerodynamic solver (Navier-Stokes), with the same stability analysis (eigenvalues of the linearized system matrix), on the hawkmoth, but with slightly different kinematics. They used more realistic kinematics, as described by Willmott and Ellington (31) who represented each of the three kinematic functions φ, η, and ϑ as a four-term Fourier series. In contrast, Sun et al. (11) used an idealized kinematics without the out-of-plane motion (ϑ) as described by Dickinson et al. (3). Although both of the kinematics are observed in nature, this slight variation of the kinematics led to different stability results. The analysis of Gao et al. (101) resulted in a stable oscillatory mode, a fast subsidence mode, and a slow subsidence mode; that is, a stable system. On the other hand, Sun et al. (11) found an unstable system. Gao et al. attributed this difference in stability to the difference in the assumed kinematics and indicated that the real part of the unstable oscillatory mode by Sun et al. is quite small. This actually shows the high sensitivity of the FWMAV/insect stability to variations in wing kinematics. Of particular interest in the work of Sun et al. (11) is their notion that the unstable oscillatory mode is decoupled from the slow subsidence mode. The first mode is associated mostly with in-phase perturbations of the forward speed u and the pitch rate q. The second mode exhibits variations of the angle of attack or the speed w. Then, they derived approximate formulas for the individual eigenvalues corresponding to each mode, in a way similar to the decoupling of the short-period mode and the phugoid mode usually performed in studying the dynamics of conventional aircraft. They obtained

$$\lambda_{1,2} \approx \sqrt[3]{\frac{\widehat{M}_u \widehat{g}}{\widehat{I}_y}} \left[\frac{1}{2}(1-2J) \pm i\frac{\sqrt{3}}{2}\right],\ \lambda_3 \approx -\sqrt[3]{\frac{\widehat{M}_u \widehat{g}}{\widehat{I}_y}}(1+J),\ \lambda_4 \approx \frac{\widehat{Z}_w}{\widehat{m}_b} \tag{1.47}$$

where $J = -\frac{1}{3}\left(\frac{\widehat{M}_q}{\widehat{I}_y} + \frac{\widehat{X}_u}{\widehat{m}_b}\right) / \sqrt[3]{\frac{\widehat{M}_u \widehat{g}}{\widehat{I}_y}}$ and $\widehat{}$ refers to a non-dimensional quantity.

Xiong and Sun (16) studied forward flight of the bumblebee and found results similar to those of Refs. (15; 11) in hover up to 3.5 m/sec forward speed, but a considerable change when the flight speed was increased from 3.5 m/sec to 4.5 m/sec. Furthermore, they found no decoupling between the modes in forward flight. These works of Sun and co-workers (15; 11; 16) discussed above are good enough for analyzing the dynamic stability near equilibrium. However, their framework may not be suitable for simulation purposes. First, they used their aerodynamic solver to obtain the stability derivatives off line and then fed them as given parameters to the dynamic model (loose aerodynamic-dynamic coupling). Second, they averaged the dynamics over one flapping cycle even for the cases in which the body natural frequencies are comparable to the beat frequencies. Third, they never made a full nonlinear time-varying simulation for the whole system. Finally, they neglected the effects of the aerodynamic forces on the wing due to body acceleration (unsteady

maneuvers).

As stated above, Dietl and Garcia (26) were the first to introduce the Poincare map and Floquet theory in the stability analysis of flapping flight. They found results similar to those of Taylor et al. (23); namely, a stable oscillatory mode, a subsidence mode, and a divergence mode of approximately one beating cycle doubling time.

Weihua and Cesink (22) used the quasi-steady aerodynamic model of Dickinson et al. (3), along with a nonlinear beam element having three nodes and four local strains: extension, twisting, and two bending strains. This beam element was introduced as a strain-based approach for the nonlinear modeling of coupled aeroelasticity and flight dynamics of very flexible aircraft (a HALE aircraft with rigid fuselage and highly flexible, high-aspect ratio wings) (132; 133). As such, their dynamic model (22) includes the 6 DOF of the rigid body and multiple flexible DOFs. They used Floquet theory in the stability analysis. For the longitudinal modes, they found an unstable oscillatory mode (phugoid), a divergence mode having a doubling time of approximately 1.4 flapping period (like that of Dietl and Garcia (26)), and a subsidence mode. As for the lateral modes, they also found an unstable oscillatory mode (Dutch Roll), a slow divergence mode, and a subsidence mode. They studied the loci of the eigenvalues as the rigidity and the wing inertia increase. Varying the rigidity does not affect much the eigenvalues, while the wing inertia has a destabilizing effect, especially on the subsidence modes.

Although there are some discrepancies among research reports concerned with the dynamics of flapping flight about the instability types or the associated modes, almost all of the studies concluded instability. This dictates the design and implementation of control algorithms to stabilize the dynamics of FWMAVs. It is also noteworthy that a full nonlinear time periodic analysis has never been applied to the dynamics of FWMAVs.

1.5 Control Design

The flight dynamics of FWMAVs are very rich and complex in the sense that they constitute a NLTP system. Advanced control techniques, including geometric and adaptive control, are possibly the best candidates for proper control of these vehicles over a wide range of operating conditions. To date, most of the proposed controllers for FWMAVs are linear controllers (7; 24; 8; 9; 10; 25) applied to the NLTP system after being averaged and linearized about one of their equilibrium states.

1.5.1 Linear Control Design

Section 1.2 discussed how Schenato, Campolo, and Sastry (7) designed and parameterized the flapping kinematics to obtain a high-control authority for FWMAVs. As for their control strategy, they applied a high-frequency periodic control; that is, instead of manipulating the time history of the actual inputs $\varphi_{LW}, \varphi_{RW}$, they manipulated the time history of some parametrization of these actual inputs (the kinematic parameters κ, ρ, and γA_0 for each wing). These parameters are referred as virtual inputs. One advantage of the high-frequency control is the gain of extra virtual inputs to solve the problem of under-actuated systems; that is, systems having less inputs than the number of their degrees of freedom. It should be noted that they do not vary the virtual inputs continuously in time, but rather periodically at the beginning of each cycle. This variation means that the kinematic parameters are considered as inputs to the averaged dynamics of the system over the flapping cycle. Mathematically, the dynamical system is represented by

$$\dot{\boldsymbol{\chi}} = \boldsymbol{f}(\boldsymbol{\chi}, \hat{\boldsymbol{u}})$$

where $\hat{\boldsymbol{u}}$ is the control input vector $(\varphi_{LW}, \varphi_{RW})$. The parametrization of the kinematics is then represented by $\hat{\boldsymbol{u}} = \hat{\boldsymbol{u}}(\hat{\boldsymbol{v}}, t+T)$ where $\hat{\boldsymbol{v}}$ represents the virtual inputs (κ, ρ, and γA_0 for each wing). This parametrization indicates the periodicity of the kinematic/input functions. Applying the averaging theorem to the dynamical system yields a NLTI system of the form

$$\dot{\overline{\boldsymbol{\chi}}} = \boldsymbol{f}(\overline{\boldsymbol{\chi}}, \hat{\boldsymbol{v}})$$

The error in the response between the averaged system and the actual system is $O(T)$, which dictates the use of relatively high frequency in order for the periodic control to work effectively. This is intuitively expected because the averaging itself is not valid unless T is relatively small. They showed that the averaged nonlinear system is locally accessible and that the linearized system about hover is controllable. Then, they used a full state feedback control law $\boldsymbol{W} = \boldsymbol{K}\overline{\boldsymbol{\chi}}$ to stabilize the system, where $\boldsymbol{W} = [\boldsymbol{B}]\hat{\boldsymbol{v}}$ is the linear map, Eq. (1.14), between the generalized forces in the body frame and the kinematic parameters. Obtaining W from the control law, they used a pseudo inverse of the linear map to determine the kinematic parameters. Furthermore, they modeled the wing thorax dynamics as a four-bar mechanism and checked that the system, using the proposed kinematics, is still controllable and that the closed-loop system remains stable. Their conclusion is that a FWMAV with a pair of wings, each having a single degree of freedom and passive rotation, is controllable even when the dynamics of the wing thorax are included. Furthermore, high-frequency periodic control can stabilize the FWMAV provided that the beat frequency is much higher than the natural frequencies of the body dynamics.

Deng et al. (97; 24) expanded their earlier work of Schenato et al. (7) to implement a similar control

law using more realistic aerodynamic loads and kinematics. They added a tangential force coefficient of the form

$$C_T = \begin{cases} 0.4\cos^2(2\alpha)\ , 0 \leq \alpha \leq 45^\circ \\ \\ 0 \qquad\qquad , \text{Otherwise} \end{cases} \tag{1.48}$$

to the normal force ($C_N = 3.4\sin\alpha$) used in their earlier work. They also included the effects of the rotational normal force $\Gamma_{rot} = \pi\dot{\eta}c^2(0.75 - \widehat{x}_0)$. They formulated two aerodynamic models; the first is based on the flapping velocity $V_a = r\dot{\varphi}$ only and the second adds the body velocity in the wing frame $V_a = r\dot{\varphi} + V_b$. They used the first model to design their controller and used the second model to check the robustness of the designed controller. As for the dynamic model, they used the 6 DOF rigid-body dynamics. They added viscous damping $\boldsymbol{F}_d = -b\boldsymbol{V}_b$ to the body, relying on the fact that, for small Reynolds numbers, viscous damping dominates the quadratic inertial damping. They neglected the effects of rotational damping, based on the experiments of Fry et al. (134).

Deng et al. (97) provided a taxonomy for the whole FWMAV system: a locomotion unit, a sensory system, a power supply, a communication unit, and a control system. They provided a thorough discussion and list of references of the sensors, which are ultra-light and having very low-power consumption to fit FWMAV applications. These sensors include the Halteres (135; 136; 137), which is a replacement of the rate gyro. It has a set of small balls at the ends of thin sticks, which move up and down at the flapping frequency in non-coplanar planes through 180° anti-phase to the wing motion. Ocelli (138; 139) is another sensor that measures the roll and pitch angles. It consists of four ideal photo receptors fixed with respect to the body frame. They proposed a magnetic compass to measure the heading angle. They pointed out that the development of such novel sensors is inevitable for FWMAV control feasibility. This is because the currently adopted sensors for avionics are too heavy and require too much power to be used for FWMAV applications. Their target FWMAV is 100 mg with a 100 mW power budget, whereas the smallest commercial gyro weighs about 500 mg and consumes about 30 mW. The proposed Halteres weighs about 30 mg with a 1 mW power consumption.

Deng et al. (24) proposed completely different kinematics from those used in their previous work of Schenato et al. (7). These include manipulating the back and forth flapping angle φ and the pitching angle η. This dictates two actuators per wing instead of one used in the previous work, which unexpectedly led to less control authority. The new proposed kinematics resulted in having control authority over four independent DOFs, versus five in the previous formulation. They stressed that these new kinematics are neither unique nor optimum, but proposed to mimic observed data from nature. Their kinematics are represented by

$$\varphi(v,t) = g_\varphi(t) + v_1 g_1(t) \ \text{ and } \ \overline{\alpha}(v,t) = g_\alpha(t) + v_2 g_2(t) \tag{1.49}$$

where the angle of attack is related to their rotation angle via $\alpha = 90^\circ - |\overline{\alpha}|$; $g_\varphi(t) = \frac{\pi}{3}\cos(\omega t)$ and $g_\alpha(t) = \frac{\pi}{4}\sin(\omega t)$ are supposed to generate symmetric motion with maximum lift; $g_1(t) = g_2(t) = \frac{\pi}{15}\sin^3(\frac{\omega}{2}t)$, with g_1 modifying the stroke amplitude and g_2 modifying the timing of rotation at the end of the down stroke. As such, they have four kinematic parameters (v_1 and v_2 for each wing).

They pointed out that trajectory tracking and stabilization of fish and snake like vehicles, which are mostly under-actuated systems, can best be performed by combining the averaging theorem, the high-frequency periodic control, and the geometric control. The goal of the geometric control is to develop a time-varying control input $\hat{\boldsymbol{u}}(\boldsymbol{\chi}, t)$ directly from the structure of the drift vector field $\boldsymbol{f}(\boldsymbol{\chi})$. The drift term greatly complicates the controllability checks and control design. Only few tools are available for systematic design of control laws for such systems, see (140; 141). For drift-less systems, some algorithms have been developed and constructive control techniques are available, see (142; 143; 141). Deng et al. (24) used the averaging theorem to convert the NLTP system into a NLTI system, where the generalized forces G are related to the kinematic parameters $\hat{\boldsymbol{v}}$ via the nonlinear map $\boldsymbol{\Pi} : \Re^4 \to \Re^6$; $\boldsymbol{G} = \boldsymbol{\Pi}(\hat{\boldsymbol{v}})$. It is difficult to determine the nonlinear map $\boldsymbol{\Pi}$ analytically. Furthermore, they look for an affine approximation $\boldsymbol{G} = \boldsymbol{\Pi}_0 + \boldsymbol{\Pi}_l\hat{\boldsymbol{v}} + \boldsymbol{\Delta}(\hat{\boldsymbol{v}})$. They randomly selected 100 different combinations of $\hat{\boldsymbol{v}}$, determined the corresponding aerodynamic forces and moments from the aerodynamic model, estimated $\boldsymbol{\Pi}_0$ and $\boldsymbol{\Pi}_l$ using the least squares technique, and found that

$$\boldsymbol{\Pi}_0 = \begin{pmatrix} 0 \\ 0 \\ -mg \\ 0 \\ 0 \\ 0 \end{pmatrix}, \boldsymbol{\Pi}_l = 0.1mg \begin{bmatrix} 0 & 0 & 1.0 & 1.0 \\ 0 & 0 & 0.3 & -0.3 \\ -0.9 & -0.9 & 0 & 0 \\ -0.4R & 0.4R & 0.1R & -0.1R \\ -0.2R & -0.2R & -0.4R & -0.4R \\ 0 & 0 & 0.5R & -0.5R \end{bmatrix} \tag{1.50}$$

where R represents the wing length.

Equation (1.50) not only indicates the FWMAV's degree of control authority, but also provides estimates for the maximum maneuverability that can be attained by the FWMAV body. Firstly, the linearized map Π_l has a full rank of four, which indicates a control authority over four DOFs. This actually was expected a priori because we have only four kinematic parameters. Hence, the best (highest control authority) one can have is independent control of the 4 DOFs, which include the vertical thrust and the three moments. This situation is similar to helicopters; however, here the pitching moment is always associated with forward thrust and the rolling and yawing moments are associated with side forces. Furthermore, one can infer from Eq. (1.50) that, in addition to the force necessary to balance the weight $\boldsymbol{\Pi}_0$, the FWMAV can generate X

or Z forces up to 0.1-0.2 mg and moments up to 0.1 mgR. As such, the maximum translational acceleration that can be generated is about 2 m/sec^2. According to Ellington (57), the principal moment of inertia for insects is O(0.1 mR^2), thus the maximum angular acceleration that can be produced is about g/R, which for a 10 mm wing length yields 5.7×10^4 deg/sec^2. In fact, this illustrates the high maneuverability of insects in some situations like chase mate, in which they are observed to have a turning velocity of more than 3000 deg/sec with less than 30 $msec$ delay time.

They represented the wing thorax dynamics by two piezoelectric actuators in the form

$$\begin{pmatrix} V_1 \\ V_2 \end{pmatrix} = \boldsymbol{T}_0^{-1} \left(\boldsymbol{M}_0 \begin{pmatrix} \ddot{\varphi}_d \\ \ddot{\overline{\alpha}}_d \end{pmatrix} + \boldsymbol{B}_0 \begin{pmatrix} \dot{\varphi}_d \\ \dot{\overline{\alpha}}_d \end{pmatrix} + \boldsymbol{K}_0 \begin{pmatrix} \varphi_d \\ \overline{\alpha}_d \end{pmatrix} \right) \tag{1.51}$$

where $\boldsymbol{T}_0, \boldsymbol{M}_0, \boldsymbol{B}_0$, and $\boldsymbol{K}_0$ are constant matrices defining the piezoelectric actuator dynamics and φ_d and $\overline{\alpha}_d$ are the desired flapping and pitch rotation angles, respectively. Because Eq. (1.49) can be written as $\hat{\boldsymbol{u}}(t) = \boldsymbol{g}(t) + \Gamma(t)\hat{\boldsymbol{v}}(t)$, it follows from Eq. (1.51) that the piezoelectric actuator voltages $\boldsymbol{V}$ can be written in terms of the kinematic parameters $\hat{\boldsymbol{v}}$ as $\boldsymbol{V}(t) = \boldsymbol{h}(t) + H(t)\hat{\boldsymbol{v}}(\boldsymbol{t})$. According to their model, the time constant of the kinematics error decay (wing thorax dynamics) is about 1-2 cycles. So for relatively fast flapping, the thorax dynamics are so fast that one could assume having direct control over the wing kinematics and neglect these dynamics.

They represented the system as a discrete time control system in the form

$$\boldsymbol{\chi}(k+1) = \boldsymbol{A}\boldsymbol{\chi}(k) + \boldsymbol{B}\hat{\boldsymbol{v}}(k) + \boldsymbol{\Delta}(k)$$

where $\boldsymbol{A}$ and $\boldsymbol{B}$ can be determined analytically. Yet, they performed system identification to obtain $\boldsymbol{A}$ and $\boldsymbol{B}$ and used the least squares technique to estimate the non-zero entries in $\boldsymbol{A}$ and $\boldsymbol{B}$. They used the pole placement technique to stabilize the linearized system $(\boldsymbol{A}, \boldsymbol{B})$. Having stabilized the system, they used the prediction error method (PEM), which cannot be applied directly to unstable systems. The PEM did a better job in the identification and provided estimates for the noise variances and biases associated with the process and measurements. These estimates can be used to design better robust controllers. They also used the linear quadratic regulator (LQR) technique for controller design; that is, they chose $\hat{\boldsymbol{v}} = -K\boldsymbol{\chi}$ to minimize the performance index function

$$J = \lim_{N \to \infty} E \left(\sum_{n=1}^{N} \boldsymbol{\chi}(n)^T \boldsymbol{Q} \boldsymbol{\chi}(n) + \hat{\boldsymbol{v}}(n)^T \boldsymbol{R} \hat{\boldsymbol{v}}(n) \right)$$

The elements of R and Q were tuned iteratively to obtain a satisfactory transient response. Then, $\hat{\boldsymbol{v}} = -K\chi$

was replaced by $\hat{\boldsymbol{v}} = -K\boldsymbol{y}$, where $\boldsymbol{y}$ is the output from the sensors models given in Ref. (97). As such, the input voltages to the piezoelectric actuators are given by

$$\boldsymbol{V} = \boldsymbol{h}(t) + \tilde{\boldsymbol{K}}\boldsymbol{y}(t) \text{ and } \boldsymbol{y}(t) = \boldsymbol{y}(kT)$$

where $\tilde{\boldsymbol{K}}$ is a T-periodic gain matrix. It is interesting to note that a simple proportional T-periodic feedback is sufficient to stabilize that complex nonlinear time-varying system, including the sensor measurements, actuator dynamics, and the process and output noise. Moreover, $\tilde{\boldsymbol{K}}$ could be calculated off-line. Then, they tested the LQR performance on the fully nonlinear system with the aerodynamic model being modified as stated before, with an initial offset in the Euler angles of 25° and an inertial position of the body center of gravity of 25 mm in each direction. The LQR took 50 cycles (2/3 sec) to reach steady state with the steady-state error being $\frac{1}{10}R$ in position and 5° in the body angles.

They proposed another formulation for the control problem, similar to that used with helicopters, where the longitudinal, lateral, heave, and yaw degrees of freedom are decoupled. They repeated the identification process, neglected some terms, and found that it is possible to apply single channel control. As such, they obtained a new gain matrix $\hat{\boldsymbol{K}} = diag[\,\boldsymbol{K}_{long}\ \boldsymbol{K}_{lat}\ \boldsymbol{K}_{heave}\ \boldsymbol{K}_{yaw}\,]$, with each sub-gain matrix being of smaller size, thereby requiring less computational costs. Actually, this idea of single channel control to the fully decoupled DOFs was exploited by Doman, Oppenheimer, and Sigthorsson (8; 9; 10; 25), as discussed in Section 1.2.

1.5.2 Nonlinear Control Design

Few investigations have implemented nonlinear control techniques for the stabilization of FWMAVs. Khan and Agrawal (2) used their experimentally-based aerodynamic model (1), as discussed in Section 1.3. They wrote the dynamic equations of motion of the rigid FWMAV in longitudinal flight as

$$\dot{\boldsymbol{\chi}} = \boldsymbol{f}(\boldsymbol{\chi}) + \Gamma\boldsymbol{F}(t)$$

where $\boldsymbol{F}(t)$ represents the periodic aerodynamic forces and moments. Applying the averaging theorem to this system yields

$$\dot{\overline{\boldsymbol{\chi}}} = \boldsymbol{f}(\overline{\boldsymbol{\chi}}) + \Gamma\boldsymbol{F}_0$$

They used a differential flatness-based controller. A system is said to be differentially flat if a set of variables, called the flat variables $\boldsymbol{y}$, can be found such that all of the state variables $\boldsymbol{\chi}$ and system inputs $\hat{\boldsymbol{u}}$ can be

determined without integration. That is, for the system $\dot{\boldsymbol{\chi}} = \boldsymbol{f}(\boldsymbol{\chi}, \hat{\boldsymbol{u}})$, there exists

$$\boldsymbol{y} = \boldsymbol{h}(\boldsymbol{\chi}, \hat{\boldsymbol{u}}, \dot{\hat{\boldsymbol{u}}}, \ddot{\hat{\boldsymbol{u}}}, ..., \hat{\boldsymbol{u}}^{(k)})$$

such that

$$\boldsymbol{\chi} = \boldsymbol{g}(\boldsymbol{y}, \dot{\boldsymbol{y}}, \ddot{\boldsymbol{y}}, ..., \boldsymbol{y}^{(j)}) \text{ and } \hat{\boldsymbol{u}} = \boldsymbol{k}(\boldsymbol{y}, \dot{\boldsymbol{y}}, \ddot{\boldsymbol{y}}, ..., \boldsymbol{y}^{(j)})$$

This property is usually used for motion planning. They stated that the FWMAV system under hand is differentially flat with the flat variables being the coordinates of the "*Huygens center of oscillation*" (144). The center of oscillation of any arbitrary shaped body is defined as the distance from the axis of oscillation to the length of a simple pendulum having the same natural frequency as the body. Thus, the flat outputs for their FWMAV are

$$y_1 = x + E\sin\theta \text{ and } y_2 = z + E\cos\theta \tag{1.52}$$

where $E = I_y/(m\Delta Z_W)$, m is the body mass, I_y is the moment of inertia about the y_b-axis, and ΔZ_W is the shift of the wing hinges from the body center of gravity along the z_b-axis.

They introduced the following new control inputs instead of the forces X and Z:

$$\begin{pmatrix} \zeta \\ E\ddot{\theta} \end{pmatrix} = \begin{bmatrix} -1 & 0 \\ 0 & -1 \end{bmatrix} \begin{pmatrix} Z \\ X \end{pmatrix} + \begin{pmatrix} -Eq^2 \\ 0 \end{pmatrix} \tag{1.53}$$

They managed to represent all of the state variables $\boldsymbol{\chi}$, ζ, and $\dot{\zeta}$ in terms of the flat outputs. Then, they decoupled the system into two linear systems in Brunovsky's form by setting $y_1^{(4)} = v_1$ and $y_2^{(4)} = v_2$. As such, they proposed control laws of the form

$$\begin{aligned} v_1 &= y_{1,d}^{(4)} - k_3(y_1^{(3)} - y_{1,d}^{(3)}) - k_2(\ddot{y}_1 - \ddot{y}_{1,d}) - k_1(\dot{y}_1 - \dot{y}_{1,d}) - k_0(y_1 - y_{1,d}) \\ v_2 &= y_{2,d}^{(4)} - \gamma_3(y_2^{(3)} - y_{2,d}^{(3)}) - \gamma_2(\ddot{y}_2 - \ddot{y}_{2,d}) - \gamma_1(\dot{y}_2 - \dot{y}_{2,d}) - \gamma_0(y_2 - y_{2,d}) \end{aligned} \tag{1.54}$$

where $y_{1,d}$ and $y_{2,d}$ are used to represent the desired trajectories for the flat outputs and the k_i and γ_i represent feedback gains. With this control law, the closed-loop characteristic equations can be written as

$$\begin{aligned} s^4 - k_3 s^3 - k_2 s^2 - k_1 s - k_0 = 0 \\ s^4 - \gamma_3 s^3 - \gamma_2 s^2 - \gamma_1 s - \gamma_0 = 0 \end{aligned} \tag{1.55}$$

They determined the feedback gains so that all of the closed-loop poles lie at $s = -2$. After determining the

control inputs v_1 and v_2, they obtained $\ddot{\zeta}$ and $\ddot{\theta}$ from

$$\begin{pmatrix} \ddot{\zeta} \\ \ddot{\theta} \end{pmatrix} = \frac{1}{\zeta} \begin{bmatrix} \zeta \sin\theta & \zeta \cos\theta \\ \cos\theta & -\sin\theta \end{bmatrix} \begin{pmatrix} v_1 - 2\dot{\zeta}\dot{\theta}\cos\theta - \zeta\dot{\theta}^2 \sin\theta \\ v_2 + 2\dot{\zeta}\dot{\theta}\sin\theta - \zeta\dot{\theta}^2 \cos\theta \end{pmatrix} \tag{1.56}$$

They simulated a circular trajectory as

$$x_d = R_{traj} \sin\frac{2\pi t}{T_f} \quad \text{and} \quad z_d = R_{traj}(\cos\frac{2\pi t}{T_f} - 1) - z_0$$

where R_{traj} is the radius of the circular trajectory and z_0 is the initial height. They specified the desired pitching angle $\theta_d = 0$ of the body during the whole maneuver, such a situation is like a gondola on a Ferris wheel. The procedure is to determine $y_{1,d}$ and $y_{2,d}$ from Eq. (1.52), v_1 and v_2 from Eq. (1.54), $\ddot{\zeta}$ and $\ddot{\theta}$ from Eq. (1.56), and finally the forces required to drive the maneuver from Eq. (1.53).

1.6 Conclusion and Recommendations

This chapter provides a thorough review of the three main blocks underpinning the dynamics of flapping-wing flight: the kinematics, the aerodynamic modeling, and the body-dynamics. Designing the flapping kinematics is usually done for two independent purposes: optimization of the aerodynamic performance and control. These two objectives may not be compatible. So, the first raised point here is the need for a multi-disciplinary framework that encompasses control authority/controllability/maneuverability and aerodynamic performance. As for the aerodynamic modeling, no moderate fidelity aerodynamic model has been proposed in the literature that captures most of the physics. Models that have been proposed include either quasi-steady, or unsteady ones that do not capture the essential leading-edge vortex. The proposed models that capture both of these effects require high-computational burdens and, hence, are not feasible for optimization and sensitivity analyses or dynamics and control purposes. So, there is a need to develop a phenomenological model that captures the leading-edge vortex, but in the form of differential equations, which can model the lift build up during the cycle and consequently provide the lag associated with the unsteadiness.

From the dynamics perspective, averaging and linearization of the FWMAVs dynamics poses serious limitations. For example, averaging is erroneous for relatively slow flapping. Furthermore, it would not capture the possible energy transfer from the high-frequency flapping modes to the low-frequency body modes. As such, there is a need to study the stability of the FWMAV system as a nonlinear time periodic system. Moreover, the above assumptions on the FWMAV dynamics, which lead to a linear time invariant

system, allow for the exploitation of tools used in linear control design, such as linear quadratic regulation and state feedback. However, the uncertainty in the aerodynamic modeling requires utilizing adaptive control for FWMAVs. Besides, the minimal actuation dictated by the size and weight constrains of FWMAVs might lead to an under-actuated system, thereby invoking the possibility of exploiting system nonlinearities via geometric control theory for example. On the other hand, this raises a need for developing efficient actuation mechanisms that might exploit nonlinearity to produce motions in the un-actuated directions.

As for simulation purposes, the literature of flight dynamics of FWMAVs lacks some fidelity in simulation and needs reexamination of some of the major assumptions. There is a need for a rigorous aeroelastic-flight dynamic model. This model has to include a moderate fidelity unsteady aerodynamic representation, which can be run every time step to determine the instantaneous aerodynamic loads, which are in turn fed to a complete dynamic model without the ubiquitous assumptions of averaging the dynamics and neglecting the wing inertia forces. Then, the dynamic model is marched forward in time using an appropriate time marching scheme. As such, one can have a fair assessment of the stability of flapping flight and hence remove the discrepancy in the literature, which rarely show agreeing results.

Chapter 2

Aerodynamic Modeling

In this chapter, a state-space formulation for the aerodynamics of flapping flight is presented. The aspect ratio effects on the empirical formulae used to predict the static lift due to a stabilized leading edge vortex (LEV) is provided in section 2.2. In section 2.3, the Duhamel's principle, applied in linear unsteady flows, is extended to non-conventional lift curves to capture the LEV contribution. The unsteady lift due to arbitrary wing motion is generated using the static lift curve. Hence, state-space representation for the unsteady lift is provided. The developed model is then applied to hovering micro-air-vehicles and insects in section 2.4. In section 2.5, the proposed model is validated through a comparison with direct numerical simulations of Navier-Stokes on hovering insects. A comparison with quasi-steady models that capture the LEV contribution is also performed to assess the role of unsteadiness. Similarly, a comparison with classical unsteady approaches is presented to assess the LEV dominancy. Then, a reduced-order model that is more suitable for flight dynamics and control analyses is derived from the full model and presented in section 2.6. Finally, estimates for the drag and power requirements are provided in section 2.7.

2.1 Introduction

The aerodynamics of flapping flight have been the focus of research investigations for almost a century. The early studies were concerned with birds and insect flights and mainly carried out by biologists, such as Demoll (46; 47). More recently, there has been a significant interest in the modeling and simulation of flapping flights for design of micro-air-vehicles (MAVs). Flapping flight of MAVs/insects generates an unsteady nonlinear flow field that exploits non-conventional mechanisms to enhance the aerodynamic loads. Almost all of the

early trials of explaining insect flight have invoked non-conventional high-lift mechanisms. Ellington et al. (63) explained how insects exploit the Leading Edge Vortex (LEV) as a high-lift mechanism, which is also known to be critical for lift generation of highly swept and delta wings aircraft. The LEV augments the bound vortex on the wing and, as such, the lift increases. This phenomenon is similar to the one observed in dynamic stall whereby the wing undergoes a rapid variation in the angle of attack. Yet, in contrast to dynamic stall, the LEV formed in insect flight has stable characteristics. This stability is attributed to an outward spanwise flow that convects the LEV towards the wing tip (63; 107; 108; 109). In the case of highly swept and delta wings, this spanwise flow is generated by the free-stream component parallel to the highly swept leading edge. In insect flight, similar to helicopters and propellers, the rotational motion creates a spanwise velocity gradient which, in turn, creates a pressure gradient that generates the spanwise flow.

Although the LEV is known to be the dominant contribution in insect flight, Dickinson et al. (3) indicated two other high-lift mechanisms, namely the rotational lift and wake-capture effects. The rotational lift is mainly due to the wing rotation at the end of each half stroke to adjust the angle of attack for the next half stroke. This rotational velocity of the wing creates a circulation that induces additional aerodynamic lift. On the other hand, Dickinson et al. observed peaks in the generated lift at the beginning of half strokes, when forward speed of the wing is almost zero. These peaks could not be explained by the previous two mechanisms. Dickinson et al. related these peaks to the lingering wake created during the previous half stroke. In addition to the non-conventional high-lift mechanisms discussed above, the role of unsteady aerodynamics in flapping flight is also quite significant. Other flow aspects that affect the aerodynamic loads include non-circulatory and viscous friction contributions. Unfortunately, it is very difficult to formulate a model for the aerodynamic forces that accurately captures all these phenomena without an expensive computational burden.

Over the two past decades, significant advancements have been made towards the understanding and modeling of the aerodynamics of flapping flight. For detailed reviews, the reader is referred to Mueller (91), Shyy et al. (92), Sane (93), Wang (94), and Ansari et al. (145). Taha et al. (146) provided a review for the aerodynamic models specifically used in flight dynamics and control analyses. Table 2.1 lists the aerodynamic models that are available in the literature to be applied to hovering MAVs/insects. It also lists the physical aspects associated with the aerodynamics of flapping flight that are captured by each of these models and the associated computational cost. Computational cost is based on the complexity level of the aerodynamic model. The first two models have algebraic forms and the third one comprises finite-state ordinary differential equations. The last two models involve simulation of the vortex kinematics at many locations on the airfoil surface and in its wake. Clearly, the first three models have a lower computational cost than the last two and hence are better-suited for flight dynamics and control analysis. It is concluded

from Table 2.1 that there is no aerodynamic model that can capture the dominant LEV contribution along with the prominent unsteadiness with a feasible computational burden so that it could be used in flight dynamics analysis, control synthesis, optimization, and sensitivity analysis.

	Dickinson et al. (3)	Berman & Wang (43)	Peters et al. (65; 66)	UVLM	Ansari et al. (80; 81)
Computational Cost	✓	✓	✓	-	×
LEV Contribution	✓	✓	×	×	✓
Unsteadiness	×	×	✓	✓	✓
Rotational Lift	✓	✓	✓	✓	✓
Added Mass	✓	✓	✓	✓	✓
Wake Capture (Hovering)	×	×	×	✓	✓
Viscous Friction	×	✓	×	×	×

Table 2.1: The aerodynamic models in the literature that could be applied to hovering MAVs/insects and the physical aspects associated with the aerodynamics of flapping flight that each of the listed models captures along with the computational cost associated with that model. UVLM refers to the unsteady vortex lattice method.

More generally, Fig. 2.1 presents a taxonomy of the flapping flight regimes. For forward flights with a low reduced frequency k, typically $k < 0.1$, the quasi-steady aerodynamics are applicable. For forward flight with a relatively high k with local angles of attack up to 20°, a number of aerodynamic theories can be applied to capture the unsteadiness with a good accuracy either for two-dimensional or three-dimensional wings, see for example, Theodorsen, Shwarz and Sohngen (see (103)), Peters et al. (65; 66; 147; 148; 149; 150), Jones (151; 77; 78), and Reissner (75). In addition, methodologies such as the unsteady lifting line theory, the unsteady vortex lattice method, and the unsteady doublet lattice method can also be used to capture the unsteady effects on three-dimensional wings. On the other hand, for hovering with very high flapping frequency ω relative to the body natural frequency ω_n, it is generally assumed that there is no coupling between the periodic aerodynamic forces and the body natural modes (146). As such, the body feels only the average forces, which might be predicted by the quasi-steady models that capture the dominant effect (LEV), for example, Dickinson et al. (3), Pesavento and Wang (4), and Andersen et al. (5; 6). For the middle regimes in Fig. 2.1, there is no aerodynamic model that could cover this gap with a feasible computational burden. The main characteristics of this regime is the LEV contribution, the prominent unsteadiness, and the coupling between the periodic aerodynamic forces and the body modes. The objective in this chapter is to develop a physics-based model in the form of ordinary-differential equations that describe the lift buildup during the flapping cycle, including the effect of the LEV on the aerodynamic loads. This model can provide

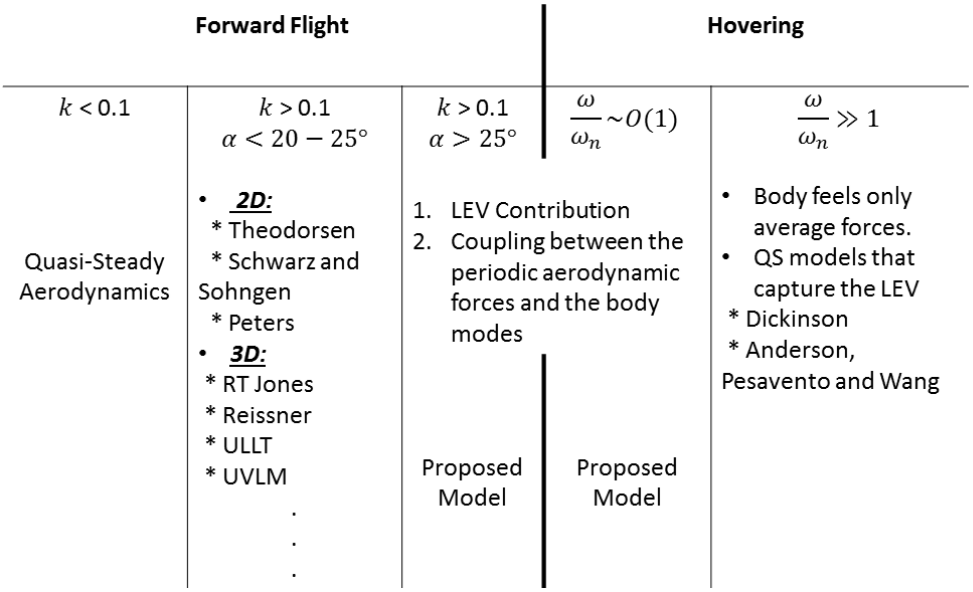

Figure 2.1: Taxonomy of hovering and forward flight regimes. In forward flight, the reduced frequency $k = \frac{\omega c}{2U}$ is the key parameter to identify the region of application for each aerodynamic model. In hovering, the ratio of the flapping frequency ω to the body natural frequency ω_n is used to characterize the flight regimes.

better assessment of the flapping flight dynamic stability, when augmented with the body equations of motion.

Motivated by developing such a model, the effects of aspect ratio are embedded in the empirical formulae used to predict the static lift due to a stabilized LEV. Then, the Duhamel superposition principle, applied in unsteady linear aerodynamics, is extended to flows with arbitrary C_L-α curves. This approach basically utilizes the static lift curve to determine the unsteady lift due to an arbitrary wing motion. A specific aspect of this approach is the use of the quasi-steady circulation as the aerodynamic forcing input rather than the angle of attack or the airfoil speed. Hence, the developed model can be used to predict the temporal lift build up due to stabilized LEV, including the lag and phase shift associated with unsteady flows. The LEV contribution is captured as included in the static lift curve, which in turn, is used to construct the quasi-steady circulation (the aerodynamic forcing input). Finally, a state-space representation of a complete unsteady aerodynamic model with application to hovering insects is provided. Validation of the derived model is performed through a comparison of time-histories of the modeled lift with corresponding results obtained by Sun and Du (87) solving Navier-Stokes equations for different insects. The results are also compared with those of the quasi-steady model of Berman and Wang (43) and those of the classical unsteady models.

2.2 Static Lift Due to a Stabilized LEV-Effect of Aspect Ratio

Due to its compactness, the model of Dickinson et al. (3) has been extensively used in dynamics and control of flapping-wing MAVs (FWMAVs), e.g., (28; 22; 7; 97; 27; 9; 25). It is a quasi-static expression; i.e., it gives an algebraic expression for the lift and drag coefficients as functions of the instantaneous angle of attack

$$\begin{aligned} C_L &= 0.225 + 1.58\sin(2.13\alpha - 7.20) \\ C_D &= 1.92 - 1.55\cos(2.04\alpha - 9.82) \end{aligned} \tag{2.1}$$

Wang et al. (110) fit their data with simpler forms; $C_L = A\sin 2\alpha$, $C_D = B - C\cos 2\alpha$ or $C_D = C_D(0)\cos^2\alpha + C_D(\frac{\pi}{2})\sin^2\alpha$, where the coefficients $A, B, C, C_D(0)$, and $C_D(\frac{\pi}{2})$ were determined experimentally.

There are two fundamental shortcomings with the quasi-steady models mentioned above. Firstly, they do not account for the unsteady aspects associated with flapping flight. Secondly, the coefficients describing the aerodynamic terms in these models are determined empirically and typically do not account for any variations in the wing shape. This latter concern can best be explained by considering the work of Polhamus (113) who was the first to model the LEV contribution on highly swept and delta wings by a leading edge suction analogy. He identified two components for the lift, namely the potential flow lift with zero leading edge suction, $C_{Lp} = K_p \sin\alpha\cos^2\alpha$, and the vortex lift $C_{Lv} = K_v \cos\alpha\sin^2\alpha$. Both K_p and K_v are functions of the aspect ratio (AR). Particularly, K_p, which becomes the lift curve slope in the limit of small angles of attack, is a strong function of the AR. Since Polhamus' formula models the same phenomenon (a stabilized LEV) as the previously mentioned quasi-steady models such as Dickinson's model, Eq. (2.1), the coefficients in these models would not be valid for any arbitrary wing, as those coefficients could considerably change with variations in the AR. In this section, a more general formula for the lift coefficient in terms of the wing AR is provided.

Wang et al. (110) showed that the static lift coefficient for a translating wing, taking into account the LEV effect, could be fit by $C_L = A\sin 2\alpha$ where A is a constant coefficient. Berman and Wang (43) provided values for A for the hawkmoth, bumblebee, and fruitfly. However, there are no general formulas for this coefficient as a function of the wing geometry. In the limit to small angles, the formula by Wang et al. reduces to $C_L = 2A\alpha$; i.e., $2A$ may be considered as the lift curve slope of the three-dimensional wing C_{L_α}. Since flapping flight is associated with low aspect ratio wings, one can use the *Extended Lifting Line Theory* (Schlichting and Truckenbrodt(105)) to obtain the dependence of C_{L_α} on the wing AR, which is given by

$$C_{L_\alpha} = \frac{\pi AR}{1 + \sqrt{(\frac{\pi AR}{a_0})^2 + 1}} \tag{2.2}$$

Insect	R (mm)	S (mm^2)	Aspect Ratio	A
Drosophila virilis	3	2.97	3.10	-
Hawk moth	51.9	947.8	2.84	1.678
Bumble bee	13.2	54.9	3.17	1.341
Fruit fly	2.02	1.36	3.00	1.833

Table 2.2: Morphological and aerodynamic parameters for the four studied insects.

with the AR being based on one wing; i.e., $AR = \frac{R^2}{S}$, and a_0 is the lift curve slope of the two-dimensional airfoil section, e.g. it is equal to 2π for a flat plate. For conventional airfoils, it could be determined from lift curves such as the ones presented by Abbott and Doenhoff (152). Using Eq. (2.2), the static lift coefficient can be written as

$$C_L = \frac{\pi AR}{2\left(1 + \sqrt{(\frac{\pi AR}{a_0})^2 + 1}\right)} \sin 2\alpha \tag{2.3}$$

A comparison is performed among the C_L-α curve using Eq. (2.3), Polhamus' formula, the potential flow lift coefficient $C_L = C_{L_\alpha} \sin\alpha$, and benchmark results for four insects: Drosophila virilis, Hawk moth, Bumble bee, and Fruit fly. Equation (2.2) was used to determine C_{L_α} in Polhamus' formula ($K_p \equiv C_{L_\alpha}$) and the potential flow equation. As for the coefficient K_v in Polhamus' formula for the lift due to LEV, the expression given in (113)

$$K_v = (K_p - K_p^2 K_i)\frac{1}{\cos\Lambda} \tag{2.4}$$

is adopted, where $K_i = \frac{\partial C_{D,induced}}{\partial C_L^2}$, which can be taken as $\frac{1}{\pi AR}$ for elliptic wings, and Λ is the sweep angle, which is assumed to be zero. Dickinson's empirical model, Eq. (2.1), was used to obtain the benchmark C_L in Fig. 2.2(a) for the Drosophila virilis wing which was used as the basis for their empirical model in (3). For the other three insects, the formula of Wang et al. $C_L = A\sin 2\alpha$ was used to obtain the benchmark C_L, taking the values of A provided by Berman and Wang (43) for those insects. Table 2.2 lists the morphological parameters (R, S and AR) for the four insects, and the aerodynamic parameter A for the three insects given in (43). It should be noted that although the range of the aspect ratio over which Eq. (3) is validated is small, it covers the typical range for hovering insects and proposed flapping-wing micro-air-vehicles.

The divergence observed in Fig. 2.2 between the potential flow lift and the benchmark results for all insects at relatively high values of α is expected. Although Polhamus (113) did not verify his results for this wide range of α, his approach shows a good agreement with the benchmark results. However, the proposed formula, Eq. (2.3), is quite simpler and yields C_L values that are closer to the benchmark results than those of Polhamus for all insects.

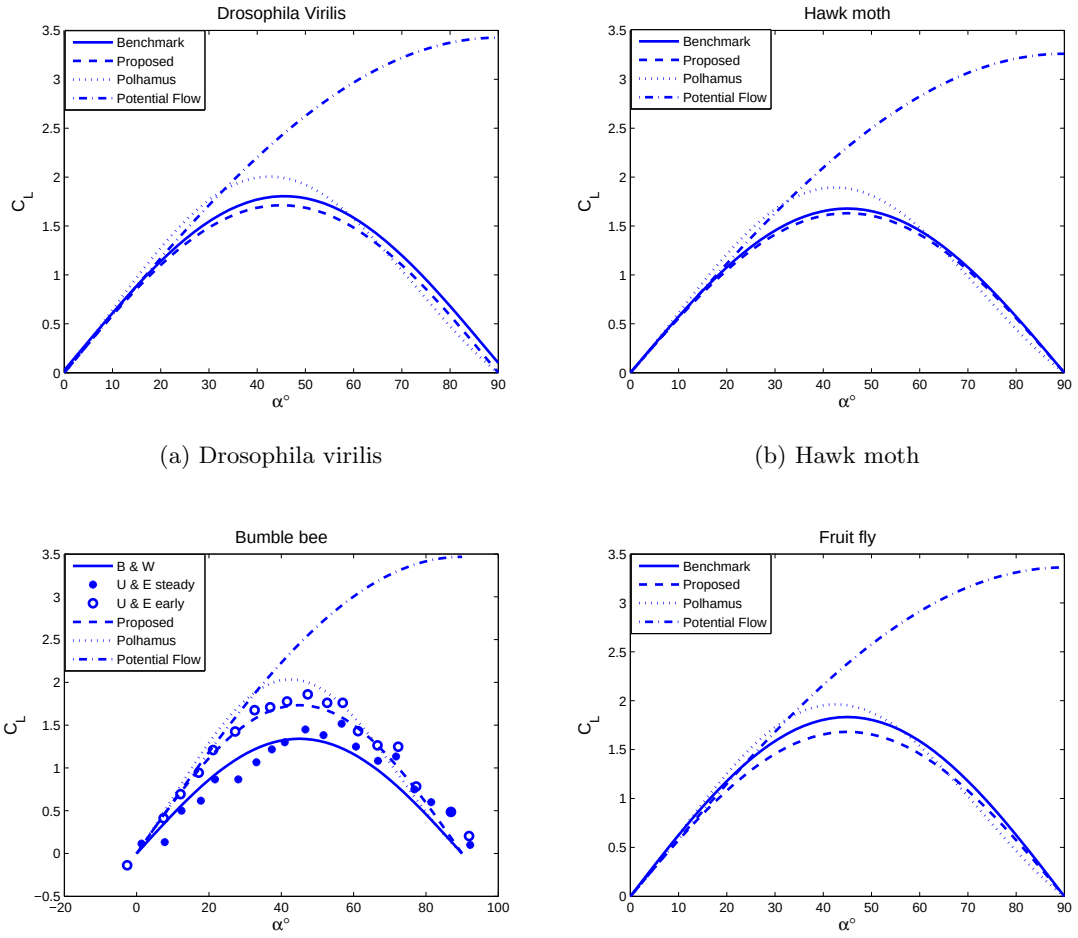

(a) Drosophila virilis

(b) Hawk moth

(c) Bumble bee

(d) Fruit fly

Figure 2.2: Comparison between the proposed formula, Polhamus, potential flow, and benchmark results for C_L due to a stabilized LEV

The bumble bee case deserves a more thorough discussion. Two benchmark results have been shown in Fig. 2.2(c), namely, those of Berman and Wang (43) and Usherwood and Ellington (153). Berman and Wang obtained the coefficient A by fitting the data of Dudley and Ellington (154), which were for steady forward flight not hovering. That is, these data were for a completely fixed wing in a wind tunnel, not a revolving wing like that of the experiments of Dickinson et al. (3) or Usherwood and Ellington (153). This may be the reason for the relatively larger discrepancy between the estimated C_L by Berman, and Wang, and the one predicted by Eq. (2.3) and that of Polhamus' formula. It should be noted that Usherwood and Ellington (153) provided two sets of C_L-measurements. They categorized them into *early* and *steady* measurements. The early set represents measurements during the first half revolution of the wing from the start time excluding transients. The steady set represents measurements from 180° to 450° (from half to one and a half revolutions). Since a steady rotation (not back and forth flapping) is considered in the experiment, the early measurements are taken before the propeller wake and downwash are fully developed and steady conditions are reached. Hence, Usherwood and Ellington suggested the use of the early set for analysis of flapping flight . The C_L values predicted by Eq. (2.3) are in a better agreement with the early results of Usherwood and Ellington than those of Berman and Wang. On the contrary, the estimated C_L by Berman and Wang is closer to the steady results of Usherwood and Ellington. In conclusion, Eq. (2.3) has been shown to provide a surrogate model that accounts for the AR effects on the lift due to a stabilized LEV.

2.3 Extension of Duhamel Principle to Arbitrary C_L-α Curves

Because of their ability to capture the unsteady effects in a compact form, finite-state aerodynamic models have been used for aeroelastic and flight dynamic simulations and control design. The basis for most of the developed finite-state aerodynamic models is either Wagner's and/or Theodorsen's model for the unsteady lift. Wagner (62) obtained the time-response of the lift on a flat plate due to a step input (indicial response problem). Theodorsen (155) obtained the frequency response of the lift; that is, lift response due to a harmonically oscillating input, and applied it to the flutter problem of fixed-wing aircraft. Garrick (156) showed that the Wagner function, $W(s)$, and the Theodorsen function, $C(k)$, are related through the Fourier transform.

The principle underpinning this investigation is the Duhamel superposition principle. Wagner (62) determined the circulatory lift due to a step change in the wing motion. The unsteady lift is then written in terms of the static lift as

$$\ell(s) = \ell_s W(s) \tag{2.5}$$

where the non-dimensional time s is defined as $s = \frac{2Ut}{c}$ for constant free-stream velocity U and defined as

$$s = \frac{2}{c}\int_0^t U(\tau)d\tau \tag{2.6}$$

for varying free-stream $U(\tau)$ in this work. As for the dynamic lift, knowing the indicial response for a linear dynamical system, the response due to arbitrary excitation (input) can be written as an integral (superposition) using the indicial response and time-variation of the input variable. As such, the variation of the circulatory lift due to an arbitrary change in the angle of attack is expressed as

$$\ell(s) = \pi\rho U^2 c\left(\alpha(0)W(s) + \int_0^s \frac{d\alpha(\sigma)}{d\sigma}W(s-\sigma)d\sigma\right) \tag{2.7}$$

It is noted that $W(s)$ can also be used as an indicial response to aerodynamic inputs other than the angle of attack. Van der Wall and Leishman (157) used it as an indicial response to the wing normal velocity, $w = U\alpha$, in the case of time-varying free stream. For a relatively high angle of attack, the Duhamel superposition is performed using a more exact normal velocity $w = U\sin\alpha$. Equation (2.7) is then re-written as

$$\ell(s) = \pi\rho U(s) c\left(U(0)\sin\alpha(0)W(s) + \int_0^s \frac{d\left(U(\sigma)\sin\alpha(\sigma)\right)}{d\sigma}W(s-\sigma)d\sigma\right) \tag{2.8}$$

This equation is usually used in dynamic stall models where relatively high α's are encountered, e.g., the Beddoes-Leishman dynamic stall model developed in (158; 159; 160; 161).

The main issue with the classical unsteady formulations discussed above is their inability to account for a non-conventional lift curve (lift mechanism), such as the LEV contribution. To remedy this, it is noted that the above discussion presumes linear dependence of the lift on α, $U\alpha$, or $U\sin\alpha$. Within the framework of potential flow, the lift is linearly dependent on the circulation. This linear dependence presents the possibility of generalizing Eq. (2.8) for an arbitrary lift curve using the circulation as an aerodynamic forcing input in the Duhamel integral. As such, the Duhamel's integral is written as

$$\ell(s) = \rho U(s)\left(\Gamma_{QS}(0)W(s) + \int_0^s \frac{d\Gamma_{QS}(\sigma)}{d\sigma}W(s-\sigma)d\sigma\right) \tag{2.9}$$

where Γ_{QS} is the quasi-steady circulation. For a translating wing, $\Gamma_{QS}(s) = \frac{1}{2}cU(s)C_L(s)$, where the static lift curve is used to predict $C_L(s)$; i.e., $C_L(s) \equiv C_{L,s}(\alpha(s))$. Equation (2.9) is the extension of the unsteady aerodynamic modeling using Duhamel superposition to arbitrary static C_L-α curves, and arbitrary-varying free-stream $U(s)$. It should be noted that Eq. (2.9) reduces to all the previous forms of Duhamel superposition for the particular cases of interest. Moreover, Eq. (2.9) allows us to account for the instantaneous rotational effects ($\dot{\alpha}$-effects). This can be achieved by splitting the translational component

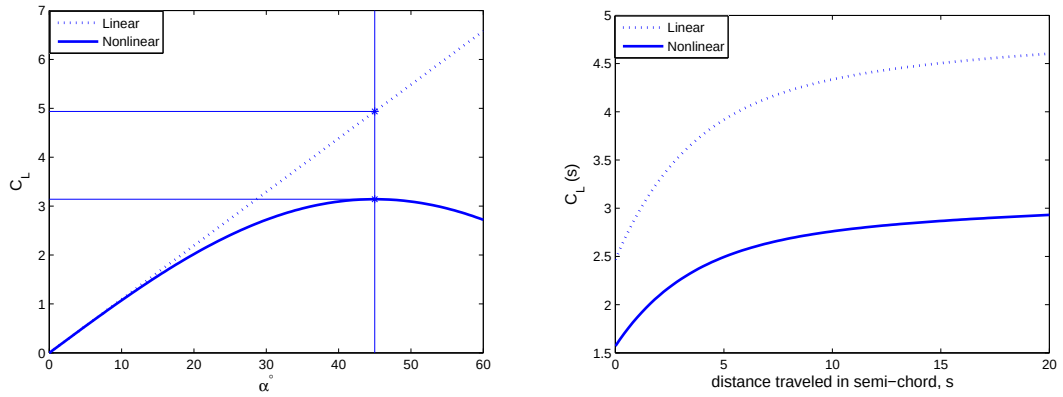

(a) Static lift variation with the angle of attack

(b) Lift build up

Figure 2.3: Linear and nonlinear lift build up.

from the rotational one and writing the total circulation as the sum of the two terms, i.e., $\Gamma = \Gamma_{trans} + \Gamma_{rot}$. As for Γ_{rot}, one could use the potential flow result of a pitching airfoil, see (162)

$$\Gamma_{rot} = \pi c^2 \dot{\alpha}(\frac{3}{4} - \widehat{x}_0) \tag{2.10}$$

This splitting is justified as Eq. (2.10) matches well the experiments of Dickinson et al. (3), Sane and Dickinson (111) and Andersen et al. (5).

The main assumption here is that the flow dynamics remain linear and the Wagner function could be used to represent the indicial response of the circulatory lift even for high values of α; that is, Eq. (2.5) is still valid for high values of α. In other words, it is assumed that the nonlinearity of the C_L-α curve is accounted for in the steady circulation term (input) and does not affect the temporal build up of the circulatory lift, as illustrated in Fig. 2.3 for a constant free stream. Figure 2.3(a) shows static linear and nonlinear lift curves, from which the C_L values at a certain angle of attack, α, are picked. Figure 2.3(b) shows the corresponding lift build up to these values. It is assumed that both the linear and nonlinear lift exhibit the same temporal lift build up but to different values; ones corresponding to the static lift curves.

To be more suitable for dynamic stability analysis and control synthesis, Eq. (2.9) would be written in a state-space form. For constant U, one could use a finite-state approximation for $W(s)$, e.g., R.T. Jones

(151) or W.P. Jones (163), which presents $W(s)$ on the form

$$W(s) = 1 - A_1 e^{-b_1 s} - A_2 e^{-b_2 s} \tag{2.11}$$

Then, one can use Laplace transform to get a transfer function and consequently to obtain the corresponding state-space model. However, for a variable free-stream, the targeted state-space model is expected to have time-varying coefficients, which eliminates the ability to use the Laplace transform. Rewriting Eq. (2.9) in terms of the dimensional time variables, t and τ, and integrating the second term by parts, one obtains

$$\ell(t) = \rho U(t)\Gamma_{eff}(t) = \rho U(t)\left(\Gamma_{QS}(t)W(0) - \int_0^t \Gamma_{QS}(\tau)\frac{dW(t-\tau)}{d\tau}d\tau\right) \tag{2.12}$$

where Γ_{eff} is the effective unsteady circulation. Using the two-state approximation of the Wagner function as presented in Eq. (2.11) and recalling the definition of the non-dimensional time from Eq. (2.6), the term $\frac{dW(t-\tau)}{d\tau}$ is written as

$$\frac{dW(t-\tau)}{d\tau} = -A_i\frac{2b_i}{c}U(\tau)e^{\frac{-2b_i}{c}\int_\tau^t U(\tau)d\tau} \quad , \quad i = 1,2 \tag{2.13}$$

where summation on the repeated indexes is used. Thus, Γ_{eff} is given by

$$\Gamma_{eff}(t) = (1 - A_1 - A_2)\,\Gamma_{QS}(t) + x_i(t) \quad , \quad i = 1,2 \tag{2.14}$$

where x_i is written as

$$x_i(t) = \int_0^t U(\tau)A_i\frac{2b_i}{c}U(\tau)e^{\frac{-2b_i}{c}\int_\tau^t U(\tau)d\tau}d\tau \quad , \quad i = 1,2 \tag{2.15}$$

Eq. (2.15) represents solution to the linear differential equation

$$\dot{x_i}(t) = \frac{2b_i U(t)}{c}\left(-x_i(t) + A_i\Gamma_{QS}(t)\right) \quad , \quad i = 1,2 \tag{2.16}$$

with $x_i(0) = 0$. In conclusion, the circulatory lift per unit span is written as

$$\ell(t) = \rho U(t)\left[(1 - A_1 - A_2)\,\Gamma_{QS}(t) + x_1(t) + x_2(t)\right] \tag{2.17}$$

where the state equations for x_1 and x_2 are given in Eq. (2.16) and $\Gamma_{QS}(t)$ is given by

$$\Gamma_{QS}(t) = \frac{1}{2}cU(t)C_{L,s}(\alpha(t)) + \pi c^2(\frac{3}{4} - \widehat{x}_0)\dot{\alpha}(t) \tag{2.18}$$

Any arbitrary wing motion $(U(t), \alpha(t))$ along with any arbitrary nonlinear $C_{L,s}$-α curve can be plugged into Eq. (2.18) to obtain the time variation of the quasi-steady circulation $\Gamma_{QS}(t)$. This term is, in turn,

considered as a forcing term in the state-space model, Eq. (2.16). The circulatory lift per unit span, ℓ, is then determined from Eq. (2.17).

2.4 Application to Hovering MAVs/Insects

In flapping-wing flight, the flapping kinematics with respect to the body is usually described by the three Euler angles: the back and forth flapping angle φ, the plunging angle ϑ, and the pitching angle η. However, it can be assumed that most insects hover in a horizontal stroke plane without an out-of-plane motion ($\vartheta = 0$) as stated by Weis and Fogh (20) and Ellington (21). Figure 2.4 shows a schematic diagram for a hovering FWMAV performing a horizontal stroke plane and the axis-systems used to describe the wing kinematics: an inertially-fixed frame x_I, y_I, and z_I; a body-fixed frame x_b, y_b, and z_b; and a wing-fixed frame x_w, y_w, and z_w. If the wing flexibility is considered, a wing-deformed frame would also be needed. The x_b-axis points forward, the y_b-axis points to the right wing, and the z_b-axis completes the triad. Two rotations are considered, in this work, from the body-frame to the wing-frame; that is φ and η. The flapping angle φ is the rotation about the z_b-axis and the pitching angle η is the rotation about the y_w-axis. As such, the total flapping velocity, seen by an airfoil section that is a distance r from the wing root, is $r\dot{\varphi}$ with the angle of attack given by

$$\alpha(t) = \begin{cases} \eta, & \dot{\varphi} > 0 \\ \pi - \eta, & \dot{\varphi} < 0 \end{cases} \tag{2.19}$$

Hence, according to the unsteady finite-state model developed above, the instantaneous lift per unit span on that airfoil section is given by

$$\ell(r,t) = \ell_{NC}(r,t) + \rho r|\dot{\varphi}(t)|\left[(1 - A_1 - A_2)\,\Gamma_{QS}(r,t) + x_1(r,t) + x_2(r,t)\right] \tag{2.20}$$

where the non-circulatory lift component, ℓ_{NC}, is given by

$$\ell_{NC}(r,t) = -m_{app}(r) a_y(r,t)\cos\eta(t) \tag{2.21}$$

where $m_{app}(r) = \frac{\pi}{4}\rho c^2(r)$ is the apparent mass of the two-dimensional strip, $a_y(r,t)$ and $\Gamma_{QS}(r,t)$ are the airfoil upward normal acceleration and the quasi-steady circulation, respectively, and are given by

$$\begin{aligned} a_y(r,t) \quad &= r(-\ddot{\varphi}(t)\sin\eta(t) - \dot{\varphi}(t)\dot{\eta}(t)\cos\eta(t)) \\ \Gamma_{QS}(r,t) &= \tfrac{1}{2}c(r)r\dot{\varphi}(t)C_{L,s}(\eta(t)) + \pi c^2(r)(\tfrac{3}{4} - \widehat{x}_0)\dot{\eta}(t) \end{aligned} \tag{2.22}$$

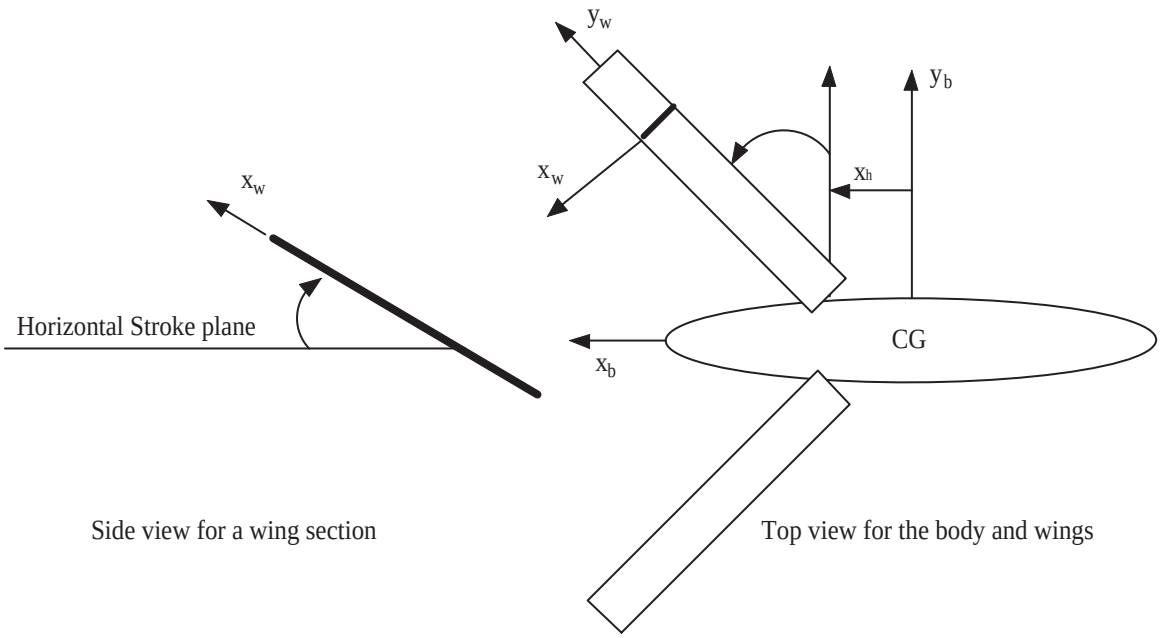

Figure 2.4: A schematic diagram for a hovering FWMAV performing a horizontal stroke plane and the axis-systems used to describe the wing kinematics.

where, for hovering MAVs having LEV shed, it has been shown in section 2.2 that Eq. (2.3) is sufficient to predict the static lift coefficient $C_{L,s}$ of the three-dimensional wing. Finally, the dynamics of the internal flow-states x_1 and x_2 are governed by

$$\dot{x_i}(r,t) = \frac{2b_i r|\dot{\varphi}(t)|}{c(r)} \left[-x_i(r,t) + A_i \Gamma_{QS}(r,t)\right], j = i = 1,2 \tag{2.23}$$

The three-dimensionality is accounted for by using strip theory and $C_{L,s}$ of the three-dimensional wing.

2.5 Validation and Comparison with Previous Models

Validation of the aerodynamic loads as predicted by the proposed model is performed by comparing its results to those obtained by Sun and Du (87). They performed direct numerical simulation (DNS) for Navier-Stokes equations on the wings of different insects that cover a wide range of operating conditions and morphological parameters. According to the above model, the lift force is driven by the wing kinematic functions, φ and η. Sun and Du considered idealized kinematics without an out-of-plane motion ($\vartheta = 0$) that closely match the observed kinematics in nature, as described by Dickinson et al. (3). Their kinematics prescribe the flapping angle to be a simple harmonic: $\varphi(t) = -\frac{\Phi}{2}\cos(\omega t)$, where $\frac{\Phi}{2}$ is the flapping amplitude. As for the pitching

angle, η, it takes a constant value, referred to as α_m, except at the beginning and near the end of each half stroke. During the rotation phase, the η variation is described by

$$\eta(t) = \frac{\Delta\alpha}{\Delta t_r}\left[(t - t_r) - \frac{\Delta t_r}{2\pi}\sin(\frac{2\pi(t - t_r)}{\Delta t_r})\right] \tag{2.24}$$

where Δt_r is the duration of each rotational phase, and t_r is the time at which this phase starts. Knowing α_m is enough to determine $\Delta\alpha$, since the wing rotates from α_m to $\pi - \alpha_m$ or vice versa. Setting Δt_r equal to $0.25T$, and considering symmetric rotation, t_r can be determined. As for the wing planform, one just needs the chord distribution, or more specifically the weighted moments of the wing area. The values of these moments can be found in (164) for the fruitfly and in (57) for all other insects. Sun and Du listed all the required morphological parameters, f, Φ, α_m, S, R, and the total mass for all the insects under study.

To further emphasize the physical aspects captured by the developed model, the obtained results are compared to the most recent quasi-steady model of Berman and Wang (43) which is based on Andersen et al. (5; 6) and Pesavento and Wang (4). This comparison is expected to show the effects of unsteadiness on the aerodynamics of flapping flight. The obtained results are also compared with the classical unsteady approach; i.e., the state-space formulation of Eq. (2.8) along with the added mass contribution. This model is described in details in (160; 161). This comparison is expected to assess the effects of the LEV on the aerodynamics of flapping flight. It should be noted that, because of the low aspect ratio of insect wings, keeping the lift curve slope at 2π like the classical unsteady approach shown in Eq. (2.8), leads to highly erroneous results (almost doubles the aerodynamic loads). So, it is opted to use the three-dimensional lift curve slope as presented in Eq. 2.2 in the classical unsteady formulation as well to make the comparison more meaningful.

Figure 2.5 shows a comparison of the steady-state periodic variation of the lift coefficient over one cycle for four insects. The lift coefficient is based on the reference speed adopted by Sun and Du, $U_{ref} = 2f\Phi r_2$, where r_2/R is the non-dimensional second moment of wing area. As such, the lift coefficient is defined as $C_L = \frac{L}{\rho U_{ref}^2 S}$. It should be emphasized that despite the complexity of the flow field and the simplicity and compactness of the proposed model, it is able to capture the LEV contribution in an unsteady fashion as the lift variation throughout the cycle matches well the benchmark results for all the insects.

It is very well known that quasi-steady models predict higher loads than their unsteady counterparts, see (106) for example. This illustrates the reason behind the higher C_L-values predicted by the model of Berman and Wang. Its unsteady counterpart (the present model) is closer to the DNS results of Sun and Du. The largest deviation amongst the four insects of the quasi-steady model of Berman and Wang from the present and the DNS results takes place in the case of fruitfly ($f = 254Hz$). This is consistent with

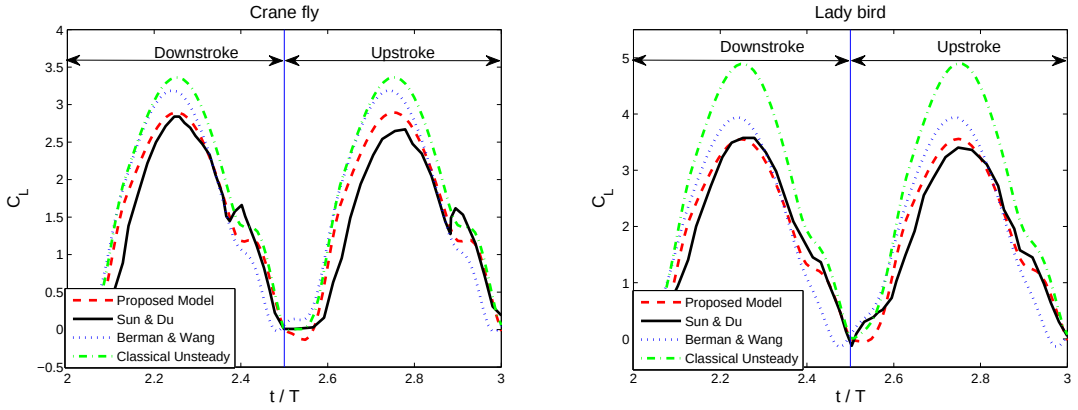

(a) Crane fly, $f = 45.5$ Hz and $\alpha_m = 30^\circ$

(b) Lady bird, $f = 54$ Hz and $\alpha_m = 43^\circ$

(c) Hover fly, $f = 160$ Hz and $\alpha_m = 29^\circ$

(d) Fruit fly, $f = 254$ Hz and $\alpha_m = 46^\circ$

Figure 2.5: Comparison of the C_L over one flapping cycle using the current state-space model, the DNS results of Sun and Du, the quasi-steady model of Andersen et al., and the classical unsteady approach for four insects.

the fact that the deviation of quasi-steady models from their unsteady counterparts is more pronounced at higher frequencies. On the other hand, the steady values for C_L due to a stabilized LEV are less than those predicted by the classical potential flow formula $C_L = C_{L_\alpha} \sin\alpha$, as shown in Fig. 2.2, particularly for angles of attack higher than 25°. This illustrates the reason behind the higher C_L-values predicted by the classical unsteady approach in the middle of half strokes where the LEV contribution is dominant. Deviations of the classical unsteady results from the present and the DNS ones are larger in the cases of $\alpha_m = 46°$ and 43 (fruitfly and ladybird) in comparison to the cases of $\alpha_m = 29°$ and 30 (hoverfly and cranefly). This is consistent with the fact that the deviation of the classical potential flow theory from the true LEV steady C_L-α curve becomes larger as the angle of attack is increased, see Fig. 2.2. It should be noted that, however, near stroke reversals where the effect of wing rotation becomes dominant, the classical unsteady approach predicts C_L-values that are very close to the present results and the DNS results. Note that they have the same models for rotational contributions.

It is noted from Fig. 2.5 that the quasi-steady model of Berman and Wang is closer to the present results and the DNS results than the classical unsteady approach in the middle of half strokes where the LEV contribution is dominant. However, its performance is poorer near stroke reversals where the rotational contribution is dominant. Thus, for symmetric flapping (identical downstroke and upstroke) where the net rotational contribution to the cycle-average lift is zero, the quasi-steady models of Berman and Wang or Dickinson et al. (3) might result in good estimates for the cycle-average lift coefficients. This notion along with their compactness make them suitable for performing preliminary designs of FWMAVs. However, because they perform poorly near stroke reversals, these models are not satisfactory when used to perform aerodynamic optimization that may depend on rotational contributions or to analyze asymmetric flapping cycles necessary for control purposes. It is noteworthy to mention that because the present model is intended to be a blend of the quasi-steady models (capturing the LEV contribution) and the classical unsteady representations, its results are always closer to the better model in its region of applicability; i.e., closer to the quasi-steady model in the middle of half strokes and closer to the unsteady model near stroke reversals.

Table 2.3 presents the operating conditions for the four insects under study along with two comparison metrics between each of the three studied models and the DNS results. These metrics are the percentage deviation in cycle average lift coefficient from the DNS value $\Delta\overline{C_L}\% = \frac{|\overline{C_L}_{model} - \overline{C_L}_{DNS}|}{\overline{C_L}_{DNS}} \times 100$ and the root-mean-squared difference of the lift coefficient in percent of maximum lift coefficient $\Delta C_{L_{rms}}\% = \frac{\sqrt{\frac{1}{T}\int_0^T \left(C_{L_{model}}(t) - C_{L_{DNS}}(t)\right)^2 dt}}{max(C_{L_{DNS}})} \times 100$. Both metrics show that the performance of the present model is better than the other two models. It should be also emphasized that the computational cost of the three models under study are almost the same. Therefore, using the present model allows capturing non-conventional lift curves/mechaisms (LEV) in an unsteady fashion without an extra computational burden. Finally, it

Insect	Φ°	α_m°	f (Hz)	Present Model $\Delta\overline{C_L}\%$ $\Delta C_{L_{rms}}\%$	Previous Unsteady $\Delta\overline{C_L}\%$ $\Delta C_{L_{rms}}\%$	Berman Wang $\Delta\overline{C_L}\%$ $\Delta C_{L_{rms}}\%$
Crane fly	123	30	45.5	7.3 7.9	26.9 15.5	13.12 14.6
Lady bird	177	43	54	1.8 5.8	43.1 22.0	7.0 12.7
Hover fly	90	29	160	3.4 10.4	14.0 13.6	8.6 25.2
Fruit fly	150	46	254	0.3 12.8	49.2 36.2	16.9 31.6

Table 2.3: The operating conditions for the four insects under study along with the two comparison metrics $\Delta\overline{C_L}$ and $\Delta C_{L_{rms}}$ between each of the three studied models and the DNS results.

is noteworthy to mention that using the two-dimensional lift-curve slope 2π as in Eq. (2.8) leads to very large deviations of the classical unsteady approach. In terms of the stated comparison metrics, it leads to $\Delta\overline{C_L}\% = 85.5, 150.9, 86.0, 183.6$ and $\Delta C_{L_{rms}}\% = 43.4, 75.9, 46.6, 111.0$ for the four insects, respectively.

2.6 Reduced-Order Modeling

The above calculations were performed using 50 spanwise stations, which required a total of 100 aerodynamic states. However, flight dynamicists may wish to have a more reduced-order model in terms of the internal aerodynamic states that is more suitable for flight dynamics and control analyses without loss of the physics being captured.

Motivated by such a goal, a fourth order model that still captures the same physical aspects (LEV, unsteadiness, and rotational contributions) is proposed. This is achieved by exploiting the knowledge of the spanwise distributions of all the lift contributors in the integration of Eq. (2.20) over the wing. This dictates the separation of the translational term from the rotational one because the two terms have different spanwise distributions: $r^2c(r)$ for the translational term versus $rc^2(r)$ for the rotational term. As such, the

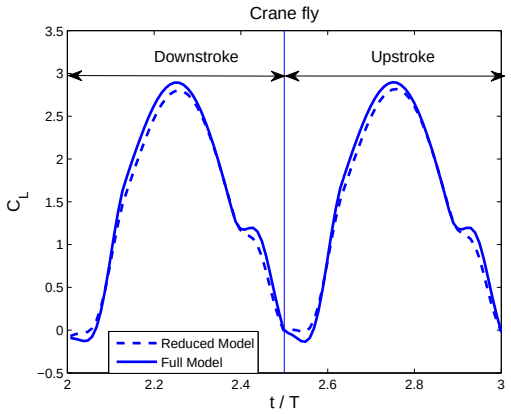

(a) Crane fly, $f = 45.5$ Hz and $\alpha_m = 30^\circ$

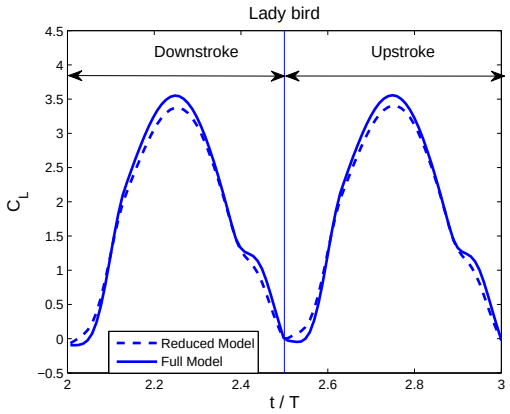

(b) Lady bird, $f = 54$ Hz and $\alpha_m = 43^\circ$

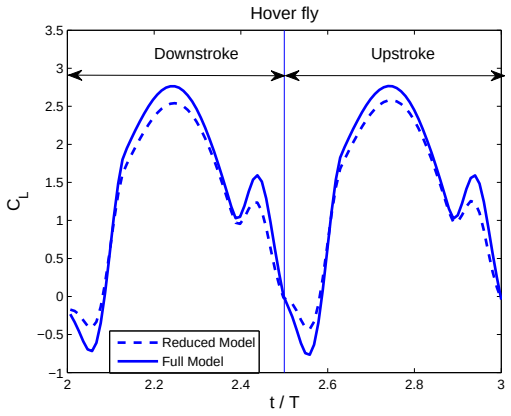

(c) Hover fly, $f = 160$ Hz and $\alpha_m = 29^\circ$

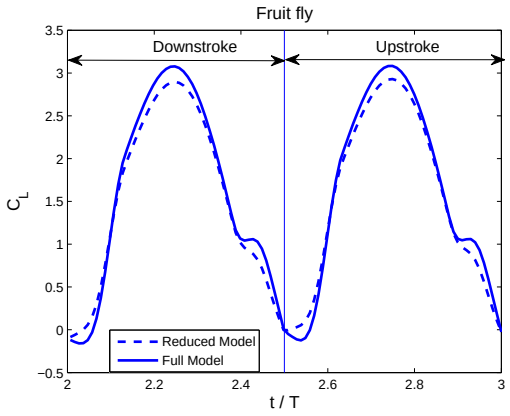

(d) Fruit fly, $f = 254$ Hz and $\alpha_m = 46^\circ$

Figure 2.6: Results for the C_L build up throughout the cycle using the reduced-order model versus the full model.

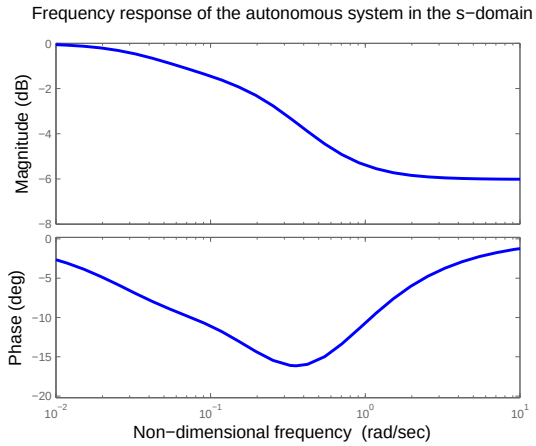

Figure 2.7: Frequency response of the autonomous system in the s-domain; an approximation to $C(k)$.

total lift on the wing is written as $L = L_{NC} + L_{trans} + L_{rot}$ where

$$\begin{aligned} L_{NC}(t) &= \tfrac{\pi}{4}\rho I_{12}\left[\ddot{\varphi}(t)\sin\eta(t) + \dot{\varphi}(t)\dot{\eta}(t)\cos\eta(t)\right]\cos\eta(t) \\ L_{trans}(t) &= \tfrac{1}{2}\rho I_{21}|\dot{\varphi}(t)|\left[(1-A_1-A_2)\,\dot{\varphi}(t)C_{L,s}(\eta(t)) + x_1(t) + x_2(t)\right] \\ L_{rot}(t) &= \rho I_{12}(\tfrac{3}{4} - \widehat{x}_0)\dot{\varphi}(t)\left[(1-A_1-A_2)\,\dot{\eta}(t) + x_3(t) + x_4(t)\right] \end{aligned} \tag{2.25}$$

where $I_{21} = 2\int_0^R r^2 c(r)\,dr$, and $I_{12} = 2\int_0^R rc^2(r)\,dr$ are the weighted moments of area for the two wing halves. The state equations for the four state variables are then given by

$$\begin{aligned} \dot{x}_i(t) &= \tfrac{2b_j\overline{r}|\dot{\varphi}(t)|}{\overline{c}}\left[-x_i(t) + A_j\dot{\varphi}(t)C_{L,s}(\eta(t))\right], \qquad j = i = 1,2 \\ \dot{x}_i(t) &= \tfrac{2b_j\overline{r}|\dot{\varphi}(t)|}{\overline{c}}\left[-x_i(t) + A_j\dot{\eta}(t)\right], \qquad\qquad j = i-2 = 1,2 \end{aligned} \tag{2.26}$$

where $\overline{r}$ and $\overline{c}$ are taken at a certain reference section. For the plots shown below, the section at $r = r_2 = \frac{I_{21}}{2SR}$ is used as a reference section.

Figure 2.6 shows a comparison between the lift coefficient obtained by using the reduced-order model (four states) and that using the full model (100 states). The plots show a very good agreement. Hence, the reduced-order model could capture the dominant contributions of the aerodynamic loads with a quite feasible computational burden. Moreover, it is represented in a compact form that is very well suited for flight dynamic stability and control analyses of FWMAVs. Finally, it is noted that a similar agreement is obtained when using the section having the mean chord length as a reference section.

It should be noted that the dynamic equation, Eq. (2.23) or Eq. (2.26), represents an autonomous system in the non-dimensional time domain (s-domain). Figure 2.7 shows the frequency response of this autonomous system, which is an approximation to Theodorsen function. It has a maximum phase shift of 15° at a frequency of 0.35 corresponding to the s-domain. According to the definition of s and the way it is applied to hovering here, the period in the s-domain is given by $\frac{4\Phi\bar{r}}{\bar{c}}$, which ranges between 14.8-28.4 for the four insects under study. As such, the frequency corresponding to the s-domain ranges between 0.22-0.42. Despite the vast variation in the operating frequency among the four insects, the variations in the frequencies corresponding to the s-domain are relatively narrow. Furthermore, all insects operate near the frequency of maximum phase shift (0.35). However, this maximum phase shift (15°) is not too high and may be neglected. In fact, this could be deduced from Fig. 2.5, where the peaks of the translatory components appear almost at the same time for the four models; i.e., the lag may be neglected. This fact is very important when considering the reduced-order-modeling for flight dynamics applications. Since the most common kinematics used in flight dynamics of FWMAVs use a constant angle of attack throughout each half stroke, e.g., (7; 9; 25; 34), the dependence of the aerodynamic loads on the α time derivatives comes only from the memory effects (lag). Noting that this lag may be neglected, the aerodynamic loads could be modeled as functions of the instantaneous angle of attack. However, this should not be thought of as a pure quasi-steady model, since there is a significant drop in the magnitude due to the unsteadiness. Figure 2.8 shows the deviation of the translatory peaks, when using the proposed model and the quasi-steady model of Andersen et al., from those of Sun and Du. As expected, the quasi-steady modeling over-estimates the aerodynamic loads. This difference is larger as the frequency increases. Noting that the frequency corresponding to the s-domain varies between 0.22-0.42 which correspond to a magnitude drop of 0.75-0.64. This fact along with the above one of neglecting the lag are important when developing a reduced-order model. These two facts justify modeling the aerodynamic loads associated with flapping flight using quasi-steady means with the amplitude of the fundamental harmonic reduced by a factor of 0.64-0.75. It is important to note, however, that this may not be true with kinematics having higher harmonics, such as the rotational kinematics considered here.

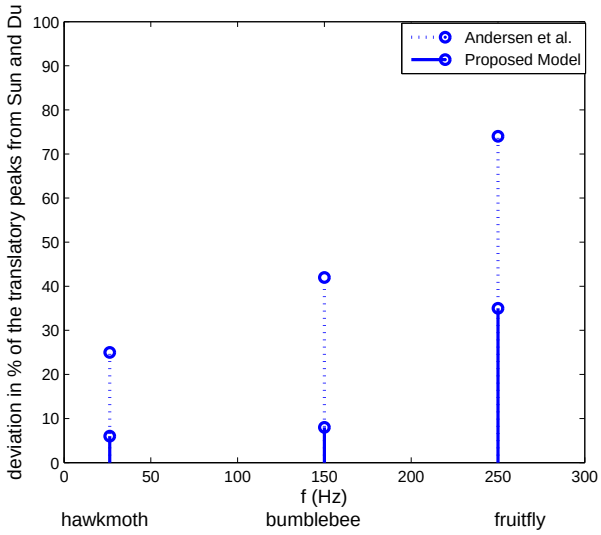

Figure 2.8: Over estimation of the translatory peaks of the quasi-steady model of Andersen et al. and the proposed model over those of Sun and Du.

2.7 Drag and Power Prediction

Since the flow under consideration is associated with the formation of a leading edge vortex, there would be no suction force. Consequently, similar to the aerodynamic drag on delta wings, the drag on flapping wings will mostly be the component of the pressure force in the direction parallel to the free stream or the instantaneous wing motion; i.e., $D = L \tan \alpha$, where the positive drag force opposes the downstroke velocity. As for the viscous drag, the experiments of (3; 79) suggest that it might be neglected in the range of Reynolds numbers of interest in hovering MAVs/insects (75-4000). Yet, a low fidelity estimate for the viscous drag; the flat plate drag with fully turbulent boundary layer, $C_{Df} = \frac{0.148}{\sqrt[5]{Re}}$ is used. As such, the viscous drag is estimated by $D_f = \frac{1}{2}\rho I_{21} C_{Df} |\dot{\varphi}| \dot{\varphi}$.

The power required to overcome the aerodynamic drag can be estimated as $P_{aero} = \frac{I_{31}}{I_{21}} D \dot{\varphi}$, where $I_{31} = 2\int_0^R r^3 c(r)\, dr$. This is the aerodynamic power required to maintain the flapping motion, φ. As for the aerodynamic power required to maintain the pitching motion, η, the work of (43) is followed, in which the power required to overcome the viscous rotational effects is written as

$$P_{rot} = \frac{\pi}{16} \rho I_{04} \left(\mu_1 f + \mu_2 |\dot{\eta}|\right) \dot{\eta}^2 \tag{2.27}$$

where $I_{04} = 2\int_0^R c^4(r)\, dr$, μ_1 and μ_2 depend on the viscosity of the fluid. Berman and Wang recommended a value of 0.2 for both of them. The power required to overcome the inertial loads is written as $P_{inertial} = 2I\dot{\varphi}\ddot{\varphi}$,

where I is the moment of inertia of one wing about the flapping axis. It is noted that there is a similar term for the η-motion. However, the corresponding moment of inertia is much smaller than that of the flapping (about 10^{-4} times) and, as such, the flapping term outweighs this latter term by far. On the other hand, there is another source for the aerodynamic rotational power that should be accounted for. This is due to the fact that the aerodynamic forces are not necessarily located at the hinge point. The rotational lift may lie at the hinge point, and the way the non-circulatory load is formulated here suggests locating it at the same point. However, in general, the circulatory lift is not located at the hinge point. Locating it at the quarter chord point yields an aerodynamic pitching moment at the hinge location. This moment is then used to calculate the average aerodynamic power which was found to be 1000 times less than the viscous rotational power, given by Eq. (2.27). Finally, for no out-of-plane kinematics, it is recommend to use the three power terms stated above; namely, $P_{aero} = \frac{I_{31}}{I_{21}} D\dot{\varphi}$, P_{rot} given by Eq. (2.27), and $P_{inertial} = 2I\dot{\varphi}\ddot{\varphi}$.

2.8 Conclusion

This chapter provides a state-space model for the unsteady lift due to flapping flight. The model is based on an extension to Duhamel's principle to non-conventional lift curves with the specific objective of capturing the contribution of the leading edge vortex (LEV). The unsteady lift due to arbitrary wing motion is generated using the static lift curve. The effects of the aspect ratio on the empirical formulae used to predict the static lift due to a stabilized LEV are also accounted for.

The derived model is validated through a comparison with direct numerical simulations of Navier-Stokes on hovering insects. The results show that the lift variation throughout the flapping cycle matches well those of the benchmark results for all insects. A comparison with quasi-steady models that capture the LEV contribution is performed to assess the role of unsteadiness. The results show that quasi-steady models, which capture the LEV contribution, result in higher aerodynamic loads. Deviations up to 16.9% in cycle-average lift coefficients and 31.6% in root-mean-squared errors of the lift coefficient were found using those quasi-steady models. On the other hand, a comparison with classical unsteady approaches is also presented to assess the LEV dominancy. It is found that the classical unsteady approaches overestimate the aerodynamic loads, particularly at high angles of attack. They perform well near stroke reversals where the rotational contribution is dominant. Deviations of the classical unsteady approach from the direct numerical simulations were up to 49.2% in cycle-average lift coefficients and 36.2% in root-mean-squared errors of the lift coefficient.

The derived model can be considered as a blend of the classical unsteady aerodynamic models and the quasi-steady models that capture the LEV contribution. Therefore, it performs better than the two

and requires almost the same computational cost. In terms of the comparison metrics, the deviation of the derived model from the DNS results ranges between 0.3%-7.3% in the cycle-average lift coefficients and between 5.8%-12.8% in root-mean-squared errors of the lift coefficient. Finally, a reduced-order model consisting of four internal aerodynamic states is derived from the full model (100 states) for flight dynamics and control analyses. The resulted lift coefficient using the reduced-order model is in a very good agreement with that of the full model.

Two conclusions can be drawn from the presented study that are useful for further reduced order modeling for flight dynamics and control purposes. Firstly, the lag associated with the unsteadiness of the flow of flapping flyers may be neglected. Secondly, for the considered vast range of operating conditions, the unsteady magnitude drop of the aerodynamic loads ranges between 0.64-0.75. These two conclusions are very vital for developing reduced-order models that are suitable for flight dynamic analysis. As such, if the wing motion has a dominant fundamental frequency, one can use the quasi-steady approaches that accounts for the dominant LEV contribution to determine the aerodynamic loads associated with flapping flight with a reduction in the amplitude of the oscillatory forces by a factor of 0.64-0.75.

Chapter 3

Kinematic Optimization

In this chapter, the wing kinematics optimization is considered for enhanced aerodynamic performance and maneuverability. In each case, an infinite-dimensional optimization problem is formulated using tools from the calculus of variations and optimal control. As such, the unnecessary constraints induced by approximating the problem to a finite-dimensional one are relaxed. Hence, theoretical upper bounds for the hovering aerodynamic performance and maneuverability are obtained. Sections 3.2, 3.3 present the formulation and solution of the aerodynamic and maneuverability optimization problems, respectively.

3.1 Introduction

The stringent weight and power constraints, imposed on the design of flapping-wing micro-air-vehicles (FWMAVs), necessitate the need for optimum design and performance. As such, many researchers have investigated optimum wing shapes, wing flapping kinematics, and flapping actuation mechanisms. This chapter is concerned with optimization of the flapping kinematics. For FWMAVs, three Euler angles are usually used to describe the flapping kinematics with respect to the body, namely, the back and forth flapping angle φ, the plunging angle ϑ, and the pitching angle η. Taha et al. (146) identified two common frameworks within which optimal time variations of these Euler angles are sought. In the first framework, the wing kinematics are optimized from the aerodynamic performance point of view. In the second framework, specific patterns along with associated parametrization for the kinematic functions are sought to achieve high control authority for the FWMAV, see Schenato et al. (7), Doman et al. (9; 10), and Oppenheimer et al. (8; 25).

3.2 Aerodynamic Optimization

Berman and Wang (43) considered optimization of the wing Euler angles with respect to the body for hovering insects, namely, the hawkmoth, bumblebee, and fruitfly. They proposed specific functional forms and kinematic parametrization (11 parameters) for the three Euler angles that sweep a very wide family of functions. They used the quasi-steady aerodynamic model developed by Pesavento and Wang(4) and Andersen et al. (5; 6). This model accounts for the translatory (leading edge vortex), rotational, viscous, and added mass effects. Berman and Wang used both gradient-based and global optimization techniques to minimize the average required power (aerodynamic + inertial) under lift constraint. Ghommem et al. (44) considered the same problem with different kinematic patterns and parametrization. They used the two-dimensional unsteady vortex-lattice method to determine the aerodynamic forces. Kurdi et al. (165) considered the same problem of wing kinematics optimization to minimize the required hovering power under a lift constraint. They used the quasi-steady aerodynamic model of Pesavento and Wang(4) and Andersen et al. (5; 6). However, they adopted a different approach for optimization of the shapes of the kinematic functions. They used 30 design variables for each Euler angle to specify the magnitudes of each angle at specific instants during the flapping cycle. Spline interpolation was then performed to obtain differentiable functions. Despite the large number of design variables, Kurdi et al. used gradient-based algorithms for their optimization problem. They also determined the effect of the levels of elastic storage and cost to dissipate negative power on the optimization problem. The elastic storage was modeled as a fraction of the inertial power, and the remaining inertial power was modeled as a dissipation cost.

Stanford and Beran (73) performed a gradient-based optimization of flapping-wing active-shape-morphing in forward flight. They performed a sensitivity analysis for the three-dimensional unsteady vortex-lattice method to obtain the gradient of their objective function with respect to the design variables. Their objective was to maximize the aerodynamic efficiency under lift and thrust constraints. They represented the wing morphing along with the flapping motions by a finite series of spatial and temporal functions. The spatial functions are the first twisting and bending modes of the wing. As for the design variables, they adopted two techniques. The first technique assumes harmonic functions for the time variation of the generalized coordinates and, as such, the design variables are the amplitudes and phase shifts of the generalized coordinates. The second technique is similar to that of Kurdi et al. (165), in which the time variations of the kinematic functions are approximated by cubic splines and the amplitudes of the generalized coordinates at specific control points represent the design variables. Ghommem et al. (74) adopted the same approaches using global and hybrid (global and gradient-based) optimization techniques.

In conclusion, all the of the previous efforts on the aerodynamic optimization of flapping wing kinematics

adopted finite-dimensional optimization, using one of two basic approaches. In the first approach, kinematic functions and their parametrization are specified. The parameters of the functions are used as design variables in the optimization process (43; 44). In the second approach, the magnitudes of the kinematic functions at specific control point throughout the flapping cycle are used as the design variables (165). In some efforts, both approaches were combined (73; 74). The second approach allows more freedom for the shape of the kinematic functions, but through using more design variables. Both approaches impose constraints on the optimization process. It is well known that less optimality is obtained when more constrains are imposed. On the other hand, the problem is essentially a calculus of variations problem, in which the shapes of the kinematic functions are chosen to minimize the required power *functional*. As such, the use of the calculus of variations to tackle such a problem is essential to obtain true optimality.

In general, the three Euler angles φ, ϑ, and η are used to describe the wing flapping kinematics with respect to the body. However, most insects have approximately a horizontal stroke plane in hover without an out-of-plane motion ($\vartheta = 0$) (20; 21). Furthermore, Doman, et al. (19; 9) emphasized the importance of minimal actuation in FWMAVs, as this aspect was the main reason for the successful flapping flight of the Harvard Robofly (30). Therefore, hovering kinematics without an out-of-plane motion are considered in this chapter. Figure 2.4 represents a schematic diagram for the Euler angles φ and η. As such, the total flapping velocity, seen by an airfoil section that is a distance r from the wing root, is $r\dot{\varphi}$ with an angle of attack $\alpha \equiv \eta$. The calculus of variations is used to obtain the optimum $\varphi(.)$ and $\eta(.)$, simultaneously, that minimize the hovering power.

3.2.1 Problem Formulation

Quasi-steady aerodynamics is used to determine the aerodynamic forces. In this formulation, the lift and drag coefficients are functions of the instantaneous angle of attack. It is important to note that this formulation do not restrict the functional form of the lift and drag coefficients to specific formulas. As such, the lift and drag coefficients can be written as $C_L = C_L(\alpha)$ and $C_D = C_D(\alpha)$, where $C_L(.)$ and $C_D(.)$ are arbitrary smooth functions.

For hovering FWMAVs, the flapping kinematics can be assumed to be symmetric; that is, identical downstroke and upstroke. As such, one needs to consider either one of the half strokes. For a horizontal stroke plane without an out-of-plane motion, the cycle-averaged lift and aerodynamic power, based on quasi-

steady aerodynamics, can be written as

$$\begin{aligned} \overline{L} &= \tfrac{\rho I_{21}}{T} \int_0^{T/2} \dot{\varphi}^2(t) C_L(\eta(t))\, dt \\ \overline{P} &= \tfrac{\rho I_{31}}{T} \int_0^{T/2} \dot{\varphi}^3(t) C_D(\eta(t))\, dt \end{aligned} \tag{3.1}$$

where $I_{21} = 2\int_0^R r^2 c(r)\, dr$ and $I_{31} = 2\int_0^R r^3 c(r)\, dr$ are the weighted moments of area for the two wing halves. The objective is to minimize the required average power during hover under a lift constraint whereby the average lift has to support the weight W. Although the required power consists of aerodynamic and inertial contributions, our concern here is the aerodynamic one only. This is because the inertial contribution can be recovered using any elastic means; e.g., a spring action in the flapping direction. It is noteworthy to mention that this spring action is needed anyway to produce the desired kinematics. In addition, Wood et al. (30) showed that driving the wing-actuator system at resonance would lead to recovery of the strain energy. As such, the functional to be minimized is the power functional given in Eq. (3.1). The lift constraint is expected to be active. As such, the cost and constraint functionals are written as

$$\begin{aligned} J(\varphi(.), \eta(.)) &= \int_0^{T/2} \dot{\varphi}^3(t) C_D(\eta(t))\, dt \\ G(\varphi(.), \eta(.)) &= \int_0^{T/2} \left[\dot{\varphi}^2(t) C_L(\eta(t)) - \tfrac{2W}{\rho I_{21}} \right] dt = 0 \end{aligned} \tag{3.2}$$

The calculus of variations problem is to find $(\varphi^*(.), \eta^*(.)) \in \Theta$, such that

$$J(\varphi^*(.), \eta^*(.)) \leq J(\varphi(.), \eta(.)), \forall (\varphi(.), \eta(.)) \in U_1(\varphi^*(.), \eta^*(.); \delta) \cap \Theta$$

and $G(\varphi^*(.), \eta^*(.)) = 0$, where

$$\Theta = \{(\varphi(.), \eta(.)) | \varphi(.) \in PWS(0, T/2), \eta(.) \in PWC(0, T/2) \text{ and } \varphi(0) = -\varphi(T/2), \eta(0) = \eta(T/2)\}$$

and $U_1(\varphi^*(.), \eta^*(.); \delta)$ is the δ-neighborhood of $(\varphi^*(.), \eta^*(.))$; that is, a weak local minimum is sought. The set of admissible functions Θ is chosen to be the largest set of functions that would make the the problem mathematically well-posed. That is, because $\varphi(.)$ has to be differentiable and its derivative has to be integrable, it must be at least piecewise-smooth (PWS). As for the pitching angle, $\eta(.)$, it has to be integrable only and, as such, piecewise-continuity (PWC) is enough. We note that allowing for these non-smooth functions may seem impractical, but is necessary to obtain the true optimality as it is the main objective of this work.

The Lagrangian functional for the constrained optimization problem is then constructed as

$$\Lambda(\varphi(.),\eta(.)) = \lambda_0 J(\varphi(.),\eta_(.)) + \lambda_1 G(\varphi(.),\eta(.))$$

where λ_0 and λ_1 are constants such that $|\lambda_0| + |\lambda_1| \neq 0$. However, one can show that $(\varphi^*(.),\eta^*(.))$ are not extremal of $G(.)$ unless $\dot{\varphi}^*(t) \equiv 0$ or $C'_L(\eta^*(t)) \equiv 0$, where $C'_L(\eta) = \frac{dC_L}{d\eta}$. These two conditions correspond to minimum or maximum lift, respectively. It is expected that neither of these conditions would be a solution to the optimization problem at hand. As such, $(\varphi^*(.),\eta^*(.))$ are not extremal of $G(.)$, and $\lambda_0 \neq 0$. Therefore, we construct the Lagrangian functional as

$$\Lambda(.) = J(.) + \lambda G(.) = \int_0^{T/2} \ell(t,\dot{\varphi}(t),\eta(t))\,dt \tag{3.3}$$

where $\lambda = \frac{\lambda_1}{\lambda_0}$. It can be proved that if $(\varphi^*(.),\eta^*(.))$ provides a weak local minimum for $J(.)$ on Θ subject to the constraint $G(\varphi^*(.),\eta^*(.)) = 0$, then

- The Euler integral equations for the Lagrangian functional can written as

$$\frac{\partial \ell}{\partial \dot{\varphi}}(t,\dot{\varphi^*}(t),\eta^*(t)) = c_1,\ \forall t \in [0,T/2] \tag{3.4}$$

$$\int_0^t \frac{\partial \ell}{\partial \eta}(\tau,\dot{\varphi^*}(\tau),\eta^*(\tau))\,d\tau = c_2,\ \forall t \in [0,T/2] \tag{3.5}$$

  where c_1 and c_2 are constants and ℓ is the integrand of the Lagrangian functional defined in Eq. (3.32).

- The essential boundary conditions are given by $\varphi^*(0) = -\varphi^*(T/2)$, and $\eta^*(0) = \eta^*(T/2)$
- The natural boundary condition is written as
  $\frac{\partial \ell}{\partial \dot{\varphi}}(0,\dot{\varphi^*}(0),\eta^*(0)) = -\frac{\partial \ell}{\partial \dot{\varphi}}(T/2,\dot{\varphi^*}(T/2),\eta^*(T/2))$

Substituting for ℓ into Eqs. (3.4, 3.5) and differentiating Eq. (3.5) with respect to t yields

$$\begin{aligned} 3\dot{\varphi}^{*2}(t)C_D(\eta^*(t)) + 2\lambda\dot{\varphi}^*(t)C_L(\eta^*(t)) &= c_1,\ \forall t \in [0,T/2] \\ \dot{\varphi}^{*3}(t)C'_D(\eta^*(t)) + \lambda\dot{\varphi}^{*2}(t)C'_L(\eta^*(t)) \quad &= 0,\ \ \forall t \in [0,T/2] \end{aligned} \tag{3.6}$$

Applying the first natural boundary condition yields a zero value for c_1. Assuming $\lambda, C'_D(\eta^*(t))$, and $C_D(\eta^*(t))$ are not zeros, and since $\dot{\varphi}^*(t) \neq 0$, we obtain from Eq. (3.6) that

$$\frac{3C'_L(\eta^*(t))}{C_L(\eta^*(t))} = \frac{2C'_D(\eta^*(t))}{C_D(\eta^*(t))},\ \forall t \in [0,T/2] \tag{3.7}$$

Integrating Eq. (3.7) yields

$$\frac{C_D^2(\eta^*)}{C_L^3(\eta^*)} = \Gamma \tag{3.8}$$

where Γ is a constant. Equation (3.8) is an algebraic equation in $\eta^*(t)$, which has any time dependance. As such, the optimal pitching angle has a constant value throughout the half-stroke, referred to as η_m. It should be noted that this piecewise continuous variation of the pitching angle is convenient for the concept of minimal actuation, because it can be passively controlled. Therefore, it has been used in the work of Schenato et al. (7), Doman et al. (19; 9; 10; 34), and Oppenheimer et al. (8; 33; 25). In fact, Eq. (3.7) is equivalent to the condition of minimum $\frac{C_D^2}{C_L^3}$, associated with minimum aerodynamic power for conventional aircraft, see Ref. (166). Thus, $\eta(t)$ has to be kept fixed at the angle of minimum $\frac{C_D^2}{C_L^3}$ of the FWMAV drag polar. As for $\dot{\varphi}^*(t)$, Eq. (3.6) yields

$$\dot{\varphi}^*(t) = -\frac{2\lambda C_L(\eta_m)}{3C_D(\eta_m)},\ t \in [0, T/2] \tag{3.9}$$

The value of either λ or $\dot{\varphi}^*(t)$ could be determined from the application of the active constraint, $G(\varphi^*(.), \eta^*(.)) = 0$. This gives

$$\lambda = \pm\frac{3C_D(\eta_m)}{2C_L(\eta_m)}\sqrt{\frac{2W}{\rho I_{21} C_L(\eta_m)}} = \pm\frac{3}{2}\sqrt{\frac{2W\Gamma}{\rho I_{21}}}$$

with the $\pm$ indicating upstroke and downstroke motions, respectively. As such, the optimum flapping angle in the downstroke is given by the following triangular wave:

$$\varphi^*(t) = \sqrt{\frac{2W}{\rho I_{21} C_L(\eta_m)}}(t - T/4),\ t \in [0, T/2] \tag{3.10}$$

which is presented in Fig. 3.1. A sufficient condition for the optimality of $\varphi(.)$ is that

$$\frac{\partial^2 \ell}{\partial \dot{\varphi}^2}(t, \varphi^*(t), \dot{\varphi}^*(t), \eta^*(t), \dot{\eta}^*(t)) \geq \mu$$

for some $\mu > 0$. This second partial derivative is given by

$$\frac{\partial^2 \ell}{\partial \dot{\varphi}^2}(t, \varphi^*(t), \dot{\varphi}^*(t), \eta^*(t), \dot{\eta}^*(t)) = 3\sqrt{\frac{2WC_D^2(\eta_m)}{\rho I_{21} C_L(\eta_m)}} \tag{3.11}$$

which is strictly positive, $\forall t \in [0, T/2]$.

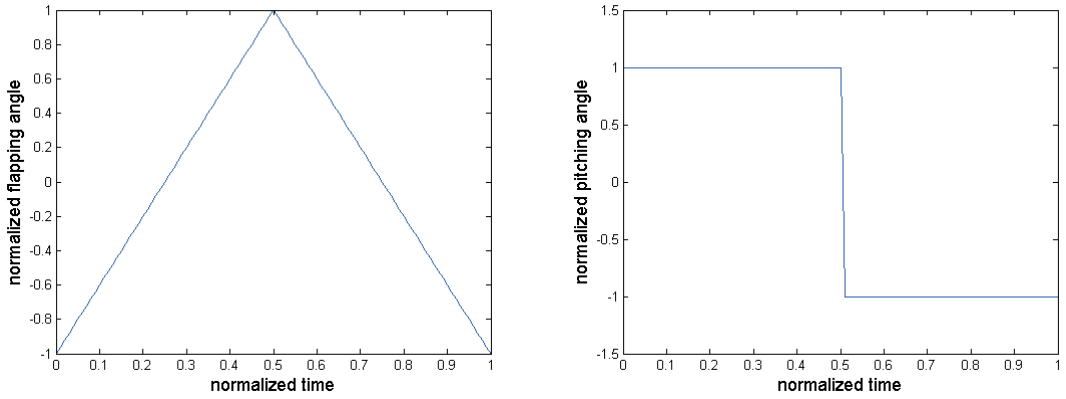

(a) $\varphi^*(t)$ (b) $\eta^*(t)$

Figure 3.1: Optimum shapes for the flapping and pitching angles.

3.2.2 Results and Discussion

Substituting the aero-optimal triangular waveform kinematic function, as obtained above, into the aerodynamic power functional $\overline{P}$ in Eq. (3.1), yields

$$\overline{P^*} = \frac{I_{31}}{I_{21}^{3/2}} \sqrt{\frac{2W^3}{\rho}} \frac{C_D(\eta_m)}{C_L^{3/2}(\eta_m)} = \frac{I_{31}}{I_{21}^{3/2}} \sqrt{\frac{2\Gamma W^3}{\rho}} \tag{3.12}$$

It is interesting to note that, similar to conventional aircraft, the minimum aerodynamic power for FWMAVs occurs when $\frac{C_D(\eta_m)}{C_L^{3/2}(\eta_m)} = \sqrt{\Gamma}$ is minimum. This is because the flapping speed and pitching angle are constant throughout the flapping cycle, which is similar to the case of a wing on a cruising aircraft. However, the drag polar of a flapping wing is quite different from that of a conventional aircraft wing. Next, the implications of this difference in the drag polar on the optimal performance of the flapping wing is assessed.

Pesavento and Wang (4) and Andersen et al. (5; 6) showed that the lift coefficient of the translatory (leading edge vortex) effect can be written as $C_L(\alpha) = A \sin 2\alpha$, where A is a constant that depends on the Reynolds number and wing geometry. Taha et al. (167; 168) showed that, in the limit of small angles of attack, $2A$ may be considered as the lift curve slope of the three-dimensional wing C_{L_α}; that is, $C_L(\alpha) = \frac{1}{2} C_{L_\alpha} \sin 2\alpha$. They also showed that the use of the extended lifting line theory to determine the dependance

of C_{L_α} on the wing aspect ratio AR is satisfactory. As such, the translatory lift coefficient can be written as

$$C_L = \frac{\pi AR}{2(\sqrt{\frac{1}{4}AR^2 + 1} + 1)} \sin 2\alpha \tag{3.13}$$

The flow considered here is associated with the formation of a leading edge vortex. As such, there is no suction force. Consequently, similar to delta wings, the drag is mostly the component of the pressure force, normal to the wing surface, in the direction parallel to the free stream or the instantaneous wing motion; that is, $C_D = C_L \tan\alpha$. Hence, the drag coefficient in such a flow can be written as

$$C_D = C_{D0} + \frac{\pi AR}{\sqrt{\frac{1}{4}AR^2 + 1} + 1} \sin^2\alpha \tag{3.14}$$

where C_{D0} is the viscous drag coefficient. Using Eq. (3.13) and (3.14) for C_L and C_D, respectively, yields

$$\frac{C_D^2}{C_L^3} = \frac{8(C_{D0} + C_{L_\alpha} \sin^2\alpha)^2}{C_{L_\alpha}^3 \sin^3(2\alpha)} \tag{3.15}$$

Equation (3.15) is written in terms of C_{L_α} for simplicity. The hawkmoth wing is considered whose aspect ratio is 2.84, see Ellington (57), and $C_{D0} = 0.07$, see Berman and Wang (43). Figure 3.2 shows variation of the resulted $\frac{C_D^2}{C_L^3}$ as a function of α for the hawkmoth wing. It is clear that the angle of attack corresponding to the minimum $\frac{C_D^2}{C_L^3}$ is relatively small with a value of 13.5°. This refutes the misconception that the optimum pitching angle is 45°. In fact, $\eta^* = 45°$ results in the maximum lift, but is not optimal for hovering. It consumes more than double of the aerodynamic power consumed when hovering by the angle of attack corresponding to the minimum $\frac{C_D^2}{C_L^3}$.

It is noteworthy to mention that the angle corresponding to the minimum $\frac{C_D^2}{C_L^3}$ decreases as C_{D0} decreases. Furthermore, the viscous effects in the range of Reynolds numbers (75-4000) of interest in hovering FWMAVs / insects can be neglected, see the experiments of Dickinson et al. (3; 79). Consequently, the smaller α is, the better obtained performance is. However, a smaller α yields a smaller C_L, which, in order to satisfy the lift constraint, requires a higher flapping velocity and/or a larger flapping amplitude. According to Eq. (3.10), the flapping amplitude Φ is given by

$$\Phi = T\sqrt{\frac{W}{8\rho I_{21} C_L(\eta_m)}} \tag{3.16}$$

So, for negligible C_{D0}, the optimization process for the aerodynamic power using quasi-steady aerodynamics results in the maximum flapping amplitude and frequency, in order to fly with the least possible angle of

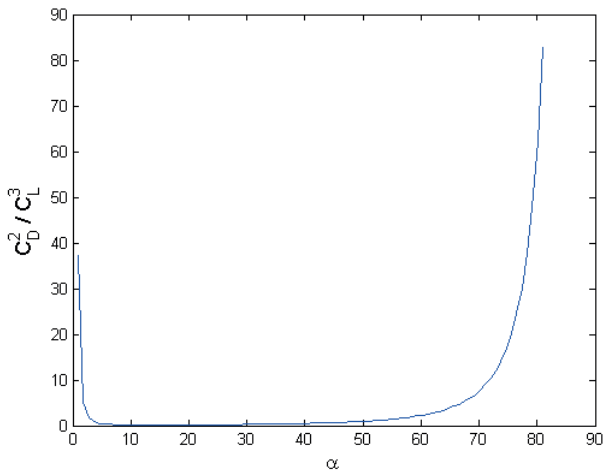

Figure 3.2: The performance index $\frac{C_D^2}{C_L^3}$ versus the angle of attack for the hawkmoth

attack, which is then given by

$$\eta_m^* = \frac{1}{2}\sin^{-1}\left(\frac{T_{min}^2 W}{4\rho C_{L_\alpha} I_{21} \Phi_{max}^2}\right) \tag{3.17}$$

We note that a limit on the flapping amplitude Φ usually exists in practical designs. However, such a limit is not imposed here because it will not affect the shape of the kinematic function at all, which is our main concern. This will rather add an additional constraint requiring the right-hand-side of Eq. (3.16) to be less than the Φ-limit. That is, it will put some limitation on the flapping frequency, wing area, and the pitch angle based on the FWMAV weight.

It is noteworthy to mention that the triangular waveform, as obtained in the preceding section, was used by Schenato et al. (7) for control purposes. They parameterized this kinematic function by three parameters. An amplitude modulation is used to control the vertical force, a relative timing between the upstroke and downstroke motions is used to control the forward force, and an offset is used to control the pitching moment. Manipulating the kinematic parameters asymmetrically yields rolling and yawing moments. The use of such a kinematic function with the described parametrization yields a rank five control effectiveness matrix; that is, authority to independently control five degrees of freedom, all but the lateral translation in the body frame.

Doman et al. (9; 10) and Oppenheimer et al. (8; 25) adopted a different kinematic function for the flapping angle $\varphi(.)$. It was a harmonic based function that has a similar parametrization. Without the offset, there is a lack in the pitch control authority, which they compensated for by adding a bob-weight that shifts the vehicle center of gravity (8; 9). In their latter work (10; 25), they added an offset to their

kinematic function, which achieved a full rank (six) control effectiveness matrix. However, the harmonic based kinematic function is not aero-optimal like the triangular one. Substituting this harmonic kinematic function $\varphi(t) = -\Phi\cos(\frac{2\pi t}{T})$ into the power functional yields

$$\overline{P} = \frac{16\pi^2 \rho I_{31} C_D(\eta_m)}{3T^3}\Phi^3 \tag{3.18}$$

Satisfying the lift constraint yields $\Phi = \frac{T}{\pi}\sqrt{\frac{W}{\rho I_{21} C_L(\eta_m)}}$, which in turn gives the following cycle-averaged power

$$\overline{P} = \frac{16 I_{31}}{3\pi I_{21}^{3/2}}\sqrt{\frac{W^3}{\rho}}\frac{C_D(\eta_m)}{C_L^{3/2}(\eta_m)} = \frac{16 I_{31}}{3\pi I_{21}^{3/2}}\sqrt{\frac{\Gamma W^3}{\rho}} \tag{3.19}$$

Equations (3.12) and (3.19) can be used to assess the difference in the power levels required to hover using the triangular and harmonic kinematic functions. The ratio of the two equations shows that the harmonic function requires 20% more aerodynamic power than the triangular waveform. In fact, this is the main motivation of this effort, which is to provide a performance basis against which the performance using any other proposed kinematic function can be evaluated.

More recently, Sigthorsson, Oppenheimer, and Doman (34) switched to the triangular kinematic function. They stated some interesting advantages when using this waveform in comparison to the previous harmonic one. First, it is much easier to derive analytic expressions for the cycle-averaged forces and moments using the triangular waveform than using the harmonic one where integrands of the form $\cos(\cos\omega t)$ and $\sin(\cos\omega t)$ are encountered. Second, Sane and Dickinson (169) indicated that the triangular waveform may be closer to the observed flapping in nature. Finally, from the actuation mechanism point of view, the use of a triangular waveform allows the wing to attain its maximum velocity almost instantaneously. As such, the actuation mechanism attains the passively controlled angle of attack more rapidly than when using the harmonic function. Hence, the assumption of constant angle of attack throughout the half stroke is more realistic. One impractical aspect of the triangular waveform is its slope discontinuity at the ends of each half stroke, which makes its exact implementation unrealistic.

3.3 Maneuverability Optimization

In this section, we consider a FWMAV equipped with one actuator performing a horizontal stroke plane. The pitching motion is passively controlled with the back and forth flapping angle φ in such a way to maintain a constant angle of attack throughout the entire stroke. This kinematics is very suitable for hovering and has been ubiquitously used in the literature of hovering FWMAVs (7; 19; 8; 9; 33; 10; 25; 34; 42; 170; 171). In the

previous section, the calculus of variations is used to derive the optimum shape of the back and forth flapping angle φ and the pitching angle η for minimum hovering power. The use of the calculus of variations allows us to obtain true optimal kinematics and, as such, a reference performance against which the performance of any other proposed kinematics could be compared to assess how close it is to the reference one. Using quasi-steady aerodynamics and neglecting the aerodynamic effect of wing rotation, it has been shown that the triangular waveform for the back and forth flapping angle φ along with constant angle of attack yields the optimum hovering performance, see Fig. 3.1.

In this section, we are concerned with the FWMAV maneuverability near hover. The objective is to use the calculus of variations and optimal control techniques to derive an optimum shape for the back and forth flapping angle φ that produces the maximum cycle-average forward thrust force under the constraint that the cycle-average lift is equal to the weight. The derived kinematics will be very suitable for fastest transition from hovering to forward flight or for minimum-time transition from one hovering point to another. The use of the calculus of variations and optimal control techniques also yields a reference performance; the maximum forward acceleration that a FWMAV can ever achieve from the hovering position using a horizontal actuator only. That is the FWMAV designer can determine the maximum theoretical ability of his designed vehicle and also have a reference maneuverability index against which he can compare the maximum achievable maneuverability to assess how far his design from the reference one.

3.3.1 Problem Formulation

For a horizontal stroke plane without an out-of-plane motion, the total flapping velocity, seen by an airfoil section that is a distance r from the wing root, is $r\dot{\varphi}$. The cycle-average lift and forward thrust forces, based on quasi-steady aerodynamics, are then given by

$$\begin{aligned} \overline{L} &= \tfrac{1}{2}\tfrac{\rho I_{21} C_{L_m}}{T}\int_0^T \dot{\varphi}^2(t)\,dt &&= K_L \int_0^T \dot{\varphi}^2(t)\,dt \\ \overline{X} &= -\tfrac{1}{2}\tfrac{\rho I_{21} C_{D_m}}{T}\int_0^T \dot{\varphi}(t)|\dot{\varphi}(t)|\cos\varphi(t)\,dt &&= -K_D \int_0^T \dot{\varphi}(t)|\dot{\varphi}(t)|\cos\varphi(t)\,dt \end{aligned} \tag{3.20}$$

where $I_{21} = 2\int_0^R r^2 c(r)\,dr$, $C_{L_m} = C_L(\alpha_m)$, and $C_{D_m} = C_D(\alpha_m)$; α_m being the fixed angle of attack used throughout the entire stroke.

The objective is to find $\varphi(.)$ that maximizes the forward thrust functional $\overline{X}(\varphi(.))$ satisfying the lift constraint $\overline{L}(\varphi(.)) = W$. As such, this kinematics would result in the highest possible forward acceleration with zero vertical acceleration on the averaged dynamics of the FWMAV, leading to fastest possible transition from hovering to forward flight or from one hovering point to another.

This problem could be tackled as a calculus of variations problem. However, because the generation of forward thrust forces by horizontal stroke plane is mainly performed by asymmetry between the downstroke and upstroke, there may not exist a weak local minimum. The wing may go arbitrary slowly and return arbitrary fast to produce arbitrary large asymmetry as shown in Fig. 3.3. This invokes the need to impose a

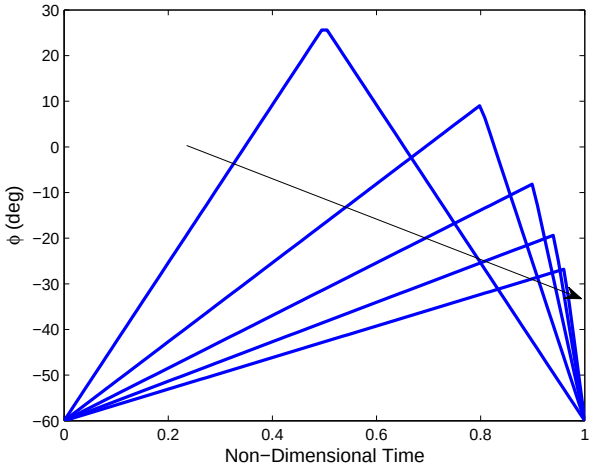

Figure 3.3: Different kinematics, each with higher returning speed while the total lift is preserved, indicating no maximum.

constraint on the returning speed or, in general, on the speed of the wing. This is a physical constraint that is imposed by the used actuator; that is, $|\dot{\varphi}(t)| \leq \dot{\varphi}_{max}$. Unfortunately, adding this hard constraint on the function derivative complicates the problem. It changes the problem from a classical calculus of variations problem into an optimal control problem. As such, the Euler-Lagrange equations can no longer be used to provide the necessary conditions for optimization. We rather apply Pontryagin maximum principle.

Optimal Control Approach

Letting $x_1(t) = \varphi(t)$ and $x_2(t) = \int_0^t \dot{\varphi}^2(\tau)\, d\tau$, we consider the following initial/boundary value problem:

$$\begin{aligned} \dot{x}_1(t) &= u \quad x_1(0) = x_1(T) \\ \dot{x}_2(t) &= u^2 \qquad x_2(0) = 0 \end{aligned} \tag{3.21}$$

and the functional

$$J(u(.)) = \int_0^T u(t)|u(t)| \cos x_1(t)\, dt = \int_0^T f_0(\boldsymbol{x}(t), u(t))\, dt$$

Then, the optimal control problem is to find a piecewise continuous control $u(.) : [0, T] \rightarrow [-\dot{\varphi}_{max}, \dot{\varphi}_{max}] \subset \Re$ that steers the system (3.21) from $(x_1(0), x_2(0)) = (\varphi_0, 0)$ to $(x_1(T), x_2(T)) = (\varphi_0, \frac{W}{K_L})$ and minimizes the functional $J(u(.))$.

The ingredients needed to apply Pontryagin's Maximum Principle (MP) are illustrated next. For a vector $\boldsymbol{\chi} \in \Re^2$, its augmented correspondence $\hat{\boldsymbol{\chi}} \in \Re^3$ is defined by $\hat{\boldsymbol{\chi}} = [\chi_0, \boldsymbol{\chi}^T]^T$. Thus, the augmented state vector $\hat{\boldsymbol{f}}$, corresponding to the state vector $\boldsymbol{f}$ representing the system dynamics, is given by

$$\hat{\boldsymbol{f}}(x_0, \boldsymbol{x}, u) = \begin{pmatrix} f_0(x_0, \boldsymbol{x}, u) \\ \boldsymbol{f}(x_0, \boldsymbol{x}, u) \end{pmatrix} = \begin{pmatrix} u|u| \cos x_1 \\ u \\ u^2 \end{pmatrix} \tag{3.22}$$

where $f_0(x_0, \boldsymbol{x}, u)$ represents the integrand of the cost functional. The Jacobian matrix, A, of the augmented state vector $\hat{\boldsymbol{f}}$ evaluated at the optimal performance is then given by

$$A(t) = \begin{bmatrix} 0 & -u^*(t)|u^*(t)| \sin x_1^*(t) & 0 \\ 0 & 0 & 0 \\ 0 & 0 & 0 \end{bmatrix} \tag{3.23}$$

where $u^*(t)$ and $\boldsymbol{x}^*(t)$ represent the optimal control and response, respectively.

According to the MP, if $u^*(.) : [0, T] \rightarrow [-\dot{\varphi}_{max}, \dot{\varphi}_{max}] \subset \Re$ minimizes $J(u(.))$, then there exists a nontrivial solution to the adjoint equation

$$\dot{\hat{\eta}} = -[A(t)]^T \hat{\boldsymbol{\eta}}$$

That is,

$$\begin{pmatrix} \dot{\eta}_0(t) \\ \dot{\eta}_1(t) \\ \dot{\eta}_2(t) \end{pmatrix} = \begin{pmatrix} 0 \\ \eta_0(t) u^*(t)|u^*(t)| \sin x_1^*(t) \\ 0 \end{pmatrix} \tag{3.24}$$

The first and last equations yield constant η_0 and η_2, respectively; that is,

$$\eta_0(t) \equiv \eta_0 \leq 0 \text{ and } \eta_2(t) \equiv \eta_2$$

It should be noted that the MP dictates a non-positive η_0 for this formulation. Also, the optimal control

$u^*(t)$ maximizes the Hamiltonian

$$\mathcal{H}(\hat{\boldsymbol{x}}, \hat{\boldsymbol{\eta}}, u) = \eta_0 f_0(x_0, \boldsymbol{x}, u) + < \boldsymbol{\eta}, \boldsymbol{f}(x_0, \boldsymbol{x}, u) >$$

on the set of admissible controls $[-\dot{\varphi}_{max}, \dot{\varphi}_{max}]$. Thus, either $u^*(t) = \pm\dot{\varphi}_{max}$ or $\frac{\partial \mathcal{H}}{\partial u} = 0$, which gives

$$u^*(t) = \begin{cases} \frac{-1}{2} \frac{\eta_1(t)}{\eta_2 + \eta_0 \cos x_1^*(t)}, \, u^*(t) > 0 \\ \frac{-1}{2} \frac{\eta_1(t)}{\eta_2 - \eta_0 \cos x_1^*(t)}, \, u^*(t) < 0 \end{cases} \tag{3.25}$$

Next, we check wether η_0 can be zero or not. If $\eta_0 = 0$, then $\eta_1(t) \equiv \eta_1$ and $\mathcal{H} = \eta_1 u + \eta_2 u^2$. Noting that the MP indicates that $u^*(t) = \max_{u \in [-\dot{\varphi}_{max}, \dot{\varphi}_{max}]} \mathcal{H}(\hat{\boldsymbol{x}}, \hat{\boldsymbol{\eta}}, u)$ and the optimal Hamiltonian has to be constant throughout the entire time period $[0, T]$, we conclude that either

$$u^*(t) = \dot{\varphi}_{max} \forall t \in [0, T] \;\; , \;\; u^*(t) = -\dot{\varphi}_{max} \forall t \in [0, T] \;\; , \text{or} \;\; \eta_1 = 0 \; , \; \eta_2 > 0 \text{ and } u^*(t) = \pm\dot{\varphi}_{max}$$

The first two options do not satisfy the periodicity boundary condition. Considering the latter possibility and calculating the lift from Eq. (3.20), we obtain $\overline{L} = K_L \dot{\varphi}_{max}^2 T$. Because K_L, $\dot{\varphi}_{max}$, and T are all specified, the obtained value for the lift may or may not match the desired value (weight). That is, we cannot satisfy the lift constraint for a FWMAV of arbitrary weight. In fact, this condition is the one corresponding to maximum lift. As such, $\eta_0 < 0$.

Having proved that $\eta_0 \neq 0$, we define $\lambda_1 = \frac{\eta_1}{-\eta_0}, \lambda_2 = \frac{\eta_2}{-\eta_0}$, and $\mathcal{H}' = \frac{\mathcal{H}}{-\eta_0}$. Thus, the equations describe the evolution of the optimal response are given by

$$\begin{aligned} \dot{x}_1^*(t) &= u^*(t) \\ \dot{x}_2^*(t) &= u^{*2}(t) \\ \dot{\lambda}_1(t) &= -u^*(t)|u^*(t)| \sin x_1^*(t) \end{aligned} \tag{3.26}$$

where the optimal control, u^*, is either $\pm\dot{\varphi}_{max}$ or

$$u^*(t) = \begin{cases} \frac{1}{2} \frac{\lambda_1(t)}{\cos x_1^*(t) - \lambda_2}, \, u^*(t) > 0 \\ \frac{1}{2} \frac{-\lambda_1(t)}{\cos x_1^*(t) + \lambda_2}, \, u^*(t) < 0 \end{cases} \tag{3.27}$$

subject to the initial and boundary conditions

$$x_1(0) = x_1(T) \ , \ x_2(0) = 0 \ , \ x_2(T) = \frac{W}{K_L}$$

The optimal Hamiltonian

$$\mathcal{H}'^*(t) = \begin{cases} (\lambda_2 - \cos x_1^*(t))u^{*2}(t) + \lambda_1(t)u^*(t),\ u^*(t) > 0 \\ (\lambda_2 + \cos x_1^*(t))u^{*2}(t) + \lambda_1(t)u^*(t),\ u^*(t) < 0 \end{cases} \tag{3.28}$$

is constant throughout the entire time period $[0, T]$.

Application of the MP yielded two possibilities for the optimal control. These are $u^* = \pm\dot{\varphi}_{max}$ and the solution given in Eq. (3.27). Because the forward thrust force $\overline{X}$ is maximized by the asymmetry between the downstroke and upstroke, the largest $\overline{X}$ is obtained by moving the wing forward (downstroke) as slowly as possible or optimally by the positive solution given in Eq. (3.27) and moving the wing back (upstroke) with the maximum allowable wing speed ($-\dot{\varphi}_{max}$). As such, the optimal control would be given by

$$u^*(t) = \begin{cases} \frac{1}{2}\frac{\lambda_1(t)}{\cos x_1^*(t) - \lambda_2},\ 0 \le t \le T_1 \\ -\dot{\varphi}_{max}, \quad T_1 \le t \le T \end{cases} \tag{3.29}$$

where T_1 is the switching time, which is unknown.

Point-to-Curve Calculus of Variations Approach

Having realized that the optimal return is performed at the maximum angular wing speed ($-\dot{\varphi}_{max}$), the problem at hand may be formulated as a point-to-curve calculus of variations problem. That is; what is the optimum $\varphi(.)$ that connects the point $(0,\varphi_0)$ to the curve $\varphi_0 + \dot{\varphi}_{max}(T - t)$ which represents returning by $-\dot{\varphi}_{max}$, and minimizes the cost functional while satisfying the lift constraint. Figure 3.4 illustrates the point-to-curve nature of the problem.

We opt to pursue with this formulation because of its physical indication and the simplicity of its sufficient condition check. Note that the φ_0 may be free, but we will solve the problem for fixed φ_0 and then optimize with respect to it. The cost functional that needs to be minimized is then the $\overline{X}$ integral over the downstroke only, which is written as

$$J(\varphi(.)) = \int_0^{T_1^*} \dot{\varphi}^2(t)\cos\varphi(t)\,dt \tag{3.30}$$

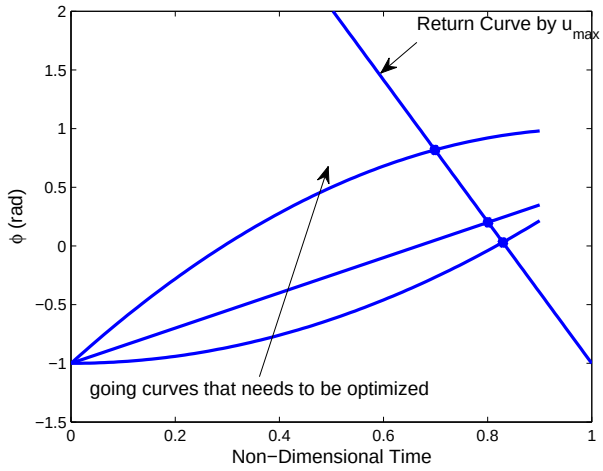

Figure 3.4: Different possible going functions intersect the returning curve. The problem is to find the one that minimizes the cost functional and satisfies the lift constraint.

The lift constraint

$$\int_0^T \dot{\varphi}^2(t)\,dt = \int_0^{T_1^*} \dot{\varphi}^2(t)\,dt + \dot{\varphi}_{max}^2(T - T_1^*) = \frac{W}{K_L} = \varpi$$

is written as

$$G(\varphi(.)) = \int_0^{T_1^*} \left[\dot{\varphi}^2(t) + \dot{\varphi}_{max}^2\left(\frac{T}{T_1^*} - 1\right) - \frac{\varpi}{T_1^*}\right] dt = 0 \tag{3.31}$$

where T_1^* is the unknown optimum intersection time. By considering the following curve $\varphi_u(.) : [0, \infty) \to \Re$ defined by

$$\varphi_u(t) = \varphi_0 + \dot{\varphi}_{max}(T - t)$$

and the set of admissible functions

$$\Theta = \{\varphi(.) \in PWS(0, \infty) | \varphi(0) = \varphi_0, \varphi(T_1) = \varphi_u(T_1) \ \ , \ \ \text{for some} T_1 > 0\}$$

the point-to-curve calculus of variations problem is then to find $\varphi^*(.) \in \Theta$, such that

$$J(\varphi^*(.)) \leq J(\varphi(.)), \forall \varphi(.) \in U_1(\varphi^*(.); \delta) \cap \Theta$$

and $G(\varphi^*(.)) = 0$, where $U_1(\varphi^*(.); \delta)$ is the δ-neighborhood of $\varphi^*(.)$; that is, we seek a weak local minimum. The set of admissible functions Θ is chosen to be the largest set of functions that would make the the problem mathematically well-posed. That is, because $\varphi(.)$ has to be differentiable and its derivative has to be integrable, it must be at least piecewise-smooth (PWS). We note that allowing for these non-smooth

functions may seem impractical, but it is necessary to obtain the true optimality as it is a main objective in this work.

Because $\eta_0 \neq 0$ in the optimal control formulation, we write the Lagrangian functional for the constrained optimization problem as

$$\begin{aligned}\Lambda(.) &= J(.) + \lambda G(.) = \int_0^{T_1^*} \ell(t, \varphi(t), \dot{\varphi}(t))\, dt \\ &= \int_0^{T_1^*} \left[\dot{\varphi}^2(t)\cos\varphi(t) + \lambda\left(\dot{\varphi}^2(t) + \dot{\varphi}_{max}^2\left(\frac{T}{T_1^*} - 1\right) - \frac{\varpi}{T_1^*}\right)\right] dt\end{aligned} \tag{3.32}$$

It can be proved that if $\varphi^*(.)$ provides a weak local minimum for $J(.)$ on Θ subject to the constraint $G(\varphi^*(.)) = 0$, then (172)

- The Euler differential equation for the Lagrangian functional can be written as

$$\frac{d}{dt}\left(\frac{\partial \ell}{\partial \dot{\varphi}}(t, \varphi^*(t), \dot{\varphi^*}(t))\right) = \frac{\partial \ell}{\partial \varphi}(t, \varphi^*(t), \dot{\varphi^*}(t)),\ \forall t \in (0, T_1^*) \tag{3.33}$$

  where ℓ is the integrand of the Lagrangian functional defined in Eq. (3.32).

- The essential boundary conditions are given by $\varphi^*(0) = \phi_0$, and $\varphi^*(T_1^*) = \phi_1$, where $\phi_1 = \varphi_0 + \dot{\varphi}_{max}(T - T_1^*)$.

- The transversality (natural) boundary condition is written as

$$\ell(T_1^*, \varphi(T_1^*), \dot{\varphi^*}(T_1^*)) + \left(\dot{\varphi}_u(T_1^*) - \dot{\varphi^*}(T_1^*)\right)\frac{\partial \ell}{\partial \dot{\varphi}}(T_1^*, \varphi(T_1^*), \dot{\varphi^*}(T_1^*)) = 0$$

3.3.2 Analytical Solution of the Point-to-Curve Problem

The Euler-Lagrangian differential equation, Eq. (3.33), yields

$$2\ddot{\varphi}^*(t)(\lambda + \cos\varphi^*(t)) = \dot{\varphi}^{*2}(t)\sin\varphi^*(t),\ \forall t \in (0, T_1^*) \tag{3.34}$$

Expanding $\ddot{\varphi}^*$ as $\dot{\varphi}^*\frac{d\dot{\varphi}^*}{d\varphi^*}$, we obtain

$$2\frac{d\dot{\varphi}^*}{\dot{\varphi}^*} = \frac{\sin\varphi^* d\varphi^*}{\lambda + \cos\varphi^*} \quad , \quad \dot{\varphi}^* \neq 0$$

Integrating the outcome yields

$$\dot{\varphi}^*(t) = \dot{\varphi}_0\sqrt{\frac{\lambda + \cos\varphi_0}{\lambda + \cos\varphi^*(t)}},\ \forall t \in (0, T_1^*) \tag{3.35}$$

Thus,

$$\sqrt{\lambda+\cos\varphi^*}d\varphi^* = \dot{\varphi}_0\sqrt{\lambda+\cos\varphi_0}dt$$

Through some mathematical manipulation, it can be shown that the integration of the previous equation yields

$$E\left(\sin\tfrac{\varphi^*(t)}{2} \setminus \tfrac{2}{1+\lambda}\right) - E\left(\sin\tfrac{\varphi_0}{2} \setminus \tfrac{2}{1+\lambda}\right) = \tfrac{\dot{\varphi}_0}{2}\sqrt{\tfrac{\lambda+\cos\varphi_0}{\lambda+1}}t,\ \forall t \in (0, T_1^*) \tag{3.36}$$

where $E(\phi \setminus m) = \int_0^\phi \sqrt{\frac{1-mt^2}{1-t^2}}\,dt$ is the incomplete elliptic integral of the second kind.

For a given φ_0, three unknowns must be determined. These are the initial speed $\dot{\varphi}_0$, the switching time T_1^*, and the lagrange multiplier λ. To determine these unknowns, we have three corresponding equations. The first condition represents continuity at the intersection

$$E\left(\sin\frac{\varphi_1}{2} \setminus \frac{2}{1+\lambda}\right) - E\left(\sin\frac{\varphi_0}{2} \setminus \frac{2}{1+\lambda}\right) = \frac{\dot{\varphi}_0}{2}\sqrt{\frac{\lambda+\cos\varphi_0}{\lambda+1}}T_1^* \tag{3.37}$$

where $\phi_1 = \varphi_0 + \dot{\varphi}_{max}(T - T_1^*)$. Secondly, we have the transversality condition which yields

$$\dot{\varphi}_1(\lambda+\cos\varphi_1)(\dot{\varphi}_1 + 2\dot{\varphi}_{max}) = \lambda\left(\dot{\varphi}_{max}^2\left(\frac{T}{T_1^*} - 1\right) - \frac{\varpi}{T_1^*}\right) \tag{3.38}$$

where $\dot{\varphi}_1 = \dot{\varphi}^*(T_1^*) = \dot{\varphi}_0\sqrt{\frac{\lambda+\cos\varphi_0}{\lambda+\cos\varphi_1}}$. Thirdly, the lift constraint, Eq. (3.31), yields

$$2\dot{\varphi}_0\sqrt{\frac{\lambda+\cos\varphi_0}{\lambda+1}}\left[F\left(\sin\frac{\varphi_1}{2} \setminus \frac{2}{1+\lambda}\right) - F\left(\sin\frac{\varphi_0}{2} \setminus \frac{2}{1+\lambda}\right)\right] + \dot{\varphi}_{max}^2(T - T_1^*) = \varpi \tag{3.39}$$

where $F(\phi \setminus m) = \int_0^\phi \sqrt{\frac{1}{(1-mt^2)(1-t^2)}}\,dt$ is the incomplete elliptic integral of the first kind.

For a fixed φ_0, Eqs. (3.37,3.38,3.39) represent a nonlinear system of algebraic equations in the three unknowns $\dot{\varphi}_0$, T_1^*, and λ. However, the forward thrust functional depends on the initial angle φ_0. Therefore, there may be an optimum value for it that should come out of the solution as well. In that case, a fourth equation should be added to determine φ_0; that is, $\frac{\partial\overline{X}}{\partial\varphi_0} = 0$. We write the thrust functional in Eq. (3.20) as

$$\overline{X} = -K_D\left[\int_{\varphi_0}^{\varphi_1}\dot{\varphi}(\varphi)\cos\varphi\,d\varphi + \dot{\varphi}_{max}\int_{\varphi_1}^{\varphi_0}\cos\varphi\,d\varphi\right] \tag{3.40}$$

Applying Leibniz integral rule, we obtain the fourth equation that completes the system as

$$\frac{\partial\overline{X}}{\partial\varphi_0} = -K_D\left[\dot{\varphi}_1\cos\varphi_1 - \dot{\varphi}_0\cos\varphi_0 + \dot{\varphi}_{max}\left(\cos\varphi_0 - \cos\varphi_1\right)\right] = 0 \tag{3.41}$$

After solving the nonlinear system of algebraic equations, Eqs. (3.37,3.38,3.39,3.41), to determine $\dot{\varphi}_0$, T_1^*,

λ, and φ_0, we need to check the sufficient condition for minimization of the cost functional J (maximization of $\overline{X}$). That is, $\frac{\partial^2 \ell}{\partial \dot{\varphi}^2}(t, \varphi^*(t), \dot{\varphi}^*(t))$ must be positive. Thus, the following condition must be satisfied:

$$\lambda + \cos\varphi^*(t) > 0 \;\; \forall t \in (0, T_1^*)$$

Given a certain design for a FWMAV that is equipped with one horizontal actuator, one can use the above constructive technique to assess the optimum kinematics that would result in the maximum forward thrust from the hovering position. Hence, the designer could determine the ability of the vehicle at hand. The design parameters needed to perform the above analysis are the FWMAV mass m, the flapping frequency f, the wing design (I_{21}), the operating $\frac{C_D}{C_L}$, and the maximum allowable wing speed $\dot{\varphi}_{max}$. We perform the above analysis using, as an example, the following data of the hawkmoth (57):

$$f = 25 \text{ Hz} \;\; , \;\; \text{m} = 1.5 \text{ gm} \;\; , \;\; \bar{\text{c}} = 18.6 \text{ mm} \;\; , \;\; \text{R} = 50 \text{ mm}$$

where $\bar{c}$ and R are the mean chord length and the wing radius, respectively. We consider a rectangular wing and a mean angle of attack of 30°. Thus, since the leading edge vortex is the main aerodynamic contributor to the loads, $\frac{C_D}{C_L} = \tan\alpha_m$. As such, the required values to perform the above analysis are given by

$$f = 25 \text{ Hz} \;\; , \;\; \text{m} = 1.5 \text{ gm} \;\; , \;\; \text{I}_{21} = 155.01 \text{ cm}^4 \;\; \text{and} \;\; \frac{\text{C}_\text{D}}{\text{C}_\text{L}} = 0.5774$$

We use the least-squares technique to solve the nonlinear system of algebraic equations with $\dot{\varphi}_{max} = 2\sqrt{\frac{\varpi}{T}}$. It should be noted that $\sqrt{\frac{\varpi}{T}}$ is the required speed to balance the weight if the wing operates with a constant speed (symmetric triangular waveform), which corresponds to the minimum hovering power as found by Taha et al. (42). The least-squares technique converges to the following solution:

$$\frac{\dot{\varphi}_0}{\dot{\varphi}_{max}} = 0.4654 \;\; , \;\; \frac{T_1^*}{T} = 0.8013 \;\; , \;\; \lambda = -0.7818 \;\; \text{and} \;\; \varphi_0 = -34.36^\circ$$

which corresponds to the kinematics shown in Fig. 3.5. The check of the sufficient condition is shown in Fig. 3.6, which shows that the Hessian of the Lagrangian is positive throughout the entire stroke.

The ability of the vehicle to generate forward thrust forces from a hovering position using a horizontal actuator having a specified maximum speed can be assessed by calculating the resulting $\overline{X}$. Recalling Eq. (3.40), substituting by $\dot{\varphi}(\varphi)$ from Eq. (3.35), and carrying out the integrations, we obtain

$$\overline{X} = -K_D \left[\dot{\varphi}_0 \sqrt{\lambda + \cos\varphi_0} I_d + \dot{\varphi}_{max} (\sin\varphi_0 - \sin\varphi_1) \right] \tag{3.42}$$

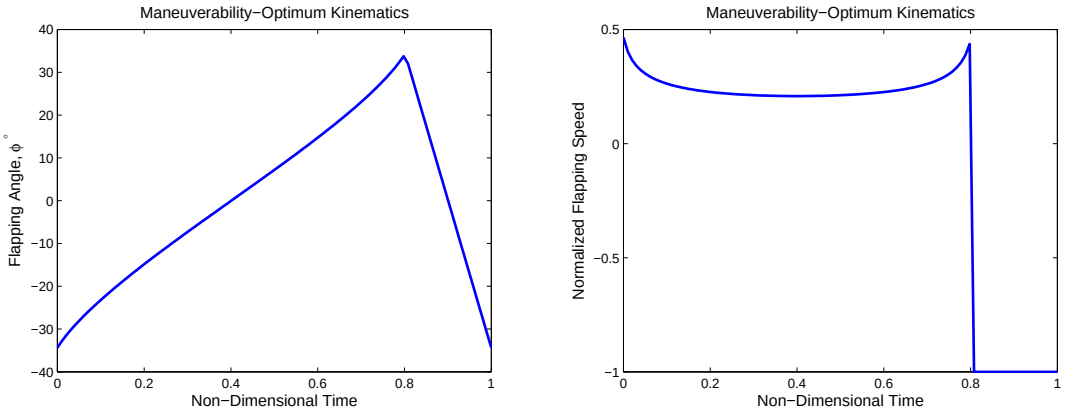

(a) $\varphi^*(t)$ (b) $\dot{\varphi}^*(t)/\dot{\varphi}_{max}$

Figure 3.5: Maneuverability-optimum kinematics for the hawkmoth using a horizontal actuator having a maximum speed double the balance speed.

where

$$I_d = 2\sqrt{2}\left[E\left(\tfrac{2}{\lambda+1}\sin\tfrac{\varphi_1}{2} \setminus \tfrac{1+\lambda}{2}\right) - E\left(\tfrac{2}{\lambda+1}\sin\tfrac{\varphi_0}{2} \setminus \tfrac{1+\lambda}{2}\right)\right] + \\ -\tfrac{2}{\sqrt{\lambda+1}}\left[F\left(\sin\tfrac{\varphi_1}{2} \setminus \tfrac{2}{1+\lambda}\right) - F\left(\sin\tfrac{\varphi_0}{2} \setminus \tfrac{2}{1+\lambda}\right)\right]$$

Now, we use Eq. (3.42) to obtain the maximum achievable forward thrust force/acceleration by a FW-MAV from the hovering position using a horizontal actuator. For the hawkmoth data using a maximum speed double the balance speed, we find that the maximum achievable cycle-average forward acceleration is $4.16 m/s^2$.

3.3.3 Results and Discussion

In this section, we compare the derived maneuverability-optimum kinematics with the asymmetric triangular waveform and the biased split-cycle kinematics proposed by Doman and Oppenheimer (10; 25).

Asymmetric Triangular Waveform (ATW)

In the previous section, it has been proven that the triangular waveform results in the best hovering performance in a horizontal stroke plane. One might also think that the triangular waveform would be optimum from a maneuverability point of view because it allows the wing to operate at a constant (possibly the favorable) speed during each half stroke and, consequently, produce the maximum aerodynamic loads. How-

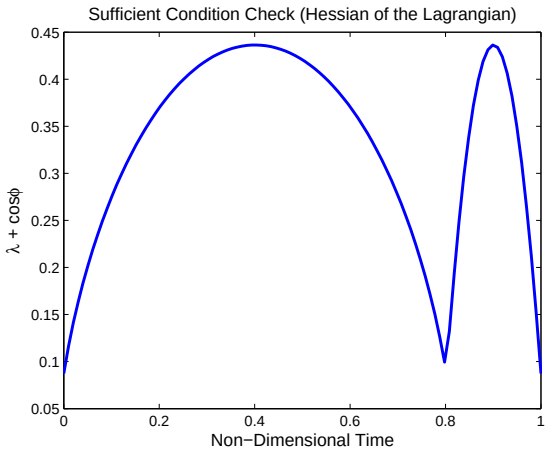

Figure 3.6: Check of the sufficient condition, positiveness of the Hessian of the Lagrangian.

ever, the objective is not to merely maximize the aerodynamic loads but to maximize their component in a certain direction (forward thrust in our case). The resolution of the aerodynamic loads (the $\cos\varphi$ in the $\overline{X}$ functional) may cause the optimum kinematics to take place at a varying wing speed rather than at a constant one. This point will be explained more below.

We consider an upstroke with $-\dot{\varphi}_{max}$ too and calculate the downstroke speed required for balance. The continuity at the intersection dictates that the downstroke speed must be given by $\dot{\varphi}_d = \dot{\varphi}_{max}\left(\frac{T}{T_1} - 1\right)$. Then, the appropriate T_1 is determined to satisfy the lift constraint

$$\int_0^T \dot{\varphi}^2(t)\,dt = \dot{\varphi}_{max}^2\left[\left(\frac{T}{T_1} - 1\right)^2 T_1 + (T - T_1)\right] = \varpi$$

Thus, the appropriate T_1 for ATW going back with $-\dot{\varphi}_{max}$ is given by

$$\frac{T_1}{T} = \frac{1}{\frac{1}{\kappa^2} + 1} \tag{3.43}$$

where $\kappa = \dot{\varphi}_{max}/\sqrt{\frac{\varpi}{T}}$ is the ratio between the maximum allowable wing speed and the balancing wing speed. Then, the corresponding cycle-average forward thrust force $\overline{X}$ is given by

$$\overline{X} = -K_D\dot{\varphi}_{max}\left(2 - \frac{T}{T_1}\right)(\sin\varphi_0 - \sin\varphi_1) \tag{3.44}$$

Also, there is an optimum φ_0, which is obtained by setting $\frac{\partial\overline{X}}{\partial\varphi_0}$ equal to 0, which yields $\cos\varphi_0 = \cos\varphi_1$.

Thus, the optimum φ_0 for the ATW is given by

$$\varphi_0 = \frac{1}{2}\dot{\varphi}_{max} T \left(1 - \frac{T_1}{T}\right)$$

The maximum $\overline{X}$ using ATW is then given by

$$\overline{X} = 2K_D \sqrt{\frac{\varpi}{T}} \frac{\kappa^2 - 1}{\kappa} \sin\left(\frac{1}{2}\sqrt{\varpi T}\frac{\kappa}{\kappa^2 + 1}\right) \tag{3.45}$$

We performed an ATW on the hawkmoth data using $\kappa = 2$ and found that the maximum cycle-average forward acceleration is $3.20 m/s^2$, which is about 23.21% less than the one achieved by the optimized kinematics.

Doman and Oppenheimer Biased Split-Cycle (BSC) kinematics (10; 25)

One of the very common kinematics that has been introduced to obtain high control authority for FWMAVs near hover is the BSC kinematics proposed by Doman, Oppenheimer and Sigthorsson (10; 25). They started with the harmonic wave form and introduced a split-cycle parameter δ to create asymmetry between the two half-strokes (8; 9). In a more recent work (10; 25), they introduced a bias to the waveform to obtain higher control authority.

Recall their kinematics, the BSC flapping angle is written as

$$\begin{aligned} \varphi_u(t) &= -\Phi \cos[(\omega - \delta)t] + \gamma, \qquad 0 \le t \le \tfrac{\pi}{\omega - \delta} \\ \varphi_d(t) &= -\Phi \cos[(\omega + \sigma)t + \zeta] + \gamma, \; \tfrac{\pi}{\omega - \delta} \le t \le \tfrac{2\pi}{\omega} \end{aligned} \tag{3.46}$$

where Φ is the amplitude of the symmetric motion, ω is the angular flapping frequency, δ is the split-cycle parameter, and γ is the bias. In order for the combination of the two modified-frequency half-strokes to have the same period as the original one, $\sigma = \frac{\omega\delta}{\omega - 2\delta}$. Then, continuity between the adjacent strokes dictates $\zeta = \frac{-2\pi\delta}{\omega - 2\delta}$. They used the parameters ω, δ, and γ for each wing as control inputs. They also found that, if the required γ for control differs from one cycle to another, the backward motion (upstroke in this case) must be split into two pieces and the amplitude of the second half of the upstroke must be modified to have continuity between strokes. Because we do not have such a case in our analysis, we will ignore it.

We adapt the BSC kinematics to be compared with the optimized and ATW kinematics. To generate forward thrust forces, a positive δ is required and, intuitively, backward speeds are larger than the forward

ones. Then, the maximum speed of the BSC kinematics needs to be constrained to $\dot{\varphi}_{max}$; i.e.,

$$\Phi(\omega+\sigma) = \dot{\varphi}_{max} \tag{3.47}$$

Also, the following lift constraint must be satisfied:

$$\int_0^T \dot{\varphi}^2(t)\,dt = \Phi^2\left[(\omega-\delta)^2\int_0^{\frac{\pi}{\omega-\delta}}\sin^2(\omega-\delta)t\,dt + (\omega+\sigma)^2\int_{\frac{\pi}{\omega-\delta}}^{\frac{2\pi}{\omega}}\sin^2[(\omega+\sigma)t+\zeta]\,dt\right] = \varpi$$

which yields

$$\pi\Phi^2\frac{(\omega-\delta)^2}{\omega-2\delta} = \varpi \tag{3.48}$$

Equations (3.47,3.48) can be solved to determine δ and Φ that satisfy the lift and maximum wing-speed constraints. They result in

$$\begin{aligned}\delta &= \tfrac{\omega}{2}\left(\kappa^2-2\right)\\ \Phi &= \tfrac{2}{\pi}\sqrt{\varpi T}\,\tfrac{\kappa}{\kappa^2+2}\end{aligned} \tag{3.49}$$

It should be noted that the balancing speed using a harmonic waveform is $\sqrt{2}$ times the balancing speed using a triangular waveform. Thus, κ must be greater than $\sqrt{2}$ in order to produce forward thrust forces using the BSC kinematics; that is, to have positive δ as shown in Eq. (3.49).

Recalling the definition of $\overline{X}$ from Eq. (3.20), the resulting $\overline{X}$ using the BSC kinematics is written as

$$\begin{aligned}\tfrac{\overline{X}}{k_D} = (\omega+\sigma)^2\textstyle\int_{\frac{\pi}{\omega-\delta}}^{\frac{2\pi}{\omega}}\sin^2[(\omega+\sigma)t+\zeta]\cos\left[-\Phi\cos[(\omega+\sigma)t+\zeta]+\gamma\right]\,dt+\\ -(\omega-\delta)^2\textstyle\int_0^{\frac{\pi}{\omega-\delta}}\sin^2(\omega-\delta)t\cos[-\Phi\cos(\omega-\delta)t+\gamma]\,dt\end{aligned}$$

These integrals are evaluated in Ref. (10), which result in

$$\overline{X} = 2\pi\Phi K_D \mathcal{J}_1(\Phi)\delta\frac{w-\delta}{w-2\delta}\cos\gamma \tag{3.50}$$

where $\mathcal{J}_1$ is the Bessel function of the first kind of order one. Because $\phi_0 = \gamma - \Phi$ and the maximum $\overline{X}$ is achieved at zero bias ($\gamma = 0$), the optimum ϕ_0 for the BSC kinematics occurs at $\phi_0 = -\Phi$. The maximum cycle-average forward acceleration using the BSC kinematics with $\kappa = 2$ is found to be $1.79 m/s^2$; that is, 56.96% less than that of the optimized kinematics.

Figure 3.7 shows a comparison among the optimized kinematics, the ATW, and the BSC kinematics for the hawkmoth case study. An explanation to why the proposed kinematics produces a larger $\overline{X}$ than the other ones can be obtained by considering Fig. 3.7(b). Because the objective is to minimize the accumulation

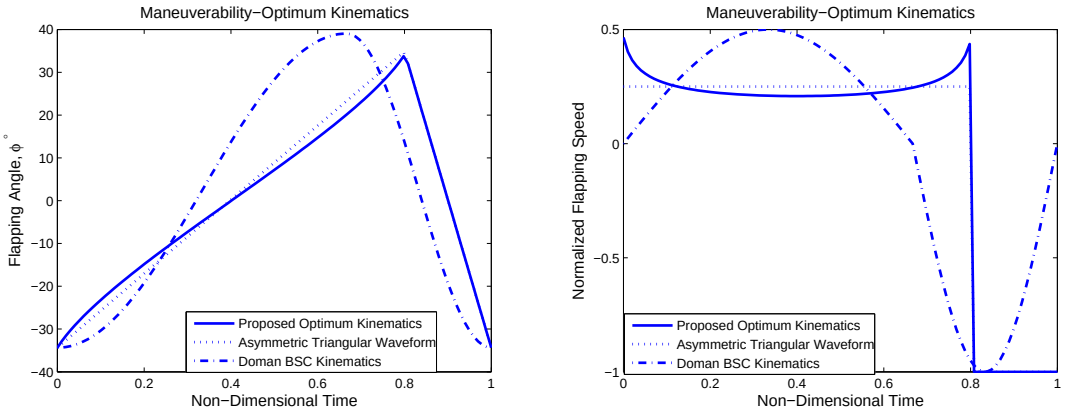

(a) $\varphi^*(t)$ (b) $\dot{\varphi}^*(t)/\dot{\varphi}_{max}$

Figure 3.7: Maneuverability-optimum kinematics for the hawkmoth versus ATW and the BSC kinematics using a horizontal actuator having a maximum speed double the balance speed.

of $\dot{\varphi}^2 \cos\varphi$, the proposed kinematics slows down during the period where φ is close to zero ($\cos\varphi$ is large), to have a smaller multiplication of $\dot{\varphi}^2 \cos\varphi$ and keep this small value for longer times. On the other hand, the ATW operates with a constant speed and, as such, results in a larger multiplication of $\dot{\varphi}^2 \cos\varphi$ in those periods. As for the BSC kinematics, it operates almost in the opposite way of the optimized kinematics and, as such, produces much smaller cycle-average forward accelerations than the optimized kinematics and the ATW. However, it does not have slope discontinuity between half-strokes.

The maximum achievable cycle-average forward thrust force is presented in Eq. (3.42) for the optimized kinematics, Eq. (3.45) for the ATW, and Eq. (3.50) with $\gamma = 0$ for the BSC kinematics. Figure 3.8 shows the variation of the maximum achievable cycle-average forward acceleration and the optimum φ_0 with $\dot{\varphi}_{max}$ (κ) for the optimized kinematics, the ATW, and the BSC kinematics for the hawkmoth case study. Some conclusions can be drawn from Fig. 3.8. Firstly, the difference between the maximum achievable forward acceleration in the three cases decreases as κ increases. Secondly, the optimum φ_0 for the proposed kinematics is very close to that of the ATW kinematics. Fig. 3.8(a) indicates that there is an asymptotic value for the maximum forward acceleration to be reached by each set of kinematics as κ increases. Figure 3.9 replicates Fig. 3.8(a) for large values of $\dot{\varphi}_{max}$ (κ) showing the asymptotic value of the maximum forward acceleration. It is interesting to note that all of the three kinematics reach the same asymptotic value. The optimized kinematics approaches it at a κ smaller than the ATW and than the BSC kinematics. Since all of the kinematics exhibit the same asymptotic value, it is easier to determine this value from the ATW equation

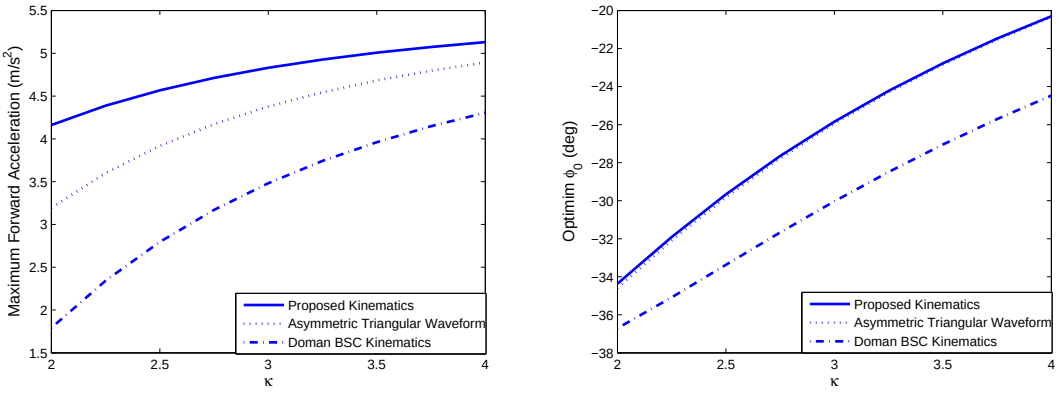

(a) Maximum Forward Acceleration Vs κ

(b) Optimum φ_0 Vs κ

Figure 3.8: Variation of the maximum forward acceleration and the optimum φ_0 with $\dot{\varphi}_{max}$ (κ) for the maneuverability-optimum kinematics, the ATW, and the BSC kinematics for the hawkmoth.

for $\overline{X}$, Eq. (3.45). The limit cycle-average forward acceleration a_{limit} is then given by

$$a_{limit} = \frac{1}{m}\lim_{\kappa\to\infty}\overline{X} = \frac{2K_D}{m}\sqrt{\frac{\varpi}{T}}\lim_{\kappa\to\infty}\frac{\kappa^2-1}{\kappa}\sin\left(\frac{1}{2}\sqrt{\varpi T}\frac{\kappa}{\kappa^2+1}\right)$$

Interestingly, the mathematical manipulation of the previous equation results in

$$a_{limit} = \frac{C_D}{C_L}g \tag{3.51}$$

In summary, the calculus of variations and optimal control techniques allowed us to derive maneuverability-optimum kinematics. For a given maximum wing speed $\dot{\varphi}_{max}$, this kinematics is able to produce higher cycle-average forward accelerations than both of the asymmetric triangular waveform and the biased split-cycle kinematics of Doman and Oppenheimer. As the allowable $\dot{\varphi}_{max}$ increases, the produced cycle-average forward accelerations from the three kinematics become closer together. As $\dot{\varphi}_{max}$ reaches infinity, the three kinematics produce the same cycle-average forward acceleration a_{limit}. Interestingly, this limit is simply given by $a_{limit} = \frac{C_D}{C_L}g$.

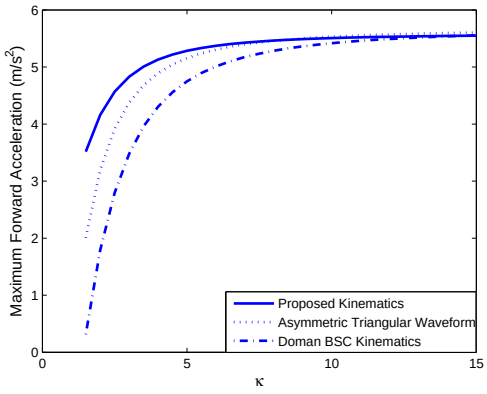

Figure 3.9: Variation of the maximum forward acceleration with κ, and the asymptotic value of the maximum forward acceleration a_{limit}.

3.4 Conclusion

Using the calculus of variations approach allows for the relaxation of the un-necessary constraints induced by parameterizing the kinematics and formulating the problem as a finite-dimensional optimization problem. As such, true optimality is obtained. The optimal back and forth flapping position angle is determined, simultaneously, with the pitching angle that minimize the aerodynamic power under a lift constraint. Use of the calculus of variations along with quasi-steady aerodynamics allowed us to obtain a reference true optimality. Because there are many objectives for the optimization problem of flapping kinematics, this reference performance is intended to represent a basis against which the performance using newly proposed kinematics can be evaluated. It is found that a triangular waveform flapping angle along with a constant pitching angle throughout the half-stroke yield the optimal performance. This pair of optimal kinematic functions is convenient for the minimal actuation concept necessary for micro-air-vehicles feasibility. It is found that the harmonic waveform requires 20% more aerodynamic power than the triangular waveform. Other mathematical and practical advantages of the triangular waveform are discussed.

The calculus of variations and optimal control techniques are also used to determine the maneuverability-optimum back and forth flapping kinematics. The optimization problem is to maximize the cycle-average forward thrust force from the hovering position under the lift equality constraint. Thus, the sought kinematics would be suitable for sudden collision avoidance and possibly for fastest transition from hovering to forward flight. It is found that an additional constraint on the wing speed must be added to have a well-posed, and also realistic, optimization problem. Addition of this constraint, which represents a hard constraint on the function derivative, turns the problem from a conventional calculus of variations problem into an

optimal control one. As such, the necessary conditions for optimization can no longer be derived from the Euler-Lagrange equation but from Pontryagin's maximum principle, which result in four possibilities for the optimal control law (wing speed). Then, physical intuition dictates use of a certain combination of these four possibilities; that is, returning back (upstroke) with the maximum allowable wing speed and going forward with the slower option. Having realized that, the problem can then be formulated as a point-to-curve calculus of variations problem; that is, what is the optimum function that connects the initial point to the returning curve (with the maximum speed) that minimizes the negative contribution to the forward thrust during the downstroke and satisfies the lift constraint.

The obtained kinematics are compared with the asymmetric triangular waveform and the biased split-cycle kinematics of Doman and Oppenheimer. For small values of the maximum allowable wing speed, the obtained kinematics results in cycle-average forward accelerations that are considerably higher than both of the asymmetric triangular waveform and Doman's biased split-cycle kinematics. As the maximum wing speed constraint is relaxed, the performances of the three set of kinematics become close to each other. Interestingly, the cycle-averaged forward accelerations resulted from each of the three set of kinematics approach the same asymptotic finite value for infinite maximum wing speed. This asymptotic value (limit), which represents the maximum cycle-averaged forward acceleration that a flapping vehicle can ever generate from the hovering position, is simply the drag-to-lift fraction of the gravitational acceleration.

Chapter 4

Saturation-Based Design of the Actuation Mechanism

In this chapter, a design methodology for the actuation mechanism of flapping-wing micro-air-vehicles (FWMAVs) is presented. The challenge stems from the fact that hovering and forward fight require different wing motions and, as such, independent actuators. Besides, the stringent weight and size constraints imposed on FWMAVs dictate using a limited number of actuators. In this chapter, a design for the actuation mechanism that provides the required kinematics in each flight condition is proposed using only one actuator. The idea is to exploit the nonlinear dynamics of the flapping wing to induce the saturation phenomenon. The equations of motion of the flapping wing are derived in Section 4.2 and the used aerodynamic model is presented in Section 4.3. An explanation of the saturation phenomenon and its origin is given in Section 4.4. Then, Section 4.5 shows how the saturation phenomenon is exploited in the proposed design of the actuation mechanism so that both kinematics would be obtained. Finally, the methodology is implemented on the hawkmoth data as a FWMAV in Section 4.6.

4.1 Introduction

The stringent weight and size constraints that are always imposed on FWMAVs invoke minimal actuation. Wood (30) noted that the concept of minimal actuation (minimum number of actuators) was a main factor that led to the first successful take off of a FWMAV (Harvard robofly). This concept is also emphasized by Doman et al. (19; 9) and used by Schenato et al. (7). This limitation represents the main motivation for this

work. Unlike conventional aircraft, the design of FWMAVs includes additional aspects, such as design of the kinematics of the wing motion relative to the body and its actuating mechanism. Many attempts aimed at optimizing the wing kinematics either for better aerodynamic performance (43; 165; 73; 74; 42), higher control authority (9; 25; 34; 7; 27), multi-objective optimization (45), or for gust resilience (173). However, when it comes to practical implementation, it is usually preferred to follow the minimal actuation concept. In fact, this is one of the main reasons for the need to decide in the early stages of the design process of a FWMAV whether the main mission of the targeted vehicle is to hover or to travel longer distances. The reason is that the kinematics of hovering and, consequently, the associated actuator are considerably different from those required for forward flight.

Following insects, Weis-Fogh (20) and Ellington (21) observed that hovering is performed in an approximate horizontal stroke plane; that is, no out-of-plane motion (the plunging angle $\vartheta \simeq 0$). In contrast, the wing motion must have a vertical component to tilt the air velocity vector and, consequently, the produced lift force to create a significant thrust force in forward flight, as shown in Fig. 4.1. As such, the hovering and forward flights require different wing-motions and, consequently, two independent actuators. However, in their trials to obtain high control authority near hover, Doman et al. (9), Oppenheimer et al. (25), and Schenato et al. (7) showed that forward thrust forces can be generated by some manipulation of the wing beat in a horizontal stroke plane. This manipulation uses asymmetric flapping (different relative times between the upstroke and downstroke) along with some offset for the back and forth flapping angle φ. This approach is convenient for generating forward thrust forces to transfer from a hovering point to another. Also, it may be essential in the initial transition from zero forward speed to some forward speed, but not efficient at higher, sustained forward speeds. This is why either a hovering or a forward-flight requirement should be included in the mission and design statements of a FWMAV.

The main objective of this work is to provide a design methodology for an actuation mechanism that is able to provide the required kinematics for both of hovering and forward flight. The idea is not as trivial as tilting the stroke plane so as to have components of the wing motion in the horizontal and vertical planes. Instead, the idea is to have almost pure horizontal motion for the wing in hovering and, when desired, the wing motion is transferred into almost pure plunging. This is done by exploiting nonlinearities to transfer energy from one mode to another. The proposed design requires a physical spring in the vertical direction along with feedback of the flapping and plunging angles and the flapping angular rate. It is noteworthy to mention that the flapping angle and angular rate feedback are needed anyway for adjusting the required kinematics in hover. As such, the plunging spring and the plunging angle feedback are the only additional items needed to implement the proposed actuation. The used actuator is in the horizontal direction, which in normal conditions provides the required kinematics in hover.

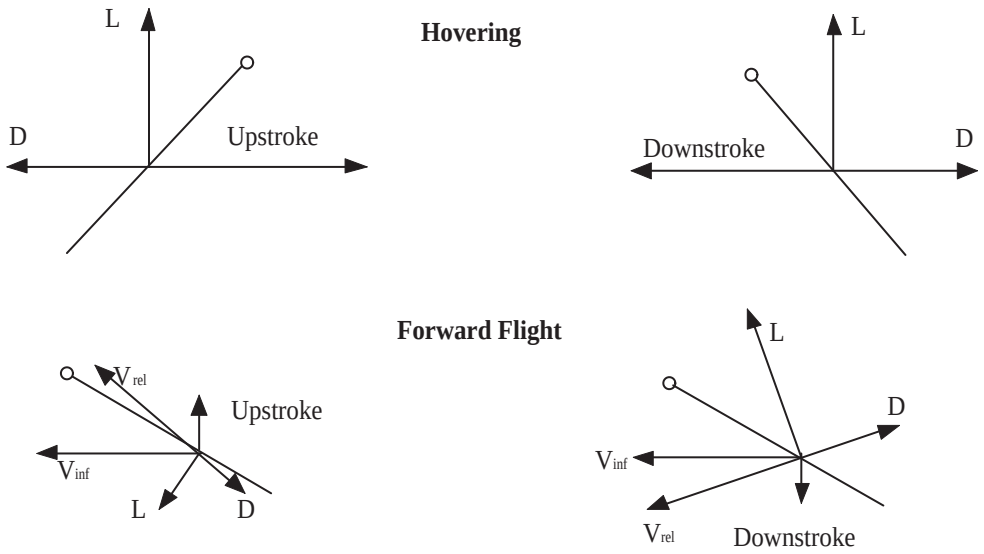

Figure 4.1: Favorable kinematics for hovering and forward flight. The dot represents the leading edge.

Noting that plunging is not effective unless some forward speed is present, we first apply a means for initial transition, as discussed above, to produce some forward speed. The feedback gains are then tuned to induce the saturation phenomenon. Thus, the motion is transferred to the plunging direction, thereby creating a considerable thrust force needed for continuing the transition phase and pursuing sustained, efficient forward flight for long periods. In addition, the amplitude of the control torque (originally actuating the back and forth flapping direction) can then be considered as a control input for the amplitude of the plunging motion and consequently the forward thrust force and speed. On the other hand, the amplitude of the horizontal flapping motion saturates and becomes independent of the amplitude of the actuating torque. Tuning the gains with the system parameters can even make the saturated value of the flapping amplitude so small that pure plunging motion is obtained.

4.2 Equations of Motion

Because both hovering and forward flight can be considered as longitudinal flight conditions, identical motions for the left and right wings are considered. As such, one needs to consider the motion of one wing only. Three consecutive rotations are used to describe the wing kinematics relative to the body: the back and forth flapping angle φ, the plunging angle ϑ, and the pitching angle η. A piecewise constant time-variation of η is assumed; that is, during hover where considerable amplitudes for φ-oscillations exist, η is assumed

to be constant throughout each half stroke and to change instantaneously between half strokes for the wing to have the same angle of attack in the next half stroke, referred to as η_m. Thus, the time variation of the pitch angle, $\eta(t)$, is given by:

$$\eta(t) = \begin{cases} \eta_m, & 0 \leq t \leq T/2, \dot{\varphi} > 0 \\ \pi - \eta_m, & T/2 \leq t \leq T, \dot{\varphi} < 0 \end{cases} \tag{4.1}$$

Taha et al. (42) showed that this time variation for η yields the minimum aerodynamic power required for hover. It is also convenient for the minimal actuation concept, as it can be passively controlled with the φ-motion. As such, this piecewise constant variation of η was used by Schenato et al. (7), Doman et al. (9; 10), and Oppenheimer et al. (8; 25). Using this time variation of η results in its time derivatives be identically zero except at the flip between half strokes where these derivatives are not defined. As such, the η-dynamics is neglected in this work.

Because the main concern is the dynamics of the wing motion, the inertial frame x_I, y_I, and z_I is attached to the vehicle body. The x_I-axis points forward, the y_I points to the right wing, and the z_I points downward to complete the triad. The wing axis system x_w, y_w, and z_w is assumed to coincide with the inertial system at zero kinematic angles. The back and forth flapping angle φ represents the rotation about the negative z_I-axis, the pitching angle η represents the rotation about the rotated y_I-axis, and the plunging angle ϑ represents the rotation about the final x_w-axis. Figure 4.2 shows the axis systems and rotations used to describe the wing kinematics with respect to the body.

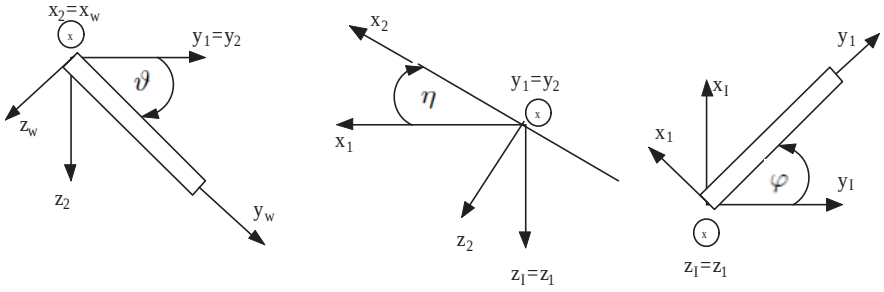

Figure 4.2: The axis systems and rotations used to describe the wing kinematics with respect to the body.

Using the above axis systems, we write the rotation matrices from the the inertial frame to the wing

frame as

$$R_{-\varphi}^{(3)} = \begin{bmatrix} \cos\varphi & -\sin\varphi & 0 \\ \sin\varphi & \cos\varphi & 0 \\ 0 & 0 & 1 \end{bmatrix} \quad , \quad R_{\eta}^{(2)} = \begin{bmatrix} \cos\eta & 0 & -\sin\eta \\ 0 & 1 & 0 \\ \sin\eta & 0 & \cos\eta \end{bmatrix} \quad \text{and} \quad R_{\theta}^{(1)} = \begin{bmatrix} 1 & 0 & 0 \\ 0 & \cos\vartheta & \sin\vartheta \\ 0 & -\sin\vartheta & \cos\vartheta \end{bmatrix} \tag{4.2}$$

The total transformation matrix is then written as

$$R = [R_{\theta}^{(1)}][R_{\eta}^{(2)}][R_{-\varphi}^{(3)}] \tag{4.3}$$

and the wing angular velocity vector $\vec{\omega}^{(w)}$ in the wing frame is given by

$$\vec{\omega}^{(w)} = [R_{\theta}^{(1)}][R_{\eta}^{(2)}](-\dot{\varphi}\vec{k_1}) + \dot{\theta}\vec{i_w} \tag{4.4}$$

where the $\vec{i}, \vec{j}$, and $\vec{k}$ represent unit vectors in the x, y, and z directions, respectively, and the superscript refers to the axis system to which these vectors belong to as shown in Fig. 4.2. Thus, $\vec{\omega}^{(w)}$ is given by

$$\vec{\omega}^{(w)} = \begin{pmatrix} \omega_1 \\ \omega_2 \\ \omega_3 \end{pmatrix} = \begin{pmatrix} \sin\eta\dot{\varphi} + \dot{\vartheta} \\ -\sin\vartheta\cos\eta\dot{\varphi} \\ -\cos\vartheta\cos\eta\dot{\varphi} \end{pmatrix} \tag{4.5}$$

Assuming the wing axis system is composed of the principal axes of the wing, we write the inertial time derivative of the angular momentum vector represented in the wing frame as

$$\vec{\dot{h}}^{(w)} = \begin{pmatrix} I_x\dot{\omega}_1 + (I_z - Iy)\omega_2\omega_3 \\ I_y\dot{\omega}_y + (I_x - Iz)\omega_1\omega_3 \\ I_z\dot{\omega}_3 + (I_y - Ix)\omega_1\omega_2 \end{pmatrix} \tag{4.6}$$

The loads applied on the wing include the aerodynamic loads $\vec{A}^{(w)} = [al_1 \quad al_2 \quad al_3]^T$, the actuating torque τ about the z_I-axis, the gravity, and the action of the plunging spring K_ϑ. As such, the total moment vector applied on the wing is written as

$$\vec{M}^{(w)} = \vec{A}^{(w)} + [R_{\theta}^{(1)}][R_{\eta}^{(2)}](-\tau\vec{k_1}) - K_\vartheta\vartheta\vec{i_w} + \vec{M}_g^{(w)} \tag{4.7}$$

where $\vec{M}_g^{(w)}$ is the moment vector due to gravity, which is given by

$$\vec{M}_g^{(w)} = (-d\vec{i_w} + r_{cg}\vec{j_w}) \times m_w g\vec{k_I} = m_w g \begin{pmatrix} r_{cg}\cos\vartheta\cos\eta \\ d\cos\vartheta\cos\eta \\ r_{cg}\sin\eta - d\sin\vartheta\cos\eta \end{pmatrix} \tag{4.8}$$

and d and r_{cg} are the distances between the wing root hinge point (the origin of the wing axis system) and the wing's center of gravity along the negative x_w-axis and the y_w-axis, respectively. Thus, the total moment vector is given by

$$\vec{M}^{(w)} = \begin{pmatrix} M_1 \\ M_2 \\ M_3 \end{pmatrix} = \begin{pmatrix} al_1 + \tau\sin\eta - K_\vartheta\vartheta + m_w g r_{cg}\cos\vartheta\cos\eta \\ al_2 - \tau\sin\vartheta\cos\eta + m_w g d\cos\vartheta\cos\eta \\ al_3 - \tau\cos\vartheta\cos\eta + m_w g(r_{cg}\sin\eta - d\sin\vartheta\cos\eta) \end{pmatrix} \tag{4.9}$$

Applying the principle of virtual power (174),

$$(\dot{\vec{h}} - \vec{M}) \cdot \frac{\partial\vec{\omega}}{\partial\dot{q}_i} = 0, \quad i = 1, 2$$

where q represents the generalized coordinates (φ, ϑ) and noting that

$$\frac{\partial\vec{\omega}^{(w)}}{\partial\dot{\varphi}} = \begin{pmatrix} \sin\eta \\ -\sin\vartheta\cos\eta \\ -\cos\vartheta\cos\eta \end{pmatrix} \quad \text{and} \quad \frac{\partial\vec{\omega}^{(w)}}{\partial\dot{\vartheta}} = \begin{pmatrix} 1 \\ 0 \\ 0 \end{pmatrix}$$

we write the dynamic equations describing the wing motion as

$$\begin{aligned} \left(I_x\sin^2\eta + (I_y\sin^2\vartheta + I_z\cos^2\vartheta)\cos^2\eta\right)\ddot{\varphi} + I_x\sin\eta\ddot{\vartheta} &= \tau - K_\vartheta\vartheta\sin\eta + aa_1 \\ I_x\sin\eta\ddot{\varphi} + I_x\ddot{\vartheta} + \tfrac{1}{2}(I_z - I_y)\sin 2\vartheta\cos^2\eta\dot{\varphi}^2 &= \tau\sin\eta - K_\vartheta\vartheta + al_1 + m_w g r_{cg}\cos\vartheta\cos\eta \end{aligned} \tag{4.10}$$

where

$$aa_1 = al_1\sin\eta - al_2\sin\vartheta\cos\eta - al_3\cos\vartheta\cos\eta$$

4.3 Aerodynamic Modeling

Considering an airfoil section that is a distance r from wing root, its velocity components in the wing frame are written as

$$\begin{aligned} V_{x_w} &= r\dot{\varphi}\cos\vartheta\cos\eta - r\dot{\vartheta}\sin\eta + V_\infty(\cos\eta\cos\phi + \sin\eta\sin\phi\sin\theta) \\ V_{z_w} &= r\dot{\varphi}\cos\vartheta\sin\eta + r\dot{\vartheta}\cos\eta + V_\infty(\sin\eta\cos\phi - \cos\eta\sin\phi\sin\theta) \end{aligned} \tag{4.11}$$

where V_∞ is the free-stream velocity (body velocity in the case of forward flight). The forces in the plane of the wing section are then given by (43)

$$\begin{aligned} dF_{x_w} &= \rho V_{z_w}\Gamma dr - dF_{dx} \\ dF_{z_w} &= \left[-\rho V_{x_w}\Gamma - m_{app}\dot{V}_{z_w}\right] dr - dF_{dz} \end{aligned} \tag{4.12}$$

where $m_{app} = \frac{1}{4}\pi\rho c^2(r)$ is the apparent (added) mass and $\Gamma = -\frac{1}{2}C_L(\alpha)c(r)V_{tot}$ is the circulation, with the signs adjusted for $\alpha = \arctan\frac{-V_{z_w}}{V_{x_w}}$ and the lift coefficient given by (167) $C_L = \frac{1}{2}C_{L_\alpha}\sin 2\alpha$ where the lift curve slope is given by

$$C_{L_\alpha} = \frac{\pi AR}{1 + \sqrt{(\frac{\pi AR}{a_0})^2 + 1}}$$

with the aspect ratio, AR, being based on one wing; that is, $AR = \frac{R^2}{S}$ and a_0 is the lift curve slope of the two-dimensional airfoil section, taken to be 2π here.

The drag force is written as

$$\begin{pmatrix} dF_{dx} \\ dF_{dz} \end{pmatrix} = \frac{1}{2}\rho c(r)C_D V_{tot}\begin{pmatrix} V_{x_w} \\ V_{z_w} \end{pmatrix} dr \tag{4.13}$$

where the drag coefficient is given by $C_D = C_{D0} + C_{L_\alpha}\sin^2\alpha$. The viscous drag coefficient is taken to be the flat plate drag with fully turbulent boundary layer, $C_{D0} = \frac{0.148}{\sqrt[5]{Re}}$ where Re is the Reynolds number.

Using the above equations, the components of the aerodynamic moment vector in the wing frame are written as

$$\vec{A}^{(w)} = \begin{pmatrix} al_1(t) \\ al_2(t) \\ al_3(t) \end{pmatrix} = -2\begin{pmatrix} \int_0^R dF_{z_w}(r,t)r\,dr \\ \int_0^R dF_{z_w}(r,t)(d-\hat{x}_{cp})c(r)\,dr \\ \int_0^R dF_{x_w}(r,t)r\,dr \end{pmatrix}$$

where $d - \hat{x}_{cp}$ is the distance between the wing root hinge point and the center of pressure, assumed to lie

at the quarter chord point.

4.4 The Saturation Phenomenon and Energy Transfer

The saturation phenomenon is one of the very interesting phenomena in the area of nonlinear dynamics. Its history can be traced back to 1863 when Froude noted that a ship whose roll frequency is close to one-half its heave frequency has undesirable sea-keeping characteristics. At that time, only linearized six-degrees-of-freedom rigid body equations of motion were used to model the ship dynamics in which the roll and heave motions are decoupled. About a hundred years later, Nayfeh, Mook, and Marshall (175) explained the nontraditional response for ship dynamics having a two-to-one frequency ratio using the nonlinear equations of motion that account for the coupling between the roll and heave motions. Several analytical and experimental investigations have shed more light on the consequences of this internal resonance to show how it promotes energy transfer and leads to the saturation phenomenon (e.g., Haddow et al. (176), and Nayfeh and Balachandran (177)).

The saturation phenomenon is associated with dynamical systems having quadratic nonlinearities and some resonance characteristics. Nayfeh et al. (175) introduced the following system as a paradigm for systems exhibiting the saturation phenomenon:

$$\begin{aligned} \ddot{u}_1 + \omega_1^2 u_1 &= -2\mu_1 \dot{u}_1 + u_1 u_2 \\ \ddot{u}_2 + \omega_2^2 u_2 &= -2\mu_2 \dot{u}_2 + u_1^2 + F\cos\Omega t \end{aligned} \tag{4.14}$$

If the u_2 mode is directly excited by a primary resonance (i.e., $\Omega = \omega_2 + \epsilon\sigma_1$, where ϵ is a small nondimensional parameter) and if it is involved in a two-to-one internal resonance with the u_1 mode (i.e., $\omega_2 = 2\omega_1 + \epsilon\sigma_2$), where σ_1 and σ_2 are detuning parameters, the saturation phenomenon is induced. That is, if the excitation amplitude F exceeds a certain threshold, the amplitude of the directly excited mode u_2 will saturate and become almost independent of the excitation amplitude. On the other hand, the amplitude of the u_1 mode, indirectly excited via the internal resonance, will increase with increasing F. The method of multiple scales (178; 179) has been used to explain this phenomenon analytically. Figure 4.3 shows typical force-response curves for the system (4.14) exihibiting the saturation phenomenon.

The bifurcation associated with the saturation phenomenon is not always a supercritical bifurcation like the one shown in Fig. 4.3, but may be a subcritical bifurcation accompanied by a *jump* and *hysteresis*. In addition, the periodic responses associated with the saturation phenomenon may undergo a secondary Hopf bifurcation for some excitation parameters, as shown by the experimental and theoretical work of

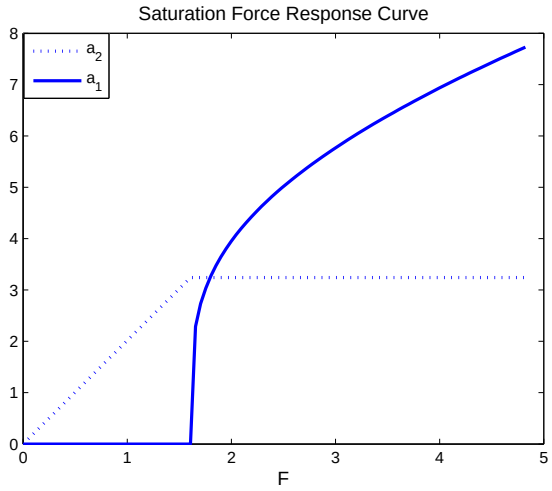

Figure 4.3: Typical force-response curve for a system (paradigm) exhibiting the saturation phenomenon.

Balachandran and Nayfeh (180).

If u_2 represents a mode of an excited linear or nonlinear system, then one can exploit the saturation phenomenon to suppress its resonant vibrations. To this end, one designs in either hardware or software another mode u_1 and couples it quadratically with u_2 using a sensor and an actuator. Oueini et al. (181) exploited the saturation phenomenon in suppressing the resonant vibrations of a single-degree-of-freedom system. Oueini et al. (182) extended the earlier work to control the vibrations of distributed parameter systems such as cantilever beams. Hall et al. (183) used the saturation phenomenon to suppress flutter of aircraft wings. For more details about the saturation phenomenon, the reader is referred to Nayfeh and Mook (184) and Nayfeh (185).

4.5 Exploitation of the Saturation Phenomenon

This section illustrates how the saturation phenomenon can be exploited in the flapping-wing dynamics governed by Eq. (4.10) to induce energy transfer from the back and forth flapping mode (i.e., φ) to the plunging mode (i.e., ϑ). As such, operating the system away from saturation, the hovering kinematics (flapping motion) is obtained. In contrast, tuning the feedback gains to meet the resonance requirements for saturation, the kinematics appropriate for forward flight (plunging motion) is obtained. The method of multiple scales (178; 179) is used to show analytically that the proposed design exhibits the saturation phenomenon.

Considering the flapping-wing dynamics governed by Eq. (4.10), note that all of the existing nonlinearities are cubic nonlinearities except the one due to gravity. Because quadratic nonlinearities are essential for activating the saturation phenomenon, a spring K_ϑ in the plunging direction is used to create an equilibrium position for the plunging angle ϑ. Expanding the trigonometric functions of ϑ around this equilibrium yields the required quadratic nonlinearities. In addition, because two parameters are required to tune the two natural frequencies to satisfy the required resonance conditions, we introduce another feedback spring action $K_\varphi\varphi$ in the actuating torque. As such, Eq. (4.10) has equilibria φ_e and ϑ_e satisfying

$$\begin{aligned} K_\varphi\varphi_e + \sin\eta K_\vartheta\vartheta_e &= 0 \\ \sin\eta K_\varphi\varphi_e + K_\vartheta\vartheta_e - m_w g r_{cg}\cos\eta\cos\vartheta_e &= 0 \end{aligned} \tag{4.15}$$

At this stage, the aerodynamic loads have been ignored and its effect will be assessed later via simulations. Equations (4.15) constitute a nonlinear algebraic system of equations, which can be solved numerically. However, because φ_e and ϑ_e are expected to be small, this system possesses the following approximate solution:

$$\vartheta_e \simeq -\frac{K_\vartheta\cos\eta}{m_w g r_{cg}} \pm \sqrt{\left(\frac{-K_\vartheta\cos\eta}{m_w g r_{cg}}\right)^2 + 2} \;\text{ and }\; \varphi_e = -\frac{K_\vartheta\vartheta_e}{K_\varphi}\sin\eta \tag{4.16}$$

Expanding the trigonometric functions of ϑ in Eq. (4.10) around ϑ_e and keeping up to quadratic nonlinearities yields

$$\begin{aligned} (\alpha_1 - \alpha_2\tilde{\vartheta})\ddot{\tilde{\varphi}} + \ddot{\tilde{\vartheta}}\sin\eta &= f - \omega_\varphi^2\tilde{\varphi} - \omega_\vartheta^2\tilde{\vartheta}\sin\eta \\ \ddot{\tilde{\varphi}}\sin\eta + \ddot{\tilde{\vartheta}} + \tfrac{1}{2}\alpha_2\dot{\tilde{\varphi}}^2 &= \sin\eta(f - \omega_\varphi^2\tilde{\varphi}) - (\omega_\vartheta^2 + \alpha_3)\tilde{\vartheta} - \alpha_3\tilde{\vartheta}^2\cot\vartheta_e \end{aligned} \tag{4.17}$$

where

$$\tilde{\varphi} = \varphi - \varphi_e \;\;,\;\; \tilde{\vartheta} = \vartheta - \vartheta_e \;\;,$$

$$\alpha_1 = \sin^2\eta + \frac{I_y\sin^2\vartheta_e + I_z\cos^2\vartheta_e}{I_x}\cos^2\eta \;\;,\;\; \alpha_2 = \frac{I_z - I_y}{I_x}\sin 2\vartheta_e\cos^2\eta \;\;,$$

$$\alpha_3 = \frac{m_w g r_{cg}}{I_x}\sin\vartheta_e\cos\eta \;\;,$$

$$f = \frac{\tau}{I_x} \;\;,\;\; \omega_\varphi^2 = \frac{K_\varphi}{I_x} \;\text{ and }\; \omega_\vartheta^2 = \frac{K_\vartheta}{I_x}$$

Note that the dynamical system (4.17) does not exhibit a saturation response because of the lack of damping and the weakness of the nonlinear terms associated with α_2. The latter issue originates from the fact that the design problem, shown below, dictates a certain tuning value for the spring K_ϑ, which in turn results in

small ϑ_e. Adding the damping term $-b\dot{\varphi}$ and the nonlinear terms $K_1\tilde{\varphi}\tilde{\vartheta}$, $K_2\dot{\tilde{\varphi}}$ to the actuating torque, we rewrite the system (4.17) as

$$\begin{aligned}(\alpha_1-\alpha_2\tilde{\vartheta})\ddot{\tilde{\varphi}}+\ddot{\tilde{\vartheta}}\sin\eta+\omega_\varphi^2\tilde{\varphi}+\omega_\vartheta^2\tilde{\vartheta}\sin\eta &= \epsilon\left(f-\zeta\dot{\tilde{\varphi}}+k_1\tilde{\varphi}\tilde{\vartheta}+k_2\dot{\tilde{\varphi}}^2\right)\\ \ddot{\tilde{\varphi}}\sin\eta+\ddot{\tilde{\vartheta}}+\omega_\varphi^2\tilde{\varphi}\sin\eta+(\omega_\vartheta^2+\alpha_3)\tilde{\vartheta} &= \epsilon\sin\eta\left(f-\zeta\dot{\tilde{\varphi}}+k_1\tilde{\varphi}\tilde{\vartheta}+k_2\dot{\tilde{\varphi}}^2\right)\\ &\quad -\epsilon\left(\tfrac{1}{2}\alpha_2\dot{\tilde{\varphi}}^2-\alpha_3\tilde{\vartheta}^2\cot\vartheta_e\right)\end{aligned} \tag{4.18}$$

where $\zeta=\frac{b}{I_x}$, $k_n=\frac{K_n}{I_x}$, and ϵ is a bookkeeping parameter that has been introduced to balance the relative weights of the different terms.

A second-order uniform expansion of the solution of Eqs. (6.12) is sought using the method of multiple scales in the form

$$\tilde{\varphi}=\tilde{\varphi}_0(T_0,T_1)+\epsilon\tilde{\varphi}_1(T_0,T_1)+...\ \text{ and }\ \tilde{\vartheta}=\tilde{\vartheta}_0(T_0,T_1)+\tilde{\epsilon}\vartheta_1(T_0,T_1)+... \tag{4.19}$$

where $T_n=\epsilon^n t$. In terms of these time scales, the time derivatives become

$$\frac{d}{dt}=D_0+\epsilon D_1+...\ \text{ and }\ \frac{d^2}{dt^2}=D_0^2+2\epsilon D_0D_1+... \tag{4.20}$$

where $D_n=\frac{\partial}{\partial T_n}$. Substituting Eqs. (6.13) and (6.14) into Eqs. (6.12) and separating coefficients of like powers of ϵ, two sets of equations are obtained, which can be solved successively.

The first set is expressed as

$$\begin{aligned}\alpha_1D_0^2\tilde{\varphi}_0+\sin\eta D_0^2\tilde{\vartheta}_0+\omega_\varphi^2\tilde{\varphi}_0+\sin\eta\omega_\vartheta^2\tilde{\vartheta}_0 &= 0\\ \sin\eta D_0^2\tilde{\varphi}_0+D_0^2\tilde{\vartheta}_0+\sin\eta\omega_\varphi^2\tilde{\varphi}_0+(\omega_\vartheta^2+\alpha_3)\tilde{\vartheta}_0 &= 0\end{aligned} \tag{4.21}$$

The solution of Eqs. (6.15) is expressed in the form

$$\begin{aligned}\tilde{\varphi}_0&=A_1(T_1)e^{i\omega_1T_0}+A_2(T_1)e^{i\omega_2T_0}+cc\\ \tilde{\vartheta}_0&=\Lambda_1A_1(T_1)e^{i\omega_1T_0}+\Lambda_2A_2(T_1)e^{i\omega_2T_0}+cc\end{aligned} \tag{4.22}$$

where cc represents the complex conjugate of all of the preceding terms, ω_1 and ω_2 are the solutions of the characteristic equation

$$(\alpha_1-\sin^2\eta)\omega^4-\left(\omega_\varphi^2\cos^2\eta+\omega_\vartheta^2(\alpha_1-\sin^2\eta)+\alpha_1\alpha_3\right)\omega^2+\omega_\varphi^2(\omega_\vartheta^2\cos^2\eta+\alpha_3)=0$$

$$\text{and } \Lambda_n = -\frac{\omega_\varphi^2 - \omega_n^2}{\omega_\vartheta^2 - \omega_n^2 + \alpha_3}\sin\eta \ , \quad n = 1, 2$$

Due to the coupling between $\tilde{\varphi}$ and $\tilde{\vartheta}$ in Eqs. (6.12), the direction in which the energy flows is not known; that is, is it from φ to ϑ or the other way around? To fix this direction, it is required that each of the degrees of freedom (φ and ϑ) has a dominant response at a specific characteristic frequency. Thus, the system is designed so that Λ_2 is negligible compared with Λ_1 so that $\tilde{\vartheta}_0$ has its dominant response at ω_1. Consequently, the dominant response of $\tilde{\varphi}_0$ will be at ω_2. Then, to transfer energy from φ to ϑ, the following external and internal resonances are required:

$$\Omega = \omega_2 + \epsilon\sigma_1 \ \text{ and } \ \omega_2 = 2\omega_1 + \epsilon\sigma_2 \tag{4.23}$$

Given the flapping frequency Ω, the values of ω_1 and ω_2 are dictated according to Eq. (4.23). Substituting the obtained values for ω_1 and ω_2 into the characteristic equation of the system yields two nonlinear algebraic equations in ω_φ and ω_ϑ. These two equations are augmented with the equations defining the α_i and ϑ_e to determine the required K_φ and K_ϑ. However, the above requirement on Λ_1 and Λ_2 is not satisfied for any arbitrary Ω. Figure 4.4 shows variations of Λ_1 and Λ_2 with Ω using the resonance conditions (4.23). Because these resonance conditions will induce energy transfer from the second mode (ω_2) to the first one (ω_1), we require Λ_1 to be much larger than Λ_2, as stated above. As such, ϑ will have its dominant response at ω_1 and φ will have its dominant response at ω_2. This scenario occurs for Ω greater than a certain threshold, as shown in Fig. 4.4. It is important to note that this threshold depends strongly on the pitching angle η; Fig. 4.4 is plotted for $\eta = 32^\circ$ and the values of the system parameters given in the next section.

Having chosen Ω to satisfy the requirements on Λ_1 and Λ_2 and then designed K_φ and K_ϑ to meet the resonance conditions, recall the first-order problem (i.e., the coefficients of ϵ in the multiple scales expansion); that is,

$$\begin{aligned}
&\alpha_1 D_0^2\tilde{\varphi}_1 + \sin\eta D_0^2\tilde{\vartheta}_1 + \omega_\varphi^2\tilde{\varphi}_1 + \sin\eta\omega_\vartheta^2\tilde{\vartheta}_1 = -D_0[2D_1(\alpha_1\tilde{\varphi}_0 + \sin\eta\tilde{\vartheta}_0) + \zeta\tilde{\varphi}_0] + +\alpha_2\tilde{\vartheta}_0 D_0^2\tilde{\varphi}_0 \\
&+k_1\tilde{\varphi}_0\tilde{\vartheta}_0 + k_2(D_0\tilde{\varphi}_0)^2 + f \\
&\sin\eta D_0^2\tilde{\varphi}_1 + D_0^2\tilde{\vartheta}_1 + \sin\eta\omega_\varphi^2\tilde{\varphi}_1 + (\omega_\vartheta^2 + \alpha_3)\tilde{\vartheta}_1 = -D_0[2D_1(\sin\eta\tilde{\varphi}_0 + \tilde{\vartheta}_0) + \sin\eta(\zeta_1\tilde{\varphi}_0 + \zeta_2\tilde{\vartheta}_0)] + \\
&+ \left(k_2\sin\eta - \tfrac{1}{2}\alpha_2\right)(D_0\tilde{\varphi}_0)^2 + k_1\sin\eta\tilde{\varphi}_0\tilde{\vartheta}_0 - \alpha_3\cot\vartheta_e\tilde{\vartheta}_0^2 + f\sin\eta
\end{aligned} \tag{4.24}$$

Substituting for $\tilde{\varphi}_0$ and $\tilde{\vartheta}_0$ from Eqs. (4.22) into Eqs. (6.16), the following expressions for their right-hand

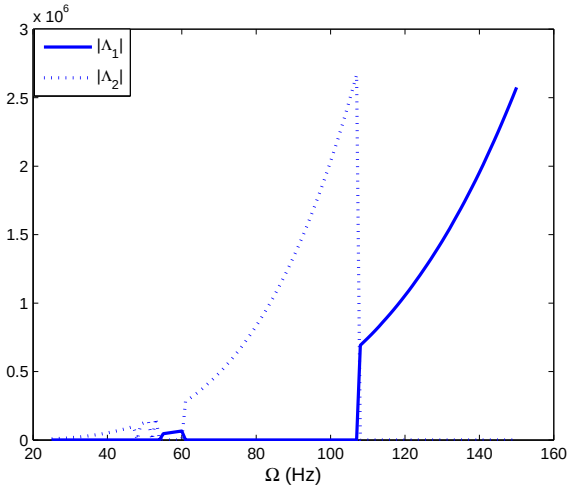

Figure 4.4: Effect of the excitation frequency Ω on the parameters Λ_1 and Λ_2 for $\eta = 32°$.

sides (the forcing terms) are obtained:

$$
\begin{aligned}
RHS_1 &= -i\omega_n[2(\alpha_1 + \sin\eta\Lambda_n)A_n' + \zeta A_n]e^{i\omega_n T_0} + \left[\Lambda_n(k_1 - \alpha_2\omega_n^2) + k_2\omega_n^2\right]\left(A_n^2 e^{2i\omega_n T_0} + A_n\bar{A}_n\right) \\
&+ \left[k_1(\Lambda_1+\Lambda_2) - 2k_2\omega_1\omega_2 - \alpha_2(\Lambda_1\omega_2^2 + \Lambda_2\omega_1^2)\right]\left(A_2A_1e^{i(\omega_2+\omega_1)T_0} + A_2\bar{A}_1e^{i(\omega_2-\omega_1)T_0}\right) + Fe^{i\Omega T_0} + cc \\
RHS_2 &= -i\omega_n[2(\sin\eta + \Lambda_n)A_n' + \sin\eta\zeta A_n]e^{i\omega_n T_0} + F\sin\eta e^{i\Omega T_0} + \\
&\left[\Lambda_n k_1\sin\eta + (\tfrac{1}{2}\alpha_2 - k_2\sin\eta)\omega_n^2 - \alpha_3\cot\vartheta_e\Lambda_n^2\right]\left(A_n^2e^{2i\omega_n T_0} + A_n\bar{A}_n\right) + \\
&+ \left[k_1(\Lambda_1+\Lambda_2) + (\alpha_2 - 2k_2\sin\eta)\omega_1\omega_2 - 2\alpha_3\cot\vartheta_e\Lambda_1\Lambda_2\right]\left(A_2A_1e^{i(\omega_2+\omega_1)T_0} + A_2\bar{A}_1e^{i(\omega_2-\omega_1)T_0}\right) + cc
\end{aligned}
\tag{4.25}
$$

where summation on the repeated indices is used, $A' = \frac{dA}{dT_1}$, $\bar{A}$ is the complex conjugate of A, and $f = 2F\cos\Omega t = Fe^{i\Omega T_0} + cc$.

Considering the resonance conditions, given in Eq. (4.23), and collecting the coefficients of $e^{\omega_1 T_0}$ and

$e^{\omega_2 T_0}$ in Eq. (4.25), we obtain

$$\begin{aligned}
R_{11} &= -i\omega_1[2(\alpha_1+\sin\eta\Lambda_1)A_1'+\zeta A_1]+\left[k_1(\Lambda_1+\Lambda_2)-2k_2\omega_1\omega_2-\alpha_2(\Lambda_1\omega_2^2+\Lambda_2\omega_1^2)\right]A_2\bar{A}_1e^{i\sigma_2T_1}\\
R_{12} &= -i\omega_2[2(\alpha_1+\sin\eta\Lambda_2)A_2'+\zeta A_2]+\left[k_1\Lambda_1-k_2\omega_1^2-\alpha_2\Lambda_1\omega_1^2\right]A_1^2e^{-i\sigma_2T_1}+Fe^{i\sigma_1T_1}\\
R_{21} &= -i\omega_1[2(\sin\eta+\Lambda_1)A_1'+\sin\eta\zeta A_1]\\
&+[k_1\sin\eta(\Lambda_1+\Lambda_2)+(\alpha_2-2k_2\sin\eta)\omega_1\omega_2-2\alpha_3\cot\vartheta_e\Lambda_1\Lambda_2]\,A_2\bar{A}_1e^{i\sigma_2T_1}\\
R_{22} &= -i\omega_2[2(\sin\eta+\Lambda_2)A_2'+\sin\eta\zeta A_2]\\
&+\left[k_1\Lambda_1\sin\eta+(\tfrac{1}{2}\alpha_2-k_2\sin\eta)\omega_1^2-\alpha_3\cot\vartheta_e\Lambda_1^2\right]A_1^2e^{-i\sigma_2T_1}+F\sin\eta e^{i\sigma_1T_1}
\end{aligned} \tag{4.26}$$

where the first index in R_{mn} refers to the equation and the second one refers to the frequency of this forcing term. Because the homogeneous Eqs. (6.16) are the same as Eqs. (6.15) and because the latter have a nontrivial solution, the nonhomogeneous Eqs. (6.16) have a solution only if a solvability condition is satisfied (179). Imposing the solvability condition, we obtain

$$\begin{vmatrix} R_{1n}\,\sin\eta(\omega_\vartheta^2-\omega_n^2) \\ R_{2n}\;\;\omega_\vartheta^2+\alpha_3-\omega_n^2 \end{vmatrix} = 0 \;\;,\;\; n=1,2$$

which in turn gives the complex-valued modulation equations

$$\begin{aligned}
2i\delta_1A_1'+i\mu_1A_1+\delta_2A_2\bar{A}_1e^{i\sigma_2T_1} &= 0\\
2i\delta_3A_2'+i\mu_2A_2+\delta_4A_1^2e^{-i\sigma_2T_1}-\delta_5Fe^{i\sigma_1T_1} &= 0
\end{aligned} \tag{4.27}$$

where

$$\begin{aligned}
\delta_1 &= \omega_1\left[(\alpha_1-\sin^2\eta)(\omega_\vartheta^2-\omega_1^2)+\alpha_3(\alpha_1+\Lambda_1\sin\eta)\right]\\
\delta_2 &= \alpha_2\left[(\Lambda_1\omega_2^2+\Lambda_2\omega_1^2+\omega_1\omega_2\sin\eta)(\omega_\vartheta^2-\omega_1^2)+(\Lambda_1\omega_2^2+\Lambda_2\omega_1^2)\alpha_3\right]+\\
&\quad -2\alpha_3\cot\vartheta_e\sin\eta\Lambda_1\Lambda_2(\omega_\vartheta^2-\omega_1^2)+[2k_2\omega_1\omega_2-k_1(\Lambda_1+\Lambda_2)]\left[(\omega_\vartheta^2-\omega_1^2)\cos^2\eta+\alpha_3\right]\\
\delta_4 &= \alpha_2\omega_1^2\left[(\Lambda_1+\tfrac{1}{2}\sin\eta)(\omega_\vartheta^2-\omega_2^2)+\Lambda_1\alpha_3\right]-\alpha_3\cot\vartheta_e\sin\eta\Lambda_1^2(\omega_\vartheta^2-\omega_2^2)+\\
&\quad +\left(k_2\omega_1^2-k_1\Lambda_1\right)\left[(\omega_\vartheta^2-\omega_2^2)\cos^2\eta+\alpha_3\right]\\
\delta_5 &= (\omega_\vartheta^2-\omega_2^2)\cos^2\eta+\alpha_3
\end{aligned}$$

and $\mu_n=\zeta\omega_n[(\omega_\vartheta^2-\omega_n^2)\cos^2\eta+\alpha_3]$. Letting $A_1=\frac{1}{2}a_1e^{i\beta_1}$ and $A_2=\frac{1}{2}a_2e^{i\beta_2}$ and separating the real and

imaginary parts of Eq. (4.27), the real-valued modulation equations are obtained

$$\begin{aligned}
&\delta_1 a_1 \beta_1' - \tfrac{1}{4}\delta_2 a_1 a_2 \cos\gamma_1 &&= 0\\
&\delta_1 a_1' + \tfrac{1}{2}\mu_1 a_1 + \tfrac{1}{4}\delta_2 a_1 a_2 \sin\gamma_1 &&= 0\\
&\delta_3 a_2 \beta_2' - \tfrac{1}{4}\delta_4 a_1^2 \cos\gamma_1 + \delta_5 F\cos\gamma_2 &&= 0\\
&\delta_3 a_2' + \tfrac{1}{2}\mu_2 a_2 - \tfrac{1}{4}\delta_4 a_1^2 \sin\gamma_1 - \delta_5 F\sin\gamma_2 &&= 0
\end{aligned} \tag{4.28}$$

where $\gamma_1 = \beta_2 + \sigma_2 T_1 - 2\beta_1$ and $\gamma_2 = \sigma_1 T_1 - \beta_2$.

Considering the steady-state solution of the modulation equations; that is,

$$\dot{a_1} = \dot{a_2} = 0 \ , \ \dot{\beta_2} = \sigma_1, \ \text{ and } \ \dot{\beta_1} = \frac{1}{2}(\sigma_1 + \sigma_2)$$

we obtain

$$\begin{aligned}
&\tfrac{1}{2}\delta_1(\sigma_1+\sigma_2)a_1 - \tfrac{1}{4}\delta_2 a_1 a_2\cos\gamma_1 &&= 0\\
&\tfrac{1}{2}\mu_1 a_1 + \delta_2 a_1 a_2 \sin\gamma_1 &&= 0\\
&\delta_3\sigma_1 a_2 - \tfrac{1}{4}\delta_4 a_1^2\cos\gamma_1 + \delta_5 F\cos\gamma_2 &&= 0\\
&\tfrac{1}{2}\mu_2 a_2 - \tfrac{1}{4}\delta_4 a_1^2\sin\gamma_1 - \delta_5 F\sin\gamma_2 &&= 0
\end{aligned} \tag{4.29}$$

The nonlinear algebraic system of equations (4.29) has two possible solutions; namely, the linear solution (a_1=0) and the nonlinear saturation solution ($a_1 \neq 0$). If a_1=0, then

$$a_2 = \pm\sqrt{\frac{\delta_5^2}{\delta_1^2\sigma_1^2 + \frac{1}{4}\mu_2^2}}\ F \tag{4.30}$$

which indicates that the amplitude a_2 of the directly excited mode is proportional to the excitation amplitude F. On the other hand, if $a_1 \neq 0$, it follows from the first two equations in Eqs. (4.29) that

$$a_2 = \pm 2\sqrt{\frac{\delta_1^2(\sigma_1+\sigma_2)^2 + \mu_1^2}{\delta_2^2}} \tag{4.31}$$

which is independent of the excitation amplitude F and

$$\cos\gamma_1 = \frac{2\delta_1}{\delta_2 a_2}(\sigma_1+\sigma_2) \ \text{ and } \ \sin\gamma_1 = -\frac{2\delta_1}{\mu_2 a_2} \tag{4.32}$$

Substituting for $\cos\gamma_1$ and $\sin\gamma_1$ from Eq. (4.32) into the last two equations in Eq. (4.29) and squaring and

adding them, a quadratic equation in a_1^2 is obtained whose solution is given by

$$a_1^2 = \Gamma_1 \pm \sqrt{16\frac{\delta_5^2}{\delta_4^2}F^2 - \Gamma_2^2} \tag{4.33}$$

where

$$\Gamma_1 = \frac{16\delta_1\delta_3}{\delta_2\delta_4}\left[\sigma_1\frac{\sigma_1+\sigma_2}{2} - \frac{\mu_1\mu_2}{4\delta_1\delta_3}\right] \text{ and } \Gamma_2 = \frac{16\delta_1\delta_3}{\delta_2\delta_4}\left[\sigma_1\frac{\mu_1}{2\delta_1} + \frac{\mu_2}{2\delta_3}\frac{\sigma_1+\sigma_2}{2}\right]$$

If $\Gamma_1 > 0$, there are two possible nontrivial solutions, one is stable and the other is unstable, when

$$|\ \frac{\delta_4\Gamma_2}{4\delta_5}\ | \leq F < \sqrt{\Gamma_1^2+\Gamma_2^2}$$

and there is only one nontrivial solution, which is stable, when

$$F \geq \sqrt{\Gamma_1^2+\Gamma_2^2}$$

see Nayfeh and Mook (184) or Nayfeh (185). In the first case, the response depends on the initial conditions. However, if $\Gamma_1 < 0$, there is only one nontrivial solution, which is stable, when

$$F > \sqrt{\Gamma_1^2+\Gamma_2^2}$$

Because the amplitude of $\tilde{\varphi}_0$ is approximately a_2 and that of $\tilde{\vartheta}_0$ is approximately $\Lambda_1 a_1$, Eqs. (4.31) and (4.33) represent the required saturation solution. That is, if the forcing amplitude F exceeds the threshold discussed above, the amplitude a_2 of the directly forced flapping motion saturates and does not increase with any further increase in F. On the other hand, the amplitude of the indirectly excited plunging motion characterized by a_1 increases with increasing F.

4.6 Results and Discussion

This section presents an implementation for the design exploiting the saturation phenomenon on the dynamics of the hawk moth flapping wing whose morphological parameters, as provided by Ellington (57), are given by

$$R = 51.9mm\ ,\ \bar{c} = 18.26mm\ ,\ m_v = 1.648g\ ,\ \frac{m_w}{m_v} = 0.0579 \text{ and } S = 947.8mm^2$$

assuming a rectangular wing, the span-wise center of gravity location r_{cg} is located at $R/2$. In addition, assuming a uniform mass distribution over the wing and that the hinge line passes through the wing center

of gravity (i.e., $d = 0$) and neglecting the wing thickness with respect to the other dimensions, we write the wing's moments of inertia as

$$I_x = \frac{1}{3} m_w R^2, \;\; I_y = \frac{1}{12} m_w \bar{c}^2, \;\; \text{and} \;\; I_z = I_x + I_y$$

The hovering frequency and flapping amplitude of the hawk moth are, respectively, 26 Hz and 60° (57). The pitch angle η_m required for balance at hover, as calculated by Sun and Du (87), is 32°. However, according to Fig. 4.4, a high flapping frequency is required to induce the required energy transfer. Therefore, instead of equipping our mechanism by a variable speed controller to operate at one frequency in hover and another in forward flight, we opted for using the same frequency. Two choices are then available to achieve balance at hover by this high frequency: either reducing the flapping amplitude or reducing the pitching angle η_m. Although the second option might be more aerodynamically efficient, as stated by Taha et al. (42), it is found that the first choice is preferable for the saturation phenomenon to take place. Keeping the pitching angle at 32°, it is found that the required flapping amplitude at hover with the flapping frequency 120 Hz is 15°.

Specifying the flapping frequency at 120 Hz dictates certain values for the natural frequencies ω_1 and ω_2 through Eq. (4.23), which in turn specify the values of K_φ and K_ϑ. On the other hand, to make the saturated value of a_2 small, we choose $\sigma_1 + \sigma_2 = 0$, as indicated in Eq. (4.31). The main objective from incorporating the nonlinear terms $K_1\varphi\vartheta + K_2\dot{\varphi}^2$ is to compensate for the weak quadratic nonlinearities associated with α_2. Knowing that the weights of the linear terms are around unity, it is found that $\alpha_2 = 0.1$ gives satisfactory results. Because α_2 affects only δ_2 and δ_4, the gains k_1 and k_2 are designed to give the same effect of the desired α_2. That is, k_1 and k_2 are determined according to

$$\begin{bmatrix} -(\Lambda_1 + \Lambda_2)\Delta_1 & 2\omega_1\omega_2\Delta_1 \\ -\Lambda_1\Delta_2 & \omega_1^2\Delta_2 \end{bmatrix} \begin{pmatrix} k_1 \\ k_2 \end{pmatrix} = \begin{pmatrix} \delta_{2d} - \delta_{2zg} \\ \delta_{4d} - \delta_{4zg} \end{pmatrix} \tag{4.34}$$

wher $\Delta_n = (\omega_\vartheta^2 - \omega_n^2)\cos^2\eta + \alpha_3$, δ_{jd} is the desired value of δ_j corresponding to the satisfactory α_2, and δ_{jzg} is the value of δ_j at zero gains. Finally, the value of the damping coefficient $b = 0.001\frac{K_\varphi}{\Omega}$ was found to be sufficient.

Figure 4.5 shows the numerical time-integration of the exact dynamics (4.10) of the flapping wing using the above values for the system parameters and the following control torque:

$$\tau = A\cos\Omega t - K_\varphi\varphi - b\dot{\varphi} + K_1\varphi\vartheta + K_2\dot{\varphi}^2 \tag{4.35}$$

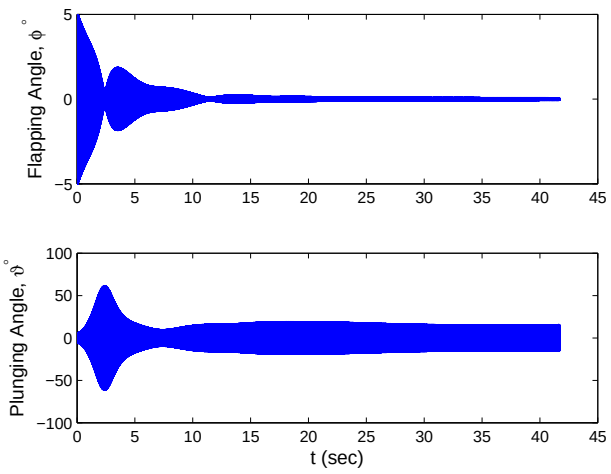

Figure 4.5: A plunging motion of amplitude 15° is obtained by tuning the gains and applying a $0.5N.\mu m$ forcing amplitude.

with the amplitude $A = 2I_xF = 0.5N.\mu m$.

The analytic solution given by Eqs. (4.33) and (4.31) yields almost pure plunging with an amplitude of 15°, which is supported by the simulation shown in Fig. 4.5. This kinematics is considerably suitable for efficient sustained forward flight. Moreover, increasing the level of the forcing amplitude A to $2.0N.\mu m$ doubles the plunging amplitude, while the flapping amplitude is saturated at very small value, as shown in Fig. 4.6. As such, due to the saturation phenomenon, the torque in the direction of the back and forth flapping provides a direct control over the amplitude of the plunging motion. Hence, one can achieve the required level of forward thrust forces and consequently forward speeds. Future work should include the wing-body dynamic interaction; that is, the effect of body dynamics on the saturation phenomenon and the effect of the kinematics associated with the proposed actuation mechanism on the vehicle's stability.

The required kinematics for forward flight (pure plunging) has been produced via exploiting the saturation phenomenon, as shown above. Since the back and forth flapping angle is directly actuated, it is expected to produce the hovering kinematics easily when desired. To do so, it is intuitive to set the gains K_1 and K_2 of the nonlinear terms equal to zero and detune the feedback spring action K_φ from the value corresponding to saturation. Since it is required to have almost a zero flapping offset φ at hover to achieve balance, one has to increase K_φ when detuning from the tuned value. Setting K_φ equal to 10 times the tuned value, keeping the same damping coefficient b, setting K_1 and K_2 equal to zero, and applying a forcing amplitude of $120N.mm$, one can produce the required hovering kinematics, as shown in Fig. 4.7.

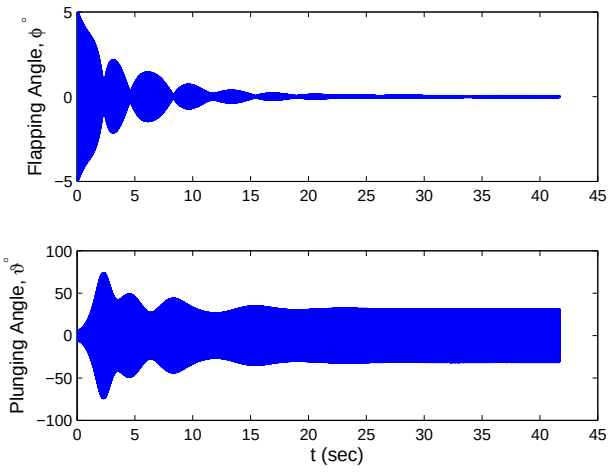

Figure 4.6: A plunging motion of amplitude 30° is obtained by tuning the gains and applying a $2.0N.\mu m$ forcing amplitude.

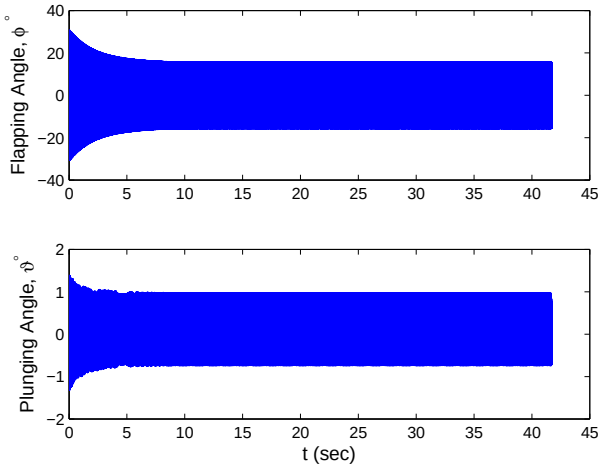

Figure 4.7: Hovering kinematics is obtained by detuning the gains and applying a $120N.mm$ forcing amplitude.

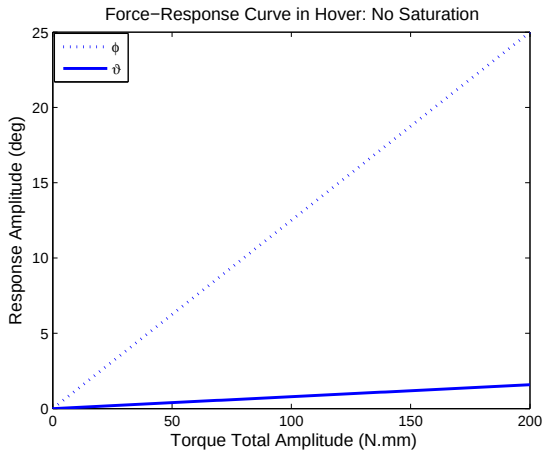

(a) Hovering: the system is away from saturation.

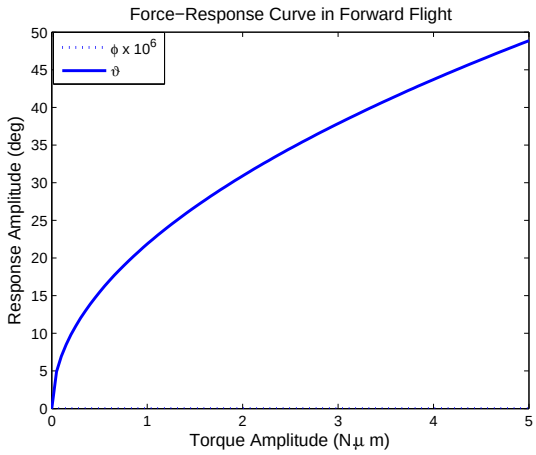

(b) Forward flight: saturation is induced.

Figure 4.8: Force-response curves in both of the hovering and forward flight operating conditions.

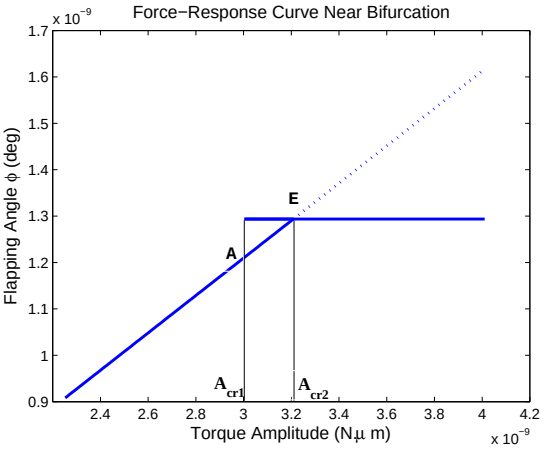

(a) Flapping response.

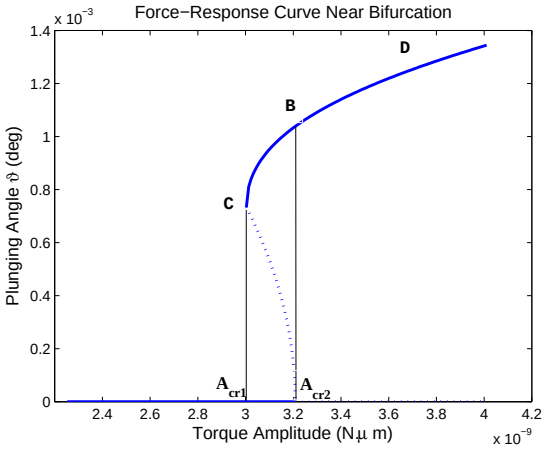

(b) Plunging response.

Figure 4.9: Zoomed-in force-response curves in the saturation case near the bifurcation point: a dotted line indicates an unstable solution while a solid line indicates a stable solution.

Figure 4.8 shows the force-response curves in both hovering and forward flight operating conditions. In the hovering case, where the system is away from saturation, the flapping amplitude varies linearly with the forcing amplitude. Because of the coupling between φ and ϑ in the flapping wing dynamics, see Eq. (4.10), there is a non-zero but small linear amplitude response for the plunging angle ϑ as shown in Fig. 4.8(a). Figure 4.8(b) shows the force-response curve in the forward flight operating condition. Although the system exhibits the saturation phenomenon in this case, the bifurcation is not shown because the system parameters are tuned such that the bifurcation occurs at a very small actuation amplitude. This results in a small saturated amplitude of the back and forth motion.

A zoomed-in version of the force-response curve in the saturation case near the bifurcation point is presented in Fig. 4.9. The dotted line represents an unstable solution while a solid line represents a stable solution. Note that this is the saturation case where the system exhibits jumps and hysteresis due to the subcritical nature of the bifurcation. The analysis presented in Section 4 shows that, for $\Gamma_1 > 0$, two critical values A_{cr1} and A_{cr2} for the forcing amplitude are determined. In addition, in the range between these two limits, two non-zero solutions for a_1 are shown. As the forcing amplitude, A, is increased from zero to A_{cr2}, a_1 remains zero, while a_2 increases linearly with A. When A exceeds A_{cr2}, a_2 assumes a constant value (i.e., saturates), while a_1 jumps to point $\boldsymbol{B}$ and increases along the curve $\boldsymbol{BD}$, as shown in Fig. 4.9(b). Decreasing A from point $\boldsymbol{D}$, a_1 decreases along the curve $\boldsymbol{DBC}$, while a_2 remains constant. When A is decreased further below A_{cr1}, a_1 jumps to zero, while a_2 jumps to the point $\boldsymbol{A}$ on the linear curve, as shown in Fig. 4.9(a). For more details about the types of bifurcations associated with the saturation phenomenon and their characterization by using the normal form, the reader is referred to Nayfeh (185).

One issue that is worth considering is the power requirement in hovering and forward flight. The instantaneous power is written as

$$P(t) = \tau(t)\left(\dot{\varphi}(t) + \dot{\vartheta}(t)\sin\eta\right) \tag{4.36}$$

where τ is given by Eq. (4.35). In the hovering configuration, the maximum peak power is 1.7029 W while the cycle-averaged value is 0.3284 W. In forward flight (15° plunging amplitude), the maximum peak power is 15.0835 W while the cycle-averaged value is 0.0090 W. Since the average power requirements are mainly due to aerodynamic resistance, the hovering configuration requires more average power than the forward flight. However, the peak power is much higher in the forward flight case as would be required to induce saturation.

4.7 Conclusion

Hovering and forward flight of flapping-wing micro-air-vehicles require different kinematics and consequently actuators. Horizontal plane flapping is preferable during hover, while plunging is essential for forward flight. However, it is very difficult to instrument a flapping-wing micro-air-vehicle with more than one actuator due to the stringent weight and size constraints. This work proposes a design for an actuation mechanism that can produce the horizontal motion during hover and, when desired, transfers the wing motion into plunging to perform forward flight using only one actuator. The energy transfer is enabled by exploiting the nonlinear dynamics of the flapping wing to stimulate the saturation phenomenon.

The proposed design of the actuation mechanism makes use of the flapping angle and angular rate feedback that are usually used for adjusting the hovering kinematics of a flapping-wing micro-air-vehicle. In addition, the proposed design requires a physical spring in the plunging direction and a plunging angle feedback. The plunging spring is necessary to create an equilibrium position. As such, expansion of the trigonometric functions of the plunging angle about this equilibrium yields the quadratic nonlinearities essential to induce the saturation phenomenon. The plunging angle feedback is required along with the flapping angle one to create a nonlinear coupling term that compensates for the weak nonlinearities of the governing equations of motion. Because the back and forth flapping angle is directly actuated, the hovering kinematics is achieved easily (tuning the feedback gains away from the saturation requirement.) On the other hand, tuning the gains to induce the saturation phenomenon transfers the motion to the plunging direction and results in saturating the flapping amplitude. That is, any further increase in the forcing amplitude will not lead to an increase in the flapping angle but rather to an increase in the plunging angle. As such, the excitation (forcing) is then providing a direct control over the plunging motion and consequently the forward thrust and speed.

Chapter 5

Aerodynamic-Dynamic Interaction and Longitudinal Flight Dynamics of Hovering MAVs/Insects

In this chapter, the longitudinal flight dynamics of hovering micro-air-vehicles and insects are considered. Section 5.2 presents the dynamic formulation and the used equations of motion. Section 5.3 presents an analytical quasi-steady aerodynamic model that captures the main contributions of the aerodynamic loads due to flapping; i.e., the leading edge vortex and rotational contributions. Knowing that hovering is usually performed at relatively high flapping frequencies relative to the body natural frequencies (this may justify averaging,) Section 5.5 presents the formal statement of the averaging theorem and the averaged dynamics of hovering insets. Section 5.6 presents a more compact aerodynamic model that is sufficient for local stability analysis. Then, the averaging theorem is used to assess the stability of such nonlinear time-periodic system. Section 5.7 provides a characterization for the dynamic stability of hovering insects by performing a parametric study on the cycle-averaged stability derivatives and the eigenvalues of the averaged, linearized system matrix.

5.1 Introduction

Unlike the longitudinal dynamics of conventional aircraft where the two common modes (short period and phugoid) are ubiquitously encountered, the studies discussed in section 1.4 did not reveal similar common modes for the dynamics of hovering insects. Moreover, one can find different studies performed on the same insect using the same aerodynamic and dynamic models and the same stability analysis, yet resulting in considerably different responses, e.g., Sun et al. (11) versus Gao et al. (101). These issues motivate an analytical study for the effects of the system parameters on the stability of hovering insects which, in turn, invokes tight coupling between the dynamic model and an analytical aerodynamic model in which the system parameters appear explicitly.

Flapping flight dynamics has a been a research topic of interest for more than a decade since the studies of Taylor and Thomas (102). Flapping flight dynamics is very rich as it constitutes a multi-body, nonlinear, non-autonomous (time-varying) dynamical system. One ubiquitous assumption about the flapping flight dynamics is to neglect the effect of the wing inertial forces on the body dynamics (2; 15; 16; 26; 7; 24; 9; 25; 186). It should be noted that this assumption is arguable within the flapping flight dynamics community, see Taha et al. (146) for a discussion about the topic. Because the mass of the wing is very small with respect to that of the body, researchers usually accept and utilize this assumption. Doing so, there will not be a multi-body nature for the dynamical system and the dynamics of the vehicle's body will be described by the exact set of equations as the conventional aircraft. However, there is still a major distinction between the nature of the dynamics of flapping flight and that of conventional aircraft. That is, because of the inevitable time-variation of the aerodynamic loads due to the essential oscillatory motion of the flapping wing, flapping flight dynamics constitutes a non-autonomous system. This is in contrast to the autonomous dynamics of conventional aircraft.

Since hovering is usually performed at relatively high frequencies with respect to the body's natural frequencies, it is usually claimed that the body of a hovering insect feels only the cycle-averaged aerodynamic loads. In fact, this is a very common assumption in the analysis of flapping flight dynamics. Some research reports utilize this assumption on the basis of physical intuition (114; 23; 15; 11; 16; 9; 25). Others use its rigorous mathematical representation (7; 24; 2); namely, the averaging theorem. There still exists some debate about the range of validity of this assumption, see Taha et al. (146) for a discussion about the topic. If the averaging assumption is acceptable or the dynamics of the insect under study are amenable to the averaging theorem, then one can convert the time-varying system into an autonomous one (averaged system). Then, stability of the averaged system implies stability of the original nonlinear time-periodic system.

The aerodynamic loads are dictated by the air velocity vector seen by the wing sections. This vector

consists of two components: one due to the flapping kinematics relative to the body and another due to the body motion itself. Hedrick et al. (17) and Faruque and Humbert (18) emphasized the effect of airfoil velocity due to the body motion. Yet, in hovering configurations, where high-frequency flapping and slow or even no body maneuvers exist, it is justifiable to neglect this component and consider only the velocity due to flapping (1; 15; 11; 16; 19; 8; 9; 7). Although this neglection may be justifiable for general aerodynamic and performance analyses at hover, it is quite erroneous when studying the dynamic stability. This is because the inherent (in)stability of any flying vehicle is mainly dictated by the aerodynamic loads due to the vehicle's motion. Hence, the notion of stability derivatives arose, see (13; 187). The stability derivatives are the first-order linear variations of the aerodynamic loads in the body frame due to changes in the state variables of the body dynamics. The notion of stability derivatives for these aerodynamic derivatives is due to their decisive role in determining stability of the motion.

Several experimental (23; 1) and computational (15; 11; 16; 101) investigations have been performed to determine the cycle-averaged stability derivatives for hovering insects and micro-air-vehicles (MAVs). However, there have been few trials that aimed at deriving analytical expressions for the stability derivatives in terms of the system parameters. Cheng and Deng (12) derived the cycle-averaged stability derivatives for hovering insects in terms of their morphological parameters. However, because they did not adopt a specific aerodynamic model, they provided general expressions in terms of the cycle-averaged aerodynamic lift and drag coefficients which, in turn, need to be expressed in terms of the system parameters. Moreover, they did not account for the aerodynamic rotational effects (3), which may considerably affect pitch damping. Also, they considered only one trim configuration at hover which yielded four non-zero longitudinal stability derivatives out of the full nine.

The main contribution of this work is to take into account the effect of the body motion on the aerodynamic loads in a full nonlinear sense. Thus, it provides a tight coupling between the aerodynamic and dynamic models. We use an analytic aerodynamic model that accounts for the dominant contributors (leading edge vortex and rotational effects) to the aerodynamic loads in hovering insects. This model allows the system parameters to appear explicitly in the lift and drag expressions. The obtained model is very useful in simulations, since it is not limited to a small neighborhood around some operating point. In addition, the obtained aerodynamic-dynamic model can be used for nonlinear analyses of the dynamics and control of hovering insects. Then, a formal derivation of the full longitudinal stability derivatives for hovering MAVs/insects is presented. For validation purposes, a numerical simulation for the aerodynamic model is performed over one cycle and a complex-step finite differencing is used to determine the stability derivatives of the hawkmoth using the kinematics and trim data considered by Sun et al. (11) in their direct numerical simulation of Navier-Stokes equations. The effects of trim configuration on the cycle-averaged

stability derivatives are then determined. The averaging theorem is used to analytically assess the stability of this time-periodic system. Finally, a parametric study for the cycle-averaged stability derivatives and the eigenvalues of the averaged, linearized system using the symmetric-flapping trim-configuration is performed.

5.2 Equations of Body Motion

In the present dynamic analysis, only rigid-body degrees of freedom are taken into account and the inertial effects due to the wing motion are neglected. In fact, these assumptions are ubiquitous in the literature of dynamics and control of flapping flight (2; 15; 16; 26; 27; 7; 24; 8; 9; 10; 25). Moreover, the interest here is in the stability of the longitudinal dynamics.

In general, three axis systems are needed to formulate the flight dynamics problem of a rigid flapping MAV. This includes an inertially-fixed frame x_I, y_I, and z_I; a body-fixed frame x_b, y_b, and z_b; and a wing-fixed frame x_w, y_w, and z_w. The x_b-axis points forward, the y_b-axis points to the right wing, and the z_b-axis completes the triad. The Euler angles sequence yaw-pitch-roll $\psi - \theta - \phi$, commonly used with conventional aircraft (13), is also used to describe the body-fixed frame with respect to the inertial frame. Since the interest here is in the longitudinal motion, only one body rotation is considered, namely, the pitching angle θ. The wing-fixed frame is considered to coincide with the body-fixed frame for zero wing kinematic angles. Thus, the sequence of Euler angles $\varphi - \vartheta - \eta$, flapping-plunging-pitching, is used to describe the wing frame with respect to the body frame. Most hovering insects perform a stroke in an approximate horizontal plane without an out-of-plane motion ($\vartheta = 0$) (20; 21). As such and because the aerodynamic loads are expressed in the relative wind frame (normal and tangential to the horizontal flapping velocity), only the kinematic flapping angle φ would be of interest to transfer the aerodynamic loads to the body frame. Figure 2.4 shows a schematic diagram for a flapping MAV whose wing sweeps in a horizontal plane.

Using the above representation, the equations of the longitudinal body motion are written similarly to those of a conventional aircraft (13); that is,

$$\dot{u} = -qw - g\sin\theta + X/m \tag{5.1}$$

$$\dot{w} = qu + g\cos\theta + Z/m \tag{5.2}$$

$$\dot{q} = M/I_y \tag{5.3}$$

$$\dot{\theta} = q \tag{5.4}$$

where m and I_y represent the body mass and moment of inertia about the y_b-axis, respectively; and u, w, q, and θ are the state variables of the longitudinal motion with u and w being the velocity of the body center of mass in the x_b- and z_b-directions, respectively; and θ and q being the pitching angle and angular velocity about the y_b-axis, respectively. The generalized forces X, Z, and M are the aerodynamic forces in the x_b- and z_b-directions and the aerodynamic moment about the y_b-axis, respectively.

5.3 Aerodynamic Modeling

The aerodynamics of flapping flight are characterized by a very complex flow field; that is, an unsteady nonlinear flow field with non-conventional contributors to the aerodynamic forces. Dickinson et al. (3) pointed out that the main contributors are the translatory effect (leading edge vortex effect), the rotational effect, and the effect of wake capture. The latter is very difficult to be modeled analytically. As for the translatory effect, Wang et al. (110) showed that the static lift coefficient for a translating wing, taking into account the leading edge vortex effect, can be fit by $C_L = A \sin 2\alpha$, where α is the angle of attack and A is a constant coefficient that is determined experimentally. Berman and Wang (43) provided values for A for the hawkmoth, bumblebee, and fruitfly. Taha et al. (167; 168) proposed a technique for estimating A taking into account the effect of the aspect ratio. As for the drag coefficient, one could assume a similar representation to the aerodynamic drag on delta wings where the effect of leading edge vortex is pronounced, i.e., $C_D = C_L \tan\alpha = 2A \sin^2\alpha$. The viscous drag is neglected here according to the experiments of Dickinson et al. (3; 79). As for the rotational lift, according to the experimental results of Dickinson et al. (3; 111) and Andersen et al. (5), it is reasonable to use the potential flow result for the two-dimensional rotational circulation

$$\Gamma_{rot} = \pi c^2 \dot{\eta} (\frac{3}{4} - \widehat{x}_0)$$

where c is the airfoil chord length and $\widehat{x}_0$ is the chord-normalized position of the pitch axis from the leading edge.

Using the above representation for the aerodynamic forces, the lift and drag forces per unit span on an airfoil section that is a distance r from the wing root are written as:

$$\ell(r,t) = \frac{1}{2}\rho A c(r) V^2(r,t) \sin 2\alpha(r,t) + \pi\rho(\frac{3}{4} - \widehat{x}_0) V(r,t) c^2(r) \dot{\eta}(t) \tag{5.5}$$

$$d(r,t) = \rho A c(r) V^2(r,t) \sin^2 \alpha(r,t) \tag{5.6}$$

where V is the horizontal velocity of the airfoil section. The aerodynamic pitching moment per unit span about the hinge axis is then given by

$$M_h'(r,t) = \left[\ell(r,t)\cos\eta(t) + sgn(V) d(r,t)\sin\eta(t)\right] \Delta\hat{x} c(r) + \tau_v(r,t) \tag{5.7}$$

where $\Delta\hat{x}$ is the normalized chordwise distance between the center of pressure and the hinge location and τ_v is the viscous rotational damping torque per unit span. The center of pressure is assumed to be located at the quarter chord point. As for τ_v, the formula provided by Berman and Wang (43) is used; that is, $\tau_v = -\frac{\pi}{16}\rho c^4 \left(\mu_1 f + \mu_2 |\dot{\eta}|\right)\dot{\eta}$, where f is the flapping frequency and μ_1 and μ_2 depend on the viscosity of the fluid. Berman and Wang recommended a value of 0.2 for both of them. Note that although τ_v may be too small to be accounted for in this medium-level of fidelity analysis, its inclusion is highly recommended for the stability analysis near hover. This is because the pitch damping plays a very important role in determining the stability and because there exists two counteracting mechanisms for pitch damping and this latter one may help one outweigh the other.

If the effects of body motion on the aerodynamic loads are neglected, the velocity of the airfoil section would just be $V(r,t) = r\dot{\varphi}(t)$, and the angle of attack would be totally determined by the pitching angle according to

$$\alpha_\eta(t) = \begin{cases} \eta, & V > 0 \\ \pi - \eta, & V < 0 \end{cases} \tag{5.8}$$

Integrating Eqs. (5.5-5.7) over the two wing-halves yields the total lift and drag forces and the pitching moment about the hinge axis as

$$L(t) = \frac{1}{2}\rho A I_{21} \dot{\varphi}(t)|\dot{\varphi}(t)| \sin 2\eta(t) + \pi\rho(\frac{3}{4} - \widehat{x}_0) I_{12} \dot{\varphi}(t)\dot{\eta}(t) \tag{5.9}$$

$$D(t) = \rho A I_{21} \dot{\varphi}^2(t) \sin^2\eta(t) \tag{5.10}$$

$$\begin{aligned} M_h(t) = &\left[\rho A I_{22} |\dot{\varphi}(t)|\dot{\varphi}(t)\sin\eta(t) + \pi\rho(\tfrac{3}{4} - \widehat{x}_0) I_{13}\dot{\varphi}(t)\dot{\eta}(t)\cos\eta(t)\right]\Delta\hat{x} + \\ &-\tfrac{\pi}{16}\rho I_{04}\left(\mu_1 f + \mu_2|\dot{\eta}(t)|\right)\dot{\eta}(t) \end{aligned} \tag{5.11}$$

where α_η is the angle of attack induced by the pitching angle and $I_{mn} = 2\int_0^R r^m c^n(r)\,dr$ are weighted

moments of area for the two wing-halves. The generalized forces X, Z, and M are then related to L, D, and M_h via

$$X(t) = -sgn(V)D(t)\cos\varphi(t) \tag{5.12}$$

$$Z(t) = -L(t) \tag{5.13}$$

$$M(t) = M_h(t)\cos\varphi(t) + L(t)x_h + M_{AF}(t) \tag{5.14}$$

where V is assumed positive in the forward (downstroke) direction, x_h is the distance between the vehicle center of mass and the root of the wing hinge line along the x_b-axis, and M_{AF} is the pitching moment due to asymmetric flapping whose distribution per unit span is given by $M'_{AF}(r,t) = \ell(r,t)r\sin\varphi(t)$. Thus, Eqs. (5.1-5.4) are written as

$$\begin{pmatrix} \dot{u} \\ \dot{w} \\ \dot{q} \\ \dot{\theta} \end{pmatrix} = \begin{pmatrix} -qw - g\sin\theta \\ qu + g\cos\theta \\ 0 \\ q \end{pmatrix} + \begin{pmatrix} -\frac{1}{m}D\cos\varphi \\ -\frac{1}{m}L \\ \frac{1}{I_y}M \\ 0 \end{pmatrix} \tag{5.15}$$

or in vector form as $\dot{\boldsymbol{\chi}} = \boldsymbol{f}(\boldsymbol{\chi}) + \boldsymbol{g}_a(\boldsymbol{\chi}, t)$.

5.4 Aerodynamic-Dynamic Interaction

In this section, we consider the aerodynamic loads due to the body motion variables in a full nonlinear sense. The vector field $\boldsymbol{g}_a$ in Eq. (5.15), which represents the aerodynamic loads, must be, in general, a function of the states χ and time. However, the way the aerodynamic loads are represented in Eqs. (5.9-5.11) yields a $\boldsymbol{g}_a$ that is independent of $\boldsymbol{\chi}$. This can be shown by substituting the temporal functions $\varphi(t)$ and $\eta(t)$ into Eqs. (5.9-5.11) to obtain $L(t), D(t)$, and $M(t)$, substituting these loads into Eq. (5.15), and averaging the outcome over the flapping period. it is found that the contribution of $\boldsymbol{g}_a$ to the averaged system is a constant drift and, as such, would not affect the stability analysis at all. Hence, the stability of the flapping MAV would be totally determined by the Hamiltonian vector field $\boldsymbol{f}(\boldsymbol{\chi})$, irrespective of the nature of the aerodynamic loads applied on the vehicle. This is not physically correct as the motion stability of a flying vehicle is mainly determined by the aerodynamic loads due to this motion.

Equations (5.9-5.11) are based on the fact that the velocity seen by the airfoil section is the flapping

velocity, $r\dot{\varphi}$, only; that is, the effect of the body motion on the aerodynamic loads is neglected. This assumption is justified in the analysis of hovering flight where body maneuvers are negligible relative to the flapping motion and, as such, was used in previous investigations (1; 15; 11; 16; 19; 8; 9; 7). However, because the objective here is to analyze the stability of the body motion, the contribution of the body motion to the aerodynamic loads must be taken into consideration. To do so, one should include the effect of the body motion variables on the velocity of the airfoil section and its angle of attack; that is, we write:

$$V = \sqrt{(r\dot{\varphi} + u\cos\varphi)^2 + w^2} \ , \ \ \alpha = \alpha_\eta + \alpha_i \ , \text{ and } \ \dot{\eta} \to \dot{\eta} + q\cos\varphi$$

where $\alpha_i = \tan^{-1}\frac{w - q(r\sin\varphi + x_h)}{V}$ is the angle of attack induced by the body motion. Cheng and Deng (12) have derived the first-order linear variations (stability derivatives) of the aerodynamic loads due to the body motion variables u, w, and q. In this work, the full nonlinear effect is considered. In addition, Cheng and Deng (12) did not account for the rotational lift and, as such, their q-contribution appears only as an induced angle of attack $\frac{q(r\sin\varphi + x_h)}{V}$. This assumption overestimates the pitch damping (known as *flapping counter torque*), since the q-contribution in the rotational lift component results in a negative pitch damping.

Recalling the basic definitions of the lift and drag forces per unit span, Eqs. (5.5,5.6), expanding their trigonometric functions of α around α_η, and keeping up to second-order terms in α_i, we obtain

$$\begin{aligned}\ell(\chi,t;r) = {} & \tfrac{1}{2}\rho A c(r) V^2(\chi,t;r)\left[\sin 2\alpha_\eta(t) + 2\cos\alpha_\eta(t)\alpha_i(\chi;r) - 2\sin 2\alpha_\eta(t)\alpha_i^2(\chi;r)\right] + \\ & + \pi\rho(\tfrac{3}{4} - \widehat{x}_0)c^2(r)V(\chi,t;r)\left[\dot{\eta}(t) + q\cos\varphi(t)\right]\end{aligned} \tag{5.16}$$

$$d(r,t) = \rho A c(r) V^2(\chi,t;r)\left[\sin^2\alpha_\eta(t) + \sin 2\alpha_\eta(t)\alpha_i(\chi;r) + \cos 2\alpha_\eta(t)\alpha_i^2(\chi;r)\right] \tag{5.17}$$

Note that the additional angle of attack, α_i, induced by the body motion would tilt the lift and drag forces so that the X and Z forces per unit span would be given by

$$X' = -sgn(V)HF'\cos\varphi \quad \text{and} \quad Z' = -VF' \tag{5.18}$$

where HF' and VF' are the horizontal (opposing the instantaneous velocity) and vertical (upward) aerodynamic forces per unit span, respectively, which are written as

$$HF' = d\cos\alpha_i - \ell\sin\alpha_i \quad \text{and} \quad VF' = \ell\cos\alpha_i + d\sin\alpha_i$$

Expanding the trigonometric functions of α_i and keeping up to second-order terms in α_i, we obtain

$$\begin{aligned} HF'(\chi,t;r) = \tfrac{1}{2}\rho Ac(r)V^2(\chi,t;r)\left[\sin^2\alpha_\eta(t)(2-\alpha_i^2(\chi;r)) + \sin 2\alpha_\eta(t)\alpha_i(\chi;r)\right] + \\ -\pi\rho(\tfrac{3}{4}-\widehat{x}_0)c^2(r)V(\chi,t;r)\alpha_i(\chi;r)\left[\dot{\eta}(t)+q\cos\varphi(t)\right] \end{aligned} \tag{5.19}$$

$$\begin{aligned} VF'(\chi,t;r) = \tfrac{1}{2}\rho Ac(r)V^2(\chi,t;r)\left[\sin 2\alpha_\eta(t)(1-\tfrac{1}{2}\alpha_i^2(\chi;r)) + 2\cos^2\alpha_\eta(t)\alpha_i(\chi;r)\right] + \\ +\pi\rho(\tfrac{3}{4}-\widehat{x}_0)c^2(r)V(\chi,t;r)\left[\dot{\eta}(t)\left(1-\tfrac{1}{2}\alpha_i^2(\chi;r)\right)+q\cos\varphi(t)\right] \end{aligned} \tag{5.20}$$

The pitching moment per unit span about the y_b-axis is then written as $M' = M'_h\cos\varphi - Z'x_h + M'_{AF}$, where the hinge moment, M'_h, is then given by

$$M'_h(\chi,t;r) = \left[VF'(\chi,t;r)\cos\eta(t) + sgn(V)HF'(\chi,t;r)\sin\eta(t)\right]\Delta\hat{x}c(r) + \tau_v(\chi,t;r)$$

and the pitching moment due to asymmetric flapping is then written as $M'_{AF} = -Z'r\sin\varphi$. Thus, the pitching moment per unit span about the y_b-axis is written as

$$\begin{aligned} M'(\chi,t;r) = -Z'(\chi,t;r)\left[\Delta\hat{x}c(r)\cos\varphi(t)\cos\eta(t) + x_h + r\sin\varphi(t)\right] + \\ -X'(\chi,t;r)\sin\eta(t)\Delta\hat{x}c(r) + \tau_v(\chi,t;r)\cos\varphi \end{aligned} \tag{5.21}$$

The aerodynamic loads (X, Z, and M) are then obtained by substituting Eqs. (5.19,5.20) into Eqs. (5.18,5.24) and integrating the outcome over the wing span. These loads can then be substituted into Eqs. (5.1-5.4) to obtain a tight coupling between the aerodynamic and dynamic models. As such, the obtained model is useful for simulation purposes as it does not rely on a linearization about some trajectory.

The derived model can be made more compact and, hence, more suitable for nonlinear dynamics and control analyses by making the following assumptions. Firstly, assume that $\alpha_i \simeq \frac{w_{eff}}{|V|}$, where $w_{eff} = w - q(r\sin\varphi + x_h)$. This assumption along with the definition of α_η given in Eq. (5.8) allow us to write X', Z', and M' as

$$\begin{aligned} X' = -\cos\varphi\{\tfrac{1}{2}\rho Ac\left[\sin^2\eta\left(2V|V| - w_{eff}^2 sgn(V)\right) + |V|w_{eff}\sin 2\eta\right] + \\ -\pi\rho(\tfrac{3}{4}-\widehat{x}_0)c^2 w_{eff}\left[\dot{\eta}+q\cos\varphi\right]\} \end{aligned} \tag{5.22}$$

$$\begin{aligned} Z' = -\{\tfrac{1}{2}\rho Ac\left[\sin 2\eta\left(V|V| - \tfrac{1}{2}w_{eff}^2 sgn(V)\right) + 2\cos^2\eta(t)|V|w_{eff}\right] + \\ +\pi\rho(\tfrac{3}{4}-\widehat{x}_0)c^2\left[\dot{\eta}\left(V - \tfrac{w_{eff}^2}{2V}\right) + Vq\cos\varphi\right]\} \end{aligned} \tag{5.23}$$

$$
\begin{aligned}
M' = \rho A c \left[\left(V|V| - \tfrac{1}{2} w_{eff}^2 sgn(V) \right) \sin\eta + |V| w_{eff} \cos\eta \right] \left((x_h + r\sin\varphi)\cos\eta + \Delta\hat{x}c\cos\varphi \right) + \\
+\pi\rho(\tfrac{3}{4} - \widehat{x}_0) c^2 \left(\dot{\eta} + q\cos\varphi\right) \left[V(x_h + r\sin\varphi + \Delta\hat{x}c\cos\varphi\cos\eta) - w_{eff}\Delta\hat{x}c\cos\varphi\sin\eta \right] + \\
-\pi\rho(\tfrac{3}{4} - \widehat{x}_0) c^2 \dot{\eta} \tfrac{w_{eff}^2}{2V} (x_h + r\sin\varphi + \Delta\hat{x}c\cos\varphi\cos\eta) + \\
-\tfrac{\pi}{16}\rho c^4 \left(\mu_1 f + \mu_2 |\dot{\eta} + q\cos\varphi|\right) \left(\dot{\eta} + q\cos\varphi\right)\cos\varphi
\end{aligned}
\tag{5.24}
$$

Secondly, assume that

$$
V \simeq r\dot{\varphi} + u\cos\varphi \;\text{ and }\; sgn(V) \simeq sgn(\dot{\varphi})
$$

It should be noted here that, while doing this, we were cautious to include the w^2-contribution in the term $V|V|$. Thirdly, expand $\frac{1}{V}$ in the term $\frac{w_{eff}^2}{2V}$ around $\frac{1}{r\dot{\varphi}}$, which yields

$$
\frac{w_{eff}^2}{2V} \simeq \frac{w_{eff}^2}{2r\dot{\varphi}} \left(1 - \frac{u\cos\varphi}{r\dot{\varphi}} \right) \simeq \frac{w_{eff}^2}{2r\dot{\varphi}}
$$

Considering the above three simplifications, the components of the aerodynamic vector field, $\boldsymbol{g}_a = [g_{a1} \;,\; g_{a2} \;,\; g_{a3} \;,\; 0]^T$, are written as

$$
\begin{aligned}
g_{a1}(\chi,t) = -\tfrac{1}{m}\cos\varphi \{ 2K_{21}\dot{\varphi}|\dot{\varphi}|\sin^2\eta + |\dot{\varphi}| [K_{11} \left(4u\cos\varphi\sin^2\eta + w_h\sin 2\eta \right) + \\
-K_{21} q \sin\varphi \sin 2\eta] + sgn(\dot{\varphi}) [K_{01} \left(2(u^2\cos^2\varphi + w^2)\sin^2\eta + w_h u\cos\varphi\sin 2\eta \right) + \\
-K_{11} uq \sin\varphi\cos\varphi\sin 2\eta - \sin^2\eta \left(K_{01} w_h^2 - 2K_{11} w_h q \sin\varphi + K_{21} q^2 \sin^2\varphi \right)] + \\
-K_{rot_{02}} w_h (\dot{\eta} + q\cos\varphi) + K_{rot_{12}} q \sin\varphi (\dot{\eta} + q\cos\varphi) \}
\end{aligned}
\tag{5.25}
$$

$$
\begin{aligned}
g_{a2}(\chi,t) = -\tfrac{1}{m} \{ K_{21}\dot{\varphi}|\dot{\varphi}|\sin 2\eta + |\dot{\varphi}| [K_{11} \left(2u\cos\varphi\sin 2\eta + 2w_h\cos^2\eta \right) + \\
-2K_{21} q \sin\varphi\cos^2\eta] + sgn(\dot{\varphi}) [K_{01} \left((u^2\cos^2\varphi + w^2)\sin 2\eta + 2w_h u\cos\varphi\cos^2\eta \right) + \\
-K_{11} uq \sin 2\varphi\cos^2\eta - \tfrac{1}{2}\sin 2\eta \left(K_{01} w_h^2 - 2K_{11} w_h q\sin\varphi + K_{21} q^2\sin^2\varphi \right)] + \\
+(\dot{\eta} + q\cos\varphi) [K_{rot_{02}} u\cos\varphi + K_{rot_{12}}\dot{\varphi}] - \tfrac{\dot{\eta}}{2\dot{\varphi}} \left(K_{rot_{-12}} w_h^2 - 2K_{rot_{02}} w_h q\sin\varphi + K_{rot_{12}} q^2\sin^2\varphi \right) \}
\end{aligned}
\tag{5.26}
$$

$$
\begin{aligned}
g_{a3}(\chi,t) = \tfrac{1}{I_y}\{&2\dot{\varphi}|\dot{\varphi}|\sin\eta\left[(K_{21}x_h + K_{31}\sin\varphi)\cos\eta + K_{22}\Delta\hat{x}\cos\varphi\right] + 2|\dot{\varphi}|[(2u\cos\varphi\sin\eta + \\
&+w_h\cos\eta)\left[(K_{11}x_h + K_{21}\sin\varphi)\cos\eta + K_{12}\Delta\hat{x}\cos\varphi\right] - q\sin\varphi\cos\eta\times \\
&\times\left[(K_{21}x_h + K_{31}\sin\varphi)\cos\eta + K_{22}\Delta\hat{x}\cos\varphi\right]] + 2sgn(\dot{\varphi})[((u^2\cos^2\varphi + w^2 - \tfrac{1}{2}w_h^2)\sin\eta + \\
&+uw_h\cos\varphi\cos\eta)\left[(K_{01}x_h + K_{11}\sin\varphi)\cos\eta + K_{02}\Delta\hat{x}\cos\varphi\right] + q\sin\varphi\left(w_h\sin\eta - u\cos\varphi\cos\eta\right)\times \\
&\times\left[(K_{11}x_h + K_{21}\sin\varphi)\cos\eta + K_{12}\Delta\hat{x}\cos\varphi\right] - \tfrac{1}{2}q^2\sin^2\varphi\sin\eta[(K_{21}x_h + K_{31}\sin\varphi)\cos\eta + \\
&+K_{22}\Delta\hat{x}\cos\varphi]] + (\dot{\eta} + q\cos\varphi)[\dot{\varphi}\left[K_{rot_{12}}x_h + K_{rot_{22}}\sin\varphi + K_{rot_{13}}\Delta\hat{x}\cos\varphi\cos\eta\right] + \\
&+u\cos\varphi\left[K_{rot_{02}}x_h + K_{rot_{12}}\sin\varphi + K_{rot_{03}}\Delta\hat{x}\cos\varphi\cos\eta\right] - K_v\cos\varphi\left(\mu_1 f + \mu_2|\dot{\eta} + q\cos\varphi|\right) + \\
&-\Delta\hat{x}\cos\varphi\sin\eta\left(K_{rot_{03}}w_h + K_{rot_{13}}q\right)] - \tfrac{\dot{\eta}}{2\dot{\varphi}}[w_h^2\left(K_{rot_{-12}}x_h + K_{rot_{02}}\sin\varphi + K_{rot_{-13}}\cos\varphi\cos\eta\right) + \\
&-2w_hq\sin\varphi\left(K_{rot_{02}}x_h + K_{rot_{12}}\sin\varphi + K_{rot_{13}}\cos\varphi\cos\eta\right) + \\
&+q^2\sin^2\varphi\left(K_{rot_{12}}x_h + K_{rot_{22}}\sin\varphi + K_{rot_{13}}\cos\varphi\cos\eta\right)]\}
\end{aligned}
\tag{5.27}
$$

where $K_{mn} = \frac{1}{2}\rho A I_{mn}$, $K_{rot_{mn}} = \pi\rho(\frac{1}{2} - \Delta\hat{x})I_{mn}$, $K_v = \frac{\pi}{16}\rho I_{04}$, and $w_h = w - qx_h$. It should be noted that integrals containing r of negative powers must not start from 0 but from an outer section to avoid singularities. This simulates the real case where the wing starts from $r_{inner} = \frac{\varpi}{2}$, where ϖ is the width of the insect abdomen or the MAV body. The expressions of the components of the aerodynamic vector field, given in Eqs. (5.25-5.27), are quite complicated. However, the aerodynamic-dynamic interaction is accounted for in a full nonlinear sense and by substituting these expressions into Eq. (5.15), a full nonlinear non-autonomous model is obtained.

5.5 Averaged Dynamics

Equation (5.15) represents a nonlinear time-periodic (NLTP) system. Two different approaches have been proposed in the literature to investigate the dynamic stability of this NLTP system. The first approach, adopted in the early studies (102; 114; 23; 15; 11; 16), is to use the averaging theorem to obtain a nonlinear time invariant (NLTI) system for which the periodic orbit of the NLTP system is reduced to a fixed point. As such, linearization of the obtained NLTI about this fixed point allows stability analysis of the fixed point. Based on the averaging theorem, if the averaged system has an exponentially stable fixed point, the NLTP system will have an exponentially stable periodic orbit. The second approach, first adopted by Dietl and Garcia (26) and then by Weihua and Cesnik (22), is to use numerical techniques to obtain the periodic solution of the NLTP system. Then, linearization about the obtained periodic orbit yields a linear

time periodic (LTP) system whose stability analysis can be performed using Floquet theory. The Floquet theory dictates solving the LTP system to obtain the state transition matrix (fundamental matrix solution) evaluated at the minimal period, called the monodromy matrix. Then, stability analysis of the periodic orbit is performed by checking the eigenvalues of this monodromy matrix. Dietl and Garcia (26) stated that the first approach, which encompasses averaging of the dynamics, is not suitable for a large ornithopter whose beat frequency is close to the natural frequencies of its body motion. In contrast, Floquet theory is suitable for analyzing the stability of LTP systems, independent of their characteristic time-scales. However, the difficulty in determining the periodic orbit and the corresponding monodromy matrix analytically makes the first approach more suitable when analytical results are required. Since the goal here is to study the effect of system parameters on the dynamic stability of hovering MAVs/insects, the first approach is adopted.

5.5.1 Averaging Theorem

A non-autonomous dynamical system is represented by

$$\dot{\boldsymbol{\chi}} = \epsilon \boldsymbol{f}(\boldsymbol{\chi}, t) \tag{5.28}$$

According to Khalil (117), if $\boldsymbol{f}$ is T-periodic in t, the averaged dynamical system corresponding to Eq. (5.28) is written as

$$\dot{\overline{\boldsymbol{\chi}}} = \epsilon \overline{\boldsymbol{f}}(\overline{\boldsymbol{\chi}}) \tag{5.29}$$

where $\overline{\boldsymbol{f}}(\boldsymbol{\chi}) = \frac{1}{T}\int_0^T \boldsymbol{f}(\boldsymbol{\chi}, \tau)\, d\tau$. According to the averaging theorem:

- If $\boldsymbol{\chi}(0) - \overline{\boldsymbol{\chi}}(0) = O(\epsilon)$, then there exist b and ϵ^* such that $\boldsymbol{\chi}(t) - \overline{\boldsymbol{\chi}}(t) = O(\epsilon)\ \forall t \in [0, b/\epsilon]$ and $\forall \epsilon \in [0,\epsilon^*]$.
- If the origin $\overline{\boldsymbol{\chi}} = 0$ is an exponentially stable equilibrium point of Eq. (5.29) and if $\boldsymbol{\chi}(0) - \overline{\boldsymbol{\chi}}(0) = O(\epsilon)$, then there exists an ϵ^* such that $\boldsymbol{\chi}(t) - \overline{\boldsymbol{\chi}}(t) = O(\epsilon)\ \forall t > 0$ and $\forall \epsilon \in [0,\epsilon^*]$. Moreover, The system (5.28) has a unique, exponentially stable, T-periodic solution $\boldsymbol{\chi}_T(t)$ with the property $\|\boldsymbol{\chi}_T(t)\| \leq k\epsilon$ for some k.

Considering the abstract form of Eq. (5.15); $\dot{\boldsymbol{\chi}} = \boldsymbol{f}(\boldsymbol{\chi}) + \boldsymbol{g}_a(\boldsymbol{\chi}, t)$ and introducing a new time variable $\tau = \omega t$, where ω is the flapping frequency, the dynamics in this new time variable is given by

$$\frac{d\boldsymbol{\chi}}{d\tau} = \frac{1}{\omega}\left(\boldsymbol{f}(\boldsymbol{\chi}) + \boldsymbol{g}_a(\boldsymbol{\chi}, \tau)\right) \tag{5.30}$$

The dynamic equations in the new time variable, Eq. (5.30), have the form of Eq. (5.28), with $\epsilon \equiv \frac{1}{\omega}$, that is amenable to the averaging theorem. Since the averaging theorem is valid in the limit $\epsilon \to 0$, this approach of using the averaging theorem in analyzing the dynamics of flapping flight works well for high flapping frequencies and vice versa.

5.5.2 Application to Hovering MAVs and Insects

Applying the averaging theorem on the NLTP system given by Eq. (5.30) and transform it back to the original time variable, t, the following autonomous system is obtained

$$\dot{\overline{\boldsymbol{\chi}}} = \boldsymbol{f}(\overline{\boldsymbol{\chi}}) + \overline{\boldsymbol{g}}_a(\overline{\boldsymbol{\chi}}) \tag{5.31}$$

where $\overline{\boldsymbol{\chi}}$ is the averaged state vector and $\overline{\boldsymbol{g}}_a(\overline{\boldsymbol{\chi}})$ is the average of the vector field $\boldsymbol{g}_a(\boldsymbol{\chi}, t)$ over the flapping period; i.e., $\overline{\boldsymbol{g}}_a(\overline{\boldsymbol{\chi}}) = \frac{1}{T}\int_0^T \boldsymbol{g}_a(\boldsymbol{\chi}, \tau)\, d\tau$.

The following piecewise constant variation for the η-kinematics is used here

$$\eta(t) = \begin{cases} \alpha_d, & 0 \le t \le T/2 \\ \pi - \alpha_u, & T/2 \le t \le T \end{cases} \tag{5.32}$$

where α_d and α_u are the set angles of attack in the downstroke and upstroke, respectively. The majority of dynamics and control investigations for hovering MAVs assumed fixed pitching angle throughout each half-stroke with an instantaneous flip between the adjacent half-strokes (15; 16; 7; 8; 9; 10; 25). The piecewise continuous variation of the pitching angle is convenient for the minimal actuation concept for flapping MAVs emphasized by Wood (30), Doman et al. (9; 10), and Oppenheimer et al. (8; 25). Substituting the η time-variation, given in Eq. (7.1) and averaging out over a flapping cycle, the cycle-averaged aerodynamic vector field is obtained as

$$\overline{\boldsymbol{g}}_a(\overline{\chi}) = \begin{pmatrix} a_0 + a_1\overline{u} + a_2\overline{w} + a_3\overline{q} + a_4\overline{u}^2 + a_5\overline{w}^2 + a_6\overline{q}^2 + a_7\overline{uw} + a_8\overline{uq} + a_9\overline{wq} \\ b_0 + b_1\overline{u} + b_2\overline{w} + b_3\overline{q} + b_4\overline{u}^2 + b_5\overline{w}^2 + b_6\overline{q}^2 + b_7\overline{uw} + b_8\overline{uq} + b_9\overline{wq} \\ c_0 + c_1\overline{u} + c_2\overline{w} + c_3\overline{q} + c_4\overline{u}^2 + c_5\overline{w}^2 + c_6\overline{q}^2 + c_7\overline{uw} + c_8\overline{uq} + c_9\overline{wq} + c_{10}\overline{q}|\overline{q}| \\ 0 \end{pmatrix} \tag{5.33}$$

where

$a_0 = \frac{-2K_{21}}{mT}\mathcal{I}_{16a}\sin^2\alpha^*$, $a_1 = \frac{-4K_{11}}{mT}\mathcal{I}_{13a}\sin^2\alpha^*$, $a_2 = \frac{-K_{11}}{mT}\mathcal{I}_{10s}\sin 2\alpha^*$

$a_3 = \frac{K_{21}}{mT}\mathcal{I}_{12s}\sin 2\alpha^* - a_2x_h$, $a_4 = \frac{-2K_{01}}{mT}\mathcal{I}_{3a}\sin^2\alpha^*$, $a_5 = \frac{-K_{01}}{mT}\mathcal{I}_{1a}\sin^2\alpha^*$

$a_6 = \frac{K_{21}}{mT}\mathcal{I}_{8a}\sin^2\alpha^* - \frac{K_{rot_{12}}}{mT}\mathcal{I}_{7s} + (a_5x_h - a_9)x_h$, $a_7 = \frac{-K_{01}}{mT}\mathcal{I}_{2s}\sin 2\alpha^*$, $a_8 = \frac{K_{11}}{mT}\mathcal{I}_{7s}\sin 2\alpha^* - a_7x_h$

$a_9 = \frac{-2K_{11}}{mT}\mathcal{I}_{6a}\sin^2\alpha^* + \frac{K_{rot_{02}}}{mT}\mathcal{I}_{2s} + 2a_5x_h$,

$b_0 = \frac{-K_{21}}{mT}\mathcal{I}_{15s}\sin 2\alpha^*$, $b_1 = \frac{-2K_{11}}{mT}\mathcal{I}_{10s}\sin 2\alpha^*$, $b_2 = \frac{-4K_{11}\Phi}{mT}(\cos^2\alpha_d + \cos^2\alpha_u)$

$b_3 = \frac{2K_{21}}{mT}\mathcal{I}_{11a}\cos^2\alpha^* - \frac{K_{rot_{12}}}{mT}\mathcal{I}_{10s} - b_2x_h$, $b_4 = \frac{-K_{01}}{mT}\mathcal{I}_{2s}\sin 2\alpha^*$, $b_5 = \frac{-K_{01}}{4m}(\sin 2\alpha_d + \sin 2\alpha_u)$

$b_6 = \frac{K_{21}}{2mT}\mathcal{I}_{5s}\sin 2\alpha^* + (b_5x_h - b_9)x_h$, $b_7 = \frac{-2K_{01}}{mT}\mathcal{I}_{1a}\cos^2\alpha^*$

$b_8 = \frac{2K_{11}}{mT}\mathcal{I}_{6a}\cos^2\alpha^* - \frac{K_{rot_{02}}}{mT}\mathcal{I}_{2s} - b_7x_h$, $b_9 = \frac{-K_{11}}{mT}\mathcal{I}_{4s}\sin 2\alpha^* + 2b_5x_h$,

$$c_0 = \frac{1}{I_yT}\left[2\Delta\hat{x}K_{22}\mathcal{I}_{16a}\sin\alpha^* + K_{31}\mathcal{I}_{17s}\sin 2\alpha^*\right] - \frac{mx_h}{I_y}b_0 \quad , \quad c_1 = \frac{2}{I_yT}\left[2\Delta\hat{x}K_{12}\mathcal{I}_{13a}\sin\alpha^* + K_{21}\mathcal{I}_{12s}\sin 2\alpha^*\right] - \frac{mx_h}{I_y}b_1 \quad ,$$

$$c_2 = \frac{2}{I_yT}\left[\Delta\hat{x}K_{12}\mathcal{I}_{10s}\cos\alpha^* + K_{21}\mathcal{I}_{11a}\cos^2\alpha^*\right] - \frac{mx_h}{I_y}b_2 \quad ,$$

$$c_3 = \frac{1}{I_yT}\left[\Delta\hat{x}(K_{rot_{13}}\mathcal{I}_{13a}\cos\alpha^* - 2K_{22}\mathcal{I}_{12s}\cos\alpha^*) - 2K_{31}\mathcal{I}_{14a}\cos^2\alpha^* + K_{rot_{22}}\mathcal{I}_{12s}\right] - \frac{K_v\mu_1 f}{I_yT}\mathcal{I}_{2s} - c_2x_h - \frac{mx_h}{I_y}(b_2x_h + b_3) \quad ,$$

$$c_4 = \frac{1}{I_yT}\left[2\Delta\hat{x}K_{02}\mathcal{I}_{3a}\sin\alpha^* + K_{11}\mathcal{I}_{7s}\sin 2\alpha^*\right] - \frac{mx_h}{I_y}b_4 \quad , \quad c_5 = \frac{1}{2I_yT}\left[\Delta\hat{x}K_{02}\mathcal{I}_{1a}\sin\alpha^* + K_{11}\mathcal{I}_{4s}\sin 2\alpha^*\right] - \frac{mx_h}{I_y}b_5 \quad ,$$

$$c_6 = \frac{-1}{I_yT}\left[2\Delta\hat{x}(K_{22}\mathcal{I}_{8a}\sin\alpha^* + K_{rot_{13}}\mathcal{I}_{2s}\sin\alpha^*) + K_{31}\mathcal{I}_{9s}\sin 2\alpha^*\right] + (c_5x_h - c_9)x_h + \frac{mx_h}{I_y}(b_5x_h^2 - b_9x_h - b_6) \quad ,$$

$$c_7 = \frac{2}{I_yT}\left[\Delta\hat{x}K_{02}\mathcal{I}_{1s}\cos\alpha^* + K_{11}\mathcal{I}_{6a}\cos^2\alpha^*\right] - \frac{mx_h}{I_y}b_7 \quad ,$$

$$c_8 = \frac{1}{I_yT}\left[\Delta\hat{x}(K_{rot_{03}}\mathcal{I}_{3a}\cos\alpha^* - 2K_{12}\mathcal{I}_{7s}\cos\alpha^*) + K_{rot_{12}}\mathcal{I}_{7s} - 2K_{21}\mathcal{I}_{8a}\cos^2\alpha^*\right] - c_7x_h - \frac{mx_h}{I_y}(b_7x_h + b_8) \quad ,$$

$$c_9 = \frac{1}{I_yT}\left[\Delta\hat{x}(2K_{12}\mathcal{I}_{6a}\sin\alpha^* - K_{rot_{03}}\mathcal{I}_{2s}\sin\alpha^*) + K_{21}\mathcal{I}_{5s}\sin 2\alpha^*\right] + 2c_5x_h + \frac{mx_h}{I_y}(2b_5x_h - b_9) \text{ and } c_{10} = \frac{-K_v\mu_2}{I_yT}\mathcal{I}_{3s}$$

where

$$\mathfrak{I}_1 = \int \cos\varphi(t)dt, \quad \mathfrak{I}_2 = \int \cos^2\varphi(t)dt, \quad \mathfrak{I}_3 = \int \cos^3\varphi(t)dt, \quad \mathfrak{I}_4 = \int \sin\varphi(t)dt,$$
$$\mathfrak{I}_5 = \int \sin^2\varphi(t)dt, \quad \mathfrak{I}_6 = \int \sin\varphi(t)\cos\varphi(t)dt, \mathfrak{I}_7 = \int \sin\varphi(t)\cos^2\varphi(t)dt, \mathfrak{I}_8 = \int \sin^2\varphi(t)\cos\varphi(t)dt,$$
$$\mathfrak{I}_9 = \int \sin^3\varphi(t)dt, \quad \mathfrak{I}_{10} = \int \dot{\varphi}(t)\cos\varphi(t)dt, \quad \mathfrak{I}_{11} = \int \dot{\varphi}(t)\sin\varphi(t)dt, \quad \mathfrak{I}_{12} = \int \dot{\varphi}(t)\sin\varphi(t)\cos\varphi(t)dt,$$
$$\mathfrak{I}_{13} = \int \dot{\varphi}(t)\cos^2\varphi(t)dt, \mathfrak{I}_{14} = \int \dot{\varphi}(t)\sin^2\varphi(t)dt, \quad \mathfrak{I}_{15} = \int \dot{\varphi}^2(t)dt, \quad \mathfrak{I}_{16} = \int \dot{\varphi}^2(t)\cos\varphi(t)dt,$$
$$\mathfrak{I}_{17} = \int \dot{\varphi}^2(t)\sin\varphi(t)dt$$

and for any $\mathfrak{I}_j$, $\mathfrak{I}_{jd}$ is the integral over the downstroke period ($0 \to T/2$ where $\dot{\varphi} > 0$), $\mathfrak{I}_{ju}$ is the integral over the upstroke period ($T/2 \to T$ where $\dot{\varphi} < 0$), and

$$\mathfrak{I}_{js}\mathcal{F}(\alpha^*) = \mathfrak{I}_{jd}\mathcal{F}(\alpha_d) + \mathfrak{I}_{ju}\mathcal{F}(\alpha_u) \text{ and } \mathfrak{I}_{ja}\mathcal{F}(\alpha^*) = \mathfrak{I}_{jd}\mathcal{F}(\alpha_d) - \mathfrak{I}_{ju}\mathcal{F}(\alpha_u)$$

5.6 Stability Analysis

For the sake of analyzing the flight dynamic stability of hovering insects near hover, the first-order variations of the aerodynamic vector field $\boldsymbol{g}_a$ with respect to the body motion variables $\boldsymbol{\chi}$ are sufficient (i.e., the stability derivatives.) Neglecting the higher-order variations of $\boldsymbol{g}_a$ with respect to $\boldsymbol{\chi}$, the following compact flight dynamic model is obtained

$$\begin{pmatrix} \dot{u}(t) \\ \dot{w}(t) \\ \dot{q}(t) \\ \dot{\theta}(t) \end{pmatrix} = \begin{pmatrix} -q(t)w(t) - g\sin\theta(t) \\ q(t)u(t) + g\cos\theta(t) \\ 0 \\ q(t) \end{pmatrix} + \begin{pmatrix} \frac{1}{m}X_0(t) \\ \frac{1}{m}Z_0(t) \\ \frac{1}{I_y}M_0(t) \\ 0 \end{pmatrix} + \begin{bmatrix} X_u(t) & X_w(t) & X_q(t) & 0 \\ Z_u(t) & Z_w(t) & Z_q(t) & 0 \\ M_u(t) & M_w(t) & M_q(t) & 0 \\ 0 & 0 & 0 & 0 \end{bmatrix} \begin{pmatrix} u(t) \\ w(t) \\ q(t) \\ \theta(t) \end{pmatrix} \tag{5.34}$$

where, assuming piecewise constant variation for the wing pitch angle ($\dot{\eta} = 0$), we write the aerodynamic loads due to the flapping motion of the wing in terms of the system parameters as

$$X_0 = -2K_{21}\dot{\varphi}|\dot{\varphi}|\cos\varphi\sin^2\eta \ , \ \ Z_0 = -K_{21}\dot{\varphi}|\dot{\varphi}|\sin 2\eta$$

$$M_0 = 2\dot{\varphi}|\dot{\varphi}|\sin\eta\left[K_{22}\Delta\hat{x}\cos\varphi + K_{21}x_h\cos\eta + K_{31}\sin\varphi\cos\eta\right]$$

and the time-varying stability derivatives as

$$X_u = -4\tfrac{K_{11}}{m}|\dot{\varphi}|\cos^2\varphi\sin^2\eta,\; X_w = -\tfrac{K_{11}}{m}|\dot{\varphi}|\cos\varphi\sin 2\eta,\; X_q = \tfrac{K_{21}}{m}|\dot{\varphi}|\sin\varphi\cos\varphi\sin 2\eta - x_h X_w$$

$$Z_u = 2X_w, \qquad Z_w = -2\tfrac{K_{11}}{m}|\dot{\varphi}|\cos^2\eta, \qquad Z_q = 2\tfrac{K_{21}}{m}|\dot{\varphi}|\sin\varphi\cos^2\eta - \tfrac{K_{rot_{12}}}{m}\dot{\varphi}\cos\varphi - x_h Z_w$$

$$M_u = 4\tfrac{K_{12}\Delta x}{I_y}|\dot{\varphi}|\cos^2\varphi\sin\eta + \tfrac{m}{I_y}\left(2X_q - x_h Z_u\right)$$

$$M_w = 2\tfrac{K_{12}\Delta x}{I_y}|\dot{\varphi}|\cos\varphi\cos\eta + 2\tfrac{K_{21}}{I_y}|\dot{\varphi}|\sin\varphi\cos^2\eta - \tfrac{mx_h}{I_y}Zw$$

$$M_q = -\tfrac{2\Delta x}{I_y}|\dot{\varphi}|\cos\varphi\cos\eta\left(K_{12}x_h + K_{22}\sin\varphi\right) + \tfrac{1}{I_y}\dot{\varphi}\cos\varphi\left(K_{rot_{13}}\Delta x\cos\varphi\cos\eta + K_{rot_{22}}\sin\varphi\right) +$$

$$-\tfrac{2}{I_y}|\dot{\varphi}|\cos^2\eta\sin\varphi\left(K_{21}x_h + K_{31}\sin\varphi\right) - \tfrac{K_v\mu_1 f}{I_y}\cos^2\varphi - \tfrac{mx_h}{I_y}Z_q$$

The averaged dynamics of Eq. (6.3) is then written as

$$\begin{pmatrix}\dot{\overline{u}}(t)\\ \dot{\overline{w}}(t)\\ \dot{\overline{q}}(t)\\ \dot{\overline{\theta}}(t)\end{pmatrix} = \begin{pmatrix}-\overline{q}(t)\overline{w}(t) - g\sin\overline{\theta}(t)\\ \overline{q}(t)\overline{u}(t) + g\cos\overline{\theta}(t)\\ 0\\ \overline{q}(t)\end{pmatrix} + \begin{pmatrix}\frac{1}{m}\overline{X}_0\\ \frac{1}{m}\overline{Z}_0\\ \frac{1}{I_y}\overline{M}_0\\ 0\end{pmatrix} + \begin{bmatrix}\overline{X}_u & \overline{X}_w & \overline{X}_q & 0\\ \overline{Z}_u & \overline{Z}_w & \overline{Z}_q & 0\\ \overline{M}_u & \overline{M}_w & \overline{M}_q & 0\\ 0 & 0 & 0 & 0\end{bmatrix}\begin{pmatrix}\overline{u}(t)\\ \overline{w}(t)\\ \overline{q}(t)\\ \overline{\theta}(t)\end{pmatrix} \tag{5.35}$$

5.6.1 Trim/Balance of the Averaged System

The advantage of the averaging theorem is that it converts the NLTP system, Eq. (6.3), into an autonomous system, Eq. (7.15). As such, the process of finding the periodic orbit reduces to finding a fixed point of the averaged system. For example, the periodic orbit of the steady hovering configuration corresponds to the origin of the autonomous system in Eq. (7.15). Thus, to find the trim conditions for steady hovering of the MAV/insect, the vector field describing the dynamics of Eq. (7.15) must vanish at the origin, i.e.,

$$\overline{X}_0 = 0 \;\;,\;\; -\overline{Z}_0 = \overline{L}_0 = mg \;\;,\;\; \overline{M}_0 = 0$$

Two approaches can be used to trim MAVs at hover. If symmetric flapping (identical downstroke and upstroke) is used, $\overline{X}_0$ will vanish automatically. This is intuitively expected because symmetric flapping yields zero cycle-averaged forward thrust at hover. However, there might be a non-zero net pitching moment (the cycle-average of the second term of M_0 proportional to x_h). Thus, to make $\overline{M}_0 = 0$, the hinge line needs to be aligned with the vehicle's center of mass ($x_h = 0$). Finally, the condition $\overline{L}_0 = mg$ ensures that the generated averaged lift balances the weight. This dictates a certain combination of flapping amplitude

Φ, frequency $f = \frac{1}{T}$, and mean angle of attack (α_m). For example, if a triangular waveform is used for $\varphi(t)$, $\alpha_m = \frac{1}{2}\sin^{-1}\left(\frac{mgT^2}{8\rho A I_{21}\Phi^2}\right)$. Using a harmonic waveform results in $\alpha_m = \frac{1}{2}\sin^{-1}\left(\frac{mgT^2}{\pi^2\rho A I_{21}\Phi^2}\right)$. This trim approach has been adopted by Doman et al. (9) and Oppenheimer et al. (25). As a second approach, if it is not possible to align the hinge line with the center of mass, one can use asymmetric flapping (with an offset in $\varphi(t)$, referred to as φ_0, and possibly different angles of attack during downstroke and upstroke $\alpha_d \neq \alpha_u$) and solve the three trim conditions to find three of the five controlling parameters $\alpha_d, \alpha_u, \Phi, \varphi_0$ and f. This trim approach has been adopted by Sun and Xiong (15) and Sun et al. (11).

5.6.2 Stability of the Averaged System

After ensuring trim at hover (the origin is a fixed point for the averaged system), the stability of this equilibrium position is investigated. By the statement of the averaging theorem, exponential stability of this fixed point yields exponential stability of the hovering periodic orbit for the original time-varying system. A necessary and sufficient condition for local exponential stability of the origin of Eq. (7.15) is that the Jacobian of its vector field evaluated at the origin be Hurwitz. The Jacobian of the non-dimensional form of the vector field of Eq. (7.15), evaluated at the origin and expressed in the terminology used by (15; 11; 16; 12) is written

$$\begin{bmatrix} \frac{X_u^+}{m^+} & \frac{X_w^+}{m^+} & \frac{X_q^+}{m^+} & -g^+ \\ \frac{Z_u^+}{m^+} & \frac{Z_w^+}{m^+} & \frac{Z_q^+}{m^+} & 0 \\ \frac{M_u^+}{I_y^+} & \frac{M_w^+}{I_y^+} & \frac{M_q^+}{I_y^+} & 0 \\ 0 & 0 & 1 & 0 \end{bmatrix} \tag{5.36}$$

where $m^+ = \frac{m}{\rho S\bar{c}}$, $I_y^+ = \frac{I_y}{\rho S\bar{c}^3}$, $g^+ = \frac{g\bar{c}}{U_2^2}$, and

$$X,Z)_{u,w}^+ = \frac{m(X,Z)_{u,w}}{\rho U_2 S} \;\;,\;\; X,Z)_q^+ = \frac{m(X,Z)_q}{\rho U_2 S\bar{c}} \;\;,\;\; M_{u,w}^+ = \frac{I_y M_{u,w}}{\rho U_2 S c} \;\;,\;\; M_q^+ = \frac{I_y M_q}{\rho U_2 S c^2}$$

where S is the area of one wing, $\bar{c}$ is the mean chord length, and U_2 is the maximum wing speed at the section of the second moment of the wing chord distribution.

The use of the above formulation is validated by comparing the hawkmoth stability results with those of Sun et al. (11) obtained by solving Navier-Stokes equations. The morphological parameters of the hawkmoth are (11; 57)

$$f = 26.3Hz \;\;,\;\; \Phi = 60.5^\circ \;\;,\;\; S = 947.8mm^2 \;\;,\;\; R = 51.9mm \;\;,\;\; \bar{c} = 18.3mm \;\;,\;\; \hat{r}_1 = 0.44 \;\;,\;\; \hat{r}_2 = 0.525$$

$$m = 1.648g \ , \ I_y = 2.08g.cm^2 \ , \ x_h = 0.22R$$

where f is the flapping frequency, Φ is the flapping amplitude, and $\hat{r}_1$ and $\hat{r}_2$ are defined as

$$I_{k1} = 2\int_0^R r^k c(r)\, dr = 2SR^k \hat{r}_k^k$$

Because the insects, in general, do not have zero x_h, Sun et al. adopted the second trim configuration (asymmetric flapping). They considered a horizontal stroke plane flapping with $\varphi(t) = \varphi_0 - \Phi\cos(2\pi f t)$. As for the pitching kinematics, they considered a constant value in each half stroke, referred to as α_d and α_u, except near the beginning and end of each half stroke. During the rotation phase, the η variation is described by

$$\eta(t) = \frac{\Delta\eta}{\Delta t_r}\left[(t - t_r) - \frac{\Delta t_r}{2\pi}\sin\left(\frac{2\pi(t-t_r)}{\Delta t_r}\right)\right] \tag{5.37}$$

where Δt_r is the duration of each rotational phase, and t_r is the time at which this phase starts. Knowing α_d and α_u is enough to determine $\Delta\eta$, since the wing rotates from α_d to $\pi - \alpha_u$ or vice versa. Setting Δt_r equal to $0.25T$, and considering symmetric rotation, t_r can be determined. As for the wing planform, the method of moments used by Ellington (57) is adopted here to obtain a chord-distribution for the insect that matches the documented first two moments $\hat{r}_1$ and $\hat{r}_2$, i.e.,

$$c(r) = \frac{\overline{c}}{\beta}\left(\frac{r}{R}\right)^{P-1}\left(1 - \frac{r}{R}\right)^{Q-1}$$

where

$$P = \hat{r}_1\left[\frac{\hat{r}_1(1-\hat{r}_1)}{\hat{r}_2^2 - \hat{r}_1^2} - 1\right] \ , \ Q = (1-\hat{r}_1)\left[\frac{\hat{r}_1(1-\hat{r}_1)}{\hat{r}_2^2 - \hat{r}_1^2} - 1\right] \ \text{and} \ \beta = \int_0^1 \hat{r}^{P-1}(1-\hat{r})^{Q-1}\, d\hat{r}$$

Sun et al. (11) obtained the following trim parameters

$$\phi_0 = 9^\circ \ , \ \alpha_d = 25.5^\circ \ \text{and} \ \alpha_u = 28^\circ$$

In the present analysis, the exact aerodynamic model, discussed in section 5.3, is used without any approximations. Then, the complex-step finite-difference is used to obtain accurate approximations for the cycle-averaged stability derivatives using the morphological parameters of the hawkmoth and the kinematics used by Sun et al. (11). For example, X_u^+ is calculated as

$$X_u^+ = \frac{1}{\rho U_2 S}\frac{\partial\overline{X}}{\partial u} \ , \ \frac{\partial\overline{X}}{\partial u} = \frac{imag\left(\overline{X}(u+ih)\right)}{h}$$

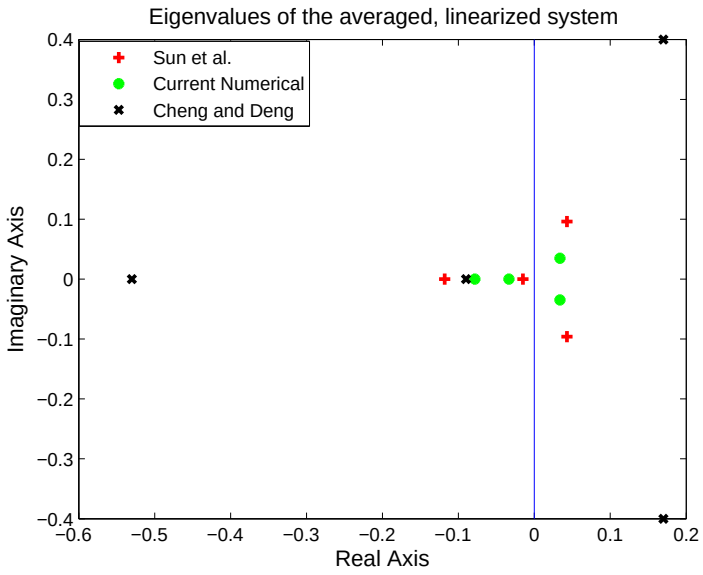

Figure 5.1: Validation of the calculated eigenvalues of the averaged, linearized dynamics of the hawkmoth at hover versus those of Sun et al. (11) and Cheng and Deng (12).

Figure 5.1 shows a comparison between the eigenvalues of the non-dimensional form of the averaged, linearized system matrix, given in Eq. (5.36), using the stability derivatives obtained by complex-step finite-difference and those of Sun et al. (11) and Cheng and Deng (12). Although the adopted aerodynamic model lacks the unsteadiness, it gives a good estimate for the cycle-averaged stability derivatives, as the eigenvalues of the averaged system are much closer to the benchmark results of Sun et al. (11) than those of Cheng and Deng (12). The deviation of the results obtained by Cheng and Deng may be attributed to their neglection of the rotational lift contribution and some of the stability derivatives.

5.7 Stability Characterization

5.7.1 Effect of Trim Configuration

In the previous section, the asymmetric-flapping trim-configuration (AFTC) has been considered. The trim configuration has a considerable effect on the cycle-averaged stability derivatives. If the other trim configuration (symmetric flapping along with zero x_h) is considered, only four derivatives remain non-zero; X_u^+, Z_w^+, M_u^+, and M_q^+. Considering this latter trim configuration, a triangular waveform for the back and forth flapping angle φ, and a piece-wise constant wing pitching angle to maintain a constant angle of attack

Table 5.1: Cycle-averaged stability derivatives for the hawkmoth case study using different kinematics and trim configurations

Trim Configuration	X_u^+	X_w^+	X_q^+	Z_u^+	Z_w^+	Z_q^+	M_u^+	M_w^+	M_q^+
AFTC using kinematics of Sun et al. (11)	-1.31	0.028	-0.021	0.05	-2.14	-0.22	0.05	1.81	-1.90
AFTC using triangular φ and constant α	-1.15	0.028	-0.022	0.06	-2.18	-0.14	0.05	1.82	-2.11
SFTC using triangular φ and constant α	-1.69	0	0	0	-1.53	0	0.13	0	-1.39

α_m, the non-dimensional, cycle-averaged stability derivatives are written in terms of the system parameters as

$$\begin{aligned} X_u^+ &= -4\tfrac{K_{11}}{\rho U_2 ST}(2\Phi + \sin 2\Phi)\sin^2\alpha_m \\ Z_w^+ &= -8\tfrac{K_{11}}{\rho U_2 ST}\Phi\cos^2\alpha_m \\ M_u^+ &= 4\tfrac{K_{12}\Delta x}{\rho U_2 S\bar{c}T}(2\Phi + \sin 2\Phi)\sin\alpha_m \\ M_q^+ &= \tfrac{1}{\rho U_2 ST}(2\Phi + \sin 2\Phi)\left[-2K_{31}\cos^2\alpha_m + K_{rot_{13}}\Delta x\cos\alpha_m - \tfrac{K_v\mu_1}{4\Phi}\right] \end{aligned} \tag{5.38}$$

Table 5.1 presents a comparison between the cycle-averaged stability derivatives for the hawkmoth case study during hover using three sets of kinematics and trim configurations. The first set is the one considered in the previous subsection (AFTC and kinematics used by Sun et al. (11)). The second set includes the AFTC using a triangular waveform and piecewise constant wing pitching angle. The third set includes the symmetric-flapping trim-configuration (SFTC) using triangular waveform and piecewise constant wing pitching angle. Thus, comparison between the first two sets will show the effects of kinematics on the cycle-averaged stability derivatives and comparison between the last two sets will show the effects of trim configuration.

Table 5.1 shows that the waveform does not have a considerable effect on the stability derivatives. It also shows that the SFTC leads to a higher damping X_u^+ in the longitudinal direction. This is because the flapping offset associated with the AFTC decreases the component of any u-perturbation perpendicular to

the leading edge. An analytical investigation using a triangular waveform shows that

$$X_u^+)_{\text{SFTC}} = -4\frac{K_{11}}{\rho U_2 ST}(2\Phi + \sin 2\Phi)\sin^2\alpha_m$$
$$X_u^+)_{\text{AFTC}} = -4\frac{K_{11}}{\rho U_2 ST}(2\Phi + \sin 2\Phi\cos 2\varphi_0)\frac{\sin^2\alpha_d + \sin^2\alpha_u}{2}$$

One should note the $\cos 2\varphi_0$ factor in the expression for the asymmetric flapping case. Also, the speed stability derivative M_u^+ is higher for the SFTC than the asymmetric one because of the same reason. On the other hand, the AFTC leads to higher damping in both of the vertical direction (Z_w^+) and pitching direction (M_q^+). It should be noted that the non-zero x_h associated with the asymmetric-flapping trim-configuration results in a considerable pitch damping. This is because any q-perturbation induces a change in the angle of attack on the wing sections and, consequently the produced lift which, in turn, produces a restoring pitching moment that is proportional to the given perturbation.

5.7.2 Parametric Study

In this section, the SFTC is used with a triangular waveform for the flapping angle $\varphi(t)$ and piecewise constant wing pitching angle η. Using such trim configuration and kinematics, the analytic expressions for the cycle-averaged stability derivatives are provided in Eqs. (5.38) in terms of the system parameters. Exploiting the analytic nature of the current formulation, the effect of the system parameters on these derivatives is assessed. Figure 5.2 shows the variation of the cycle-averaged stability derivatives for the hawkmoth at different mean angles of attack α_m, flapping frequencies f, and hinge locations $\widehat{x}_0$. It includes four sub-figures; each for a different value of $\widehat{x}_0$. Three plots corresponding to different values of f are presented in each sub-figure.

Recalling the non-dimensional Jacobian of the averaged dynamics evaluated at the fixed point, Eq. 5.36, and eliminating the vanishing stability derivatives due to the SFTC, the characteristic polynomial of this Jacobian matrix is given by

$$(\lambda - Z_w^+)[\lambda^3 - (X_u^+ + M_q^+)\lambda^2 + X_u^+ M_q^+\lambda + g^+ X_u^+] \tag{5.39}$$

The negative signs in the analytic expressions of the derivatives X_u^+ and Z_w^+ indicate positive damping in the x_b and z_b directions. As for the rotational damping about the y_b-axis (dictated by the sign of M_q^+), there are three sources of pitch damping. Recall the analytic expression for M_q^+ presented in Eq. (5.38). The first term yields positive pitch damping (flapping counter torque); the one discussed by Cheng and Deng (12). The other two terms were not considered in their work. The second term, which provides a

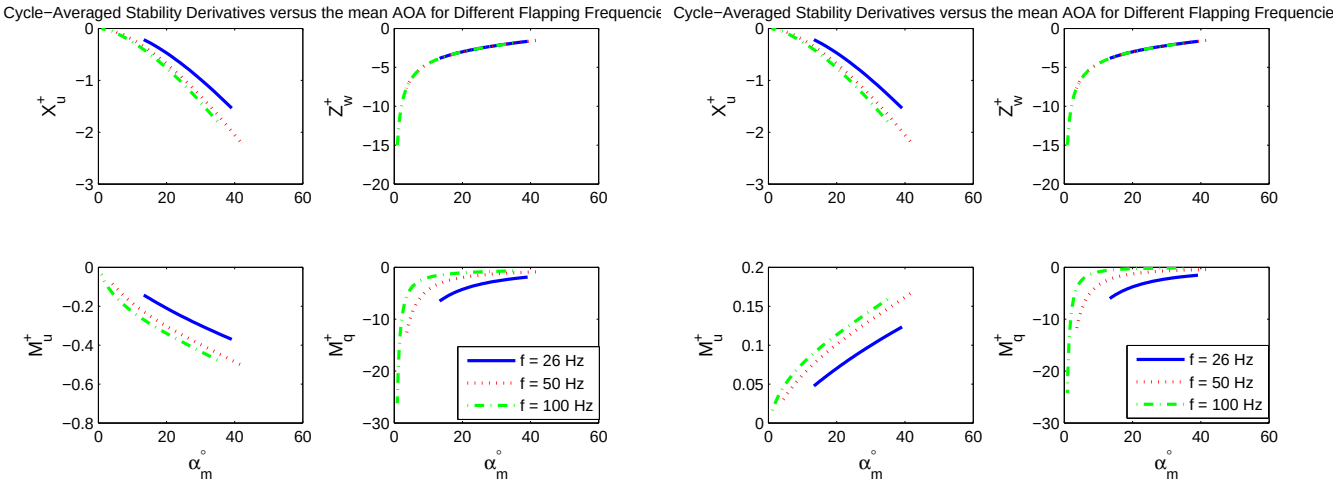

(a) $\widehat{x}_0 = 10\%$ (b) $\widehat{x}_0 = 30\%$

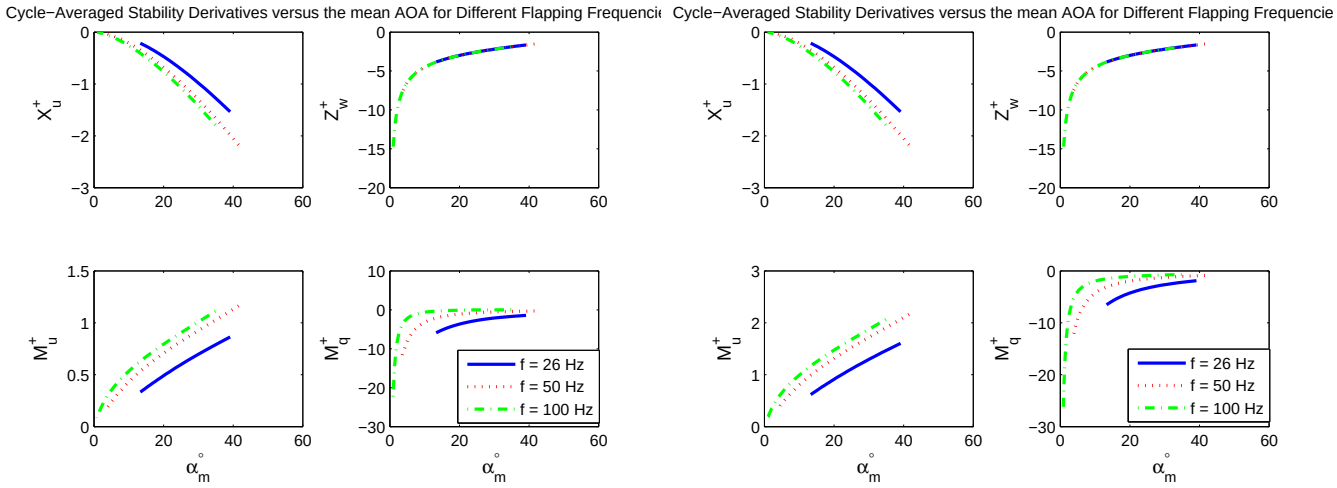

(c) $\widehat{x}_0 = 60\%$ (d) $\widehat{x}_0 = 90\%$

Figure 5.2: Variation of the cycle-averaged stability derivatives for the hawkmoth with the mean angle of attack α_m at different flapping frequencies f and hinge locations $\widehat{x}_0$, using symmetric-flapping trim-configuration, triangular waveform, and piecewise constant wing pitching angle.

negative contribution to the pitch damping, is a result of the induced pitch rate at the wing sections due to q-perturbation. This creates a rotational lift component which may result in a destabilizing pitching moment. Therefore, one should be cautious to include models for almost all the considerable aspects of pitch damping. Hence, a third component is added. This is a viscous component adopted from the model of Berman and Wang (43) and definitely augments the pitch damping. It is noted that the second destabilizing component is proportional to $K_{rot_{13}}\Delta x$ which, in turn is proportional to $(\frac{1}{2} - \Delta x)\Delta x$. Thus, negative Δx (fore hinge locations) or $\Delta x > \frac{1}{2}$ (backward hinge locations far enough from the quarter-chord; center of pressure) results in a stabilizing contribution instead.

It is clear from the characteristic polynomial in Eq. (5.39) that the stability of the motion in the z_b-direction is decoupled from the other motions. In addition, since Z_w^+ is negative, it yields one of the stable eigenvalues. This is similar to the results of Sun et al. (11) where the eigenvector analysis showed decoupling between the w-degree-of-freedom and the other ones. The other three eigenvalues may be analyzed using the Routh-Hurwitz criterion, which requires checking the signs of the sequence $-(X_u^+ + M_q^+), X_u^+ M_q^+ + \frac{g^+ M_u^+}{X_u^+ + M_q^+}$, and $g^+ M_u^+$. They all have to be positive for a stable system. In most cases, the first and the latter are positive but the middle is not, which indicates two unstable poles. Although this trim configuration is characterized by zero pitch stiffness (M_α, or M_w), stability is still achievable via proper damping in all directions and speed stability.

Figure 5.2(a) shows that fore hinge locations lead to speed instability (negative M_u^+), which according to the above stability analysis concludes instability for the averaged system irrespective of the damping values in all directions. This can be explained by looking at the analytic expression for M_u^+ presented in Eq. (5.38). It is noted that M_u^+ is proportional to the chord-normalized distance between the hinge line and the center of pressure along the x_b-axis, Δx. Therefore, unlike conventional aircraft, using the SFTC for hovering MAVs/insects leads to the fact that if the hinge line (coincident with the center of gravity) is ahead of the wing's center of pressure, negative M_u^+ results and, consequently the system is unstable. On the other hand, for all hinge locations behind the center of pressure (located at the quarter-chord), Fig. 5.2 shows positive M_u^+ that increases as α_m and f increase, and increases considerably as the hinge is located further backward. Figure 5.2 also shows that the damping in the longitudinal direction ($-X_u^+$) increases as α_m and f increase. This is because any increase in α_m or f leads to a decrease in the flapping amplitude Φ to maintain balance. Thus, the flapping wing sweeps smaller angles which, in turn, increases both of the components of the u-perturbation perpendicular to the wing leading edge and the resulting wing drag along the x_b-axis. Also, the drag curve slope increases with the operating angle of attack in the range of interest. As for the damping in the vertical direction ($-Z_w^+$), it is independent of the hinge location and frequency. The hinge location affects only the moment derivatives. Z_w^+ is proportional to the flapping speed

$\frac{4\Phi}{T}$, which is fixed upon specifying α_m to achieve balance. Thus, any change in the frequency at a fixed α_m is associated with a change in Φ so as to maintain the same $\frac{\Phi}{T}$, and consequently the same Z_w^+. In addition, the damping in the vertical direction decreases as the mean angle of attack increases. This is because any increase in α_m leads to a considerable decrease in the ratio $\frac{\Phi}{T}$ to maintain balance. Also, the lift curve slope decreases as the operating angle of attack increases. Finally, Fig. 5.2 shows a positive pitch damping for all cases that decreases as α_m and f increase for the same reasons. In addition, there is a sweet range of hinge locations over which a considerable pitch damping is obtained. This range can be specified based on the analytical investigation of M_q^+ contributors, discussed above. This range is for fore hinge locations $\Delta x < 0$ ($\hat{x}_0 < \hat{x}_{cp} = \frac{1}{4}$) or for backward hinge locations far enough from the quarter-chord $\Delta x > \frac{1}{2}$ ($\hat{x}_0 >= \frac{3}{4}$) where the rotational contribution augments the other translatory and viscous contributions for pitch damping.

If the averaging assumption is acceptable, or the system is amenable to the application of the averaging theorem, the current study (due to its analytic formulation) would be useful in determining the effect of the system parameters on the hovering stability. Figure 5.3 includes root locus plots of the characteristic polynomial of the dimensional form of the averaged, linearized system for the hawkmoth for varying mean angles of attack α_m. It includes four sub-figures; each for a different value of hinge location $\widehat{x}_0$. Three root locus plots corresponding to different values of flapping frequency f are presented in each sub-figure. For each combination of α_m and f, a balancing amplitude is calculated to ensure trim. Then, stability is studied around this newly established hovering equilibrium position. The dimensional form of the system is used here to produce more clear plots. Some conclusions can be drawn from these root locus plots. Firstly, increasing the frequency and/or the mean angle of attack has a destabilizing effect, since the above discussion about the variation of the stability derivatives with the system parameters shows a decrease of the pitch damping (crucial in maintaining stability) with α_m and f. It should be noted that according to Taha et al. (42), higher f leads to lower aerodynamic power consumption. However, the above dynamic analysis shows that higher f values lead to a more unstable system. This is a common contradiction between performance and stability found in flight vehicles. Secondly, lack of pitch stability (negative M_u^+) for fore hinge locations explains the instability shown in Fig. 5.3(a) for all values of α_m and f. On the other hand, the relatively weak pitch damping shown in Fig. 5.2(c) may explain the instability shown in Fig. 5.3(c) for all values of α_m and f. Although backward hinge locations far enough from the quarter-chord leads to favorable speed stability and pitch damping as discussed above, the term $X_u^+ M_q^+ + \frac{g^+ M_u^+}{X_u^+ + M_q^+}$, which must be positive for stability, requires some proper combination of the involved stability derivatives. A positive, small enough M_u^+ and a negative, large enough $(X_u^+ + M_q^+)$ must exist for stability to be concluded. Thus, the considerable large values of M_u^+ observed at $\hat{x}_0 = 90\%$, as shown in Fig. 5.2(d), may also explain the instability shown in Fig. 5.3(d) for all values of α_m and f. Thus, small positive values of $\hat{x}_0$ and f, though lead to relatively weak pitch damping, may provide the required combination. Hence, Fig. 5.3(b) shows a narrow region of stability for

the hawkmoth when $\widehat{x}_0 = 30\%$ at low values of η_m (less than 38°) and consequently larger Φ (higher than 62.4°) at the natural $f = 26$ Hz. This region becomes narrower at higher frequencies as expected; $\eta_m < 10°$ ($\Phi > 55.3°$) at $f = 50$ Hz. This observation shows the potential for passive stabilization of hovering MAVs.

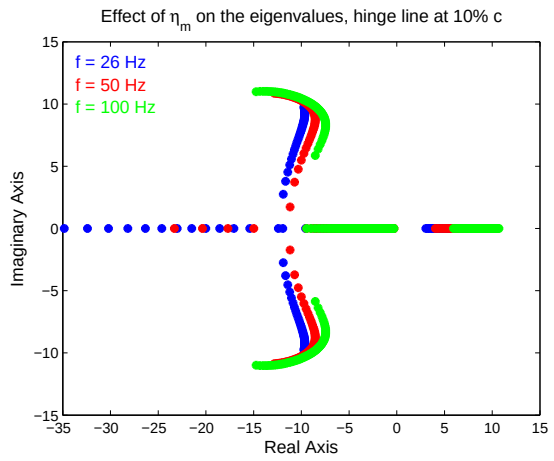

(a) $\widehat{x}_0 = 10\%$

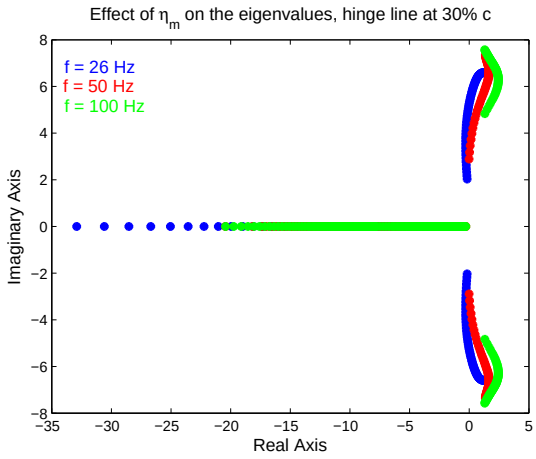

(b) $\widehat{x}_0 = 30\%$

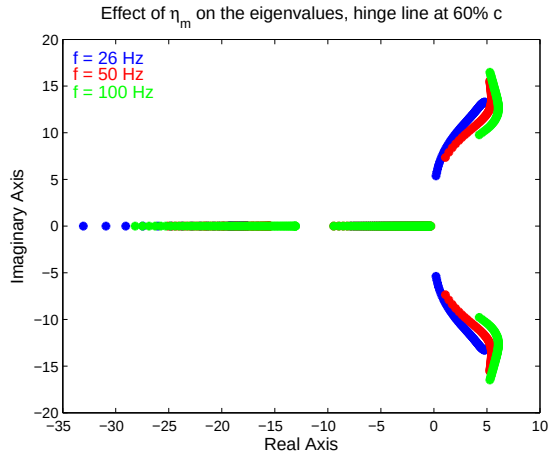

(c) $\widehat{x}_0 = 60\%$

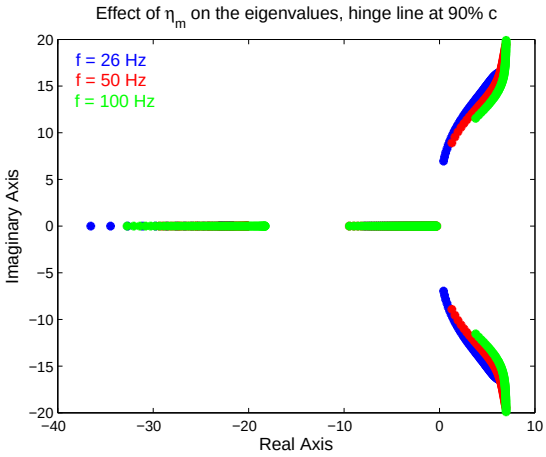

(d) $\widehat{x}_0 = 90\%$

Figure 5.3: Root locus plots of the eigenvalues of the averaged linearized system for varying α_m, f and $\widehat{x}_0$.

5.8 Conclusion

A longitudinal hovering flight dynamics and stability analysis of flapping flight is performed. A quasi-steady aerodynamic model that captures the dominant leading edge vortex and the rotational effects is used to obtain an analytical representation of the flight dynamics. The effects of the body motion variables on the aerodynamic forces is included in a full nonlinear sense. Consequently, the proposed model accounts for the aerodynamic-dynamic interaction essential for investigating dynamics of flying vehicles. Stability derivatives in terms of first order linear variations of the aerodynamic loads due to the body motion variables and the second order nonlinear contributions are derived. The obtained model, though complicated, has a quite wide region of application and, as such, can be used for simulation purposes. The nonlinear nature of the proposed model allows for further nonlinear dynamics and control analyses; e.g., geometric mechanics and control.

A more compact flight dynamic model that is sufficient for local stability analysis is obtained by neglecting the higher-order variations of the aerodynamic loads with respect to the body motion variables. The aerodynamic-dynamic interaction is then validated in terms of the stability results against those obtained via direct numerical simulation of Navier Stokes equations on the hawkmoth wings. Despite of the lack of unsteadiness in the reduced model, a good agreement for the eigenvalues of the averaged, linearized system is obtained. The analytical formulation of the problem has led to some interesting results. Firstly, two approaches are found to trim MAVs at hover. The first one is to flap symmetrically with aligning the hinge line with the vehicle center of gravity. If this alignment is not possible, the MAV has to flap asymmetrically with a prescribed flapping offset angle to satisfy balance at hover. The symmetric-flapping trim-configuration leads to vanishing of five cycle-averaged stability derivatives out of nine. Also, it leads to a higher damping in the longitudinal direction, higher speed stability derivative, and lower damping in both of the vertical and pitching directions. Secondly, increasing the mean angle of attack and/or flapping frequency has similar effects on the stability derivatives; i.e., it leads to a higher damping in the longitudinal direction, higher speed stability derivative, and lower damping in both of the vertical and pitching directions. Thirdly, backward hinge locations are favorable for speed stability. Realizing, via Routh Hurwitz stability analysis, that speed stability is a must to conclude stability for the whole system, fore hinge locations (specifically ahead of the wing's center of pressure) leads to instability of the system irrespective of the values of the other parameters and derivatives. Thus, unlike conventional aircraft, stability of the symmetric-flapping trim-configuration necessitates backward center of gravity position (coincident with the hinge location). Finally, passive stability of the hawkmoth is achievable at lower mean angles of attack and flapping frequencies (higher flapping amplitudes) and hinge locations that are backward and too close to the wing's center of pressure.

Chapter 6

Effects of the Aerodynamic-Induced Parametric Excitation on the Longitudinal Stability of Hovering MAVs/Insects: Necessity of Higher-Order Techniques

In this chapter, we assess the effects of the aerodynamic-induced parametric excitation terms on the longitudinal flight dynamics of hovering micro-air-vehicles and insects. Since, these terms are neglected by the direct application of the averaging theorem. The presented study is used to provide a region of applicability of such a theorem. In Section 6.2, we present the used flight dynamic model. Then, we discuss the shortcomings of the previous approaches (direct averaging and Flouet theorem) in Section 6.3. Section 6.4 provides the approaches we propose to overcome these shortcomings; namely the method of multiple scales and the generalized averaging theorem. Using these approaches, we assess the effects of the aerodynamic-induced parametric excitation on the hovering stability of the hawkmoth in Section 6.5. By considering four other insects, we study the region of applicability of direct averaging in Section 6.6. Finally, we use second-order averaging to show the effects of the interaction between the high-amplitude, periodic aerodynamic-forcing due to the flapping motion of the wing and those due to the body motion in Section 6.7.

6.1 Introduction

The dynamics of flapping flight has been a research topic of interest for more than a decade. In addition to the complex dynamics associated with flapping flight, the periodicity aspect of the flapping motion gives the flapping flight dynamics a time-varying characteristic. Since hovering is usually performed at relatively high frequencies with respect to the body's natural frequencies, it is usually claimed that the body of a hovering insect feels only the cycle-averaged aerodynamic loads. In fact, this is a very common assumption in the analysis of flapping flight dynamics. Some research reports utilize this assumption on the basis of physical intuition (114; 23; 15; 11; 16; 9; 25). Others use its rigorous mathematical representation (7; 24; 2; 186); namely, the averaging theorem. There exist interesting discussions about the range of validity of this assumption in (114; 146). However, there has been no mathematical investigations that rigorously support or refute the direct use of averaging in the stability analysis of hovering insects and micro-air-vehicles (MAVs).

One major issue with the direct application of the averaging theorem is the neglection of the periodic, parametric excitation terms with zero-mean, which may provide a stabilizing action. In fact, this is a proved characteristic of high-frequency, high-amplitude periodic forcing, known as vibrational stabilization, see Bullo (140) and Sarychev (188). One example is the linear, time-periodic Matieu equation, see Nayfeh (179). To assess the effects of these neglected terms and whether they lead to a change in the system's dynamic behavior, one has to take into account the effect of the flow along the non-autonomous vector field comprising these terms. In this work, we assess the validity of the direct application of the averaging theorem to the hovering flight dynamics of flapping MAVs/insects. Particularly, we determine the range of frequency ratios over which this theorem is valid. We use higher order perturbation techniques (namely the method of multiple scales) to determine the effect of the aerodynamic-induced parametric excitation terms on the longitudinal stability of hovering MAVs/insects. In addition, we use second-order averaging to assess the interaction between the high-amplitude aerodynamic periodic forcing due to the flapping motion and the time-periodic dynamics of the system (represented in the time-varying stability derivatives.)

6.2 Flight Dynamic Model

Neglecting the effect of the wing inertial forces, the body dynamics is described by the same set of equations as that of conventional aircraft. That is,

$$\dot{\boldsymbol{x}} = \boldsymbol{f}(\boldsymbol{x}) + \boldsymbol{g}_a(\boldsymbol{x}, t) \tag{6.1}$$

with the exception that the aerodynamic vector field $\boldsymbol{g}_a$ has an explicit time dependance. We focus on longitudinal flight dynamics and use the standard set of body axes (13) to formulate the flight dynamic problem; that is, the x_b-axis points forward, the y_b-axis points to the right wing, and the z_b-axis completes the triad. Then, the vector of state variables is $\boldsymbol{x} = [u, w, q, \theta]^T$, where u and w are the velocity of the body center of mass in the x_b- and z_b-directions, respectively, and θ and q are the pitching angle and angular velocity about the y_b-axis, respectively. Then, Eq. (6.1) is written as

$$\begin{pmatrix} \dot{u} \\ \dot{w} \\ \dot{q} \\ \dot{\theta} \end{pmatrix} = \begin{pmatrix} -qw - g\sin\theta \\ qu + g\cos\theta \\ 0 \\ q \end{pmatrix} + \begin{pmatrix} \frac{1}{m}X(\boldsymbol{x},t) \\ \frac{1}{m}Z(\boldsymbol{x},t) \\ \frac{1}{I_y}M(\boldsymbol{x},t) \\ 0 \end{pmatrix} \tag{6.2}$$

where g is the gravitational acceleration, m and I_y represent the body mass and moment of inertia about the y_b-axis, respectively. The generalized forces X, Z, and M are the aerodynamic forces in the x_b- and z_b-directions and the aerodynamic moment about the y_b-axis, respectively.

The flight dynamic model used in this work was developed in (170) and presented in the previous chapter. Neglecting the higher order dependance of $\boldsymbol{g}_a$ on $\boldsymbol{x}$, we obtain

$$\begin{pmatrix} \dot{u}(t) \\ \dot{w}(t) \\ \dot{q}(t) \\ \dot{\theta}(t) \end{pmatrix} = \begin{pmatrix} -q(t)w(t) - g\sin\theta(t) \\ q(t)u(t) + g\cos\theta(t) \\ 0 \\ q(t) \end{pmatrix} + \begin{pmatrix} \frac{1}{m}X_0(t) \\ \frac{1}{m}Z_0(t) \\ \frac{1}{I_y}M_0(t) \\ 0 \end{pmatrix} + \begin{bmatrix} X_u(t) & X_w(t) & X_q(t) & 0 \\ Z_u(t) & Z_w(t) & Z_q(t) & 0 \\ M_u(t) & M_w(t) & M_q(t) & 0 \\ 0 & 0 & 0 & 0 \end{bmatrix} \begin{pmatrix} u(t) \\ w(t) \\ q(t) \\ \theta(t) \end{pmatrix} \tag{6.3}$$

where, assuming a horizontal stroke plane (parametrized by the back and forth flapping angle φ) and a piecewise constant variation for the wing pitch angle ($\dot{\eta} = 0$), one obtains

$$X_0 = -2K_{21}\dot{\varphi}|\dot{\varphi}|\cos\varphi\sin^2\eta \ , \quad Z_0 = -K_{21}\dot{\varphi}|\dot{\varphi}|\sin 2\eta$$

$$M_0 = 2\dot{\varphi}|\dot{\varphi}|\sin\eta\left[K_{22}\Delta\hat{x}\cos\varphi + K_{21}x_h\cos\eta + K_{31}\sin\varphi\cos\eta\right]$$

where x_h is the distance between the vehicle center of mass and the root of the wing hinge line along the x_b-axis, $\Delta\hat{x}$ is the normalized chordwise distance between the center of pressure and the hinge location, $K_{mn} = \frac{1}{4}\rho C_{L_\alpha} I_{mn}$, ρ is the air density, C_{L_α} is the three-dimensional lift curve slope of the wing, $I_{mn} = 2\int_0^R r^m c^n(r)\,dr$, $c(r)$ is the spanwise chord distribution, and R is the wing radius. The time-varying stability

derivatives are written directly in terms of the system parameters as

$$X_u = -4\frac{K_{11}}{m}|\dot{\varphi}|\cos^2\varphi\sin^2\eta,\ X_w = -\frac{K_{11}}{m}|\dot{\varphi}|\cos\varphi\sin 2\eta,\ X_q = \frac{K_{21}}{m}|\dot{\varphi}|\sin\varphi\cos\varphi\sin 2\eta - x_h X_w$$

$$Z_u = 2X_w, \qquad Z_w = -2\frac{K_{11}}{m}|\dot{\varphi}|\cos^2\eta, \qquad Z_q = 2\frac{K_{21}}{m}|\dot{\varphi}|\sin\varphi\cos^2\eta - \frac{K_{rot_{12}}}{m}\dot{\varphi}\cos\varphi - x_h Z_w$$

$$M_u = 4\frac{K_{12}\Delta x}{I_y}|\dot{\varphi}|\cos^2\varphi\sin\eta + \frac{m}{I_y}(2X_q - x_h Z_u)$$

$$M_w = 2\frac{K_{12}\Delta x}{I_y}|\dot{\varphi}|\cos\varphi\cos\eta + 2\frac{K_{21}}{I_y}|\dot{\varphi}|\sin\varphi\cos^2\eta - \frac{mx_h}{I_y}Zw$$

$$M_q = -\frac{2\Delta x}{I_y}|\dot{\varphi}|\cos\varphi\cos\eta\,(K_{12}x_h + K_{22}\sin\varphi) + \frac{1}{I_y}\dot{\varphi}\cos\varphi\,(K_{rot_{13}}\Delta x\cos\varphi\cos\eta + K_{rot_{22}}\sin\varphi) +$$

$$-\frac{2}{I_y}|\dot{\varphi}|\cos^2\eta\sin\varphi\,(K_{21}x_h + K_{31}\sin\varphi) - \frac{K_v\mu_1 f}{I_y}\cos^2\varphi - \frac{mx_h}{I_y}Z_q$$

where $K_{rot_{mn}} = \pi\rho(\frac{1}{2} - \Delta\hat{x})I_{mn}$ and $K_v = \frac{\pi}{16}\rho I_{04}$.

6.3 Issues With the Previous Approaches

The dynamics of flapping-wing MAVs are represented by a nonlinear, time-periodic (NLTP) system. Stability of such systems is usually performed using either one of two ways as showing in Fig. 6.1. The first approach has been adopted in the early studies either on the basis of physical intuition (114; 23; 15; 11; 16; 9; 25), or on the basis of its rigorous mathematical representation (7; 24; 2). That is to use the averaging theorem to obtain a nonlinear time-invariant (NLTI) system for which the periodic orbit of the NLTP system is reduced to a fixed point. As such, linearization of the obtained NLTI system about this fixed point allows stability analysis of the fixed point. Based on the averaging theorem, if the averaged system has an exponentially stable fixed point, the NLTP system will have an exponentially stable periodic orbit. The second approach, first adopted independently by Dietl and Garcia (26) and Bierling and Patil (189), then by Weihua and Cesnik (22), is to use numerical techniques to obtain the periodic solution of the NLTP system. Then, linearization about the obtained periodic orbit yields a linear time periodic (LTP) system whose stability analysis can be performed using Floquet theorem. Floquet theorem dictates solving the LTP system to obtain the state transition matrix (fundamental matrix solution) evaluated at the minimal period, called the monodromy matrix. Then, stability analysis of the periodic orbit is performed by checking the eigenvalues of this monodromy matrix.

Hovering is usually performed using relatively high flapping frequencies compared to forward flight; flapping frequencies of hovering insects typically fall within the range of 25-250 Hz (57). So, the dynamics of hovering insects exhibit two time scales; a fast time scale for the variation of the aerodynamic loads due to fast flapping, and a slow time scale for the body motion. For example, the insect motion is noticeable

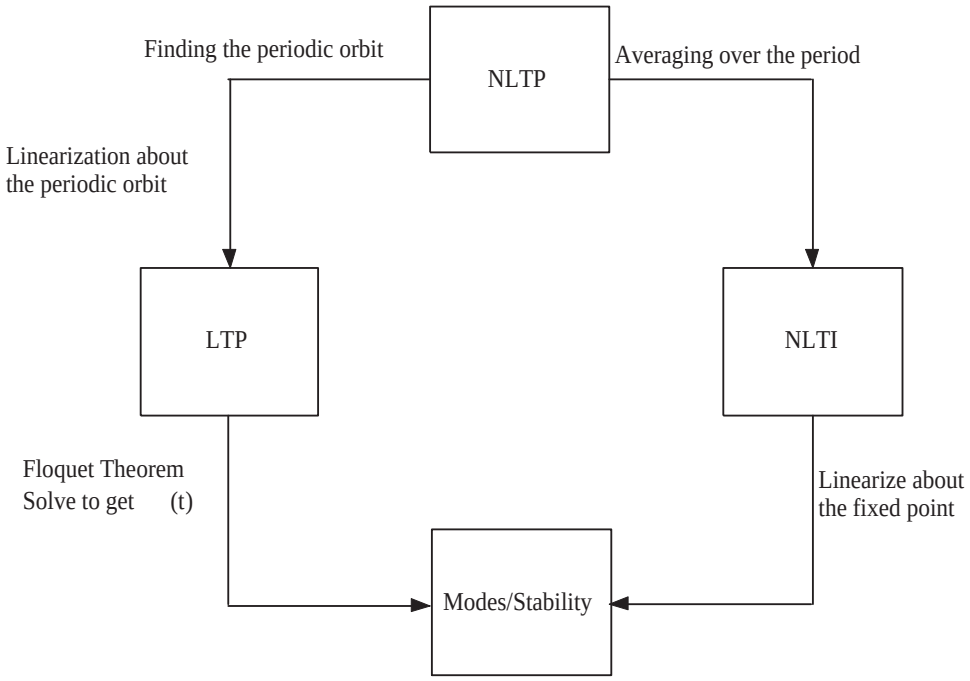

Figure 6.1: The typical two approaches to study the stability of nonlinear, time-periodic systems.

to a human's eye while the motion of its wings is not. Clearly, if the ratio of the two time scales is quite large, averaging may be intuitively justifiable. One great advantage of the second approach incorporating application of Floquet theorem is that it does not depend at all on this ratio; i.e. it is valid irrespective of the time scales of the system dynamics. However, finding the periodic orbit and the application of Floquet theorem (solving for the fundamental matrix solution) is quite difficult to be performed analytically, even for the simplest systems. As such, there will be an unavoidable error because of the numerical nature of its implementation. This error may lead to false conclusions about the stability and dynamics as shown below. In contrast, the other approach incorporating the averaging theorem is very tractable and can be performed analytically for most of the mechanical systems (as well as the non-conventional forces on the system are modeled analytically.) However, it is only valid for large ratios between the two time scales of the system dynamics, as stated above.

This section shows that direct application of the averaging theorem is not sufficient to capture the true stability characteristics of the hovering hawkmoth. In addition, it shows that because of the numerical nature of applying Floquet theorem, it may lead to false conclusions about the system stability. In the following calculations, a triangular waveform for the back and forth flapping angle $\varphi(t)$ and a piecewise constant variation for the pitching angle $\eta(t)$, that maintains a constant angle of attack α_m throughout the entire

stroke, are used.

$$\varphi(t) = \begin{cases} \frac{4\Phi}{T}\left(t - \frac{T}{4}\right), & 0 \le t < \frac{T}{2} \\ -\frac{4\Phi}{T}\left(t - \frac{3T}{4}\right), & \frac{T}{2} \le t < T \end{cases}, \eta(t) = \begin{cases} \alpha_m, & 0 \le t < \frac{T}{2} \\ \pi - \alpha_m, & \frac{T}{2} \le t < T \end{cases} \tag{6.4}$$

It should be noted that this combination of $\varphi(t)$ and $\eta(t)$ yields hovering with minimum aerodynamic power (42). Table 6.1 shows the morphological parameters of the hawkmoth as well as the other insects under study. The hinge line is set at $30\%c$ ($\Delta\hat{x} = 0.05$) and the value of C_{L_α} is calculated based on the wing aspect ratio using the extended lifting theory according to Taha et al. (167; 168).

Insect	$f(Hz)$	Φ°	$S(mm^2)$	$R(mm)$	$\overline{c}(mm)$	$\hat{r}_1$	$\hat{r}_2$	$m(mg)$	$I_y(mg.cm^2)$
Hawkmoth	26.3	60.5	947.8	51.9	18.3	0.440	0.525	1648	2080
Cranefly	45.5	61.5	30.2	12.7	2.38	0.554	0.601	11.4	0.95
Bumblebee	155	58.0	54.9	13.2	4.02	0.490	0.550	175	21.3
Dragonfly	157	54.5	36.9	11.4	3.19	0.481	0.543	68.4	7.0
Hoverfly	160	45.0	20.5	9.3	2.20	0.516	0.570	27.3	1.84

Table 6.1: The morphological parameters for the five studied insects.

The moments of the wing chord distribution $\hat{r}_1$ and $\hat{r}_2$ are defined as

$$I_{k1} = 2\int_0^R r^k c(r)\, dr = 2SR^k \hat{r}_k^k$$

As for the wing planform, the method of moments used by Ellington (57) is adopted here to obtain a chord-distribution for the insect that matches the documented first two moments $\hat{r}_1$ and $\hat{r}_2$, i.e.,

$$c(r) = \frac{\overline{c}}{\beta}\left(\frac{r}{R}\right)^{\alpha-1}\left(1 - \frac{r}{R}\right)^{\gamma-1}$$

where

$$\alpha = \hat{r}_1\left[\frac{\hat{r}_1(1-\hat{r}_1)}{\hat{r}_2^2 - \hat{r}_1^2} - 1\right] \;,\; \gamma = (1-\hat{r}_1)\left[\frac{\hat{r}_1(1-\hat{r}_1)}{\hat{r}_2^2 - \hat{r}_1^2} - 1\right] \text{ and } \beta = \int_0^1 \hat{r}^{\alpha-1}(1-\hat{r})^{\gamma-1}\, d\hat{r}$$

6.3.1 Direct Averaging Approach

A non-autonomous dynamical system is represented by

$$\dot{\boldsymbol{x}} = \epsilon \boldsymbol{Y}(\boldsymbol{x}, t) \tag{6.5}$$

If $\boldsymbol{Y}$ is T-periodic in t, the averaged dynamical system corresponding to Eq. (6.5) is written as

$$\dot{\overline{\boldsymbol{x}}} = \epsilon \overline{\boldsymbol{Y}}(\overline{\boldsymbol{x}}) \tag{6.6}$$

where $\overline{\boldsymbol{Y}}(\boldsymbol{x}) = \frac{1}{T}\int_0^T \boldsymbol{Y}(\boldsymbol{x}, \tau)\, d\tau$. According to the averaging theorem, see Khalil (117) for example, if ϵ is small enough, then exponential stability of the averaged system concludes exponential stability of the original time-periodic system.

Applying the averaging theorem to Eq. (6.1), the averaged dynamics is written as (170)

$$\dot{\overline{\boldsymbol{x}}} = \boldsymbol{f}(\overline{\boldsymbol{x}}) + \overline{\boldsymbol{g}_a}(\overline{\boldsymbol{x}}) \tag{6.7}$$

where $\overline{\boldsymbol{x}}$ is the averaged state vector and $\overline{\boldsymbol{g}_a}(\overline{\boldsymbol{x}})$ is the average of the vector field $\boldsymbol{g}_a(\boldsymbol{x}, t)$ over the flapping period; i.e., $\overline{\boldsymbol{g}_a}(\boldsymbol{x}) = \frac{1}{T}\int_0^T \boldsymbol{g}_a(\boldsymbol{x}, \tau)\, d\tau$.

One of the big advantages of using the averaging approach is its extremely easy trim procedure in comparison to the Floquet theorem approach. For example, if balance/trim at hover is required, the trim problem is stated as follows. What are the flapping parameters $\boldsymbol{P}$ (frequency, amplitude and angle of attack) necessary to ensure $\boldsymbol{f}(\boldsymbol{0}) + \overline{\boldsymbol{g}_a}(\boldsymbol{0}; \boldsymbol{P}) = \boldsymbol{0}$? This is easily answered by solving a set of algebraic equations. In contrast, the trim problem using the Floquet theorem approach is stated as follows. What are the flapping parameters $\boldsymbol{P}$ and the periodic orbit $\boldsymbol{x}^*(t)$ such that $\dot{\boldsymbol{x}^*}(t) = \boldsymbol{f}(\boldsymbol{x}^*(t)) + \boldsymbol{g}_a(\boldsymbol{x}^*(t), t; \boldsymbol{P})$, with $\overline{\boldsymbol{x}^*} = \boldsymbol{0}$? Obviously, it is a much harder question and cannot be solved analytically. It requires a double iteration loop, where the inner one is to capture a periodic orbit corresponding to some set of flapping parameters, and the outer one is to iterate on $\boldsymbol{P}$ to obtain a periodic orbit with zero mean for hovering.

Adopting the averaging approach to achieve balance/trim at hover yields the well-known conditions

$$\overline{X}_0 = 0 \ , \ -\overline{Z}_0 = \overline{L}_0 = mg \ , \ \overline{M}_0 = 0$$

where $\overline{L}_0$ is the cycle-averaged lift force due to flapping. This trim approach leads to the known intuitive facts that symmetric flapping automatically ensures zero cycle-averaged forward thrust force. In addition,

aligning the hinge line to coincide with the vehicle's center of mass ($x_h = 0$) ensures self pitch trim ($\overline{M}_0 = 0$). Then, the hovering vehicle has to flap enough to support its weight. This dictates a certain combination of flapping amplitude Φ, frequency $f = \frac{1}{T}$, and mean angle of attack α_m. For example, if a triangular waveform is used for $\varphi(t)$, $\alpha_m = \frac{1}{2}\sin^{-1}\left(\frac{mgT^2}{4\rho C_{L_\alpha} I_{21} \Phi^2}\right)$, and if a harmonic waveform is used instead, $\alpha_m = \frac{1}{2}\sin^{-1}\left(\frac{2mgT^2}{\pi^2 \rho C_{L_\alpha} I_{21} \Phi^2}\right)$. After ensuring trim at hover (the origin is a fixed point for the averaged system), the stability of this equilibrium position is investigated. By the statement of the averaging theorem, exponential stability of this fixed point yields exponential stability of the hovering periodic orbit for the original time-varying system. A necessary and sufficient condition for local exponential stability of the origin of Eq. (6.7) is that the Jacobian of its vector field evaluated at the origin be Hurwitz.

For the hawkmoth case, the resulting eigenvalues of the averaged, linearized system matrix are

$$0.19 \pm 5.74i \ , \ -11.89 \ , \ -3.30$$

which indicates an unstable system. This approach has been adopted in (114; 23; 15; 11; 16; 100; 115; 12; 170) to assess the stability of flapping dynamics. Similar to the obtained results, almost all of the previous studies concluded instability for hovering flight. Deceivably, simulating the original system (6.3) supports this conclusion, as shown in Fig. 6.2. The states of the system do not oscillate about zero means, but rather deviate from the hovering equilibrium. However, this deviation from the equilibrium is not because of the instability concluded by the averaging theorem. In fact, a deeper look into the dynamics is required. To show that, consider the following example.

Note that the aerodynamic vector field $\boldsymbol{g}_a$ in Eq. (6.2) is written as

$$\boldsymbol{g}_a(\boldsymbol{x}, t) = \boldsymbol{g}_0(t) + [\boldsymbol{G}(t)]\boldsymbol{x}$$

where $\boldsymbol{g}_0$ represents the aerodynamic loads due to the flapping motion of the wing and the matrix $\boldsymbol{G}$ represents the time-varying stability derivatives; i.e., the aerodynamic loads due to body motion. The periodic terms $\boldsymbol{g}_0$ and $\boldsymbol{G}$ can be written as

$$\boldsymbol{g}_0(t) = \overline{\boldsymbol{g}_0} + \boldsymbol{g}_1(t) \ , \ \boldsymbol{G}(t) = \overline{\boldsymbol{G}} + \boldsymbol{G}_1(t)$$

where $\overline{\boldsymbol{g}_0}$ and $\overline{\boldsymbol{G}}$ are the cycle-averaged quantities of $\boldsymbol{g}_0$ and $\boldsymbol{G}$, respectively, while $\boldsymbol{g}_1$ and $\boldsymbol{G}_1$ are the corresponding zero-mean parts, which are mainly neglected by the direct application of the averaging theorem. It should be noted that, because $\boldsymbol{g}_1$ and $\boldsymbol{G}_1$ are of zero-mean, stability analysis by direct application of the averaging theorem yield the same result for the cases where both exist, Eq. (6.3), both do not exist, Eq.

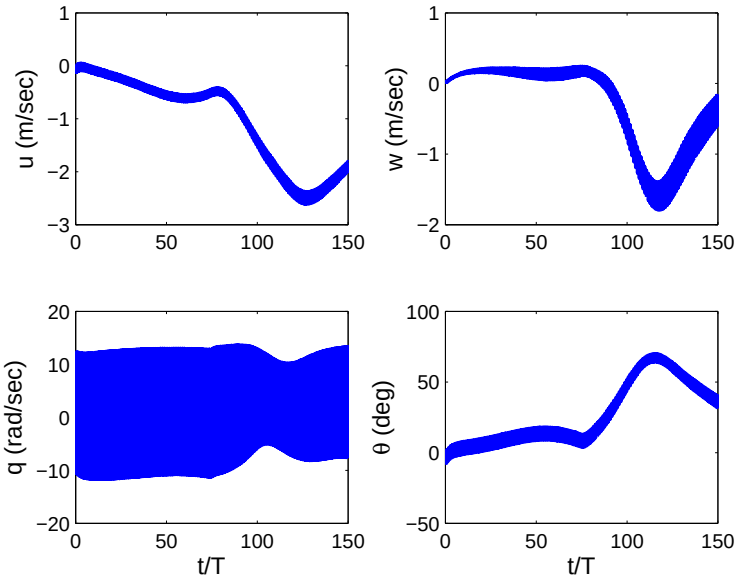

Figure 6.2: Simulation of the nonlinear flight dynamics of the hovering hawkmoth.

(6.7), or one of them exists, such as

$$\dot{\boldsymbol{x}} = \boldsymbol{f}(\boldsymbol{x}) + \overline{\boldsymbol{g}_0} + [\overline{\boldsymbol{G}} + \boldsymbol{G}_1(t)]\boldsymbol{x} \tag{6.8}$$

Firstly, the system represented in Eq. (6.8) has a fixed point at the origin at all times. This is because the above trim procedure (based on the average) yields $\boldsymbol{f}(\boldsymbol{0}) + \overline{\boldsymbol{g}_0} = \boldsymbol{0}$. Secondly, the averaged, linearized version of this system has the exact same eigenvalues as the original system presented in Eq. (6.3); i.e., direct application of the averaging theorem concludes instability too. However, Fig. 6.3 shows that the system (6.8) is stable.

Figure 6.3 shows that direct application of the averaging theorem is not sufficient to analyze the stability of the system (6.8) which, with respect to the averaging theorem, is exactly the same as the original hovering flight dynamics (6.3). Hence, the instability deduced from the simulation shown in Fig. 6.2 is not attributed to the averaging analysis. In addition, Fig. 6.3 shows that the high-frequency periodic signals of the hovering dynamics may provide stabilizing actions. In fact, this is a proved characteristic of high-frequency, high-amplitude periodic forcing, known as vibrational stabilization, see Bullo (140) and Sarychev (188).

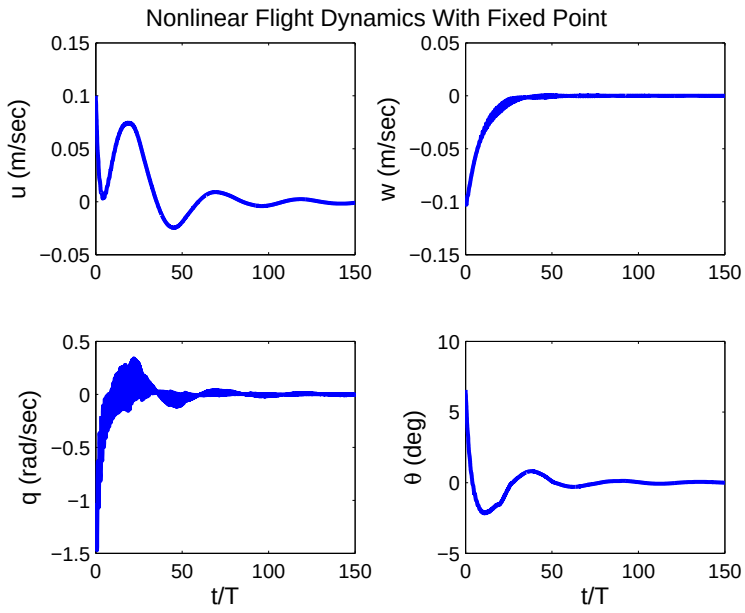

Figure 6.3: Simulation of the nonlinear flight dynamics of the hovering hawkmoth assuming balance (having a fixed point).

6.3.2 Floquet Theorem Approach

It is easier to apply Floquet theorem to the system (6.8) than the system (6.3) because the former has a fixed point representing the equilibrium not a periodic orbit. So, the step of finding the periodic orbit is skipped. Linearizing the system (6.8) about the origin, one obtains

$$\dot{\boldsymbol{x}}(t) = [D\boldsymbol{f}(\boldsymbol{0}) + \overline{\boldsymbol{G}} + \boldsymbol{G}_1(t)]\boldsymbol{x}(t) \tag{6.9}$$

which is a linear, time-periodic system that is amenable to the Floquet theorem. Even in this relatively simple case, Floquet theorem has to be applied numerically. The system (6.9) is simulated due to four independent initial conditions. They are collected in a matrix called $[\boldsymbol{IC}]$. Then, the solution due to all initial conditions are evaluated at the period T. The four obtained vectors are collected in a matrix called $[\boldsymbol{\Xi}]$. The Monodromy matrix is then given by

$$[\boldsymbol{M}] = [\boldsymbol{IC}]^{-1}[\boldsymbol{\Xi}]$$

The eigenvalues of $\boldsymbol{M}$ are called the Floquet multipliers, see Nayfeh and Balachandran (129) for example. If all of the Floquet multipliers lie inside the unit circle, then the origin is an exponentially stable fixed point

for the system (6.9), which concludes exponential stability of the origin of the system (6.8) by Lyaponuv indirect method (117).

Using $[\boldsymbol{IC}] = 0.1[\boldsymbol{II}]$, where $[\boldsymbol{II}]$ represents the identity matrix, and Matlab ode45 solver (adaptive step), the following floquet multipliers are obtained

$$0.78 \pm 0.074i \ , \ 1.0497 \ , \ 0.8887$$

which indicates an unstable system in spite of the stability of the system shown in Fig. 6.3. If a traditional, fixed step (100 points per cycle), fourth-order Runge-Kutta solver is used instead, the following Floquet multipliers are obtained

$$0.96 \pm 0.11i \ , \ 0.6881 \ , \ 0.8889$$

which all lie inside the unit circle and, hence, truly capture the system stability characteristics. Thus, the inevitable error associated with the numerical implementation of Floquet theorem may lead to false conclusion about the system stability. In fact, this is one of the main motivations of this work; is to provide an analytic compact approach that can be robustly used to analyze the flight dynamics of hovering MAVs/insects.

6.4 Proposed Approaches

In this section, we propose two approaches that can be used to assess the effects of the aerodynamic-induced parametric excitation terms that have a zero-mean; terms that are neglected when applying the averaging theorem directly. These are the method of multiple scales and the generalized averaging theorem.

6.4.1 The Method of Multiple Scales

Consider the linearized, time-periodic dynamics in Eq. (6.9) that is written as

$$\dot{\boldsymbol{x}}(t) = [\boldsymbol{A}]\boldsymbol{x}(t) + [\boldsymbol{G}_1(t)]\boldsymbol{x}(t) \tag{6.10}$$

where $\boldsymbol{A} = D\boldsymbol{f}(\boldsymbol{x} = 0) + \overline{\boldsymbol{G}}$ is the system matrix obtained by direct application of the averaging theorem.

To determine the effects of the aerodynamic-induced parametric excitation term $[\boldsymbol{G}_1(t)]\boldsymbol{x}$, we consider the transformation $\boldsymbol{x} = \boldsymbol{P}\boldsymbol{\zeta}$, where $\boldsymbol{P}$ is the invertible matrix constructed from the eigenvectors of the matrix

$\boldsymbol{A}$ as its columns. As such, we write the dynamics of the system in Eq. (6.10) in the new coordinates as

$$\dot{\boldsymbol{\zeta}}(t) = [\boldsymbol{P}^{-1}\boldsymbol{A}\boldsymbol{P}]\boldsymbol{\zeta}(t) + [\boldsymbol{P}^{-1}\boldsymbol{G}_1(t)\boldsymbol{P}]\boldsymbol{\zeta}(t)$$

The diagonal (Jordan diagonal) matrix $\boldsymbol{J} = \boldsymbol{P}^{-1}\boldsymbol{A}\boldsymbol{P}$ can be partitioned into two parts. The first block represents the stable part (having eigenvalues with negative real part) and the second block represents the unstable part. The above equation can be written as

$$\begin{pmatrix} \dot{\boldsymbol{\zeta}}_s(t) \\ \dot{\boldsymbol{\zeta}}_u(t) \end{pmatrix} = \begin{bmatrix} \boldsymbol{J}_s & \boldsymbol{0} \\ \boldsymbol{0} & \boldsymbol{J}_u \end{bmatrix} \begin{pmatrix} \boldsymbol{\zeta}_s(t) \\ \boldsymbol{\zeta}_u(t) \end{pmatrix} + \begin{bmatrix} \boldsymbol{V}_{11}(t) & \boldsymbol{V}_{12}(t) \\ \boldsymbol{V}_{21}(t) & \boldsymbol{V}_{22}(t) \end{bmatrix} \begin{pmatrix} \boldsymbol{\zeta}_s(t) \\ \boldsymbol{\zeta}_u(t) \end{pmatrix} \tag{6.11}$$

Next, we use the method of multiple scales (184; 179) to obtain a second order uniform expansion for Eq. (6.11). We rewrite Eq. (6.11) as

$$\begin{aligned} \dot{\boldsymbol{\zeta}}_s(t) &= [\boldsymbol{J}_s]\boldsymbol{\zeta}_s(t) + \epsilon\left([\boldsymbol{V}_{11}(t)]\boldsymbol{\zeta}_s(t) + [\boldsymbol{V}_{12}(t)]\boldsymbol{\zeta}_u(t)\right) \\ \dot{\boldsymbol{\zeta}}_u(t) &= \epsilon\left([\boldsymbol{V}_{21}(t)]\boldsymbol{\zeta}_s(t) + [\boldsymbol{V}_{22}(t)]\boldsymbol{\zeta}_u(t)\right) + \epsilon^2[\boldsymbol{J}_u]\boldsymbol{\zeta}_u(t) \end{aligned} \tag{6.12}$$

Then, we expand $\boldsymbol{\zeta}_s$ and $\boldsymbol{\zeta}_u$ as

$$\boldsymbol{\zeta}_{s,u}(T_0, T_2) = \boldsymbol{\zeta}_{s,u_0}(T_0, T_2) + \epsilon\boldsymbol{\zeta}_{s,u_1}(T_0, T_2) + \epsilon^2\boldsymbol{\zeta}_{s,u_2}(T_0, T_2) + ... \tag{6.13}$$

where ϵ is a bookkeeping parameter, $T_n = \epsilon^n t$ and

$$\frac{d}{dt} = D_0 + \epsilon D_1 + \epsilon^2 D_2 + ... \tag{6.14}$$

where $D_n = \frac{\partial}{\partial T_n}$. Substituting Eqs. (6.13) and (6.14) into Eq. (6.12) and separating coefficients of like powers of ϵ, we obtain three sets of equations, which can be solved successively.

The first set is expressed as

$$\begin{aligned} D_0\boldsymbol{\zeta}_{s_0} &= [\boldsymbol{J}_s]\boldsymbol{\zeta}_{s_0} \\ D_0\boldsymbol{\zeta}_{u_0} &= 0 \end{aligned} \tag{6.15}$$

Since $\boldsymbol{J}_s$ is a Hurwitz matrix, $\boldsymbol{\zeta}_{s_0}$ will exponentially decay to a zero steady state value. On the other hand,

$\boldsymbol{\zeta}_{u_0} = \boldsymbol{\zeta}_{u_0}(T_2)$. The second set of equations is given by

$$\begin{aligned} D_0\boldsymbol{\zeta}_{s_1} + D_1\boldsymbol{\zeta}_{s_0} &= [\boldsymbol{J}_s]\boldsymbol{\zeta}_{s_1} + [\boldsymbol{V}_{11}(T_0)]\boldsymbol{\zeta}_{s_0} + [\boldsymbol{V}_{12}(T_0)]\boldsymbol{\zeta}_{u_0} \\ D_0\boldsymbol{\zeta}_{u_1} + D_1\boldsymbol{\zeta}_{u_0} &= [\boldsymbol{V}_{21}(T_0)]\boldsymbol{\zeta}_{s_0} + [\boldsymbol{V}_{22}(T_0)]\boldsymbol{\zeta}_{u_0} \end{aligned} \tag{6.16}$$

Since $[\boldsymbol{V}_{12}(T_0)]$ is periodic in T_0, it can be represented in Fourier series as

$$[\boldsymbol{V}_{12}(T_0)] = \Re\left(\sum_n [\overline{\boldsymbol{V}_{12}}]_n e^{in\omega T_0}\right)$$

where $[\overline{\boldsymbol{V}_{12}}]_n$ is a matrix of complex entries. Thus, the steady state solution of Eq. (6.16) is written as

$$\begin{aligned} \boldsymbol{\zeta}_{s_1}(T_0, T_2) &= \Re\left(\sum_n \mathcal{Z}_n e^{in\omega T_0}\right) \\ \boldsymbol{\zeta}_{u_1}(T_0, T_2) &= \int_0^{T_0} [\boldsymbol{V}_{22}(\tau)]\, d\tau \boldsymbol{\zeta}_{u_0}(T_2) \end{aligned} \tag{6.17}$$

where $\mathcal{Z}_n = [i\omega_n I - A]^{-1}[\overline{\boldsymbol{V}_{12}}]_n \boldsymbol{\zeta}_{u_0}$. Finally, the third set is given by

$$\begin{aligned} D_0\boldsymbol{\zeta}_{s_2} + D_1\boldsymbol{\zeta}_{s_1} + D_2\boldsymbol{\zeta}_{s_0} &= [\boldsymbol{J}_s]\boldsymbol{\zeta}_{s_2} + [\boldsymbol{V}_{11}]\boldsymbol{\zeta}_{s_1} + [\boldsymbol{V}_{12}]\boldsymbol{\zeta}_{u_1} \\ D_0\boldsymbol{\zeta}_{u_2} + D_1\boldsymbol{\zeta}_{u_1} + D_2\boldsymbol{\zeta}_{u_0} &= [\boldsymbol{V}_{21}]\boldsymbol{\zeta}_{s_1} + [\boldsymbol{V}_{22}]\boldsymbol{\zeta}_{u_1} + [\boldsymbol{J}_u]\boldsymbol{\zeta}_{u_0} \end{aligned} \tag{6.18}$$

The first system ($\boldsymbol{\zeta}_{s_2}$-dynamics) is a stable autonomous system that is subjected to periodic forcing. Thus, $\boldsymbol{\zeta}_{s_2}$ will not diverge. On the other hand, the second system ($\boldsymbol{\zeta}_{u_2}$-dynamics) has trivial dynamics and is also subjected to periodic forcing. Thus, to have a bounded solution, the sum of all of the T_0-independent terms must vanish. As such, we obtain the following solvability condition

$$\boldsymbol{\zeta'}_{u0}(T_2) = \frac{1}{T}\int_0^T \left\{[\boldsymbol{V}_{21}(t)]\boldsymbol{\zeta}_{s_1}(t, T_2) + [\boldsymbol{V}_{22}(t)]\boldsymbol{\zeta}_{u_1}(t, T_2)\right\} dt + [\boldsymbol{J}_u]\boldsymbol{\zeta}_{u_0}(T_2) \tag{6.19}$$

where $\boldsymbol{\zeta'}_{u0} = \frac{d\boldsymbol{\zeta}_{u0}}{dT_2}$. The above equation represents a linear time-invariant system for $\boldsymbol{\zeta}_{u_2}$. Hence, the matrix

$$[\boldsymbol{B}_{\text{MMS}}] = \left[\frac{1}{T}\int_0^T \left\{[\boldsymbol{V}_{21}(t)]\Re\left(\sum_n [i\omega_n I - \boldsymbol{J}_s]^{-1}[\overline{\boldsymbol{V}_{12}}]_n e^{in\omega t}\right) + [\boldsymbol{V}_{22}(t)]\int_0^t [\boldsymbol{V}_{22}(\tau)]\, d\tau\right\} dt + \boldsymbol{J}_u\right] \tag{6.20}$$

must be Hurwitz for stability.

6.4.2 The Generalized Averaging Theorem

While direct averaging is valid only for weakly forced systems or very high-frequency forcing, the generalized averaging theory (GAT) can be applied successfully to high-amplitude periodic forcing, because it provides an arbitrarily higher-order approximation to the flow along the time-periodic vector field. In addition, unlike the Floquet theorem approach, the GAT provides a compact way of analyzing nonlinear time-periodic systems. Thus, it can be used analytically and, hence, avoids any numerical errors. In fact, the analytical tractability allows better understanding of the system dynamics as shown below.

Agrachev and Gamkrelidze have laid the foundation for the GAT in their seminal work (190). A solution to the non-autonomous differential equation (6.5) with $\boldsymbol{x}(0) = \boldsymbol{x}_0$ can be written using the Volterra series expansion as

$$\boldsymbol{x}(t) = \boldsymbol{x}_0 + \sum_{m=1}^{\infty} \int_0^t \int_0^{\tau_1} ... \int_0^{\tau_{m-1}} \left(\boldsymbol{Y}_{\tau_1} \circ \boldsymbol{Y}_{\tau_2} \circ ... \circ \boldsymbol{Y}_{\tau_m}\right)(\boldsymbol{x}_0) d\tau_m ... d\tau_1 \tag{6.21}$$

where $\boldsymbol{Y}_\tau = \boldsymbol{Y}(., \tau)$ and $\circ$ is the composition between maps, i.e., $\left(\boldsymbol{Y}_{\tau_1} \circ \boldsymbol{Y}_{\tau_2}\right)(\boldsymbol{x}) = \boldsymbol{Y}_{\tau_1}(\boldsymbol{Y}_{\tau_2}(\boldsymbol{x}))$. Agrachev and Gamkrelidze have provided the conditions of convergence of the series presented in Eq. (6.21). Similar to the exponential representation of solutions to autonomous differential equations, Agrachev and Gamkrelidze have denoted the flow of the non-autonomous vector field $\boldsymbol{Y}_\tau$ as $\overrightarrow{\exp}\left(\int_0^t \boldsymbol{Y}_\tau d\tau\right)$ and called it the *chronological exponential*. They, then, have defined the *logarithm* of this exponential map as

$$\boldsymbol{V}_t = \ln \ \overrightarrow{\exp}\left(\int_0^t \boldsymbol{Y}_\tau \mathrm{d}\tau\right)$$

That is, the flow along the autonomous vector field $\boldsymbol{V}_t$ for a unit time is equivalent to the flow along the non-autonomous vector field $\boldsymbol{Y}_\tau$ for a time t. Although $\boldsymbol{V}_t$ is an autonomous vector field, it is parametrized by time; i.e., if the final time t is changed, the vector field will change. Agrachev and Gamkrelidze have shown that $\boldsymbol{V}_t = \sum_{m=1}^{\infty} \boldsymbol{V}_t^{(m)}$ where

$$\boldsymbol{V}_t^{(m)} = \int_0^t \int_0^{\tau_1} ... \int_0^{\tau_{m-1}} \mathcal{G}_m(\boldsymbol{Y}_{\tau_1}, ..., \boldsymbol{Y}_{\tau_m}) d\tau_m ... d\tau_1$$

and $\mathcal{G}_m$ are commutator polynomials. The first three polynomials are written as

$$\mathcal{G}_1(\zeta_1) = \zeta_1 \ , \ \mathcal{G}_2(\zeta_1, \zeta_2) = \frac{1}{2}[\zeta_2, \zeta_1] \ , \ \mathcal{G}_3(\zeta_1, \zeta_2, \zeta_3) = \frac{1}{6}\left([\zeta_3, [\zeta_2, \zeta_1]] + [[\zeta_3, \zeta_2], \zeta_1]\right)$$

where $[.,.]$ is the commutator which, for vector fields, is the Lie bracketing operation. Thus, Agrachev and Gamkrelidze have provided an algorithmic approach to analytically determine the logarithm of time-periodic vector fields.

Sarychev (188) and Vela (191) have utilized the above concepts to develop a generalization for the classical averaging theorem. Sarychev (188) has introduced the notion of *complete averaging* to denote the following averaged vector field corresponding to the time-periodic system (6.5)

$$\overline{\boldsymbol{Y}} = \frac{1}{T}\ln \overrightarrow{\exp}\left(\int_0^{\mathrm{T}} \boldsymbol{Y}_\tau \mathrm{d}\tau\right) = \boldsymbol{V}_{\mathrm{T}} \tag{6.22}$$

Thus, one can write the averaged system corresponding to the NLTP system in (6.5) as

$$\dot{\overline{\boldsymbol{x}}} = \epsilon\overline{\boldsymbol{Y}} = \epsilon\boldsymbol{\Lambda}_1(\overline{\boldsymbol{x}}) + \epsilon^2\boldsymbol{\Lambda}_2(\overline{\boldsymbol{x}}) + ... \tag{6.23}$$

where

$$\boldsymbol{\Lambda}_1(\overline{\boldsymbol{x}}) = \frac{1}{T}\int_0^T \boldsymbol{Y}(\boldsymbol{x},t)\,dt \;\;,\;\; \boldsymbol{\Lambda}_2(\overline{\boldsymbol{x}}) = \frac{1}{2T}\int_0^T \left[\int_0^t \boldsymbol{Y}(\boldsymbol{x},\tau)\,d\tau, \boldsymbol{Y}(\boldsymbol{x},t)\right]$$

The power of the GAT lies in the fact that the $\boldsymbol{\Lambda}$'s can be computed analytically in terms of the Lie brackets between the vector fields describing the time-periodic dynamics. Sarychev (188) and Vela (191) have related this generalization of the averaging theorem to the nonlinear extension of Floquet theorem and shown that the averaged vector field $\overline{\boldsymbol{Y}}$ is the logarithm of the the Monodromy map in the nonlinear case.

6.5 Effects of Aerodynamic-Induced Parametric Excitation

In this subsection, we show that the effect of the aerodynamic-induced parametric excitation on the dynamics in Eq. (6.8). Both the method of multiple scales and second-order averaging are able to capture the true stability characteristic of the time-periodic system at hand. That is, using both methodologies, we could prove stability for the system in Eq. (6.8).

Figure 6.4 shows the resulting eigenvalues that determines the stability of the system (6.8) using first-order averaging, second-order averaging, method of multiple scales, Floquet theorem with the traditional Runge-Kutta solver, Floquet theorem with Matlab ode45 solver. To have the same eigenvalue representation, the presented eigenvalues using Floquet theorem approach are the Floquet multipliers transformed from the $\mathcal{Z}$-plane to the $\mathcal{S}$-plane (192) via the common transformation $z = e^{Ts}$. On the other hand, the eigenvalues obtained using the method of multiple are the stable ones using direct averaging and the modified unstable ones; i.e., eigenvalues of the matrix presented in Eq. (6.20).

Figure 6.4 shows that the proposed approaches capture the true stability characteristics of the system in comparison to direct averaging and the Floquet theorem approach using the Matlab ode45 solver. One

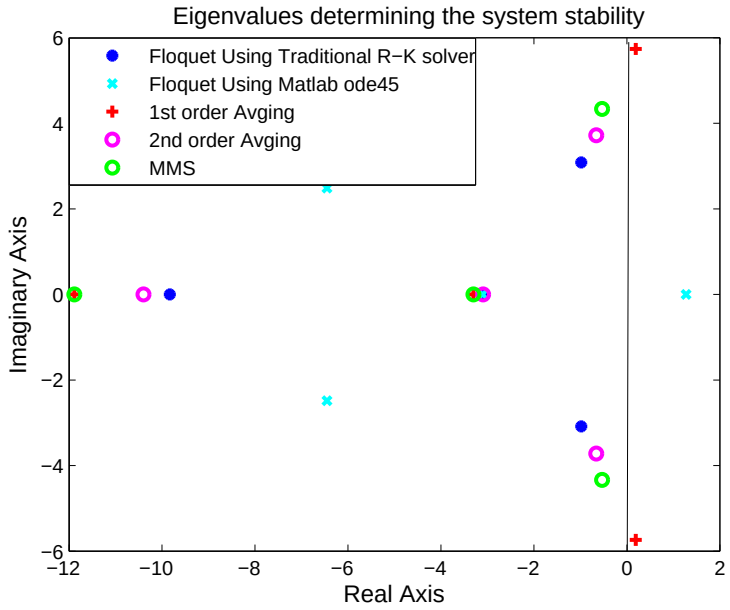

Figure 6.4: Eigenvalues determining the stability of the time-periodic system (6.8) for the hawkmoth case using first-order averaging, second-order averaging, method of multiple scales (MMS), Floquet theorem with the traditional Runge-Kutta solver, Floquet theorem using the Matlab ode45 solver.

interesting note from Fig. 6.4 is that all the approaches resulted in the same eigenvalue at -3.09 for the vertical motion. It should be noted that the vertical motion is decoupled from the forward and pitching motions near hover (11; 170). Thus, the direct averaging can provide a good estimate for the eigenvalue corresponding to the vertical motion

$$\lambda_w = \overline{Z_w} = -8\frac{K_{11}\Phi}{mT}\cos^2\alpha_m$$

for constant angle of attack α_m with any $\varphi(t)$-waveform. One of the interesting outcomes from the GAT is the ability to specifically determine the stabilizing action due to the high-amplitude periodic signals. That is, it provides an answer to the question: what is the stabilizing mechanism provided by the high-amplitude periodic signals? Consider the linearized, first-order averaged system-matrix for the hawkmoth case

$$D(\mathbf{\Lambda}_1)(\mathbf{0}) = \begin{bmatrix} -3.59 & 0 & 0 & -9.81 \\ 0 & -3.30 & 0 & 0 \\ 39.95 & 0 & -7.92 & 0 \\ 0 & 0 & 1 & 0 \end{bmatrix}$$

Using the adopted trim procedure (symmetric flapping along with zero x_h), the system lacks any pitch-stiffness (170). There cannot exist a pitching moment M due to the body pitching angle θ in most of the flying vehicles. Moreover, the adopted trim procedure leads to zero M due to w (or α); the essential stability derivative for the static stability of conventional aircraft (13). However, due to the high-amplitude, high-frequency, periodic signals, the system gains a considerable pitch-stiffness that is shown in the linearized, second-order averaged system-matrix

$$D(\mathbf{\Lambda}_1 + \mathbf{\Lambda}_2)(\mathbf{0}) = \begin{bmatrix} -3.58 & 0 & 0 & -9.81 \\ 0 & -3.09 & 0 & 0 \\ 29.98 & 0 & -8.13 & -28.45 \\ -2.90 & 0 & 0.96 & 0 \end{bmatrix}$$

The periodic signals have led to a little decrease in the damping in the forward and vertical directions. It also leads to a decrease in the speed stability (M due to u) which is a favorable effect (170). The pitch damping is increased however. Of particular interest, the creation of a considerable pitch stiffness (negative M due to θ). Thus, the GAT allows specifying the stabilizing mechanism due to the high-amplitude periodic forcing. It is also interesting to note that the kinematic equation $\dot{\theta} = q$ is changed to $\dot{\theta} = -2.90u + 0.96q$. This is because the time-periodic signals do not satisfy the condition $\int_0^T \int_0^t v(\tau) d\tau dt = 0$, where v is the zero-mean signal.

6.6 On the Applicability of Direct Averaging

In this section, we consider the hovering dynamics of four other insects; namely, the cranefly, bumblebee, dragonfly, and hoverfly. These insects, along with the hawkmoth, cover a wide range of operating conditions. Their morphological parameters are given in Table 6.1. The objective is to determine an estimate for the region of applicability of direct averaging in analyzing the flight dynamics of hovering MAVs/insects. This is performed by comparing the stability characteristics using direct averaging and the proposed approaches for all of the insects. We use the ratio between the flapping frequency to the natural frequency of body dynamics as the basis of comparison.

Table 6.2 shows the ratios of flapping frequency to the body natural frequency for the five insects, and the eigenvalues revealing the stability of the system in Eq. (6.8) using direct averaging and the proposed approaches. It is noteworthy to mention that the ratio $\frac{2\pi f}{\omega_n}$ is not monotonically increasing with f as the increase in the flapping frequency f may be associated with larger increase in the natural frequency ω_n, as

shown in the hoverfly case in comparison to the dragonfly. Note that the body mass of the hoverfly is considerably smaller than that of the dragonfly as shown in Table 6.1. Table 6.2 shows that the high-frequency,

Insect	$\frac{2\pi f}{\omega_n}$	$\lambda_{1\text{st}-\text{avg}}$	$\lambda_{2\text{nd}-\text{avg}}$ λ_{MMS}	$\overline{C_{M_\theta}}$
Hawkmoth	28.78	$[-11.89,\ -3.30,\ 0.19 \pm 5.74i]$	$[-10.40,\ -3.09,\ -0.66 \pm 3.72i]$ $[-11.89,\ -3.30,\ -0.53 \pm 4.34i]$	-0.0302
Cranefly	50.62	$[-47.71,\ -17.31,\ -1.13 \pm 5.53i]$	$[-45.76,\ -16.26,\ -13.16,\ 7.90]$ $[-47.71,\ -17.31,\ -12.42,\ 7.41]$	-0.0661
Bumblebee	144.46	$[-11.63,\ -4.39,\ 1.58 \pm 6.55i]$	$[-11.26,\ -4.37,\ 1.38 \pm 6.17i]$ $[-11.63,\ -4.39,\ 1.39 \pm 6.24i]$	-0.0033
Dragonfly	145.50	$[-13.11,\ -7.03,\ 1.34 \pm 6.65i]$	$[-12.56,\ -6.98,\ 1.04 \pm 5.99i]$ $[-13.11,\ -7.03,\ 1.06 \pm 6.09i]$	-0.0038
Hoverfly	113.98	$[-14.01,\ -7.27,\ 2.13 \pm 8.56i]$	$[-13.37,\ -7.24,\ 1.79 \pm 7.92i]$ $[-14.01,\ -7.27,\ 1.81 \pm 8.03i]$	-0.0083

Table 6.2: The eigenvalues revealing the stability of the system in Eq. (6.8) using direct averaging and the proposed approaches for the five insects along with the ratio between the flapping frequency to the natural frequency ω_n of the flight dynamics. $\overline{C_{M_\theta}}$ is the pitch stiffness coefficient that is induced by the high-frequency, high-amplitude periodic signals. It is calculated using second-order averaging.

high-amplitude, periodic signals do not impact the stability characteristics of hovering MAVs/insects for large $\frac{2\pi f}{\omega_n}$ ratios (above 100). That is, direct averaging is capable of capturing the true stability characteristics over this range. It should be noted that all the insects exhibit creation of stabilizing pitching stiffness due to the high-frequency, high-amplitude, periodic signals. However, Table 6.2 shows that there are cases where this stabilizing effect is not strong enough (clearly the cases of $\frac{2\pi f}{\omega_n} > 100$), cases where the net result is a destabilizing effect rather (cranefly), and cases where the induced pitch stiffness is enough to stabilize the system dynamics. Unlike all the other insects, the hovering dynamics of the cranefly exihibits a considerable increase in the speed stability (M_u), which is a harmful effect as shown in (170). As such, although the cranefly hovering dynamics exhibits the largest induced pitch stiffness, the net effect of the high-frequency, high-amplitude periodic signals is destabilizing.

6.7 Aerodynamic-Dynamic Interaction: Hovering Dynamics With Periodic Orbit and Change of Equilibrium

So far, we have studied the flight dynamics of hovering MAVs/insects ignoring the zero-mean forcing term $\boldsymbol{g}_1(t)$; the zero-mean part of the aerodynamic loads due to the flapping motion of the wing. Doing so yields a system with fixed point, Eq. (6.8), that has been shown to be stabilized for the hawkmoth case due to the high-amplitude periodic signals. The full dynamics (6.3) can be regarded as the system (6.8) subjected to a bounded, zero-mean, periodic forcing $\boldsymbol{g}_1(t)$. A matter which, knowing that the system (6.8) is stable, may deceivably indicate stability of the periodic orbit produced by the forcing $\boldsymbol{g}_1(t)$. In this section, we determine the effect of $\boldsymbol{g}_1(t)$ on the system dynamics.

First of all, incorporating $\boldsymbol{g}_1(t)$, the system cannot have a fixed point for all times and its equilibrium will rather be described by a periodic orbit. Knowing that, if the vehicle is balanced based on the average $\boldsymbol{f}(\boldsymbol{0})+\overline{\boldsymbol{g}_0}=\boldsymbol{0}$ (e.g., the cycle-averaged lift force is equal to the weight), then the origin is ensured to be a fixed point for the first-order averaged dynamics but not necessarily for the higher-order averaged dynamics. That is, the forcing term $\boldsymbol{g}_1(t)$ may interact with the time-varying dynamics (represented in $\boldsymbol{G}_1(t)$) resulting in a constant drift in the higher-order averaged dynamics. This constant drift, in turn, changes the equilibrium state of the system. This is an important note because if the system dynamics (6.3) is simulated using the flapping parameters that achieve balance/trim based on the average, the system will certainly deviate from hovering to another equilibrium. This behavior has nothing to do with the stability characteristics of hovering. It is just because the hovering itself is not balanced. This is why most of the previous studies concluded hovering instability; direct averaging falsely concludes instability and simulation deceivably shows divergence from hovering.

Using second-order averaging, the flapping parameters $\boldsymbol{P}$ are required to satisfy

$$\boldsymbol{\Lambda}_1(\boldsymbol{x}_{\text{eqm}};\boldsymbol{P})+\boldsymbol{\Lambda}_2(\boldsymbol{x}_{\text{eqm}};\boldsymbol{P})=\boldsymbol{0} \tag{6.24}$$

to achieve trim/balance. If hovering equilibrium is desired, then, $\overline{u}=0$, $\overline{w}=0$, and $\overline{q}=0$, while $\overline{\theta}$ can be any admissible value. That is, $\boldsymbol{x}_{\text{eqm}}=[0,0,0,\theta_{\text{eqm}}]^T$. It should be noted that triangular waveform for the back and forth flapping $\varphi(t)$ along with a piecewise constant variation for the wing pitching angle will be used in the computations below.

6.7.1 Symmetric Flapping

Similar to the observed change in the kinematic equation $\dot{\theta} = q$ in the previous example, incorporating $\boldsymbol{g}_1(t)$ results in a constant drift in the corresponding second-order averaged equation

$$\boldsymbol{\Lambda}_{2,4}(\boldsymbol{x}_{\text{eqm}}) = 8\frac{K_{22}\Delta x \Phi \sin\Phi \sin\alpha_m}{TI_y}$$

Thus, the only choice to eliminate this constant drift in the symmetric flapping case is to have $\Delta x = 0$; i.e., the hinge line has to be aligned with the wing's line of center of pressure. The drift in the pithing moment is then given by

$$\boldsymbol{\Lambda}_{2,3}(\boldsymbol{x}_{\text{eqm}}; \Delta x = 0) = -g\sin\theta_{\text{eqm}}\frac{K_{21}\sin 2\alpha_m(\sin 2\Phi - 2\cos 2\Phi)}{4\Phi I_y}$$

which is eliminated by choosing $\theta_{\text{eqm}} = 0$. Now, we are left with two trim equations to be satisfied

$$\begin{aligned} &\boldsymbol{\Lambda}_{2,1}(\mathbf{0}; \Delta x = 0, \Phi, \alpha_m) &&= 0 \\ &\boldsymbol{\Lambda}_{1,2}(\mathbf{0}; \Delta x = 0, \Phi, \alpha_m) + \boldsymbol{\Lambda}_{2,2}(\mathbf{0}; \Delta x = 0, \Phi, \alpha_m) &&= 0 \end{aligned} \tag{6.25}$$

These are two nonlinear algebraic equations in flapping amplitude Φ and the angle of attack α_m. One feasible solution to this set of equations in the hawkmoth case is

$$\Phi = 83.05^\circ \ , \ \alpha_m = 18.35^\circ$$

Many researchers have used the intuitive, ubiquitous balancing methodology based on the average, either for aerodynamic optimization (minimum power or maximum thrust with cycle-averaged lift equal to the weight) (43; 165; 74; 45; 193) or flight dynamics and control analyses (15; 11; 16; 12; 9; 25; 7; 24; 170). However, the above study shows that such methodology is not sufficient to ensure trim/balance. That is, symmetric flapping does not ensure zero cycle-averaged forward thrust force, cycle-averaged lift equal to the weight does not ensure balance in the vertical direction, and aligning the hinge line with the vehicle's center of gravity is not enough to achieve self pitch trim. In particular, Fig. 6.5 shows the first and second-order averaging results for the variation of the generated upward acceleration with the angle of attack α_m using triangular waveform and the documented $\Phi = 60.5^\circ$ for the hawkmoth. Figure 6.5 shows that direct averaging overestimates the generated lift force. That is, the oscillatory motion of the body due to the periodic forcing leads to a decrease in the generated lift force, which is consistent with the result of Wu et al. (194). In other words, the flapping-wing MAV/insect has to flap so as to produce cycle-averaged lift (due to flapping) that is more than its weight. It should be noted that the total cycle-averaged lift (due to flapping

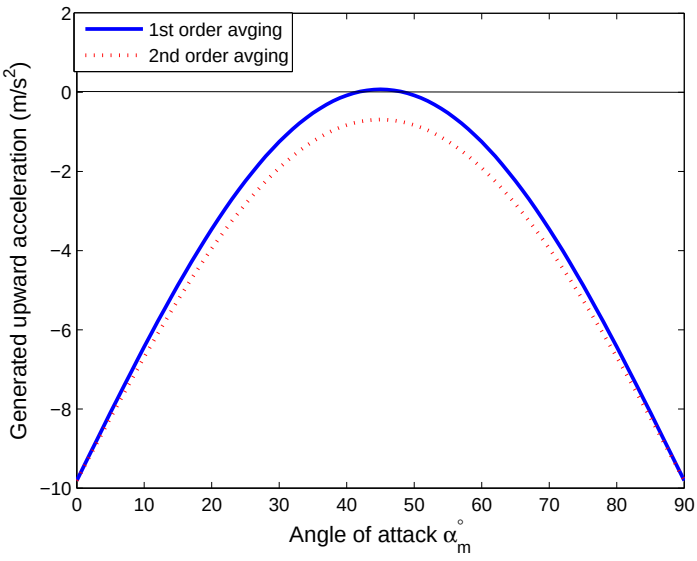

Figure 6.5: First and second-order averaging results for the variation of the generated upward acceleration with the angle of attack α_m using triangular waveform and the documented $\Phi = 60.5^\circ$ for the hawkmoth. Zero acceleration is required for trim.

+ due to body motion), however, equals the weight at balance.

Because of their potential importance, a general representation for the trim equations (6.25) is provided to be used in the future aerodynamic and dynamic analyses

$$
\begin{aligned}
\mathbf{\Lambda}_{2,1}(\mathbf{0}) &= \tfrac{1}{2T}\int_0^T [\tfrac{1}{m}\left(X_u(t)\int_0^t X_0(\tau)d\tau - X_0(t)\int_0^t X_u(\tau)d\tau + X_w(t)\int_0^t Z_0(\tau)d\tau - Z_0(t)\int_0^t X_w(\tau)d\tau\right) + \\
&\quad + \tfrac{1}{I_y}\left(X_q(t)\int_0^t M_0(\tau)d\tau - M_0(t)\int_0^t X_q(\tau)d\tau\right)]dt \\
\mathbf{\Lambda}_{1,2}(\mathbf{0}) + \mathbf{\Lambda}_{2,2}(\mathbf{0}) &= \tfrac{1}{2T}\int_0^T [\tfrac{1}{m}\left(Z_u(t)\int_0^t X_0(\tau)d\tau - X_0(t)\int_0^t Z_u(\tau)d\tau + Z_w(t)\int_0^t Z_0(\tau)d\tau - Z_0(t)\int_0^t Z_w(\tau)d\tau\right) + \\
&\quad + \tfrac{1}{I_y}\left(Z_q(t)\int_0^t M_0(\tau)d\tau - M_0(t)\int_0^t Z_q(\tau)d\tau\right)]dt + \underbrace{g + \frac{1}{mT}\int_0^T Z_0(t)dt}_{\text{1st order contribution}}
\end{aligned}
\tag{6.26}
$$

To give an estimate about how high the amplitude of the periodic forcing that hovering MAVs/insects experience, it is worthy to mention that the term $\frac{1}{I_y}M_0(t)$ has an amplitude about 2700 rad/s^2 in the hawkmoth case. It should also be noted that the constant drift (change of the equilibrium) becomes more considerable for light vehicles flapping at low frequencies; i.e., it is inversely proportional with the mass, moment of inertia, and flapping frequency.

Although the matrix representing the linearized, second-order averaged dynamics $[D(\mathbf{\Lambda}_1 + \mathbf{\Lambda}_2)(\mathbf{0})]$ is

exactly the same as that of the previous example (nonlinear flight dynamics with fixed point), evaluating it at the new flapping parameters that achieve trim ($\Phi = 83.05°$, $\alpha_m = 18.35°$, and $\Delta x = 0$) yields an unstable fixed point with the following eigenvalues for the hawkmoth case

$$3.64 \ , \ -5.16 \ , \ -28.02 \ , \ -6.49$$

The new set of flapping parameters results in another fixed point at

$$\overline{\boldsymbol{x}} = [1.45m/s \ , \ -3.03m/s \ , \ 0.00 \ , \ -180°]^T$$

which corresponds to a vertical descent with a rate of 3.03 m/s and a backward motion at a speed of 1.45 m/s at a pitching angle of $-180°$. The eigenvalues of the matrix representing the linearization of the second-order averaged dynamics about this fixed point are

$$-2.81 \pm 3.03i \ , \ -23.93 \ , \ -6.48$$

which indicates stability of the vertical descent equilibrium. This analysis shows that any perturbation from the hovering equilibrium will lead to pitching down while descending and moving backward until the MAV/insect reaches a stable upside-down descending equilibrium while moving backward. Figure 6.6 shows simulation of the system (6.3) using the new trim parameters.

6.7.2 Asymmetric Flapping

Using symmetric flapping, we could not achieve balance at the documented Φ for the hawkmoth ($\Phi = 60.5°$ (57)). Hence, the stability results obtained in the last subsection may not be quite representative to a hovering hawkmoth. To obtain stability results that are more representative for the hovering hawkmoth, we use asymmetric flapping on the form

$$\varphi(t) = \begin{cases} \phi_0 + \frac{4\Phi}{T}\left(t - \frac{T}{4}\right), & 0 \le t < \frac{T}{2} \\ \phi_0 - \frac{4\Phi}{T}\left(t - \frac{3T}{4}\right), & \frac{T}{2} \le t < T \end{cases}, \eta(t) = \begin{cases} \alpha_d, & 0 \le t < \frac{T}{2} \\ \pi - \alpha_u, & \frac{T}{2} \le t < T \end{cases} \tag{6.27}$$

where ϕ_0 is an offset angle to create asymmetry for the triangular waveform of $\varphi(t)$ and α_d and α_u are the angles of attack during the downstroke and upstroke, respectively. In addition, we use the documented x_h of the hovering hawkmoth ($x_h = 0.22R$ (11)). Then, we seek the flapping parameters α_d, α_u, ϕ_0, and Δx and the operating θ_{eqm} to ensure trim of the second-order averaging at hover; i.e., to satisfy Eq. (6.24). Using

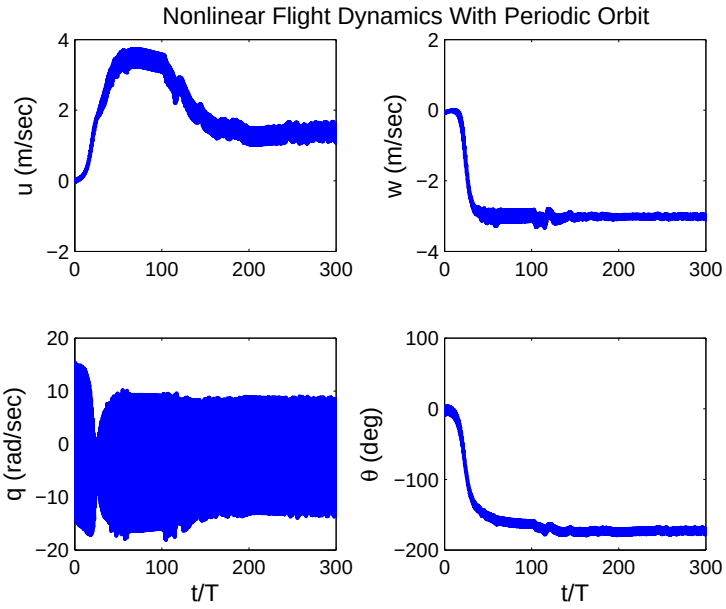

Figure 6.6: Simulation of the full nonlinear flight dynamics with periodic orbit for the hawkmoth case.

the least squares, we obtain

$$\alpha_d = 44.93^\circ \ , \ \alpha_u = 44.93^\circ \ , \ \phi_0 = -38.1569^\circ \ , \ \Delta x = 0.42 \ , \ \theta_{\text{eqm}} = 2.48^\circ$$

Linearizing the second-order averaged dynamics about the ensured fixed point, the eigenvalues of the system matrix are

$$2.73 \ , \ -4.80 \pm 4.57i \ , \ -2.77$$

which indicates instability of the hovering hawkmoth. Although this conclusion about the instability of the hawkmoth at hover is not new, the technical justification for that conclusion is. Moreover, the adopted methodology reveals some interesting facts about the dynamics of flapping flight. Specifically, the high-amplitude periodic forcing may lead to stabilizing actions as shown in the case of dynamics with fixed point. It may also lead to a change in the equilibrium state which dictates that the flapping MAV/insect has to flap more to keep balance.

6.8 Conclusion

Longitudinal flight dynamics of flapping-wing micro-air-vehicles (MAVs) and insects are considered. It is shown that direct averaging is not sufficient to assess the hovering stability of the relatively low flapping frequency. Typically, direct averaging is applicable over the range of flapping-to-natural frequency ratio above 100. On the other hand, the complication of the Floquet theorem approach dictates numerical implementation whose associated error may lead to false conclusions about the stability of the system. It is shown that either the method of multiple scales or higher-order averaging is suitable to analyze the flight dynamics of hovering MAVs/insects as it overcomes the issues with the other approaches (direct averaging and Floquet theorem). In particular, using second-order averaging, it is shown that the high-amplitude periodic forcing associated with flapping cannot be neglected as it induces stabilizing pitch stiffness for the studied five insects. It may also lead to a change in the equilibrium state. This refutes the previous common intuition about balancing a hovering vehicle. That is, symmetric flapping does not ensure zero cycle-averaged forward thrust force, cycle-averaged lift equal to the weight does not ensure balance in the vertical direction, and aligning the hinge line with the vehicle's center of gravity is not enough to achieve self pitch trim. In contrast, The flapping MAV/insect has to provide average lift due to flapping that is more than its weight to keep balance.

Chapter 7

A Geometric Control Approach for Enhanced Maneuverability of FWMAVs Near Hover

In this chapter, the maneuverability of flapping-wing micro-air-vehicles near hover is revisited. We propose an algorithmic approach that brings the maneuverability early in the design problem by combining tools from geometric control and averaging theory. Sections 7.2 and 7.3 provide the wing-kinematics and the used aerodynamic model, respectively. In Section 7.4, we derive the coupled equations of motion of the multi-body dynamics problem using the principle of virtual power. Section 7.5 provides the required tools from geometric control and averaging theory to analyze the dynamics of mechanical systems subjected to high-frequency, high-amplitude, periodic forcing. In Section 7.6, we apply these tools on the flapping-wing micro-air-vehicle dynamics near hover. In Section 7.7, we formulate a design optimization problem for a flapping-wing to maximize a desired maneuverability index. The tools from geometric control and averaging give relations between the cycle-averaged accelerations of the body and the components of the analytically-computed symmetric product vector fields.

7.1 Introduction

The dynamics of flapping flight is challenging to model and analyze. The propulsion and control mechanization results in a fundamentally underactuated system and for even the simplest models, the governing equations are nonlinear and time-varying. Wood (30) noted that minimal actuation was an important factor in the success of the first flapping-wing micro-air vehicle (FWMAV), the Harvard Robofly. The concept was also emphasized by Doman *et al* (19; 9) and Schenato *et al* (7) in their design and analysis efforts. The use of time-periodic inputs to generate motion in underactuated mechanical systems is a well-established concept and leads naturally to the use of geometric control and averaging theory for analysis of these systems (195).

A fundamental challenge in modeling and analyzing the flight dynamics of FWMAVs is the inertial effects of the wings. Treating the wings as elements in a multi-body system results in a more accurate, but more complicated flight dynamics model. In fact, wing inertial effects have often been ignored altogether in analysis of flapping flight (102; 114; 23; 95; 2; 15; 16; 26; 27; 9; 25). Neglecting the multi-body wing effects results in the rigid body dynamic equations for a conventional, fixed-wing aircraft. Sun *et al* (11) derived the dynamic equations for flapping flight including wing inertial effects, hence, identified the usually neglected terms. They, then, performed numerical simulations using the reduced model and quantified the neglected terms illustrating that the reduced model is justifiable in hover. On the other hand, Orlowski and Girard (100) showed that neglecting the wing mass may result in erroneous predictions and Bolender (116) argued that wing mass should be included when developing flight control systems for FWMAVs. Weihua and Cesnik (22) studied the dynamic stability of flexible FWMAVs and found that increasing the wing inertia tends to destabilize both the longitudinal and the lateral flight dynamics. For more details about the inertial effects of the wing motion on the dynamics of flapping flight, the reader is referred to the review article by Taha *et al* (146).

In this work, we consider the longitudinal flight of FWMAVs near hover and use averaging and tools from geometric control theory to derive analytical expressions characterizing the net control force and moment that a given configuration can generate. Specifically, we develop analytical expressions for the Lie bracket and symmetric product vector fields that play a fundamental role in the averaged dynamic equations (195). These expressions include parameters that define the system's geometry and gait; maximizing elements of the symmetric products directly influences the vehicle's maneuverability. The work illustrates a design optimization approach for enhancing the maneuverability of a FWMAV.

7.2 Wing Kinematics

In general, three types of reference frames are required to formulate the flight dynamic model for a rigid-winged FWMAV: an inertial reference frame $\{x_{\mathrm{I}}, y_{\mathrm{I}}, z_{\mathrm{I}}\}$, a body-fixed reference frame $\{x_{\mathrm{b}}, y_{\mathrm{b}}, z_{\mathrm{b}}\}$, and a wing-fixed reference frame $\{x_{\mathrm{w}}, y_{\mathrm{w}}, z_{\mathrm{w}}\}$ for each of the flight vehicle's wings. Because only longitudinal flight is considered in this work, symmetric wing motions are assumed.

By convention, the x_{b}-axis points forward defining the vehicle's longitudinal axis, the y_{b}-axis points to starboard, and the z_{b}-axis completes the right-handed frame. The conventional yaw-pitch-roll (ψ-θ-ϕ) Euler angle sequence traditionally used with fixed-wing aircraft (13) is adopted here to describe the body's inertial orientation. Because only longitudinal flight is considered, however, only the body's pitch angle θ is required.

The wing-fixed frame is defined such that it is aligned with the body-fixed reference frame when the wing kinematic angles are zero. Wing motion relative to the body is typically described using three Euler angles: the flapping angle φ (describing back and forth motion), the plunging angle ϑ (describing up and down motion), and the pitching angle η (describing rotation of the wing about a chord line). Consistent with observations of biological flyers (20; 21), the wing motion is restricted such that the plunging angle ϑ remains zero. Figure 2.4 shows a schematic diagram for a FWMAV hovering using a horizontal stroke plane.

As for the pitching angle, η, it is assumed to experience the following piecewise constant variation

$$\eta(t) = \begin{cases} \alpha_d, & \dot{\varphi} > 0 \\ \pi - \alpha_u, & \dot{\varphi} < 0 \end{cases}$$

where α_d and α_u are the setting angles of attack in the downstroke and upstroke, respectively. The majority of dynamics and control investigations for hovering FWMAVs assumed fixed pitching angle throughout each half-stroke with instantaneous flip between the adjacent half-strokes (15; 16; 7; 8; 9; 10; 25). This piecewise constant kinematics for η is asymptotically realized through passive control along with the flapping velocity $\dot{\varphi}$ and, hence, is convenient for the minimal actuation concept. Moreover,symmetric flapping is assumed here; that is, $\alpha_d = \alpha_u = \alpha_m$, where α_m is the mean angle of attack maintained throughout the entire stroke. As such, we can write

$$\sin\eta = \sin\alpha_m \quad \text{and} \quad \cos\eta = sign(\dot{\varphi})\cos\alpha_m$$

7.3 Aerodynamic Model

The aerodynamics of flapping flight has been a subject of interest for almost a century. The flow field resulting from flapping motion is unsteady and nonlinear, resulting in nonconventional mechanisms for aerodynamic force production. Dickinson *et al* (3) pointed out that these nonconventional mechanisms are the translatory effect (due to the leading edge vortex), the rotational effect, and the effect of wake capture. With regard to the translatory effect, Wang *et al* (110) showed that the static lift coefficient for a translating wing, taking into account the leading edge vortex effect, is reasonably well-described as $C_L = A \sin 2\alpha$ where the parameter A may be determined experimentally. Berman and Wang (43) provided values for A for the hawkmoth, bumblebee, and fruitfly. Taha *et al* (167; 168) proposed a technique for estimating A taking into account the effect of aspect ratio. Hence, the lift coefficient is written as

$$A = \frac{\pi \mathcal{AR}}{2\left[1 + \sqrt{(\frac{\pi \mathcal{AR}}{a_0})^2 + 1}\right]}$$

with the $\mathcal{AR}$ based on one wing; i.e., $\mathcal{AR} = \frac{R^2}{S}$, where R is the wing radius, S is the area of one wing and a_0 is the lift curve slope of the two-dimensional airfoil section (taken here 2π). As for the drag coefficient, similarly to aerodynamic drag on delta wings where the effect of the leading edge vortex is pronounced, one may write $C_D = C_L \tan\alpha = 2A \sin^2\alpha$. This model neglects the viscous drag, relying on the experiments of Dickinson *et al* (3; 79).

Since constant angle of attack is maintained throughout the entire stroke and because symmetric flapping is used, no rotational lift is produced. The effect of wake capture is difficult to be modelled analytically; in model-based control design, this effect is typically ignored, with the expectation that well-designed feedback control can compensate for unmodeled dynamics.

Considering the above setup, the total flapping velocity seen by an airfoil section that is a distance r from the wing root is $r\dot{\varphi}$. The lift and drag force per unit span on that section are

$$\ell(r,t) = \frac{1}{2}\rho A r^2 c(r) \dot{\varphi}^2(t) \sin 2\alpha_m dr$$
$$d(r,t) = \rho A r^2 c(r) |\dot{\varphi}(t)| \dot{\varphi}(t) \sin^2 \alpha_m dr$$

where the drag force above is defined positive opposite to the wing motion in the down-stroke. The aerodynamic pitching moment per unit span about the hinge axis is then given by

$$M_h'(r,t) = [\ell(r,t)\cos\eta(t) + d(r,t)\sin\eta(t)]\,\Delta\hat{x}c(r)$$

where $\Delta\hat{x}$ is the normalized chordwise distance between the center of pressure and the hinge location. The center of pressure is assumed to rest at the the quarter-chord line. Writing η in terms of α_m and integrating over the two (left and right) wings yields the total lift and drag and the pitching moment about the hinge axis in the form

$$\begin{aligned} L(t) &= \frac{1}{2}\rho A I_{21}\dot{\varphi}^2(t)\sin 2\alpha_m \\ D(t) &= \rho A I_{21}|\dot{\varphi}(t)|\dot{\varphi}(t)\sin^2\alpha_m \\ M_h(t) &= \rho A I_{22}|\dot{\varphi}(t)|\dot{\varphi}(t)\sin\alpha_m \end{aligned} \tag{7.1}$$

where the $I_{mn} = 2\int_0^R r^m c^n(r)\,dr$ are weighted moments of area for the two wings.

7.4 Equations of Motion

Recall that the pitch angle is kept constant throughout each half-stroke, $\dot{\eta} \equiv 0$ except between half-strokes where the derivative is not defined. As such, it is convenient to neglect the wing pitching dynamics. Since the two wings move symmetrically, the equations of motion are defined in terms of four generalized coordinates: $\boldsymbol{q} = [x\ ,\ z\ ,\ \theta\ ,\ \varphi]^T$, where x and z are "quasicoordinates" associated with body velocity components u and w along the x_b and z_b directions, respectively. In the following subsections, the principle of virtual power (174) is used to derive the equations of motion:

$$\sum_{i=b,w}[m_i(\dot{\boldsymbol{v}}_i + \ddot{\boldsymbol{\rho}}_{\boldsymbol{c}i}) - \boldsymbol{f}_i]\cdot\frac{\partial\boldsymbol{v}_i}{\partial\dot{q}_j} + [\dot{\boldsymbol{h}}_i + m_i\boldsymbol{\rho}_{\boldsymbol{c}i}\times\dot{\boldsymbol{v}}_i - \boldsymbol{m}_i]\cdot\frac{\partial\boldsymbol{\omega}_i}{\partial\dot{q}_j} = 0 \tag{7.2}$$

where $j = 1-4$ and $\boldsymbol{\rho}_{\boldsymbol{c}i}$ is the vector pointing from the reference point of the i^{th} rigid body to its center of gravity.

7.4.1 Body

Setting the origin of the body frame at the body center of gravity, the velocity of the origin of the body axis system and the corresponding angular velocity are written as

$$\boldsymbol{v}_\mathrm{b} = u\boldsymbol{i}_\mathrm{b} + w\boldsymbol{k}_\mathrm{b} \qquad \text{and} \qquad \boldsymbol{\omega}_\mathrm{b} = \dot{\theta}\boldsymbol{j}_\mathrm{b}$$

where i, j, and k are unit vectors along the x, y, and z directions in the axis-system indicated by the subscript. Thus,

$$\frac{\partial \boldsymbol{v}_\mathrm{b}}{\partial u} = \boldsymbol{i}_\mathrm{b} \quad \frac{\partial \boldsymbol{v}_\mathrm{b}}{\partial w} = \boldsymbol{k}_\mathrm{b} \quad \frac{\partial \boldsymbol{v}_\mathrm{b}}{\partial \dot{\theta}} = \boldsymbol{0} \quad \frac{\partial \boldsymbol{v}_\mathrm{b}}{\partial \dot{\varphi}} = \boldsymbol{0}$$
$$\frac{\partial \boldsymbol{\omega}_\mathrm{b}}{\partial u} = \boldsymbol{0} \quad \frac{\partial \boldsymbol{\omega}_\mathrm{b}}{\partial w} = \boldsymbol{0} \quad \frac{\partial \boldsymbol{\omega}_\mathrm{b}}{\partial \dot{\theta}} = \boldsymbol{j}_\mathrm{b} \quad \frac{\partial \boldsymbol{\omega}_\mathrm{b}}{\partial \dot{\varphi}} = \boldsymbol{0}$$

and

$$\dot{\boldsymbol{v}}_\mathrm{b} = (\dot{u} + w\dot{\theta})\boldsymbol{i}_\mathrm{b} + (\dot{w} - u\dot{\theta})\boldsymbol{k}_\mathrm{b}$$

The angular momentum vector of the body about the body center of gravity and its inertial derivative are given by

$$\boldsymbol{h}_\mathrm{b} = I_{yb}\dot{\theta}\boldsymbol{j}_\mathrm{b}, \qquad \dot{\boldsymbol{h}}_\mathrm{b} = I_{yb}\ddot{\theta}\boldsymbol{j}_\mathrm{b}$$

The body exhibits gravitational forces only with no moments. Thus, the body forces in the body frame are written as

$$\boldsymbol{f}_\mathrm{b}^{(\mathrm{b})} = m_\mathrm{b} g[-\sin\theta, \;\; 0, \;\; \cos\theta]^T$$

7.4.2 Wing

Locating the origin of the wing frame at the hinge root, the velocity of the origin of the wing frame and its angular velocity are written as

$$\boldsymbol{v}_\mathrm{w} = u\boldsymbol{i}_\mathrm{b} + (w - x_h\dot{\theta})\boldsymbol{k}_\mathrm{b}, \qquad \boldsymbol{\omega}_\mathrm{w} = \dot{\theta}\boldsymbol{j}_\mathrm{b} - \dot{\varphi}\boldsymbol{k}_\mathrm{b}$$

Thus,

$$\frac{\partial \boldsymbol{v}_\mathrm{w}}{\partial u} = \boldsymbol{i}_\mathrm{w} \quad \frac{\partial \boldsymbol{v}_\mathrm{w}}{\partial w} = \boldsymbol{k}_\mathrm{b} \quad \frac{\partial \boldsymbol{v}_\mathrm{w}}{\partial \dot{\theta}} = -x_h\boldsymbol{k}_\mathrm{b} \quad \frac{\partial \boldsymbol{v}_\mathrm{w}}{\partial \dot{\varphi}} = \boldsymbol{0}$$
$$\frac{\partial \boldsymbol{\omega}_\mathrm{w}}{\partial u} = \boldsymbol{0} \quad \frac{\partial \boldsymbol{\omega}_\mathrm{w}}{\partial w} = \boldsymbol{0} \quad \frac{\partial \boldsymbol{\omega}_\mathrm{w}}{\partial \dot{\theta}} = \boldsymbol{j}_\mathrm{b} \quad \frac{\partial \boldsymbol{\omega}_\mathrm{w}}{\partial \dot{\varphi}} = -\boldsymbol{k}_\mathrm{b}$$

and

$$\dot{\boldsymbol{v}}_\mathrm{w} = [\dot{u} + (w - x_h\dot{\theta})\dot{\theta}]\boldsymbol{i}_\mathrm{b} + (\dot{w} - x_h\ddot{\theta} - u\dot{\theta})\boldsymbol{k}_\mathrm{b}$$

The rotation matrices from the the body frame to the wing frame are

$$\boldsymbol{R}_{\varphi} = \begin{bmatrix} \cos\varphi & -\sin\varphi & 0 \\ \sin\varphi & \cos\varphi & 0 \\ 0 & 0 & 1 \end{bmatrix} \quad , \quad \boldsymbol{R}_{\eta} = \begin{bmatrix} \cos\eta & 0 & -\sin\eta \\ 0 & 1 & 0 \\ \sin\eta & 0 & \cos\eta \end{bmatrix}$$

and

$$\boldsymbol{R}_{\mathrm{wb}} = \boldsymbol{R}_{\eta}\boldsymbol{R}_{\varphi}$$

The wing angular velocity vector in the wing frame is

$$\boldsymbol{\omega}_{\mathrm{w}}^{(\mathrm{w})} = \begin{pmatrix} \omega_1 \\ \omega_2 \\ \omega_3 \end{pmatrix} = [\boldsymbol{R}_{\mathrm{wb}}] \begin{pmatrix} 0 \\ \dot{\theta} \\ -\dot{\varphi} \end{pmatrix} = \begin{pmatrix} \dot{\varphi}\sin\eta - \dot{\theta}\cos\eta\sin\varphi \\ \dot{\theta}\cos\varphi \\ -\dot{\varphi}\cos\eta - \dot{\theta}\sin\eta\sin\varphi \end{pmatrix}$$

The position vector pointing from the hinge root to the wing center of gravity is $\boldsymbol{\rho}_{\boldsymbol{c}_{\mathrm{w}}} = -d\boldsymbol{i}_{\mathrm{w}} + r_{cg}\boldsymbol{j}_{\mathrm{w}}$ where d and r_{cg} are the distances between the wing root hinge point and the wing center of gravity along the negative x_{w}-axis and the y_{w}-axis, respectively. Thus, we obtain the the inertial acceleration

$$\ddot{\boldsymbol{\rho}}_{\boldsymbol{c}_{\mathrm{w}}}^{(\mathrm{w})} = \begin{pmatrix} \ddot{\rho}_1 \\ \ddot{\rho}_2 \\ \ddot{\rho}_3 \end{pmatrix} = \begin{pmatrix} d(\omega_2^2 + \omega_3^2) - r_{cg}(\dot{\omega}_3 - \omega_1\omega_2) \\ -d(\dot{\omega}_3 + \omega_1\omega_2) - r_{cg}(\omega_1^2 + \omega_3^2) \\ d(\dot{\omega}_2 - \omega_1\omega_3) + r_{cg}(\dot{\omega}_1 + \omega_2\omega_3) \end{pmatrix}$$

Assuming the wing reference frame is fixed in the wing principal axes, the inertial time derivative of the angular momentum vector represented in the wing frame is written as

$$\dot{\boldsymbol{h}}_{\mathrm{w}}^{(\mathrm{w})} = \begin{pmatrix} \dot{h}_1 \\ \dot{h}_2 \\ \dot{h}_3 \end{pmatrix} = \begin{pmatrix} I_x\dot{\omega}_1 + (I_z - Iy)\omega_2\omega_3 \\ I_y\dot{\omega}_y + (I_x - Iz)\omega_1\omega_3 \\ I_z\dot{\omega}_3 + (I_y - Ix)\omega_1\omega_2 \end{pmatrix}$$

The wing is subject to aerodynamic and gravitational forces. The force vector applied on the wing is

$$\boldsymbol{f}_{\mathrm{w}}^{(\mathrm{b})} = \begin{pmatrix} -D\cos\varphi \\ 0 \\ -L \end{pmatrix} + m_{\mathrm{w}} g \begin{pmatrix} -\sin\theta \\ 0 \\ \cos\theta \end{pmatrix}$$

The moment vector contains three contributions: aerodynamic, gravitational, and the control torque. The first is written as $\boldsymbol{M}_{\boldsymbol{a}_{\mathrm{w}}} = M_h \boldsymbol{j}_{\mathrm{w}} + N\boldsymbol{k}_{\mathrm{b}}$, where M_h is the hinge moment as presented in Eq. (7.1) and N is the opposing moment due to the drag force distribution along the wing:

$$N(t) = \rho A I_{31} |\dot{\varphi}(t)| \dot{\varphi}(t) \sin^2 \alpha_m$$

The second contribution, the moment due to gravity, is $\boldsymbol{M}_{\boldsymbol{g}_{\mathrm{w}}} = (-d\boldsymbol{i}_{\mathrm{w}} + r_{cg}\boldsymbol{j}_{\mathrm{w}}) \times m_{\mathrm{w}} g \boldsymbol{k}_{\mathbf{I}}$. The last contribution, the control torque, is $\boldsymbol{M}_{\boldsymbol{c}_{\mathrm{w}}} = -\tau_\varphi \boldsymbol{k}_{\mathrm{b}}$, where τ_φ is the actuating torque in the flapping direction.

Having prepared all the required terms to apply the principle of virtual power (7.2), the equations of motion are obtained.

$$\begin{aligned}
&m_v(\dot{u} + w\dot{\theta} + g\sin\theta) + m_w(\ddot{\rho}_1 \cos\eta\cos\varphi + \ddot{\rho}_2 \sin\varphi + \ddot{\rho}_3 \sin\eta\cos\varphi - x_h\dot{\theta}^2) && = -D\cos\varphi \\
&m_v(\dot{w} - u\dot{\theta} - g\cos\theta) + m_w(\ddot{\rho}_3\cos\eta - \ddot{\rho}_1\sin\eta - x_h\ddot{\theta}) && = -L \\
&m_w[d\sin\eta\dot{u} + (d\cos\eta\cos\varphi - r_{cg}\sin\varphi - x_h)\,\dot{w} + x_h\ddot{\theta}\,(x_h - d\cos\eta\cos\varphi + r_{cg}\sin\varphi) + \\
&+x_h(\ddot{\rho}_1\sin\eta - \ddot{\rho}_3\cos\eta + u\dot{\theta} + g\cos\theta) + d\sin\eta\dot{\theta}(w - x_h\dot{\theta}) - (d\cos\eta\cos\varphi - r_{cg}\sin\varphi)\times \\
&(u\dot{\theta} + g)] + I_{yb}\ddot{\theta} + \dot{h}_2\cos\varphi - \dot{h}_1\cos\eta\sin\varphi - \dot{h}_3\sin\eta\sin\varphi && = Lx_h + M_h\cos\varphi \\
&m_w(d\cos\eta\sin\varphi + r_{cg}\cos\varphi)\left[\dot{u} + (w - x_h\dot{\theta})\dot{\theta}\right] + (\dot{h}_1\sin\eta - \dot{h}_3\cos\eta) && = \tau_\varphi
\end{aligned} \tag{7.3}$$

Note that the contributions of the opposing moment N from the two wing-halves cancel each others.

7.5 Averaging for Mechanical Systems

This section provides a brief discussion of the tools to be used in our analysis. Our primary references are Bullo's work on vibrational control for mechanical systems (140) and a series of papers by Vela *et al* concerning geometric methods for biomimetic locomotion (196; 197; 191).

7.5.1 Averaging and the Variation of Constants Formula

In discussing vibrational control, Bullo (140) considers a system with a time-invariant drift vector field and with high-amplitude, high-frequency forcing

$$\frac{d}{dt}\boldsymbol{x} = \boldsymbol{f}(\boldsymbol{x}) + \frac{1}{\epsilon}\boldsymbol{g}(\boldsymbol{x}, t/\epsilon), \qquad \boldsymbol{x}(0) = \boldsymbol{x}_0 \tag{7.4}$$

where $0 < \epsilon \ll 1$. The time-varying vector field $\boldsymbol{g}(\boldsymbol{x}, t/\epsilon)$ is assumed to be periodic in its second argument with period T. Let $\boldsymbol{\Phi}^g_{0,\tau}$ denote the flow of the vector field $\boldsymbol{g}(\boldsymbol{x}, \tau)$. Define the time-varying vector field

$$\boldsymbol{F}(\boldsymbol{x}, \tau) = \left(\left(\boldsymbol{\Phi}^g_{0,\tau}\right)^* \boldsymbol{f}\right)(\boldsymbol{x})$$

where the *pull-back* of the vector field $\boldsymbol{f}$ along the diffeomorphism $\boldsymbol{\Phi}^g_{0,\tau}$ is

$$\left(\left(\boldsymbol{\Phi}^g_{0,\tau}\right)^* \boldsymbol{f}\right)(\boldsymbol{x}) = \left(\frac{d}{dx}\left(\boldsymbol{\Phi}^g_{0,\tau}\right)^{-1} \circ \boldsymbol{f} \circ \boldsymbol{\Phi}^g_{0,\tau}\right)(\boldsymbol{x}) \tag{7.5}$$

By the variation of constants formula (195)

$$\boldsymbol{\Phi}^{f+g}_{0,\tau} = \boldsymbol{\Phi}^g_{0,\tau} \circ \boldsymbol{\Phi}^{\left(\boldsymbol{\Phi}^g_{0,\tau}\right)^* \boldsymbol{f}}_{0,\tau}$$

the solution of (7.4) satisfies

$$\frac{d}{dt}\boldsymbol{x} = \frac{1}{\epsilon}\boldsymbol{g}(\boldsymbol{x}, t/\epsilon), \qquad \boldsymbol{x}(0) = \boldsymbol{z}(t)$$

where $\boldsymbol{z}(t)$ satisfies

$$\frac{d}{dt}\boldsymbol{z} = \boldsymbol{F}(\boldsymbol{z}, t/\epsilon), \qquad \boldsymbol{z}(0) = \boldsymbol{x}_0$$

Solutions $\boldsymbol{x}(t)$ of (7.4) exhibit a slow and a fast time scale as $\epsilon \to 0^+$ and the behavior of a given solution over time scales of order one (i.e., the slow time scale) matches that of the following T-*averaged* system

$$\frac{d}{dt}\boldsymbol{x} = \bar{\boldsymbol{F}}(\boldsymbol{x}) := \frac{1}{T}\int_0^T \boldsymbol{F}(\boldsymbol{x}, \tau)d\tau, \qquad \boldsymbol{x}(0) = \boldsymbol{x}_0 \tag{7.6}$$

Moreover, if the system (7.6) has an asymptotically stable equilibrium point and $\boldsymbol{x}_0$ is within an ϵ-neighborhood of it, then the true and averaged solutions remain ϵ-close for all time. That is, asymptotic stability of an equilibrium of (7.6) implies asymptotic stability of a periodic orbit of (7.4).

To show that the system (7.4) is in a form amenable to conventional averaging theorems (see (198), for

example), one defines a new independent variable $\tau = t/\epsilon$. Recognizing that

$$\frac{d}{d\tau}\boldsymbol{x}(t(\tau)) = \frac{d\boldsymbol{x}}{dt}\frac{dt}{d\tau} = \epsilon\frac{d\boldsymbol{x}}{dt},$$

one obtains the following system

$$\frac{d}{d\tau}\boldsymbol{x} = \epsilon\boldsymbol{f}(\boldsymbol{x},\tau) + \boldsymbol{g}(\boldsymbol{x},\tau), \qquad \boldsymbol{x}(0) = \boldsymbol{x}_0.$$

The essential obstacle to computing the averaged dynamics for periodically forced control systems of the form (7.4) is in computing the pull-back of $\boldsymbol{f}$ along $\boldsymbol{\Phi}^g_{0,\tau}$ defined in (7.5), given that $\boldsymbol{g}$ is time-varying. Bullo discusses an integral series representation, attributed to Agrachev and Gamkrelidze (190). Although computation (and convergence) of the series are problematic, in general, the series terminates under certain structural conditions on the vector fields. Such structural conditions are exhibited by a special class of mechanical control systems.

7.5.2 Mechanical Control Systems

Bullo (140) considers mechanical control systems with n degrees of freedom and $m \leq n$ inputs, which can be written in the form

$$\boldsymbol{m}(\boldsymbol{q})\ddot{\boldsymbol{q}} + \boldsymbol{C}(\boldsymbol{q},\dot{\boldsymbol{q}})\dot{\boldsymbol{q}} = \hat{\boldsymbol{X}}_0(\boldsymbol{q}) + \boldsymbol{E}(\boldsymbol{q},\dot{\boldsymbol{q}}) + \hat{\boldsymbol{X}}_a(\boldsymbol{q})v^a(t) \tag{7.7}$$

where $\boldsymbol{C}(\boldsymbol{q},\dot{\boldsymbol{q}})$ represents the "Coriolis and centripetal" effects associated with the positive definite kinetic energy metric $\boldsymbol{m}(\boldsymbol{q})$. On the right hand side, the vector $\hat{\boldsymbol{X}}_0(\boldsymbol{q})$ represents configuration-dependent effects such as forces arising from a scalar potential function (e.g., moments due to gravity). In Bullo's work, $\boldsymbol{E}(\boldsymbol{q},\dot{\boldsymbol{q}}) = \hat{\boldsymbol{R}}(\boldsymbol{q})\dot{\boldsymbol{q}}$ represents dissipation that is linear in velocity. The configuration-dependent vector fields $\hat{\boldsymbol{X}}_a$, where $a \in \{1,\ldots,m\}$, are the input vector fields. The dynamic equations then become

$$\ddot{\boldsymbol{q}} = \underbrace{-\boldsymbol{m}^{-1}(\boldsymbol{q})\boldsymbol{C}(\boldsymbol{q},\dot{\boldsymbol{q}})\dot{\boldsymbol{q}}}_{\boldsymbol{Z}(\boldsymbol{q},\dot{\boldsymbol{q}})} + \underbrace{\boldsymbol{m}^{-1}(\boldsymbol{q})\hat{\boldsymbol{X}}_0(\boldsymbol{q})}_{\boldsymbol{X}_0(\boldsymbol{q})} + \underbrace{\boldsymbol{m}^{-1}(\boldsymbol{q})\hat{\boldsymbol{R}}(\boldsymbol{q})\dot{\boldsymbol{q}}}_{\boldsymbol{R}(\boldsymbol{q})\dot{\boldsymbol{q}}} + \underbrace{\boldsymbol{m}^{-1}(\boldsymbol{q})\hat{\boldsymbol{X}}_a(\boldsymbol{q})}_{\boldsymbol{X}_a(\boldsymbol{q})}v^a(t) \tag{7.8}$$

Define the $2n$-dimensional state vector $\boldsymbol{x} = \left[\boldsymbol{q}^T,\ \dot{\boldsymbol{q}}^T\right]^T$. The dynamic equations (7.8) become

$$\dot{\boldsymbol{x}} = \boldsymbol{Z}(\boldsymbol{x}) + \boldsymbol{Y}_0(\boldsymbol{x}) + \boldsymbol{R}(\boldsymbol{x}) + \boldsymbol{Y}_a(\boldsymbol{x})v^a(t), \tag{7.9}$$

where terms are defined by obvious correspondence.

The vector fields on the right hand side of equations (7.9) are polynomials of known degree in $\dot{\boldsymbol{q}}$. Bullo notes several consequences of this special structure. For example, the Lie bracket of any two input vector fields vanishes:

$$[\boldsymbol{Y}_a, \boldsymbol{Y}_{\mathrm{b}}] = \boldsymbol{0} \tag{7.10}$$

This observation, together with the Jacobi identity for Lie brackets of vector fields, implies that $[\boldsymbol{Y}_a, [\boldsymbol{f}, \boldsymbol{Y}_b]] = [\boldsymbol{Y}_b, [\boldsymbol{f}, \boldsymbol{Y}_a]]$ for any smooth vector field $\boldsymbol{f}(\boldsymbol{x})$. Bullo therefore introduces the following *symmetric product* with respect to $\boldsymbol{Z}(\boldsymbol{x})$: $\langle \boldsymbol{X}_a : \boldsymbol{X}_b \rangle = \langle \boldsymbol{X}_b : \boldsymbol{X}_a \rangle$ is the last n-components of the $2n$ vector field $[\boldsymbol{Y}_a, [\boldsymbol{Z}, \boldsymbol{Y}_b]]$. This is the coordinate representation of the intrinsic definition given in (195). There, the symmetric product of vector fields on a smooth Riemannian manifold is given in terms of the geodesic spray for the Levi-Civita connection associated with the Riemannian metric.

In discussing locomotion methods for underwater vehicles, Vela *et al* (196; 197) relax some of Bullo's assumptions and consider the case where

$$\boldsymbol{E}(\boldsymbol{q}, \dot{\boldsymbol{q}}) = \boldsymbol{E}_0(\boldsymbol{q}, \dot{\boldsymbol{q}}) + \boldsymbol{R}(\boldsymbol{q})\dot{\boldsymbol{q}},$$

letting $\boldsymbol{E}_0(\boldsymbol{q}, \dot{\boldsymbol{q}})$ represent "state-feedback terms" that are quadratic in velocity. In the case of a FWMAV, the terms in $\boldsymbol{E}_0(\boldsymbol{q}, \dot{\boldsymbol{q}})$ might instead represent aerodynamic effects more complicated than linear damping. Standard models for lift and drag, for example, are quadratic in velocity. Vela and colleagues (196) make the following important observation:

$$[\boldsymbol{Y}_c, [\boldsymbol{Y}_{\mathrm{b}}, [\boldsymbol{Y}_a, \boldsymbol{Z} + \boldsymbol{Y}_0 + \boldsymbol{R}]]] = \boldsymbol{0} \tag{7.11}$$

Equations (7.10) and (7.11) imply that the integral series representation of $\left(\boldsymbol{\Phi}_{0,\tau}^{g}\right)^{*} \boldsymbol{f}$ terminates.

Bullo (140) showed that if the mechanical system structure satisfies (7.10) and (7.11) and the control inputs $v^a(t)$ satisfy

$$\int_0^T v^a(\tau)\, d\tau = 0 \quad \text{and} \quad \int_0^T \int_0^\tau v^a(s)\, ds\, d\tau = 0 \tag{7.12}$$

then the averaged dynamics corresponding to the system (7.8) are written as

$$\ddot{\boldsymbol{r}} = \boldsymbol{Z}(\boldsymbol{r}, \dot{\boldsymbol{r}}) + \boldsymbol{X}_0(\boldsymbol{r}) + \boldsymbol{R}(\boldsymbol{r})\dot{\boldsymbol{r}} - \sum_{a,b=1}^{m} \Lambda_{ab} \langle \boldsymbol{X}_a(\boldsymbol{r}) : \boldsymbol{X}_{\mathrm{b}}(\boldsymbol{r}) \rangle \tag{7.13}$$

where

$$\Lambda_{ab} = \frac{1}{2T} \int_0^T \left(\int_0^\tau v^a(s)\, ds \right) \left(\int_0^\tau v^b(s)\, ds \right) d\tau$$

That is, there exists $\epsilon_0 > 0$ such that, for all $\epsilon \in (0, \epsilon_0]$,

$$\begin{aligned} \boldsymbol{q}(t) &= \boldsymbol{r}(t) + O(\epsilon) \\ \dot{\boldsymbol{q}}(t) &= \dot{\boldsymbol{r}}(t) + \left(\int_0^t v^a(s)\, ds \right) \boldsymbol{X}_a + O(\epsilon) \end{aligned} \tag{7.14}$$

7.6 The FWMAV System Revisited

This section shows the FWMAV model developed in Section 7.4 in the context of Section 7.5. Noting that one of the system parameters depends on one of the generalized velocities $\eta = \eta(\dot{\varphi})$, the FWMAV system structure may not be amenable to apply the averaging results of the previous section. However, since the dependence is on the sign of $\dot{\varphi}$ only, the dynamic structure of the FWMAV still satisfies the conditions (7.10) and (7.11). In particular, we have the generalized inertia

$$\boldsymbol{m}(\boldsymbol{q}) = \begin{bmatrix} m_v & 0 & M_{13} & M_{14} \\ 0 & m_v & M_{23} & 0 \\ M_{13} & M_{23} & M_{33} & M_{34} \\ M_{14} & 0 & M_{34} & M_{44} \end{bmatrix}$$

where

$$\begin{aligned} M_{13} &= m_w d \sin\eta \\ M_{14} &= m_w (d \cos\eta \sin\varphi + r_{cg} \cos\varphi) \\ M_{23} &= m_w (d \cos\eta \cos\varphi - r_{cg} \sin\varphi - x_h) \\ M_{33}(x_h = 0) &= I_{yb} + I_y \cos^2\varphi + \sin^2\varphi (I_x \cos^2\eta + I_z \sin^2\eta) \\ M_{34} &= \sin\varphi \sin\eta \cos\eta (I_z - I_x) \\ M_{44} &= (I_x \sin^2\eta + I_z \cos^2\eta) \end{aligned}$$

and the input vector field is written as

$$\hat{\boldsymbol{X}}_{\tau_\varphi}(\boldsymbol{q}) = [0\ 0\ 0\ 1]^T$$

It has been shown in chapter 5 that there are two ways to achieve trim for a FWMAV in hover. The first of these is considered here, in which the wing hinge is aligned with the body center of gravity ($x_h = 0$) and the wings execute symmetric flapping motions (identical upstroke and downstroke). The control input

is written as

$$\tau_\varphi(t) = U\cos\omega t$$

which satisfies (7.12). Then its corresponding coefficient Λ is given by $\Lambda = \frac{U^2}{4\omega^2}$.

The symmetric product $\langle \boldsymbol{X}_{\tau_\varphi} : \boldsymbol{X}_{\tau_\varphi} \rangle$ may be easily determined using symbolic software, resulting in (lengthy) expressions involving the generalized coordinates $\boldsymbol{q}$ and the geometric and aerodynamic parameters. Using an overbar to indicate time-averaged quantities, the averaged dynamics of (7.3) is then written as

$$\ddot{\bar{\boldsymbol{q}}} = \boldsymbol{Z}(\bar{\boldsymbol{q}}, \dot{\bar{\boldsymbol{q}}}) + \boldsymbol{X}_0(\bar{\boldsymbol{q}}) + \boldsymbol{R}(\bar{\boldsymbol{q}})\dot{\bar{\boldsymbol{q}}} - \frac{U^2}{4\omega^2}\langle \boldsymbol{X}_{\tau_\varphi}(\bar{\boldsymbol{q}}) : \boldsymbol{X}_{\tau_\varphi}(\bar{\boldsymbol{q}}) \rangle \tag{7.15}$$

7.7 Maneuverability Optimization

One can relate the maneuverability of the FWMAV to the elements of the symmetric product defined earlier, as these components directly affect acceleration in the averaged dynamics. Our objective is to formulate an optimization problem in which the design variables are the system parameters and the objective function is a specific element of a symmetric product evaluated at the desired fixed point of the averaged dynamics. This fixed point should correspond to the desired periodic orbit of the original system.

Symmetric downstroke/upstroke flapping at hover is considered; that is $(\bar{\boldsymbol{q}}_0, \dot{\bar{\boldsymbol{q}}}_0) = (\boldsymbol{0}, \boldsymbol{0})$. For this state to be a fixed point for the averaged dynamics, the right hand side of Eq. (7.15) evaluated at the origin must vanish. The vector fields in Eq. (7.15) evaluated at the origin with zero $x_h = 0$ have the following components

$$\begin{aligned} \boldsymbol{Z}(\boldsymbol{0},\boldsymbol{0}) + \boldsymbol{X}_0(\boldsymbol{0}) &= [0 \ , \ g \ , \ 0 \ , \ 0]^T \\ \langle \boldsymbol{X}_{\tau_\varphi} : \boldsymbol{X}_{\tau_\varphi} \rangle(\boldsymbol{0}) &= [0 \ , \ 2K_{21}\sin 2\alpha_m \times \tfrac{WIC}{m_v} \ , \ 0 \ , \ 0]^T \end{aligned}$$

where $K_{21} = \frac{1}{2}\rho A I_{21}$ and WIC represents a lengthy expression containing the wing-inertia contribution. Thus, similar to the results obtained by neglecting the wing dynamics, aligning the hinge line with the body center of gravity along with symmetric flapping automatically ensures zero cycle-averaged forward thrust force and pitching moment, see Doman *et al* (9) and Taha *et al* (170). In addition, it ensures zero cycle-averaged flapping acceleration. Hence, we are left with one trim equation to be satisfied; that is, the cycle-average lift has to balance the weight.

$$K_{21}\sin 2\alpha_m \frac{U^2 \times WIC}{2\omega^2} = m_v g \tag{7.16}$$

This equation is analogous to the one determined by neglecting the wing dynamics and considering $\varphi(t) =$

$\Phi\cos\omega t$. The lift constraint

$$\overline{L} = \frac{\omega}{2\pi}\int_0^{\frac{2\pi}{\omega}} 2\int_0^R \frac{1}{2}\rho r^2\dot{\varphi}^2(t)c(r)A\sin 2\alpha_m\, dr\, dt = m_v g$$

is then written as

$$K_{21}\sin 2\alpha_m \frac{\omega^2\Phi^2}{2} = m_v g \tag{7.17}$$

It is interesting to note that $\lim_{m_w\to 0} WIC = \frac{1}{I_x^2\sin^2\alpha_m}$. Thus, in the limit to a vanishing wing mass, the flapping amplitude is related to the torque amplitude via $\Phi = \frac{U}{\omega^2 I_x\sin^2\alpha_m}$.

Having achieved balance (trim) at hover, our objective is then to maximize the upward acceleration of the averaged dynamics from the hovering position; that is $\dot{\overline{w}}(\mathbf{0})$ due to the maximum allowable torque. This quantity is considered as the maneuverability index in this analysis and is given by

$$\dot{\overline{w}}(\mathbf{0})_{max} = \frac{U_{max}^2 - U_0^2}{4\omega^2}\boldsymbol{X}_{\varphi\varphi 2} \tag{7.18}$$

where U_{max} is the maximum allowable torque amplitude, U_0 is the balancing torque amplitude (required for trim) which satisfies Eq. (7.16), and $\boldsymbol{X}_{\varphi\varphi 2}$ is the second entry of the symmetric product vector field $\langle \boldsymbol{X}_\varphi : \boldsymbol{X}_\varphi\rangle$. Note that using the above configuration, the pitch angular acceleration cannot be manipulated because setting $x_h = 0$ results in lack of pitch control authority at hover (9). In addition, zero x_h along with symmetric flapping results in lack of forward thrust control authority at hover too.

We consider a trapezoidal wing having a radius R, aspect ratio AR, taper ratio λ, and planform area S. The vector of design variables is $x = [AR\ \lambda\ f\ \alpha_m]^T$. Given a fixed mass of the body m_b, the mass of the vehicle is then $m_v = m_\mathrm{b} + m_\mathrm{w}$, where $m_\mathrm{w} = 2\int_0^R m'c(r)\,dr = 2m'S$ and m' is the wing mass per unit area, which is assumed to be uniform. The following approximations are used

$$I_x = 2\int_0^R m' r^2 c(r)\,dr = m' I_{21}$$

$$I_y = 2\int_0^R m'\hat{d}c^3(r)\,dr = m'\hat{d}I_{03}$$

where $\hat{d}$ is the chord-normalized distance from the wing hinge line to the center of gravity line.

$$I_z = I_x + I_y \ \text{ and } \ r_{cg} = \frac{\int_0^R m' r c(r)\,dr}{m_\mathrm{w}/2} = \frac{I_{11}}{2S}$$

The optimization problem is formulated as follows

$$\max_{x} \quad \dot{\overline{w}}(\mathbf{0})_{max} \quad \text{subject to}$$

$$U_0 = \omega\sqrt{\frac{2m_v g}{K_{21} W I C \sin 2\alpha_m}} \leq U_{max}$$

$$\text{and} \;\; x_{\text{LB}} < x < x_{\text{UB}}$$

where x_{LB} and x_{UB} are the lower and upper bounds of the design variables, respectively. The hawkmoth data is considered as a case study. The values for the wing radius, body mass, and moment of inertia about the y_{b}-axis (11) are given by

$$R = 51.9\ mm, \;\; m_{\text{b}} = 1.648\ \text{g} \;\text{ and }\; I_{yb} = 2.080\ \text{g cm}^2$$

Assuming uniform areal distribution for the wing mass, its density is deduced from Ellington (57) to be $m' = 0.005\ \text{g/cm}^2$. A maximum allowable torque for tiny actuators is considered as $U_{max} = 1\ mN.m$. The hinge is assumed to lie at the 30% chord station ($\Delta\hat{x} = 0.05$) and the wing-section center of gravity to lie at the 45% chord station ($\hat{d} = 0.15$). The distance between the wing root hinge point and the wing center of gravity along the negative x_w-axis is then given by

$$d = \hat{d} c_r \left(1 - (\lambda - 1)\frac{r_{cg}}{R}\right)$$

where c_r is the root chord dictated from the trapezoidal chord distribution as $c_r = \frac{2S}{(1+\lambda)R}$, and $S = \frac{R^2}{AR}$. Table 7.1 shows the lower and upper bounds for the design variables.

Table 7.1: Design parameter bounds.

Variable	x_{LB}	x_{UB}
Wing aspect ratio, AR	1	10
Wing taper ratio, λ	0	1
Flapping frequency, f	0	∞
Mean Angle of Attack, α_m	0	$\frac{\pi}{2}$

It is found that the optimum solution lies on the boundaries of the design variables. A parametric study, which is shown in Fig. 7.1, is performed on the objective function, $\dot{\overline{w}}(\mathbf{0})_{max}$, to support the optimizer converged solution. While varying one of the design variables to assess its effect on the objective, the other

design variables assume the following values

$$x = [3,\ 1,\ 25Hz,\ 30^\circ]^T$$

Some interesting conclusions can be drawn from the performed analysis either for the FWMAV hovering example per se or for the general optimization of a vehicle's maneuverability.

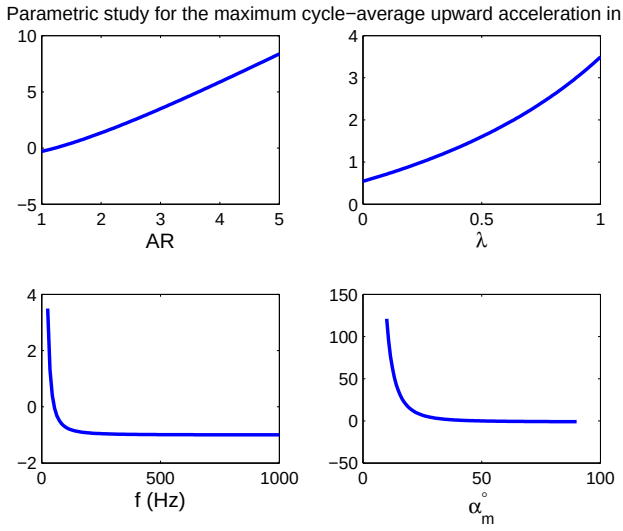

Figure 7.1: Parametric Study for the maximum cycle-average upward acceleration $\dot{\overline{w}}(\mathbf{0})_{max}$ with fixed R.

Including the effects of wing mass and inertia results in considerably different behaviors from those obtained by neglecting the wing dynamics. Firstly, although increasing the aspect ratio for a given wing radius results in a decreased wing area and consequently decreased aerodynamic loads, the inertial contributions leads to a favorable effect of AR on $\dot{\overline{w}}$. It should be noted that, however, fixing the wing area instead leads to an unfavorable effect of AR on $\dot{\overline{w}}$, as shown in Fig. 7.2. Therefore, if the wing radius is specified, a high aspect ratio rectangular wing will result in the maximum cycle-average upward acceleration. Secondly, neglecting the wing dynamics and dealing with a specified kinematics for the flapping angle $\varphi(t)$ suggests higher flapping frequencies for higher aerodynamic loads (particularly the lift force) and consequently higher accelerations. However to achieve the required flapping amplitude with a very high frequency a considerably large torque amplitude is required which is constrained to U_{max}. Since the lift is proportional to $\omega^2\Phi^2$, $\Phi \propto \frac{U}{\omega^2}$, and U is set to U_{max}, the net result is that a lower $f(\omega)$ is recommended for higher $\dot{\overline{w}}$. Thirdly, the kinematic analysis suggests a 45° mean angle of attack for the maximum lift and consequently $\dot{\overline{w}}$ because of the $\sin 2\alpha$ in the lift expression. However, as shown previously (at least in the limit to vanishing m_w) $\Phi = \frac{U}{\omega^2 I_x \sin^2 \alpha_m}$;

that is, $\dot{\overline{w}}$ approaches infinity as α_m approaches zero. Therefore, the maneuverability-optimum mean angle of attack is no longer 45° but as low as possible.

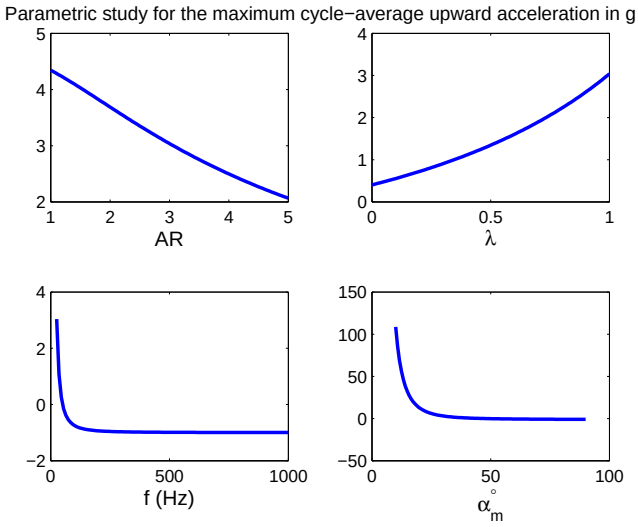

Figure 7.2: Parametric Study for the maximum cycle-average upward acceleration $\dot{\overline{w}}(\mathbf{0})_{max}$ with fixed S.

One of the very important and intuitive questions that may arise with this analysis is that "As far as the vehicle's maneuverability is concerned, why one does not directly maximizes the elements of the input vector fields instead of following the proposed approach?" This intuitive question stems from the fact that those elements of the input vector fields are known to directly affect, not only the averaged, but also the instantaneous accelerations. In fact, the answer to this question represents the main motivation and novelty of the proposed approach. It should be noted that the above claim may be misleading for systems forced by high-frequency periodic inputs. In the worked example of hovering FWMAVs, the input vector field $\boldsymbol{X}_{\tau_\varphi}$ includes non-zero components in all directions. In addition, it has non zero components in both of the longitudinal and pitching accelerations even at the trim configuration ($x_h = 0$ and $\overline{\varphi} = 0$). However, it has been already shown that the corresponding contributions to the averaged dynamics (corresponding components of the symmetric product $\langle \boldsymbol{X}_\varphi : \boldsymbol{X}_\varphi \rangle$) are zero. In fact, this is one of the main drawbacks of the adopted trim configuration (symmetric flapping and zero x_h); that is, it leads to a lack in forward thrust and pitch control authority. Thus, although there are nonzero instantaneous contributions to those accelerations, because of the high frequency periodic nature of the applied torque and consequently the resulting kinematics, there are no contributions to the corresponding averaged accelerations; contributions cancel out over the flapping cycle. One more issue that is noteworthy is the deceptive indication of having a lack of control authority in some direction. Projecting on the adopted example, the second entry of the vector

field $\boldsymbol{X}_{\tau_\varphi}$ evaluated at the trim configuration is zero, falsely indicating the lack of vertical motion control authority at hover. On the contrary, there is a considerable ability to produce upward acceleration which is considered as an objective in maximizing maneuverability. This is a common trait of the geometric control theory; that is to allow us to generate motions in unactuated directions. Finally, a clear issue, though, needs to be stressed is the necessity to apply the variation of constants formula before averaging. Otherwise, direct averaging is not useful in this analysis as it leads to vanishing contributions from the zero-mean periodic inputs.

7.8 Conclusion

In this work, we have considered the problem of optimizing maneuverability of a flapping-wing micro-air vehicle in longitudinal flight near hover. In modeling the vehicle, we have accounted for the wing-dynamics of the back and forth flapping degree of freedom, so that the flight dynamic model has four degrees of freedom. The resulting system is an under-actuated, nonlinear mechanical system with time-periodic forcing. We have used tools from geometric control and averaging theory to derive analytical expressions for vector fields, known as *symmetric products*, which play a crucial role in the averaged dynamics. Because these vector fields are directly related to the vehicle's acceleration, and they depend on system parameters, we have proposed formulating and solving design optimization problems, such as maximizing maneuverability. We have provided an example to illustrate this approach for design optimization of a flapping-wing micro-air vehicle, focusing on the cycle-averaged upward acceleration of the body as a maneuverability index: fast vertical takeoff.

It has been found that direct optimization of the elements of the input vector fields does not guarantee optimization of the resulted vehicle's accelerations for a high-frequency periodically forced system. This is due to the fact that the generated accelerations may cancel each other resulting in a zero cycle-averaged acceleration and net motion. The proposed approach resolves this by maximizing the elements of the symmetric product vector fields instead, which directly affect the averaged dynamics. It also gives the ability to produce motions in unactuated directions.

Chapter 8

Conclusions and Future Work

8.1 Conclusions

In this dissertation, we have provided analytical formulations for the unsteady aerodynamics, kinematic optimization, flight dynamics, and control of flapping-wing micro-air-vehicles (FWMAVs). A FWMAV represents a complex multi-disciplinary system whose analysis invokes the frontiers of the aerospace engineering disciplines. From the aerodynamic point of view, a nonlinear, unsteady flow is created by the flapping motion. In addition, non-conventional contributors, such as the leading edge vortex, to the aerodynamic loads become dominant in flight. On the other hand, the flight dynamics of a FWMAV constitutes a nonlinear, non-autonomous dynamical system. Furthermore, the stringent weight and size constraints that are always imposed on FWMAVs invoke a design with minimal actuation. The main conclusions/contributions of this dissertation are stated below.

A thorough literature survey: We have provided a thorough literature review of the significant work done in the mechanics of flapping flight. This includes aerodynamic modeling, kinematic design, flight dynamics and control. Based on this review, we have proposed some un-answered technical questions which have been tackled throughout the dissertation.

Analytical unsteady aerodynamic model: The literature survey has revealed that there exists no unsteady aerodynamic model that could capture the dominant contribution to the aerodynamic loads on hovering insects (i.e., leading edge vortex) with a feasible computational burden so that it could be used in optimization, sensitivity analysis, dynamics and control. Literature is teeming with potential-flow, linear, unsteady models whose asymptotic steady behavior is the pure linear lift curve. These

models cannot capture the effects of any non-conventional lift mechanisms such as the leading edge vortex. On the other hand, there have been recent experimental efforts that have lead to simple empirical algebraic relations for the quasi-steady effects of the leading edge vortex on hovering insects. Clearly, these steady empirical models cannot be used solely because the unsteady effects of such flow filed are quite significant.

In this dissertation, we have developed an unsteady aerodynamic model whose asymptotic steady behavior is dictated by the empirical models that capture the quasi-steady effects of the leading edge vortex. This is achieved by extending Duhamel's superposition principle to non-conventional lift mechanisms. The underpinning assumption is the linearity of the lift with respect to the circulation and the use of the quasi-steady circulation as an aerodynamic input to Duhamel's integral. In addition, finite-state unsteady aerodynamics have been adopted to derive a two-dimensional, second-order model that is quite suitable for aeroelasticity and flight dynamic analyses. Moreover, a three-dimensional, fourth-order model has been developed that is even more suitable for such applications. The lift generated by the developed models has been validated against the lift resulting from direct numerical simulation of Navier-Stokes equations on the wings of different hovering insects. Good agreement with the results of Navier-Stokes equations has been shown in comparison to those of the linear unsteady models and the nonlinear quasi-steady models. In particular, during the mid-stroke periods, where the leading-edge-vortex contribution becomes dominant, the developed models show a significant improvement over the classical (linear) unsteady models. Also, during stroke reversals, where the rotational contribution becomes dominant, the developed model show a significant improvement over the quasi-steady empirical models.

Kinematic optimization as a calculus of variations problem The wing kinematics (wing motion with respect to the body) is usually described by three Euler angles; the back and forth flapping angle, the pitching angle, and the plunging angle. Two frameworks have been identified within which optimal time-variations of these Euler angles are usually sought; aerodynamic performance and control authority. In one framework, specific patterns along with some parametrization for the kinematic angles are assumed from the outset. Then, the parameters of the assumed functions are used as design variables in a finite dimensional optimization problem to enhance the desired aerodynamic performance index; e.g., minimum power or maximum thrust. This approach induces more constraints to the optimization problem because the true optimal functions do not have to be on the assumed forms, irrespective of what these forms are. Thus, the obtained results are the optimal ones within the family of the assumed functions but not the absolutely optimal ones. In this dissertation, we have relaxed these additional constraints that are induced by approximating the infinite-dimensional optimization problem to a finite-dimensional one. We have formulated and solved a calculus of variations problem to obtain the

true optimal time-variations of the flapping and pitching angles that result in hovering with minimum aerodynamic power. We have shown that a triangular waveform for the flapping angle along with a piecewise constant variation for the pitching angle form the true optimal pair. The aerodynamic performance due to this true optimality forms a reference performance against which the performance of any other proposed kinematics can be compared to assess how far the performance of this proposed kinematics from the reference one (like the Carnot cycle in thermodynamics or the Betz law in the operation of wind turbines.)

In the other framework, no constructive techniques have been used to derive the wing kinematics. The kienamtic functions are also assumed from the outset with some parametrization to achieve high control authority for the averaged dynamics. In this dissertation, we have used the calculus of variations and optimal control techniques to derive the optimal time-variation of the flapping angle that maximizes the cycle-averaged forward acceleration from a hovering position using a horizontal stroke plane subject to the lift equality constraint. The sought kinematics would be suitable for sudden collision avoidance and possibly for fastest transition from hovering to forward flight. It has been found that an additional constraint on the wing speed must be added to have a well-posed, and also realistic, optimization problem. The addition of this constraint has changed the problem from a conventional calculus of variations problem to an optimal control one where Pontryagin's maximum principle provides the necessary conditions. Picking the physically intuitive solution from the possible outcomes of Pontryagin's principle, the problem has been formulated as a point-to-curve calculus of variations problem. The analytical formulation of the problem has lead to an interesting result. That is, the cycle-averaged forward acceleration resulted from any set of kinematics approach some fixed asymptotic finite value for infinite maximum wing speed. This asymptotic value (limit), which represents the maximum cycle-averaged forward acceleration that a flapping vehicle can ever generate from the hovering position, is simply the drag-to-lift fraction of the gravitational acceleration.

Saturation-based design of the actuation mechanism: Hovering and forward flight require different wing motions and consequently independent actuators. Horizontal stroke plane is preferred for hovering while plunging is essential for forward flight. In addition, there are stringent weight and size constraints imposed on the design of FWMAVs. In this dissertation, we have proposed a design methodology for the actuation mechanism that can provide the required kinematics in both flight conditions using only one actuator. The idea is not as trivial as instrumenting the FWMAV by a single actuator in a tilted plane so as to have components in both directions. The idea is to achieve almost pure horizontal motion for the wing (appropriate for hovering) and when desired, the motion is transferred to have almost pure vertical motion that is appropriate for forward flight. This is achieved by exploiting the nonlinearities of the wing dynamics to induce the saturation phenomenon such that the energy is

transferred in the favorable direction.

The saturation phenomenon takes place when a two degree-of-freedom mechanical system having a special quadratic nonlinearity exhibits an external resonance and a two-to-one internal resonance. Then, if the amplitude of the oscillating force exceeds a specific threshold, the steady-state amplitude of the directly forced mode saturates and does not increase with any further increase in the forcing amplitude. On the other hand, the other unforced mode sinks the energy and its steady-state amplitude increases as the forcing amplitude increases. This idea has been exploited in the flapping wing dynamics where the two modes are the horizontal flapping and vertical plunging. Horizontal actuator is used to directly provide the required kinematics at hover. If forward flight is required instead, linear feedback gains are tuned to achieve the saturation resonance requirements and nonlinear feedback gains are tuned to provide the quadratic nonlinearities essential to induce saturation. As such, the motion is transferred from the horizontal flapping to the vertical flapping mode. The system parameters can be tuned to make the saturated amplitude of the horizontal motion vanishingly small.

Analytical flight dynamic analysis: In this dissertation, we have developed an analytical flight dynamic model that accounts for the aerodynamic loads due to the body motion variables in a nonlinear sense. The used aerodynamic model captures the dominant contributions of flapping flight; the leading edge vortex and rotational effects. This tight aerodynamic-dynamic coupling along with the analytical formulation of the problem have lead to interesting results about the dynamics of hovering insects. Firstly, the symmetric-flapping trim-configuration leads to vanishing of five out of the nine cycle-averaged stability derivatives. Also, it leads to a higher damping in the longitudinal direction, higher speed stability derivative, and lower damping in both of the vertical and pitching directions. Secondly, increasing the mean angle of attack and/or flapping frequency has similar effects on the stability derivatives; that is, the lead to a higher damping in the longitudinal direction, higher speed stability derivative, and lower damping in both of the vertical and pitching directions. Thirdly, backward hinge locations are favorable for speed stability. Realizing, via Routh-Hurwitz stability analysis, that speed stability is a must to conclude stability for the whole system, a fore hinge location (specifically ahead of the wing's center of pressure) leads to instability of the system irrespective of the values of the other parameters and derivatives. Thus, unlike conventional aircraft, stability of the symmetric-flapping trim-configuration necessitates backward center of gravity position (coincident with the hinge location).

Higher-order techniques in the stability analysis: Flapping flight dynamics constitutes a nonlinear, time-periodic systems. Two basic approaches are usually adopted to analyze the dynamic stability of such system; the Floquet theorem approach and the averaging approach. In this dissertation,

we have shown that the numerical error associated with the implementation of the Floquet theorem approach may lead to false conclusions about the system's stability. Also, we have shown that the zero-mean aerodynamic-induced parametric excitation terms that are neglected by direct averaging provide stabilizing actions to the flight dynamics of hovering insects. Two methodologies have been proposed to overcome the shortcomings of the previous approaches; the method of multiple scales and the generalized averaging theory. In particular, using the generalized averaging approach (second-order averaging), we have determined the specific stabilizing mechanism that is induced by the aerodynamic-induced parametric excitation; a pitch stiffness action. Also, using second-order averaging, we have shown that the interaction between the high-amplitude, periodic aerodynamic loads due to the flapping motion of the wing and the time-varying dynamics results in an unbalanced (untrimmed) system and consequently leads to another equilibrium (not hovering). That is, a cycle-averaged lift that is equal to the weight does not guarantee balance in the vertical direction because the periodic aerodynamic forces interact with the body oscillation resulting in a negative lift force. As such, the FWMAV/insect has to flap more to support its weight. Unfortunately, this new operating parameters (higher flapping amplitude) leads to an unstable hovering dynamics in spite of the aerodynamic-induced pitch stiffness.

Geometric control and maneuverability: Geometric control theory and averaging can be combined to provide useful analysis tools for mechanical systems subject to high-frequency, high-amplitude, periodic forcing. Using such tools, the effects of these forces on the body averaged accelerations appear through what is called *symmetric product* vector fields. In this dissertation, we have proposed a design methodology that considers the vehicle's maneuverability early in the design process instead of designing the vehicle for minimum operating cost and assessing the maneuverability level at a later stage. Since symmetric product vector fields directly affect the averaged acceleration of the body, maximization of the components of these symmetric products will result in a vehicle with optimum maneuverability. Relying on the ability to analytically determine these symmetric products, we have formulated a design optimization problem in which the vertical acceleration component of the symmetric product vector field is maximized. Such a design will lead to fast vertical takeoff. We have shown that direct maximization of the components of the input vector fields (that directly affect not only the averaged but also the instantaneous accelerations of the body) may be deceptive. This is because the oscillation of the input signal may lead to a zero net averaged acceleration for the body. Thus, following the proposed approach for maneuverability maximization of periodically-forced vehicles is necessary in comparison to any direct or brute-force approach. Moreover, we have shown that the proposed approach will exploit the ability to generate motions in unactuated directions due to high-frequency, high-amplitude periodic forcing. That is, it will remove any deceptive lack of control authority.

8.2 Future Work

Indeed, analysis of flapping flight invokes the frontiers of the aerospace engineering disciplines. Throughout this dissertation, we have proposed a number of research points that need to be addressed in the future.

Unsteady, nonlinear aerodynamic modeling: In general, there are two common shortcomings when applying the classical linear unsteady models to non-conventional flights or to a high angle of attack regime. These are the nonlinearity of the flow dynamics and the nonlinearity of the asymptotic steady behavior. In this dissertation, we have come up with a methodology to overcome the second shortcoming while assuming the linearity of the flow dynamics to hold. Therefore, there is still a need to develop unsteady models that account for the nonlinearity of the lift build up.

Kinematic optimization: In this dissertation, we have formulated and solved a calculus of variations problem to obtain the true optimal wing kinematics that minimizes the hovering aerodynamic power; i.e., aerodynamic power under lift constraint. The intuitive, ubiquitous lift constraint is that the cycle-averaged lift due to flapping is equal to the weight. However, we have shown in chapter 6 that this balancing methodology is not sufficient to achieve trim because the interaction of the periodic aerodynamic forcing with the oscillation of the body motion results in a negative lift force. This raises the need to formulate a design optimization problem in which the balancing constraint accounts for this interaction determined by the second-order averaged dynamics; that is, use Eq. (6.26) as the trim constraint. Because of the structure of Eq. (6.26), the formulated problem will not be a classical calculus of variations problem but an optimal control one. The effect of this new trim constraint on the optimum performance should be of interest.

Another extension to the kinematic optimization problem is to use the full dynamics (not the averaged one) and apply Pontryagin's maximum principle to drive the system from some periodic orbit (not a fixed point), say hover, to another periodic orbit, say forward flight with some speed, while minimizing a given cost functional, say final time. On the other hand, there is a need to extend Pontryagin's principle to handle a periodicity constraint of a control input.

Transition from hovering to forward flight: In this dissertation, we have proposed a design methodology for an actuation mechanism that can provide the required kinematics for both of hovering and forward flight using one actuator. However, there is still a need to analyze the flight dynamics during the transition phase (from hovering to forward flight) and to design control laws that achieve this objective efficiently.

Adaptive nonlinear control: We have shown that the aerodynamics of flapping flight can be described by simple analytical models that include some parameters (e.g., lift curve slope and drag coefficient).

However, exact determination of these parameters for all of the regimes and types of flapping flight might be impossible. Thus, adaptive control is an appropriate candidate for designing robust controllers for flapping-wing micro-air-vehicles.

Nonlinear controllability: We have shown that high-frequency, high-amplitude, periodic forcing may lead to motions in un-actuated directions and may also lead to stabilizing actions. So, it would be of great interest to analyze the flight dynamics of hovering insects in a geometric control framework so as to relate their morphological changes to locomotion and stability. For example, it has been noticed that the humming bird performs an almost pure pitching maneuver at hover. So, the question is "what is the symmetric product vector field that spans this direction in the tangent space (direction of body pitching)?" Then, what is the morphological change that realizes the flow along this symmetric product vector field?

Bibliography

[1] Khan, Z. A. and Agrawal, S. K., "Force and Moment Characterization of Flapping Wings for Micro Air Vehicle Application," IEEE American Control Conference, 2005, pp. 1515–1520.

[2] Khan, Z. A. and Agrawal, S. K., "Control of Longitudinal Flight Dynamics of a Flapping Wing Micro Air Vehicle Using Time Averaged Model and Differential Flatness Based Controller," IEEE American Control Conference, 2007, pp. 5284–5289.

[3] Dickinson, M. H., Lehmann, F.-O., and Sane, S. P., "Wing rotation and the aerodynamic basis of insect flight." *Science*, Vol. 284, No. 5422, 1999, pp. 1954–1960.

[4] Pesavento, U. and Wang, Z. J., "Navier-stokes solutions, model of fluid forces, and center of mass elevation," *Phys. Rev. Lett.*, Vol. 93, 2004.

[5] Andersen, A., Pesavento, U., and Wang, Z., "Unsteady aerodynamics of fluttering and tumbling plates," *Journal of Fluid Mechanics*, Vol. 541, 2005, pp. 65,90.

[6] Andersen, A., Pesavento, U., and Wang, Z. J., "Analysis of Transitions Between Fluttering, Tumbling and Steady Descent of Falling Cards," *Journal of Fluid Mechanics*, Vol. 541, 2005, pp. 91,104.

[7] Schenato, L., Campolo, D., and Sastry, S. S., "Controllability Issues in Flapping Flight for Biomemetic MAVs," Vol. 6, 42nd IEEE conference on Decision and Control, 2003, pp. 6441–6447.

[8] Oppenheimer, M. W., Doman, D. B., and Sigthorsson, D. O., "Dynamics and Control of a Minimally Actuated Biomimetic Vehicle, Part II- Control," No. 2009-6161, AIAA Guidance, Navigation, and Control Conference, Chicago, Illinois.

[9] Doman, D. B., Oppenheimer, M. W., and Sigthorsson, D. O., "Wingbeat Shape Modulation for Flapping-Wing Micro-Air-Vehicle Control During Hover," *Journal of Guidance, Control and Dynamics*, Vol. 33, No. 3, 2010, pp. 724–739.

[10] Doman, D. B., Oppenheimer, M. W., and Sigthorsson, D. O., "Dynamics and Control of a Biomimetic Vehicle Using Biased Wingbeat Forcing Functions: Part II: Controller," AIAA-paper 2010-1024, Jan 2010.

[11] Sun, M., Wang, J., and Xiong, Y., "Dynamic Flight Stability of Hovering Insects," *Acta Mechanica Sinica*, Vol. 23, No. 3, 2007, pp. 231–246.

[12] Cheng, B. and Deng, X., "Translational and Rotational Damping of Flapping Flight and Its Dynamics and Stability at Hovering," *IEEE Transactions On Robotics*, Vol. 27, No. 5, 2011, pp. 849–864.

[13] Nelson, R. C., *Flight Stability and Automatic Control*, McGraw-Hill, 1989.

[14] Gebert, G. and Gallmeier, P., "Equations of Motion for Flapping Flight," AIAA Atmospheric Flight Mechanics Conference, 2001.

[15] Sun, M. and Xiong, Y., "Dynamic flight stability of a hovering bumblebee." *Journal of Experimental Biology*, Vol. 208, No. 3, 2005, pp. 447–459.

[16] Xiong, Y. and Sun, M., "Dynamic Flight Stability of a Bumble Bee in Forward Flight," *Acta Mechanica Sinica*, Vol. 24, No. 3, 2008, pp. 25–36.

[17] Hedrick, T. L., Cheng, B., and Deng, X., "Wingbeat Time and the Scaling of Passive Rotational Damping in Flapping Flight," *Science*, Vol. 324, No. 5924, 2009, pp. 252–255.

[18] Faruque, I. and Humbert, J. S., "Dipterian Insect Flight Dynamics. Part 1 Longitudinal Motion About Hover," *J. Theor. Biol.*, Vol. 264, No. 2, 2010, pp. 538552.

[19] Doman, D. B., Oppenheimer, M. W., and Sigthorsson, D. O., "Dynamics and Control of a Minimally Actuated Biomimetic Vehicle, Part I- Aerodynamic Model," No. 2009-6160, AIAA Guidance, Navigation, and Control Conference, Chicago, Illinois.

[20] Weis-Fogh, T., "Quick Estimates of Flight Fitness in Hovering Animals, Including Novel Mechanisms for Lift Production," *Journal of Experimental Biology*, Vol. 59, No. 1, 1973, pp. 169–230.

[21] Ellington, C. P., "The aerodynamics of hovering insect flight: III. Kinematics," *Philosophical Transactions Royal Society London Series B*, Vol. 305, 1984, pp. 41–78.

[22] Su, W. and Cesnik, C. E. S., "Flight Dynamic Stability of a Flapping Wing MAV in Hover," AIAA-Paper 2011-2009, Apr 2011.

[23] Taylor, G. K. and Thomas, A. L. R., "Dynamic Flight Stability in the Desert Locust," *Journal of Theoretical Biology*, Vol. 206, 2003, pp. 2803–2829.

[24] Deng, X., Schenato, L., Wu, W. C., and Sastry, S. S., "Flapping Flight for Biomemetic Robotic Insects: Part II Flight Control Design," *IEEE Transactions on Robotics*, Vol. 22, No. 4, 2006, pp. 789–803.

[25] Oppenheimer, M. W., Doman, D. B., and Sigthorsson, D. O., "Dynamics and Control of a Biomimetic Vehicle Using Biased Wingbeat Forcing Functions," *Journal Guidance, Control and Dynamics*, Vol. 34, No. 1, 2011, pp. 204–217.

[26] Dietl, J. M. and Garcia, E., "Stability in Ornithopter Longitudinal Flight Dynamics," *Journal of Guidance, Control and Dynamics*, Vol. 31, No. 4, 2008, pp. 1157–1162.

[27] Chung, S.-J. and Dorothy, M., "Neurobiologically Inspired Control of Engineered Flapping Flight," *J. Guidance, Control and Dynamics*, Vol. 33, No. 2, 2010, pp. 440–452.

[28] Su, W. and Cesnik, C. E. S., "Coupled Nonlinear Aeroelastic and Flight Dynamic Simulation of a Flapping Wing Micro AirVehicle," International Forum on Aeroelasticity and Structural Dynamics, 2009.

[29] Su, W. and Cesnik, C. E. S., "Nonlinear Aeroelastic Simulations of a Flapping Wing Micro Air Vehicle Using Two Unsteady Aerodynamic Formulations," 51st AIAA/ASME/ASCE/AHS/ASC Structures, Structural Dynamics, and Materials Conference, 2010.

[30] Wood, R. J., "The First Takeoff of a Biologically Inspired At-Scale Robotic Insect," *IEEE Transactions on Robotics and Automation*, Vol. 24, No. 2, 2008, pp. 341–347.

[31] Willmott, A. P. and Ellington, C. P., "The mechanisms of Flight in the Hawkmoth Manduca Sexta, I: Kinematics of Hovering and Forward Flight," *Journal of Experimental Biology*, Vol. 200, No. 21, 1997.

[32] Gradshteyn, I. S. and Ryzhik, I. M., *Table of Integrals, Series and Products*, Academic Press, 6th ed., 200.

[33] Oppenheimer, M. W., Doman, D. B., and Sigthorsson, D. O., "Dynamics and Control of a Biomimetic Vehicle Using Biased Wingbeat Forcing Functions: Part I: Aerodynamic Model," No. 2010-1023, AIAA.

[34] Sigthorsson, D. O., Oppenheimer, M. W., and Doman, D. B., "Flapping Wing Micro-Air-Vehicle Control Employing Triangular Wave Strokes and Cycle-Averaging," AIAA-paper 2010-7553, Aug 2010.

[35] Hooper, S. L., "Central Pattern Generators," *Nature Encyclopedia of Life Sciences*, 2001.

[36] Strogatz, S., *Nonlinear Dynamics and Chaos with applications to Physics, Biology, Chimestry, and Engineering*, Perseus Books Group, 1994.

[37] Pham, Q.-C. and Slotine, J.-J. E., "Stable Concurrent Synchronization in Dynamic System Networks," *Neural Networks*, Vol. 20, No. 1, 2007, pp. 62–77.

[38] Lohmiller, W. and Slotine, J.-J., E., "Contraction Analysis for Nonlinear Systems," *Automatica*, Vol. 34, No. 6, 1998, pp. 683–696.

[39] Kato, N. and Kamimura, S., *Bio-Mechanisms of Swimming and Flying: Fluid Dynamics, Biomimetic Robots, and Sports Science*, Springer Verlag, 2008.

[40] Seo, K., Chung, S.-J., and Slotine, J.-J. E., "CPG-Based Control of a Turtle-Like Uderwater Vehicle," *Autonomous Robots*, Vol. 28, No. 3, 2010, pp. 247269.

[41] Liberzon, D., *Switching in Systems and Control*, Birkhauser Boston, 2003.

[42] Taha, H. E., Hajj, M. R., and Nayfeh, A. H., "Wing Kinematics Optimization for Hovering Micro Air Vehicles Using Calculus of Variation," *Journal of Aircraft*, Vol. 50, No. 2, 2013, pp. 610–614.

[43] Berman, G. J. and Wang, Z. J., "Energy-minimizing kinematics in hovering insect flight," *Journal of Fluid Mechanics*, Vol. 582, No. 1, 2007, pp. 153,168.

[44] Ghommem, M., *Modeling and Analysis for Optimization of Unsteady Aeroelastic Systems*, Ph.D. thesis, Virginia Polytechnic Institute and State University, November 2011.

[45] Stanford, B. K., Beran, P. S., Snyder, R., and Patil, M., "Stability and Power Optimality in Time-Periodic Flapping Wing Structures," 53rd AIAA/ASME/ASCE/AHS/ASC Structures, Structural Dynamics and Materials Conference, Honolulu, Hawaii, April 2012, AIAA 2012-1638.

[46] Demoll, R., "Der Flug der Insekten und der Vogel," *Jena: G. Fischer*, 1918.

[47] Demoll, R., "Der Flug der Insekten," *Naturewissenschaften*, Vol. 7, 1919, pp. 480–481.

[48] Weis-Fogh, T. and Jensen, M., "Biology and Physics of Locust Flight. I. Basic Principles of Insect Flight. A Critical Review," *Philos. Trans.R. Soc. Lond. Ser. B*, Vol. 239, 1956, pp. 415–458.

[49] Holst, E. V. and Kuchemann, D., "Biologische und aerodynamische Probleme des Tierfluges," *Naturwissenschaften*, Vol. 29, 1941, pp. 348–362.

[50] Walker, G. T., "The Flapping Fligh of Birds," *J. R. Aero. Soc.*, Vol. 29, 1925, pp. 590–594.

[51] Walker, G. T., "The Flapping Fligh of Birds II," *J. R. Aero. Soc.*, Vol. 31, 1927, pp. 337–342.

[52] Osborne, M. F. M., "Aerodynamics of Flapping Flight With Application to Insects," *Journal of Experimental Biology*, Vol. 28, 1951, pp. 221–245.

[53] Parry, A. D., "The swimming of whales and a discussion of Gray's paradox," *Journal of Experimental Biology*, Vol. 26, 1949, pp. 24–34.

[54] Stolpe, M. and Zimmer, K., "Der Vogelflug. Leipzig: Akademische Verlagsgesellschaft," 1939.

[55] Chadwick, *Insect Physiology*, John Wiley and Sons, Inc., London: Chapman and Hall, Ltd., 1953.

[56] Ellington, C. P., "The aerodynamics of hovering insect flight: I. The quasi-steady analysis," *Philosophical Transactions Royal Society London Series B*, Vol. 305, 1984, pp. 1–15.

[57] Ellington, C. P., "The aerodynamics of hovering insect flight: II. Morphological parameters," *Philosophical Transactions Royal Society London Series B*, Vol. 305, 1984, pp. 17–40.

[58] Ellington, C. P., "The aerodynamics of hovering insect flight: IV. Aerodynamic mechanisms," *Philosophical Transactions Royal Society London Series B*, Vol. 305, 1984, pp. 79–113.

[59] Ellington, C. P., "The aerodynamics of hovering insect flight: V. A vortex theory," *Philosophical Transactions Royal Society London Series B*, Vol. 305, 1984, pp. 115–144.

[60] Ellington, C. P., "The aerodynamics of hovering insect flight: VI. Lift and power requirements," *Philosophical Transactions Royal Society London Series B*, Vol. 305, 1984, pp. 145–181.

[61] Weis-Fogh, T., "Energetics of Hovering Flight in Hummingbirds and Drosophila," *Journal of Experimental Biology*, Vol. 56, 1972, pp. 79–104.

[62] Wagner, H., "Uber die entstehung des dynamischen auftriebs von tragflugeln," *ZAMM*, Vol. 5, 1925.

[63] Ellington, C. P., den Berg C., V., Willmott, A. P., and Thomas, A. L. R., "Leading-edge vortices in insect flight," *Nature*, Vol. 384, 1996, pp. 626–630.

[64] Shkarayev, S. and Silin, D., "Applications of Actuator Disk Theory to Membrane Flapping Wings," *AIAA Journal*, Vol. 48, No. 10, 2010, pp. 22272234.

[65] Peters, D. A., Karunamoorthy, S., and Cao, W., "Finite-state induced flow models, Part I: two-dimensional thin airfoil." *J. Aircraft*, Vol. 44, 1995.

[66] Peters, D. A., "Two-dimensional incompressible unsteady airfoil theoryAn overview," *J. Fluids and Structures*, Vol. 24, 2008, pp. 295312.

[67] Ellington, C. P., "Unsteady aerodynamics of insect flight," Vol. 49, Soc. Exp. Biol., 1995, pp. 109–129.

[68] Phlips, P. J., East, R. A., and Pratt, N. H., "An unsteady lifting line theory of flapping wings with application to the forward flight of birds," *J. Fluid Mech.*, Vol. 112, 1981, pp. 97–125.

[69] Rayner, J. M. V., "A vortex theory of animal flight. Part 1. The vortex wake of a hovering animal," *J. Fluid Mech.*, Vol. 91, 1979, pp. 697–730.

[70] Rayner, J. M. V., "A vortex theory of animal flight. Part 2. The forward flight of birds," *J. Fluid Mech.*, Vol. 91, 1979, pp. 731–763.

[71] Rayner, J. M. V., "A new approach to animal flight mechanics," *Journal of Experimental Biology*, Vol. 80, 1979, pp. 17–54.

[72] Fritz, T. E. and Long, N. L., "Object-Oriented Unsteady Vortex Lattice Method for Flapping Flight," *J. Aircraft*, Vol. 41, No. 6, 2004, pp. 464–474.

[73] Stanford, B. K. and Beran, P. S., "Analytical Sensitivity Analysis of an Unsteady Vortex-Lattice Method for Flapping-Wing Optimization," *Journal of Aircraft*, Vol. 47, No. 2, 2010, pp. 647–662.

[74] Ghommem, M., Hajj, M. R., Mook, D. T.and Stanford, B. K., Beran, P. S.and Snyder, R. D., and Watson, L. T., "Global optimization of actively morphing flapping wings," *Journal of Fluids and Structures*, Vol. 33, 2012, pp. 210–228.

[75] Reissner, E., "Effect of Finite Span on the Air load Distributions for Oscillating Wings, I- Aerodynamic Theory of Oscillating Wings of Finite Span," Tech. Rep. 1194, NACA T.N., 1947.

[76] Reissner, E. and Stevens, J. E., "Effect of Finite Span on the Air load Distributions for Oscillating Wings, II- Methods of Calculation and Examples of Application," Tech. Rep. 1195, NACA T.N., 1947.

[77] Jones, R. T., "The Unsteady Lift of a Finite Wing," Tech. Rep. 682, NACA, 1939.

[78] Jones, R. T., "The Unsteady Lift of a Wing of Finite Aspect Ratio," Tech. Rep. 681, NACA, 1940.

[79] Dickinson, M. H. and Gotz, K. C., "Unsteady Aerodynamic Performance of Model Wings at Low Reynolds Numbers." *Journal of Experimental Biology*, Vol. 174, No. 1, 1993, pp. 45–64.

[80] Ansari, S. A., Zbikowski, R., and Knowles, K., "Non-linear Unsteady Aerodynamic Model for Insect-Like Flapping Wings in the Hover. Part1: Methodology and Analysis," *J. Aerospace Engineering*, Vol. 220, 2006, pp. 61–83.

[81] Ansari, S. A., Zbikowski, R., and Knowles, K., "Non-linear Unsteady Aerodynamic Model for Insect-Like Flapping Wings in the Hover. Part2: Implementation and Validation," *J. of Aerospace Engineering*, Vol. 220, 2006, pp. 169–186.

[82] Von Karman, T. and Sears, W. R., "Airfoil theory for nonuniformmotion." *J. Aeronautical Sciences*, Vol. 5, No. 10, 1938, pp. 379–390.

[83] Gogulapati, A., Friedmann, P. P., and Shyy, W., "Nonlinear Aeroelastic Effects in Flapping Wing Micro Air Vehicles," 49th AIAA / ASME / ASCE / AHS / ASC Structures, Structural Dynamics, and Materials Conference, Schaumburg, Illinois, 2008.

[84] Gogulapati, A. Friedmann, P. P. and Shyy, W., "Approximate Aeroelastic Analysis of Flapping Wings in Hover," IFASD, CEAS / AIAA / DGLR International Forum on Aeroelasticity and Structural Dynamics, Seattle, Washington, 2009.

[85] Ramamurti, R. and Sandberg, W., "A three-dimensional computational study of the aerodynamic mechanisms of insect flight," *Journal of Experimental Biology*, Vol. 205, No. 10, 2002, pp. 15071518.

[86] Sun, M. and Tang, J., "Lift and power requirements of hovering flight in Drosophila virilis," *Journal of Experimental Biology*, Vol. 205, 2002, pp. 2413–2427.

[87] Sun, M. and Du, G., "Lift and power requirements of hovering insect flight," *Acta Mech. Sin.*, Vol. 19, No. 5, 2003, pp. 458–469.

[88] Sun, M. and Wu, J. H., "Lift generation and power requirements of fruit fly in forward flight with modeled wing motion," *Journal of Experimental Biology*, Vol. 206, 2003, pp. 3065–3083.

[89] Sun, M. and Tang, J., "Unsteady Aerodynamic Force Generation by a Model Fruitfly Wing in Flapping Motion," *Journal of Experimental Biology*, Vol. 205, 2002, pp. 55–70.

[90] DeLaurier, J. D., "An Aerodynamic Model for Flapping Wing Flight," *Aeronautical Journal*, 1993, pp. 125–130.

[91] Mueller, T. H., *Fixed and Flapping Wing Aerodynamics for Micro Air Vehicles Applications*, AIAA Inc., 2001.

[92] Shyy, W., Lian, Y., Tang, J., Viiero, D., and Liu, H., *Aerodynamics of Low Reynolds Number Flyers*, Cambridge University Press, 2008.

[93] Sane, S. P., "The Aerodynamics of Insect Flight," *Journal of Experimental Biology*, Vol. 206, 2003, pp. 4191–4208.

[94] Wang, Z. J., "Dissecting Insect Flight," *Annual Review of Fluid Mechnics*, Vol. 37, 2005, pp. 183–210.

[95] Taylor, G. K. and Zbikowski, R., "Nonlinear Time Periodic Models of the Longitudinal Flight Dynamics of Desert Locusts," *J. Roy. Soc. Interface*, Vol. 1, 2005.

[96] Taylor, G. K., Bomphrey, R. J., and Hoen, J., "Insect Flight Dynamics and Control," AIAA Aerospace Sciences Meeting and Exhibit, 2006.

[97] Deng, X., Schenato, L., Wu, W. C., and Sastry, S. S., "Flapping Flight for Biomemetic Robotic Insects: Part I System Modeling," *IEEE Transactions on Robotics*, Vol. 22, No. 4, 2006, pp. 776–788.

[98] Orlowski, C. T., Girard, A. R., and Shyy, W., "Derivation and Simulation of the Nonlinear Dynamics of a FlappingWing Micro-Air Vehicle," European Micro-Air Vehicle Conference and Competition, Delft, The Netherlands, 2009.

[99] Orlowski, C. T., Girard, A. R., and Shyy, W., "Open Loop Pitch Control of a FlappingWing Micro AirVehicle Using a Tail and Control Mass," Institute of Electrical and Electronics Engineers, American Control Conference, Baltimore, MD, 2010, p. 536541.

[100] Orlowski, C. T. and Girard, A. R., "Modeling and Simulation of the Nonlinear Dynamics of Flapping Wing MAVs," *AIAA Journal*, Vol. 49, No. 5, 2011, pp. 969–981.

[101] Gao, N., Aono, H., and Liu, H., "A Numerical Analysis of Dynamic Flight Stability of Hawkmoth Hovering," *Journal of Biomechanical Science and Engineering*, Vol. 4, No. 1, 2009, pp. 105–116.

[102] Thomas, A. L. R. and Taylor, G. K., "Animal flight dynamics I. Stability in gliding flight." *Journal of Theoretical Biology*, Vol. 212, No. 1, 2001, pp. 399–424.

[103] Bisplinghoff, R. L., Ashley, H., and Halfman, R. L., *Aeroelasticity*, Dover Publications, New York, 1996.

[104] Pistolesi, E., "Betrachtungen uber die gegenseitige Beeinflussung von Tragflugelsystemen," *Ges. Vor. Lil.-Ges. Lufo*, 1937, pp. 214–219.

[105] Schlichting, H. and Truckenbrodt, E., *Aerodynamics of the Airplane*, McGraw-Hill, 1979.

[106] Cebeci, T., Platzer, M., Chen, H., Chang, K.-C., and Shao, J. P., *Analysis of Low Speed Unsteady Airfoil Flows*, Horizons Publishing Inc., Long Beach and Springer Berlin Heidelberg New York, 2005.

[107] Van den Berg, C. and Ellington, C. P., "The Vortex Wake of a Hovering Model Hawkmoth," *Philos. Trans.R. Soc. Lond. Ser. B*, Vol. 352, 1997, pp. 317–328.

[108] Van den Berg, C. and Ellington, C. P., "The Three-Dimensional Leading-Edge Vortex of a Hovering Model Hawkmoth," *Philos. Trans.R. Soc. Lond. Ser. B*, Vol. 352, 1997, pp. 329–340.

[109] Willmott, A. P., Ellington, C. P., and Thomas, A. L. R., "Flow Visualization and Unsteady Aerodynamics in the Flight of the Hawkmoth Manduca Sexta," *Philos. Trans.R. Soc. Lond. Ser. B*, Vol. 352, 1997, pp. 303–316.

[110] Wang, Z. J., Birch, J. M., and Dickinson, M. H., "Unsteady forces in hovering flight: computation vs experiments," *Journal of Experimental Biology*, Vol. 207, 2004, pp. 449–460.

[111] Sane, S. P. and Dickinson, M. H., "The aerodynamic effects of wing rotation and a revised quasi-steady model of flapping flight." *Journal of Experimental Biology*, Vol. 205, 2002, pp. 1087–1096.

[112] Dickson, W. B. and Dickinson, M. H., "The Effect of Advance Ratio on the Aerodynamics of Revolving Wings," *Journal of Experimental Biology*, Vol. 207, 2004, pp. 4269–4281.

[113] Polhamus, E. C., "A Concept of The Vortex Lift of Sharp-Edge Delta Wings Based on a Leading-Edge-Suction Analogy," Tech. Rep. NASA TN D-3767, Langely Research Center, Langely Station, Hampton, Va, 1966.

[114] Taylor, G. K. and Thomas, A. L. R., "Animal Flight Dynamics II. Longitudinal Stability in Flapping Flight," *Journal of Theoretical Biology*, Vol. 214, 2002.

[115] Orlowski, C. T. and Girard, A. R., "Averaging of the Nonlinear Dynamics of Flapping Wing MAV for Symmetrical Flapping," Aerospace Sciences Meeting, 2011.

[116] Bolender, M. A., "Rigid Multi-Body Equations-of-Motion for Flapping Wing MAVs Using Kanes Equations," AIAA Guidance, Navigation, and Control Conference, Chicago,IL, 2009.

[117] Khalil, H. K., *Nonlinear Systems*, Prentice Hall, 3rd ed., 2002.

[118] Lanchester, F. W., *Aerodenetics*, London: Constable, 1908.

[119] Cook, M., V., *Flight Dynamics Principles*, Elsevier Ltd., 2007.

[120] Nayfeh, A. H. and T.Mook, D., "Energy transfer from high-frequency to low-frequency modes in structures," *ASME Special Combined Issue of the J. Mech. Des. and J. Vib. Acoust.*, Vol. 117, 1995, pp. 186–195.

[121] Nayfeh, A. H., *Nonlinear Interactions*, John Wiley and Sons, Inc., New York, 2000.

[122] Anderson, T. J., Balachandran, B., and Nayfeh, A. H., "Nonlinear resonances in a flexible cantilever beam," *J. Vib. Acoust.*, Vol. 116, 1994, pp. 480–484.

[123] Tabaddor, M. and Nayfeh, A. H., "An experimental investigation of multimode responses in a cantilever beam," *J. Vib. Acoust.*, Vol. 119, 1997, pp. 532–538.

[124] Nayfeh, S. A. and Nayfeh, A. H., "Energy transfer from high- to low-frequency modes in a flexible structure via modulation," *J. Vib. Acoust.*, Vol. 116, 1994, pp. 203–207.

[125] Oh, K. and Nayfeh, A. H., "High- to low-frequency modal interactions in a cantilever composite plate," *J. Vib. Acoust.*, Vol. 120, 1998, pp. 579–587.

[126] Popovic, P., Nayfeh, A. H., Oh, K., and Nayfeh, S. A., "An experimental investigation of energy transfer from a high-frequency mode to a low frequency mode in a flexible structure," *J. Vib. Cont.*, Vol. 1, 1995, pp. 115–128.

[127] Nayfeh, S. A. and Nayfeh, A. H., "Nonlinear interactions between two widely spaced modes - external excitation," *Int. J. Bif. Chaos*, Vol. 3, 1993, pp. 417–427.

[128] Nayfeh, A. H. and Chin, C.-M., "Nonlinear interactions in a parametrically excited system with widely spaced frequencies," *Nonlinear Dyn.*, Vol. 7, 1995, pp. 195–216.

[129] Nayfeh, A. H. and Balachandran, B., *Applied Nonlinear Dynamics*, John Wiley and Sons, Inc., 1995.

[130] Nayfeh, A. H. and Mook, D. T., *Nonlinear Oscillations*, John Wiley and Sons, Inc., New York, 1995.

[131] Lust, K., "Improved Numerical Floquet Multipliers," *International Journal of Bifurcation and Chaos in Applied Sciences and Engineering*, Vol. 11.

[132] Cesnik, C. E. S. and Brown, E. L., "Modeling of High Aspect Ratio Active Flexible Wings for Roll Control," AIAA/ASME/ASCE/AHS/ASC Structures, Structural Dynamics, and Materials Conference, Denver, Colorado, 2002.

[133] Cesnik, C. E. S. and Brown, E. L., "Active Wing Warping Control of a Joined-Wing Airplane Configuration," AIAA/ASME/ASCE/AHS/ASC Structures, Structural Dynamics, and Materials Conference, Norfolk, Virginia, 2003.

[134] Fry, S., Sayman, R., and Dickinson, M. H., "The aerodynamics of free-flight maneuvers in Drosophila," *Science*, Vol. 300, No. 5618, 2003, pp. 495498.

[135] Hengstenberg, R., "Mechanosensory control of compensatory head roll during flight in the blowfly Calliphora erythrocephala," *J. Compar. Physiol. A, Sensory Neural Behav. Physiol.*, Vol. 163, 1988, pp. 151165.

[136] Nalbach, G., "The halteres of the blowfly Calliphora: I. Kinematics and dynamics," *J. Compar. Physiol. A*, Vol. 173, 1993, pp. 293300.

[137] Nalbach, G. and Hengstenberg, R., "The halteres of the blowfly Calliphora: I. Three-dimensional organization of compensatory reactions to real and simulated rotations," *J. Compar. Physiol. A*, Vol. 175, 1994, pp. 695708.

[138] Taylor, C., "Contribution of compound eyes and ocelli to steering of locusts in flight: III," *Journal of Experimental Biology*, Vol. 93, 1981, pp. 131.

[139] Kastberger, R., "The ocelli control the flight course in honeybees," *Physiolog. Entomol.*, Vol. 15, 1990, pp. 337346.

[140] Bullo, F., "Averaging and vibrational control of mechanical systems," *SIAM Journal on Control and Optimization*, Vol. 41, No. 2, 2002, pp. 542–562.

[141] Bloch, A. M., *Nonholonomic mechanics and control*, Applied Mathematics, Springer-Verlag, Berlin, Germany, 2003.

[142] Sussmann, H. J. and Liu, W., "Limits of highly oscillatory controls and the approximation of general paths by admissible trajectories," Vol. 1, 30th IEEE Conf. Decision Control, New York, 2001, p. 437425.

[143] Vela, P. A., *Averaging and Control of Nonlinear Systems (with Application to Biomimetic Locomotion)*, Ph.D. thesis, California Institute of Technology, Pasadena, CA, May 2003.

[144] Sira-Ramirez, H. and Agrawal, S. K., *Differentially Flat Systems*, Marcel Dekker, Inc., 2004.

[145] Ansari, S. A., Zbikowski, R., and Knowles, K., "Aerodynamic modelling of insect-like flapping flight for micro air vehicles," *Progress in Aerospace Sciences*, Vol. 42, 2006, pp. 129–172.

[146] Taha, H. E., Hajj, M. R., and Nayfeh, A. H., "Flight Dynamics and Control of Flapping-Wing MAVs: A Review," *Nonlinear Dynamics*, Vol. 70, No. 2, 2012, pp. 907–939.

[147] Peters, D. A. and Johnson, M. J., "Finite-state airloads for deformable airfoils on fixed and rotating wings," No. 44, ASME Winter Annual Meeting, Aeroelasticity and Fluid/ Structures Interaction Problems, a Mini-Symposium, Chicago, 1994, pp. 1–28.

[148] Peters, D. A., Barwey, D., and Johnson, M. J., "Finite-state airloads modeling with compressibility and unsteady free-stream," Sixth International Workshop on Dynamics and Aeroelastic Stability Modelling of Rotorcraft systems, UCLA, 1995.

[149] Peters, D. A. and Karunamoorthy, S., "State-space inflow models for rotor aeroelasticity," Stanford University, Proceedings of the Holt Ashley 70th Anniversary Symposium, 1993.

[150] Peters, D. A. and Karunamoorthy, S., "State-space inflow models for rotor aeroelasticity," AIAA, 12th Applied Aerodynamics Conference, Colorado Springs, 1994.

[151] Jones, R. T., "Operational treatment of the nonuniform lift theory to airplane dynamics," Tech. Rep. 667, NACA, 1938.

[152] Abbott, I. H. and Von Doenhoff, A. E., *Theory of Wing Sections*, Dover Publications, New York, 1959.

[153] Usherwood, J. R. and Ellington, C. P., "The aerodynamics of revolving wings I. Model hawkmoth wings," *Journal of Experimental Biology*, Vol. 205, 2002.

[154] Dudley, R. and Ellington, C. P., "MECHANICS OF FORWARD FLIGHT IN BUMBLEBEES II. QUASI-STEADY LIFT AND POWER REQUIREMENTS," *Journal of Experimental Biology*, Vol. 148, 1990, pp. 53–88.

[155] Theodorsen, T., "General Theory of Aerodynamic Instability and the Mechanism of Flutter," Tech. Rep. 496, NACA, 1935.

[156] Garrick, I. E., "On some reciprocal relations in the theory of nonstationary flows," Tech. Rep. 629, NACA, 1938.

[157] Van der Wall, B. and Leishman, J. G., "The Influence of Variable Flow Velocity on Unsteady Airfoil Behavior," *J. American Helicopter Soc.*, Vol. 39, No. 4, 1994.

[158] Beddoes, T. S., "Representation of Airfoil Behavior," *Vertica*, Vol. 7, No. 2, 1983, pp. 183–197.

[159] Leishman, J. G. and Beddoes, T. S., "A Generalized Model for Unsteady Aerodynamic Behavior and Dynamic Stall Using the Indicial Method," 42nd Annual Forum of the American Helicopter Society, Washingotn D.C., June 1986.

[160] Leishman, J. G. and Nguyen, k. Q., "State-Space Representation of Unsteady Airfoil Behavior," *AIAA Journal*, Vol. 28, No. 5, 1990, pp. 836–844.

[161] Leishman, J. G. and Crouse, G. L., "State-Space Model for Unsteady Airfoil Behavior and Dynamic Stall," No. 89-1319, AIAA, 1989, pp. 1372–1383.

[162] Fung, Y. C., *An Introduction to the Theory of Aeroelasticity*, New York: Dover., 1969.

[163] Jones, W. P., "Aerodynamic forces on wings in non-uniform motion," Tech. Rep. 2117, British Aeronautical Research Council, 1945.

[164] Ennos, A. R., "The Kinematics and Aerodynamics of the Free Flight of Some Diptera," *Journal of Experimental Biology*, Vol. 142, 1989, pp. 49–85.

[165] Kurdi, M., Stanford, B., and Beran, P., "Kinematic Optimization of Insect Flight for Minimum Mechanical Power," AIAA paper 2010-1420, Jan 2010.

[166] Roskam, J. and Lan, C.-T. E., *Airplane Aerodynamics and Performance*, DARcorporation, Lawrence, Kansas, 1997.

[167] Taha, H. E., Hajj, M. R., and Beran, P. S., "Unsteady Nonlinear Aerodynamics of Hovering MAVs/Insects," AIAA-Paper 2013-0504, Jan 2013.

[168] Taha, H. E. and Hajj, M. R., "State Space Representation of the Unsteady Aerodynamics of Flapping Flight," *submitted to Aerospace Science and Technology*, 2013.

[169] Sane, S. P. and Dickinson, M. H., "The Control of Flight Force by a Flapping Wing: Lift and Drag Force Production," *Journal of Experimental Biology*, Vol. 204, 2001, pp. 2607–2626.

[170] Taha, H. E., Hajj, M. R., and Nayfeh, A. H., "On the Longitudinal Flight Dynamics of Hovering MAVs/Insects," *Journal of Guidance Control and Dynamics, In Press*.

[171] Taha, H. E., Nayfeh, A. H., and Hajj, M. R., "Saturation-Based Actuation for Flapping MAVs in Hovering and Forward Flight," *Nonlinear Dynamics*, Vol. 73, No. 1, 2013, pp. 1125–1138.

[172] Lee, E. B. and Markus, L., *Foundations of Optimal Control Theory*, John Wiley and Sons, Inc., 1976.

[173] Bhatia, M., Patil, M., Woolsey, C., Stanford, B., and Beran, P., "LQR Controller for Stabilization of Flapping Wing MAVs in Gust Environments," AIAA, Atmospheric Flight Mechanics Conference, Minneapolis, Minnesota, Aug 2012.

[174] Greenwood, D. T., *Advanced Dynamics*, Cambridge University Press, The Edinburgh Building, Cambridge CB2 2RU, UK, 2003.

[175] Nayfeh, A. H., Mook, D. T., and Marshall, L. R., "Nonlinear Coupling of Pitch and Roll Modes in Ship Motion," *J. Hydronautics*, Vol. 7, No. 4, 1973, pp. 145–152.

[176] Haddow, A. G., Barr, A. D. S., and Mook, D. T., "Theoretical and Experimental Study of Modal Interaction in a Two-Degree-of-Freedom Structure," *J. Sound and Vibration*, Vol. 97, No. 3, 1984, pp. 451–473.

[177] Nayfeh, A. H. and Balachandran, B., "Modal Interactions in Dynamical and Structural Systems," *Appl. Mech. Reviews*, Vol. 42, No. 11, 1989, pp. 175–202.

[178] Nayfeh, A. H., *Perturbation Methods*, John Wiley and Sons, Inc., 1973.

[179] Nayfeh, A. H., *Introduction to Perturbation Techniques*, John Wiley and Sons, Inc., 1981.

[180] Balachandran, B. and Nayfeh, A. H., "Nonlinear motions o f beam-mass structure," *Nonlinear Dynamics*, Vol. 1, 1990, pp. 39–61.

[181] Oueini, S. S., Nayfeh, A. H., and Gonaraghi, M. A., "A theoretical and experimental implementation of a control method based on saturation," *Nonlinear Dynamics*, Vol. 13, 1997, pp. 189–202.

[182] Oueini, S. S., Nayfeh, A. H., and Pratt, J. R., "A Nonlinear Vibration Absorber for Flexible Structures," *Nonlinear Dynamics*, Vol. 15, No. 3, 1998, pp. 259–282.

[183] Hall, B. D., Mook, D. T., Nayfeh, A. H., and Preidikman, S., "Novel Strategy for Suppressing the Flutter Oscillations of Aircraft Wings," *AIAA Journal*, Vol. 39.

[184] Nayfeh, A. H. and Mook, D. T., *Nonlinear Oscillations*, John Wiley and Sons, Inc., 1979.

[185] Nayfeh, A. H., *Nonlinear Interactions: Analytical, Computational, and Experimental Methods*, John Wiley and Sons, Inc., 2002.

[186] Taha, H. E., Nayfeh, A. H., and Hajj, M. R., "Aerodynamic-Dynamic Interaction and Longitudinal Stability of Hovering MAVs/Insects," No. AIAA 2013-1707, 54th Structural Dynamics and Materials Conference, Boston, Apr 2013.

[187] Etkin, B., *Dynamics of Flight - Stabililty and Control*, JOHN WILEY and SONS, 1996.

[188] Sarychev, A., "Stability Criteria for Time-periodic Systems via High-order Averaging Techniques," *Nonlinear Control in the Year 2000*, Vol. 2 of *Lecture Notes in Control and Information Sciences*, Springer-Verlag, 2001.

[189] Bierling, T. and Patil, M., "Nonlinear Dynamics and Stability of Flapping-Wing Flight," International Forum on Aeroelasticity and Structural Dynamics, 2009, pp. 2–5.

[190] Agrachev, A. A. and Gamkrelidze, R. V., "The exponential representation of flows and the chronological calculus," *Mathematics of the USSR: Sbornik*, Vol. 35, No. 6, 1979, pp. 727–785.

[191] Vela, P. A., *Averaging and Control of Nonlinear Systems (with Application to Biomimetic Locomotion)*, Ph.D. thesis, California Institute of Technology, Pasadena, CA, May 2003.

[192] Ogata, K., *Discrete-Time Control Systems*, Vol. 1, Prentice-Hall, Englewood Cliffs, NJ, 1987.

[193] Taha, H. E., Hajj, M. R., Roman, A. H., and Nayfeh, A. H., "A Calculus of Variations Approach for Optimum Maneuverability of Flapping MAVs Near Hover," *submitted to Journal of Guidance Control and Dynamics*.

[194] Wu, J. H., Zhang, Y. L., and Sun, M., "Hovering of model insects: simulation by coupling equations of motion with Navier-Stokes equations," *The Journal of Experimental Biology*, Vol. 212, No. 20, 2009, pp. 3313–3329.

[195] Bullo, F. and Lewis, A. D., *Geometric control of mechanical systems*, Applied Mathematics, Springer-Verlag, Berlin, Germany, 2004.

[196] Vela, P. A., Morgansen, K. A., and Burdick, J. W., "Second order averaging methods for oscillatory control of underactuated mechanical systems," *Proc. American Control Conference*, Anchorage, AK, May 2002.

[197] Vela, P. A., Morgansen, K. A., and Burdick, J. W., "Underwater locomotion from oscillatory shape deformations," *Proc. IEEE Conference on Decision and Control*, Vol. 2, Las Vegas, NV, December 2002, pp. 2074–2080.

[198] Guckenheimer, J. and Holmes, P., *Nonlinear Oscillations, Dynamical Systems, and Bifurcations of Vector Fields*, Academic Press, New York, NY, 1983.